Development of nanostructured materials based on manganese oxides and produced by an electrochemical method for water electrolysis

Wenchao Yu

Université Pierre et Marie Curie

Chimie Physique et Chimie Analytique de Paris-Centre

(ED 388)

Laboratoire Interfaces et Systèmes Electrochimiques

(LISE, UMR8235)

Development of nanostructured materials based on manganese oxides and produced by an electrochemical method for water electrolysis

Par Wenchao YU

Thèse de doctorat de Chimie Physique et Chimie Analytique

Dirigée par Alain PAILLERET

Présentée et soutenue publiquement le 17 Octobre 2016

Devant un jury composé de :

M. **KOKOH Kouakou Boniface**	Professeur, SFA-UMR7285-IC2MP, UFR Sciences Fondamentales et Appliquées Université de Poitiers	Rapporteur
M. **AUBERT Pierre-Henri**	Maître de Conférences-HDR, Département de Chimie, Université de Cergy-Pontoise	Rapporteur
Mme. **JOLIVALT Claude**	Professeur, UMR 7197-LRS, Université Pierre et Marie CURIE	Examinateur
M. **PAILLERET Alain**	Maître de Conférences-HDR, UMR 8235- LISE, Université Pierre et Marie CURIE	Directeur de Thèse

Acknowledgements

This thesis comes from a doctoral program between Université Pierre et Marie CURIE (UPMC, Paris VI), Centre National de la Recherche Scientifique (CNRS) and China Scholarship Council (CSC). All experiments were performed in Laboratoire Interfaces et Systèmes Electrochimiques (LISE, UMR 8235). Thanks to those who made this thesis possible. The financial support from China Scholarship Council is appreciated.

I would like to thank my tutor Dr. Alain Pailleret (Maître de Conférences HDR, UPMC) for his instruction to this thesis. He is always very kind to answer my questions and help me figure out problems. Also, he helped me a lot when I first arrived in Paris, France. It was very difficult for a foreigner starting a new life in a totally strange country, especially for me, a Chinese student who never went abroad before. Without his help, it would not be easy to get into the new life here. In addition, he cares much about my life, my accommodation, my roommate, my holidays, and he tells me much information about Paris, about France, all of these make me feel warm in my heart. He is my supervisor, and also a best friend, I really appreciate all the help and concerns he gives me.

Then, I would like to thank Franck Hui (Chargé de Recherche HDR, CNRS) for his help during my Ph.D. application. Thanks to him for providing this doctoral program and choosing me as a candidate. He helped me a lot for preparation of the documents so that I could get the financial support for my studies in France. He was supposed to be the co-director of this thesis; unfortunately, he fell sick since the beginning. I wish he could recover as quickly as possible.

In addition, I would like to thank: Dr. Cyrille Bazin for the XRD analysis and the discussion about the electrodeposition techniques; Ms. Françoise Pillier for the SEM and EDS analysis, and the French conversation; and Florence Billon for the substrate material preparation. They always respond and meet my requests in the first time, making sure my work goes on well. Their contribution is very important to this thesis. Many thanks to the lab director François Huet for giving the impedance spectroscopy course, and two secretaries Ms. Martine Chaduc and Ms. Isabelle Lefèbvre for the paper work and daily management. I also want to give my gratitude to my colleagues: Achraf Blout, Adrien Mocaër, Edgard Ngaboyamahina, Marie Steffenhagen, Nour Eddin Yakdi, Pierluca Messina, Pierre Aubertin,

Simon Rano, Wanli Gao and the others. I enjoyed the food they cooked, which gives me a chance to taste homemade French cooking, and I had very great time during traveling to Lisbon and Berlin with them. I will cherish these memories forever.

Next, I want to thank my parents and my elder sister for all their understanding and support. Most of my childhood friends already have a job, a family and even a child now; their parents could rest more and enjoy life. However, my parents still have to work very hard in order to make me an easier future life. My elder sister is always by my side and tries to satisfy any of my requests. She has constructed a family two years ago and my nephew is one year old by September. My family is getting bigger and bigger. I can feel their love anywhere and anytime. I really appreciate all the things they have done for me. At the same time, I want to thank my uncles, my grandmas and my childhood friends for their concerns. I wish you all the best.

Moreover, I would like to thank my roommate Lin Chi. We share our apartment for almost the whole three years, and she is the one that I get along with for the longest time during my stay here. She is very generous and tolerant, which makes the home time easy and relaxed. Thanks a lot to Mr. Alain Rolland, the owner of my apartment, for offering a very good apartment with a very low price and convenient surroundings and transportation. I also want to thank my best friend Zhengfang Wang, a happy and optimistic boy. I learned how to swim under his instruction, and benefit a lot from that. Thank all the other friends who spent time with me for new-year get-togethers, playground, shopping and trips.

I would like to take this chance to give my special gratitude to my girlfriend, Jianling Zou. She is a strong and diligent girl, and very good at cooking. She made all schedules for our trips in France and in Europe, which gave us pleasant and unforgettable memories. I enjoy the food she cooked and the time with her very much. With her accompany, life in Paris becomes much more beautiful and wonderful. Thank you very much!

At last, I would like to thank all people appeared in my life, I could not become the person I am today without you. Thank you all!

Content

General Introduction

Along with the development of human society, the energy demand is continuously increasing. Nowadays, the energy we are using mainly comes from the combustion of traditional fossil fuels such as oil and coal. However, the reserve of these fuels is limited on earth. The optimistic estimation for the depletion of fossil fuels is just a few centuries, and then comes the energy crisis. After that, how could we maintain our life? Moreover, the combustion of oil and coal is well known to cause severe environmental problems including air pollution, global warming, and the consequent respiratory system disease and extreme weather. All of these urge the development of alternative energy sources that are sustainable and friendly to environment. Several possible techniques have been developed and some of them have been introduced to current energy systems, including nuclear energy, photovoltaics, wind power and so on.

On the other hand, the sun provides people a hopeful way to solve the energy problems. If we could use solar energy efficiently, even a small part is enough to support the energy requirement of the whole human society. The utilization of solar energy has long been a research highlight from years ago, and some techniques have great potential for large-scale applications. Among them, solar fuel cells draw vast attention. The concept is similar to the natural photosynthesis, which absorbs solar energy to fix CO_2 molecules in the form of organic molecules. In a solar fuel cell, water molecules are split into oxygen and hydrogen using solar energy, while hydrogen, which is a totally green fuel, acts as the energy storage role to fix solar energy. It contains two reactions: the hydrogen evolution reaction (HER) and the oxygen evolution reaction (OER), in which the latter one is much more difficult to carry out due to the slow kinetic and high energy demand. Thus to find a cheap and efficient catalyst to promote the OER efficiency becomes the key point for the application of this technique.

In the past years, different materials have been employed for OER and by far, the best catalysts are still based on precious metal oxides such as IrO_2 and RuO_2. In recent years, transition metal oxide becomes another research direction, which could provide promising efficiency and greatly lower the expense of the catalyst comparing with precious metal oxides. As the natural oxygen evolution complex in photosystem II is revealed to be a Mn_4CaO_5 cluster, manganese oxides are considered as promising photoelectrochemical oxygen

evolution catalysts and draw much attention. Among the different manganese oxides with different crystalline structures, the birnessite-type MnO_2 is more interesting because it bears many similarities to the natural Mn_4CaO_5 cluster. Chemical synthesis and electrodeposition are two commonly used preparation methods. Using the first method always produces powder like catalysts, which necessitates more steps to elaborate an electrode; while using the later one can directly lead to MnO_2 catalyst films that can be used immediately, making the preparation easier and more simple. However, the main problems lie in the catalytic activity and mechanical stability of this kind of catalyst.

In this thesis, MnO_2 thin films were prepared using electrodeposition method, different parameters including the pH value, ion concentration and electrodeposition techniques were evaluated in order to obtain stable either amorphous or birnessite-type MnO_2 films. Then the influence of electrodeposition potential and substrate material on the film properties and OER performances were illustrated. After that, the post heat treatment was carried out on selected MnO_2 films in order to investigate the effect on their electrocatalytic activity and stability. At last, different cations were introduced in the electrodeposition solution for the preparation of MnO_2 films, and the function of those cations was discussed.

Through this thesis, MnO_2 films are proved to be effective (photo-) electrocatalysts for the electrochemical and photoelectrochemical oxygen evolution reaction. But still, its efficiency can be further promoted. There is a long way to go before electrodeposited MnO_2 films can answer the demand of large-scale applications.

Chapter I: Introduction

Energy is the foundation of our daily life and society's development. Nowadays, the main energy sources are based on fossil fuels, such as oil, coal and natural gas. They contribute about 85% of the total global consumption, and for developed countries, the number could approach 90%[1]. As our living standard increases, the demand of energy supply increases too. However, the problem we are facing is that the remaining resources of these fossil fuels are limited. According to a report written by Lewis and Nocera *et al*.[2], the global energy consumption rate would increase to ~ 27 TW by 2050, which is doubled the consumption of 13.5 TW in 2001, while at this high consumption rate, the estimated fossil energy resources could only support for several centuries. This is a relatively optimistic estimation. Based on Shahriar Shafiee and Erkan Topal's calculation, the reserves of oil and gas will run out in the next 40 years and coal in 100 years, which makes the alternative energy development extremely urgent[3]. Furthermore, the combustion of fossil fuels would release greenhouse gases and other air pollutants, therefore causing severe environmental problems. As the fossil fuel consumption is doubled, the emission of carbon dioxide is also doubled (from 24.07 Gt CO_2/year in 2001 to 40.03 Gt CO_2/year by 2050[4]). As a consequence, global warming becomes an emerging and long lasting issue to which more and more attention has been paid. Thus, to find alternative practical, clean, and most importantly carbon-free energy sources becomes a crucial strategy for the continuous development of human society in the future.

In the past years, great efforts have been spent on investigating new energy sources other than traditional fossil fuels, such as nuclear energy, wind and tidal wave power, or yet photovoltaics. Nuclear energy could be a good candidate as it could provide huge amount of energy and possesses all of the necessary elements for an alternative energy source. In 2007, 436 nuclear power plants operated by 30 countries generated 370 GW of electricity, accounted for 14 % of the global generated electricity[5]. At the same time, the application of nuclear energy is constrained by its dangerous and capital intensive feature. In addition, the high cost of construction of nuclear plant and waste disposal are also suppression factors[6]. As some accidents happened in the past years (Three mile island in 1979; Chernobyl in 1986; Fukushima in 2011), the application of nuclear energy is more and more questioned. Wind and tidal wave power are all periodic sources that influenced by the environmental conditions,

which makes these kinds of energy improper for large scale applications. Photovoltaics is a promising method to generate electricity. By the end of 2014, a total amount of 178 GW of photovoltaic energy sources had been installed all over the world and a 540 GW capacity was expected in the next five-year period[7]. On the contrary, the pollution and carbon emission during the fabrication of solar cells is still high. The efficiency of photovoltaics is also affected by the weather and solar intensity, and it could not support the entire energy demand alone without an adapted and mature large-scale energy storage strategy. As a consequence, new alternative energy sources remain a key problem that human beings are facing in the near future.

Considering the drawbacks of photovoltaics, storing solar energy into chemical bonds is more feasible for storage and transportation. Thus, converting sunlight energy into chemical fuels, the so-called "solar-to-fuels" strategy becomes the new frontier of scientific research.

I.1 Photosynthesis

Solar energy is a kind of totally green and infinite renewable energy source. The energy that sunlight gives to the earth in one hour is equal to the annual energy consumption from traditional fossil fuels [2]. Unfortunately, its development and utilization is still limited. If we could find an efficient way to take advantage of solar energy, all of the energy problems would be settled.

In nature, plants and trees have an original mechanism to take advantage of solar energy, named photosynthesis. It plays an important role in the evolution of ecosystem on the earth, even the fossil fuels we rely on today were produced from photosynthesis of the ancient plants. The mechanism of natural photosynthesis has been studied for years and the details have been revealed. Figure I.1 shows the brief energy flow in natural photosynthesis.

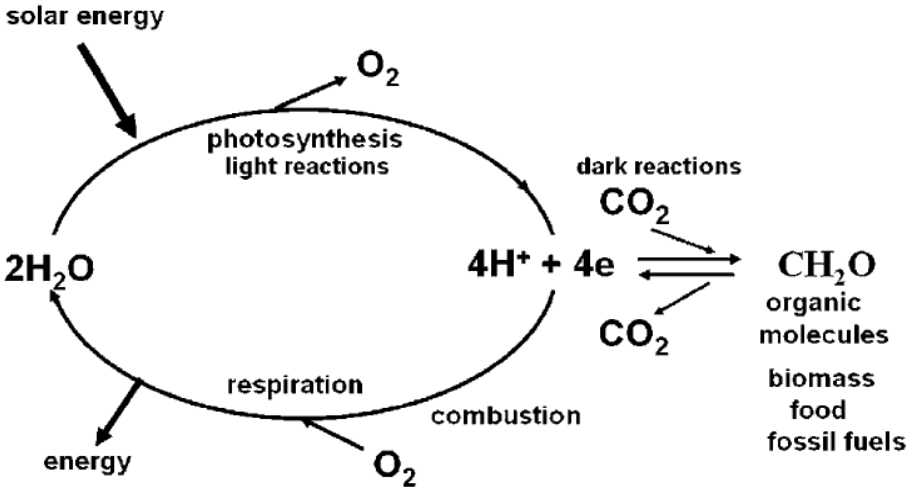

Figure I.1: A schematic diagram of energy flow in nature world. Taken from ref 8[8].

Photosynthesis is not merely a single reaction, instead, it contains a series of complex reactions happening inside organic molecules. Briefly, solar energy is absorbed and converted to chemical energy and stored as carbohydrates. It contains two sets of reactions: light reactions and dark reactions. In the light reaction part (energy storage), solar energy (photon) is absorbed by chlorophyll to generate oxygen molecules, activated electrons (e^-, always referred to as "reducing equivalents") and protons (H^+); while in the dark reaction part (hydrogen storage), the generated H^+ and e^- species react with carbon dioxide to form carbohydrate molecules and act as the ingredient of natural plants. In this way, solar energy is converted and stored in the organic chemical bonds. On the other hand, the consumption of carbohydrates via plant combustion or organisms respiration would release the energy initially originated from the sunlight, forming then water and carbon dioxide. Thus a cycle is completed.

As the investigations went deeper, the detailed mechanism of photosynthesis was more clearly understood by scientists. Figure I.2 shows a simplified model of the light-driven reactions. Photons are absorbed by the reaction center in photosystem II (PSII), and activated electrons and electron holes are generated. Those electrons are transferred through a series of redox-active cofactors including plastoquinol (PQH_2), plastocyanin (PC), cytochrome b6f (cyt b6f) complex and others, finally arrive at ferredoxin (Fd) which is bounded to photosystem I (PSI). The process is also called proton-coupled electron transfer (PCET). Then, protons combine with nicotinamide adenine dinucleotide phosphate ($NADP^+$) under

the action of ferredoxin/$NADP^+$ reductase (FNR) to form NADPH, this later react with CO_2 to finish the dark reaction in Figure I.1. On the other hand, electron holes generated as a consequence of the electron transfer are passed to the oxygen-evolving complex (OEC) inside PSII and assist the splitting of water into oxygen and protons.

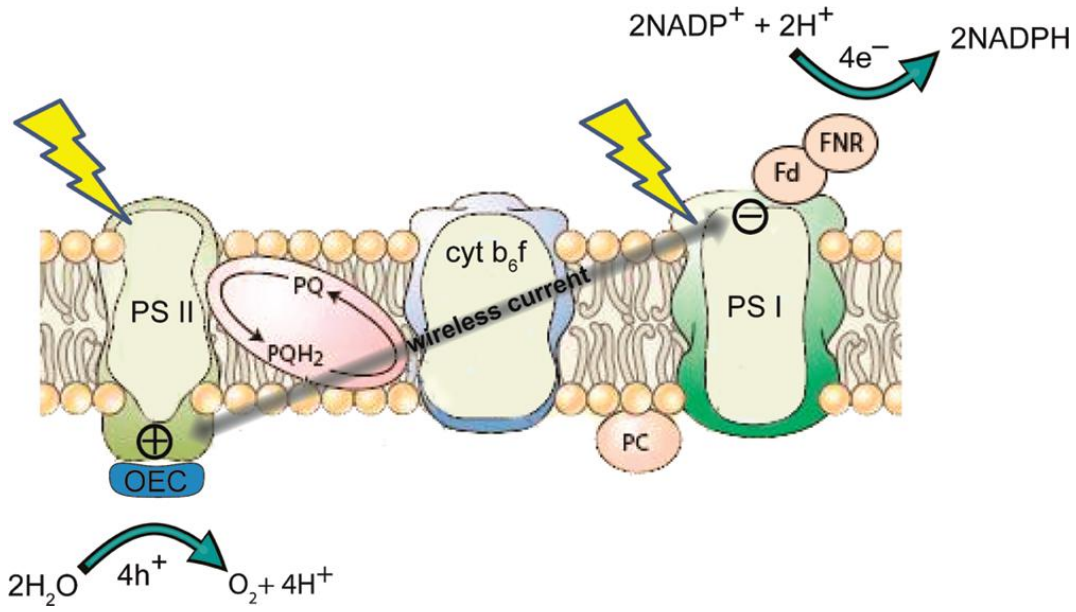

Figure I.2: A simplified scheme showing the light-driven reactions of photosynthesis. Taken from ref 9[9].

I.2 Oxygen evolving complex (OEC)

The development of microscopic analysis techniques enables the study of the fine structure of the natural photosynthesis complex. PSII, which catalyzes the photoinduced oxidation of water, is regarded as the center of photosynthesis. Nowadays, after years of investigations, its structure has been revealed by several studies. Barber's group revealed the fine structure of the PSII in cyanobacterium with a 3.5 Å resolution, suggesting that the OEC is constituted of a manganese-calcium cluster in which 3 Mn, 1 Ca and 4 O atoms form together a cubane-like structure (Mn_3CaO_4) and a fourth Mn atom links to the cubane by a mono-μ-oxo bridge[8]. This structure has been confirmed by Umena's group under a 1.9 Å resolution, and the metal atoms of the Mn_4CaO_5 cluster as well as their ligands are clearly located[10], as shown in Figure I.3. To make it easily understood, a simplified structure of Mn_4CaO_5 is also presented in this Figure.

The formation of dioxygen is known as the S-state cycle, as shown in Figure I.4. It contains at least 5 intermediate Mn valence states to finish a cycle, denoted as S_0 to S_4 respectively. During the state evolution S_0 to S_4, four photons are absorbed by the primal electron donor P680 to form activated electron and hole pairs, which are transferred through the redox active cofactor Y_z to the Mn_4CaO_5 cluster step by step, leading to the rising of the oxidation state of Mn ions. Under the action of those high potential Mn ions, a dioxygen molecule is formed with the expense of two water molecules during the last step S_4 to S_0[8].

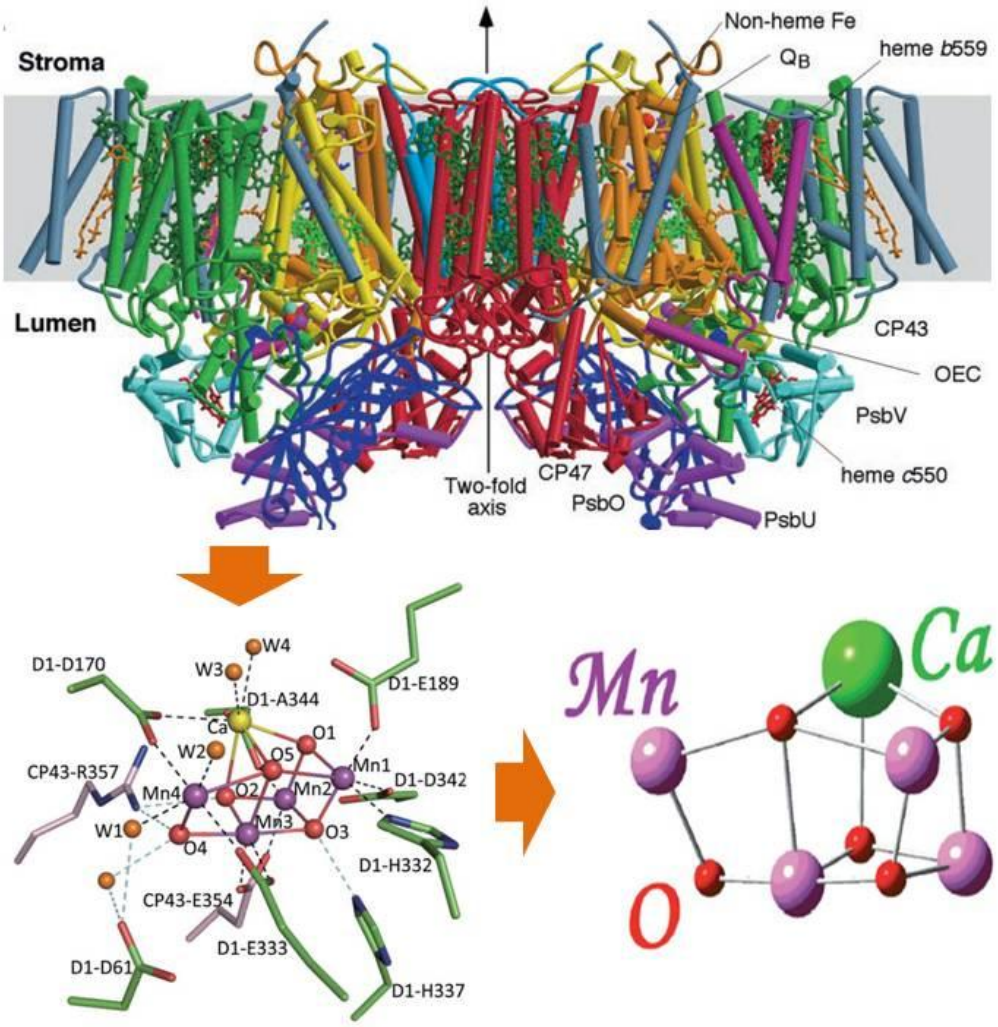

Figure I.3: Structure of PSII and OEC. Upper is the side view of PSII dimer. Lower left is a sketch map of the Mn_4CaO_5 cluster and its surrounding protein residues. Lower right is a simplified structure of Mn_4CaO_5 cluster. Adapted from ref 1 and 10[1,10].

Two mechanisms are proposed to explain the formation of the O=O bond: nucleophilic attack and oxyl radical attack, as shown in Figure I.4. In nucleophilic attack mechanism, a highly electrophilic oxo intermediate is formed during the deprotonation of the

water molecule associated with the fourth Mn ion linked to the cubane structure in S-state cycle. It forms an oxygen molecule under the nucleophilic attack from another water molecule coordinated to Ca[11]. On the other hand, in the oxyl radical attack mechanism, an oxyl radical is preferred to form and act as the attack target instead of oxo[12]. In both cases, the existence of tightly bounded Ca^{2+} close to Mn ions is necessary for the formation of O=O double bonds.

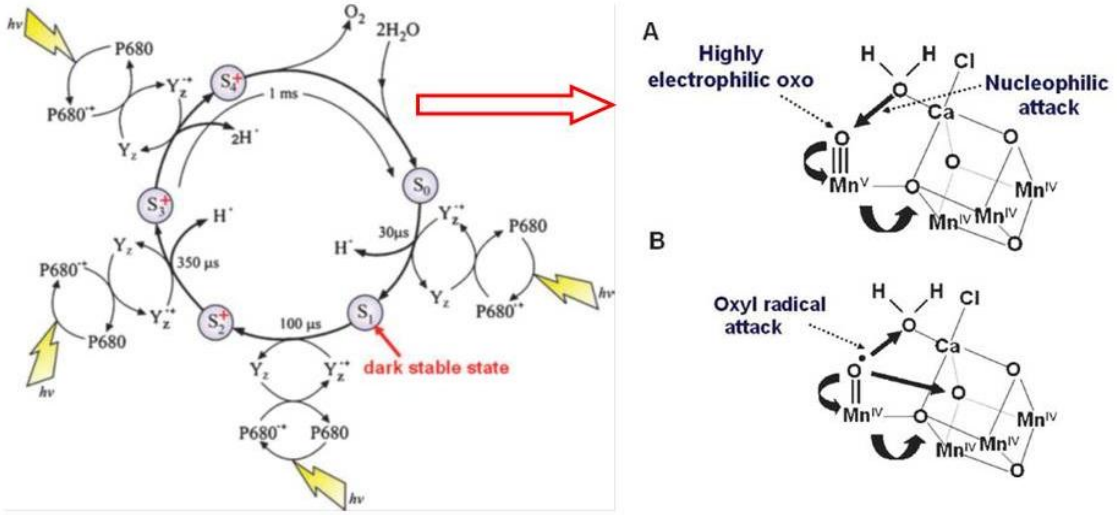

Figure I.4: The S-state cycle showing the formation of dioxygen and two mechanisms of the O=O bond formation. Adapted from ref 8[8].

I.3 Artificial photosynthesis

As mentioned above, to solve the coming energy crisis, using solar energy to generate solar fuel is supposed to be a promising technique. Numerous studies have been carried out to accomplish this purpose. Figure I.5 shows a brief summary of the strategies deriving solar fuels from solar energy, including indirect processes, direct processes and semi-direct photo-biological processes[13].

Indirect processes of solar fuel generation include transformation of the electricity from photovoltaics to H_2 or carbohydrates through water electrolysis, and biofuel generation from photosynthesis and conversion of trees or other plants into energy forms. These two strategies, however, need integrated systems, and the construction and maintenance cost might be huge. In addition, the intricate process engineering would cause partial loss of energy, which, as a consequence, decreases the total efficiency of the energy utility.

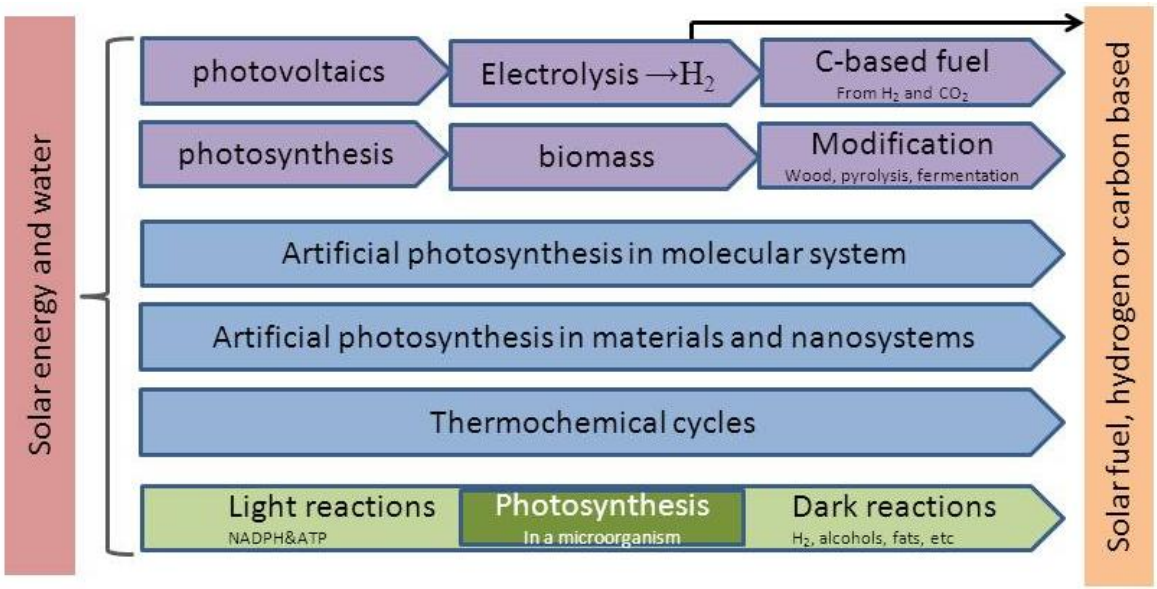

Figure I.5: The different strategies of solar fuel generation. Purple arrows: indirect processes, blue arrows: direct processes; green arrows: semi-direct photo-biological processes. Modified from ref 13[13].

Direct processes allow money savings by comparison with indirect processes because only one single system is needed; another advantage is the decrease of energy losses. Artificial photosynthesis is the main technique in this series, with the employment of either organic or inorganic catalysts. The technique of thermochemical cycles is to produce solar fuel under the high temperature generated from concentrated solar illumination, in which a huge and complicated system is necessary.

Photo-biological process is to harvest fuels such as H_2, oils, alcohols secreted from natural organisms. The variety of organisms is limited but it is a promising method to acquire solar fuels because the forming of fuels is sustainable. In addition, the efficiency is another factor hindering the application of the technique because organisms need a significant energy to maintain their life.

Among all these strategies, artificial photosynthesis gains the most attention because of the high theoretical efficiency and the facile facility construction. Inspired by natural photosynthesis, the concept of "artificial photosynthesis" was first anticipated a hundred years ago by Italian chemist Giacomo Ciamician[14]. The storage of solar energy in the form of chemical bonds by a photochemical reaction was a fantastic idea at that time. In the 1960s, the discovery of the photocatalytic properties of titanium oxide made the notion realizable. As analytical techniques were developed, the mechanism of natural photosynthesis was

understood, which gave a hint for the construction of devices allowing artificial photosynthesis. In recent years, great efforts have been made to realize the solar fuel generation via artificial photosynthesis and a great success has been achieved.

I.4 Water splitting

The overall reaction of natural photosynthesis, carbon hydrate production could be written in the form of equation (I.1), as shown below, the standard potential versus normal hydrogen electrode (NHE) is 1.24 V. However, the standard potential of the water splitting reaction performed by OEC, as shown in equation (I.2), is 1.23 V vs. NHE. According to the thermodynamic potentials, the energy consumed in dark reaction part (hydrogen storage) contains only 0.01 eV, whereas the light reaction part consumed 99.2 % of the total requested energy during the whole photosynthesis process. Obviously, it is the water splitting reaction that dominates the solar energy consumption during photosynthesis. In this sense, the core strategy to achieve the biomimetic storage of solar energy, i.e. artificial photosynthesis, is to find an efficient method to split water in an ambient environment.

$$CO_2 + H_2O \rightarrow \frac{1}{6}C_6H_{12}O_6 + O_2 \qquad E^\circ\ (CO_2/C_6H_{12}O_6) = 1.24\ \text{V vs. NHE} \qquad \text{(I.1)}$$

$$H_2O \rightarrow H_2 + \frac{1}{2}O_2 \qquad E^\circ(O_2/H_2O) = 1.23\ \text{V vs. NHE} \qquad \text{(I.2)}$$

In an artificial photosynthesis system, water splitting could be separated into two half reactions: water oxidation (also called oxygen evolution reaction, or OER) and hydrogen evolution reaction (or HER), as shown in equation (I.3) and (I.4) respectively. Naturally, both reactions could not happen spontaneously and extra energy is necessary. Photons from sunlight could be the extra energy source, the main problem focus on finding a good catalyst that could utilize photons efficiently and perform the water splitting.

$$2H_2O \rightarrow O_2 + 4H^+ + 4e^- \qquad E^\circ\ (H_2O/O_2) = 1.23\ \text{V vs. NHE} \qquad \text{(I.3)}$$

$$4H^+ + 4e^- \rightarrow 2H_2 \qquad E^\circ(H^+/H_2) = 0\ \text{V vs. NHE} \qquad \text{(I.4)}$$

There are two primary approaches to perform overall water splitting[15]. One approach is a one-step water splitting using a single catalyst to split water to H_2 and O_2 simultaneously. The high requirements such as thermodynamic property, band gap structure and stability

against corrosion make this approach difficult to carry out. The other approach is two-step water splitting using two different catalysts for oxygen and hydrogen generation. Figure I.6 provides a scheme of this approach. In this system, the O_2 catalyst drives OER whereas the H_2 catalyst drives HER. Between these two half reactions, OER is the more thermodynamically demanding, with a driving potential of 1.23 V vs. NHE. Considering the kinetic factors, the water oxidation reaction could not happen in an aqueous solution even if the 1.23 V vs. NHE potential value is reached. Because of the high kinetic barrier, large overpotential (potential difference between a thermodynamically predicted potential and the experimentally observed potential) is required to achieve oxygen generation. Therefore, the fabrication of an OER catalyst which could overcome the high kinetic barrier at lower overpotential becomes the prerequisite of the overall application of artificial photosynthesis.

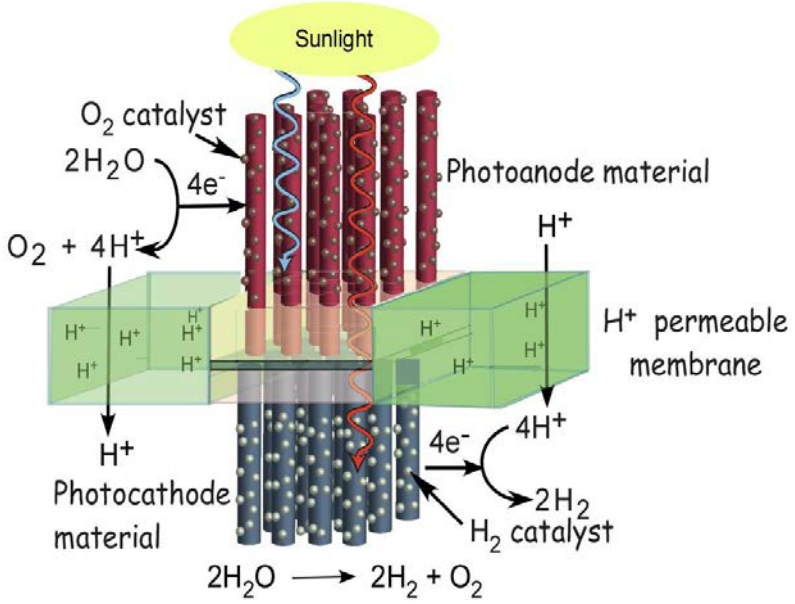

Figure I.6: Schematic of Artificial Photosynthesis of H_2 and O_2 from Water Splitting. Taken from ref 16[16].

I.5 Oxygen evolution reaction (OER) catalyst

Oxygen evolution reaction plays a crucial role not only in water splitting but also in fuel cell and rechargeable battery[17]. In the last decade, researchers have devoted many efforts to find inorganic or composite materials capable of catalyzing oxygen generation, either by structure approach or by composition approach. Recently, more and more materials have been found to be active for OER, including both organic and inorganic materials. The determination of the fine OEC structure provides a new strategy to construct highly efficient

and practical catalysts, not only in the composition but also in the structure. Inspired by the Mn_4CaO_5 cluster in natural OEC, scientists have dedicated great efforts to mimic the photosynthesis process by employing different kinds of catalysts. Based on the constitution of the materials, OER catalysts could be roughly divided into molecular catalysts, precious metal catalysts, transition metal oxide catalysts, and other materials such as hydroxide and sulfide catalysts[18].

Molecular catalysts, as reviewed in ref 19-21, are mainly composed of organo-metallic chemicals derived or inspired from natural organisms and always combined with metal complex[19-21]. "Blue dimer" ($[(bpy)_2(H_2O)RuORu(H_2O)(bpy)_2]^{4+}$) found by Meyer in the 1980s is considered as the first active OER molecular catalyst. Since then, the investigation of molecular catalysts focused on Ru-oxo species. Until nowadays, Ir, Mn, Fe, Co and other metal elements have been introduced in the fabrication of multicomponent molecular catalysts and the catalytic efficiency varies depending on the composition[20-22]. The major problem of this category is their short life duration under OER conditions: the failure of bridging ligands between the organic components and the metal element leads to the catalytic disability and consequently shortens the lifetime.

Precious metals oxides such as RuO_2 and IrO_2 have been employed as OER catalysts long time ago and they are still the most efficient electrocatalysts for OER by far[18,23-26]. However, the scarce resources, high manufacturing cost and poor operating stability block the large-scale application of these materials, which explains why precious metal-free catalysts have long been a research target[18,23]. On the contrary, they are usually used as references to express the activity performances of the other materials, e.g. the commercial IrO_2 electrodes.

On the other hand, transition metal oxides are promising candidates due to their relatively low cost and good activity. In the past years, TiO_2, ZnO, MnO_x, Fe_2O_3, Co_3O_4, NiO_x, Cu_2O and other transition metal oxide materials have been studied for oxygen evolution[27-31]. In recent years, transition metal oxides have become the main research direction and more and more reports have shown their exciting perspectives in view of the elaboration of OER catalysts, some of them possess an OER activity even better than the commercial precious metal catalysts[18,32]. Among those materials, catalysts based on Mn, Fe, Co and Ni are most promising and draw more attention.

Hydroxide catalysts based on transition metals are also active for OER. Burke reviewed the activity trend of transition metal oxides and (oxy)hydroxides, and proposed that hydrated species is more thermodynamically favorable comparing with crystalline oxides under OER conditions[33], and Ni(Fe)O_xH_y displayed very good OER activity[34]. Recent research shows that layered double hydroxides (LDHs, also known as hydrotalcite-like clays), could be a hopeful candidate. In this structure, divalent and trivalent metal cations coordinate with hydroxide anions and form overlapped layer structure, always with additional CO_3^{2-} as guest anions[35]. For example, NiFeMn-LDH[35] and FeNiCo-LDH[36] have shown a good performance in OER.

In addition, perovskite-type materials are another group of catalysts based on transition metal oxide materials. They have an ABO_3 structure in which A is mainly a rare earth or alkaline earth element (Ca, Ba, La and Sr), and B is always a transition metal element (Fe, Co, Ni, Mn, Cr)[17,37]. They are mainly adopted in batteries because they always possess both oxygen evolution and reduction properties. Apart from that, composite materials based on transition metals are another emerging catalyst family for oxygen generation, such as dichalcogenide materials and phosphate materials [38,39]. Except for traditional and common materials, new rising materials are continuously joining the OER catalyst group in recent years, such as the carbon nanotube [40,41].

As a conclusion, numerous materials could be OER catalysts, their activity and durability vary dramatically. There is still a lot of work to do to find a very efficient candidate with long operating time that suitable for large-scale application.

I.6 Manganese dioxides

Comparing with other transition metals, manganese has its own advantages. It has a high natural abundance, thus the cost is much lower than Ni, Co, Ir and other scarce elements. MnO_2 can be used in a wide pH range, even in highly acidic solutions, as shown by the Pourbaix diagram in Figure I.7, while the other transition metal oxides, except for TiO_2, cannot bear the acid corrosion. In addition, it has a variety of oxidation states among which +2, +3 and +4 are the most common in nature. Furthermore, it is environmentally benign and has little contribution to the environmental pollution. The last and the most important, it is the

element employed by natural photosynthesis, which makes it an interesting and promising candidate for OER catalyst.

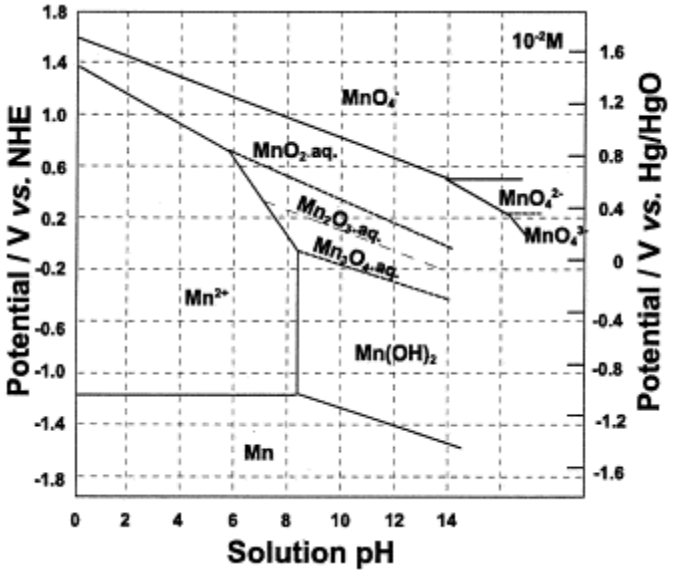

Figure I.7: Pourbaix diagram shows the relation between solution pH and potential of stable Mn species. Taken from ref 42 [42].

The study of manganese oxides as OER catalysts has begun a long time ago. For most manganese oxides, the MnO_6 octahedral units constitute the basic structure. By either sharing edges and / or corners, such units form a large number of crystalline structures, including two major groups: chain, tunnel structure and layer structures[43]. Figure I.8 shows some common structures of manganese dioxide, in which α-MnO_2, β-MnO_2, γ-MnO_2 and λ-MnO_2 have the tunnel structure while δ-MnO_2 is layered structure. Viewing from this structure sketch diagram, the tunnel size of the MnO_2 materials strongly depends on crystalline structure and this is always considered a crucial factor related to the activity performance[44].

Many researchers have investigated the relationship between structure difference and the electrochemical performance of MnO_2. S. Devaraj *et al.* compared the electrochemical capacitance properties of five common MnO_2 structures and found that the specific capacitance values follow the order: $\alpha \cong \delta > \gamma > \lambda > \beta$[45]. Feng Jiao *et al.* investigated the solar water splitting activity of α, β and other structured MnO_2, and found that α-MnO_2 nanowires possess the highest turnover frequency, followed by α-MnO_2 nanotubes and β-MnO_2 nanowires[46]. As a conclusion, the structure of manganese dioxides plays an important role on their electrochemical properties.

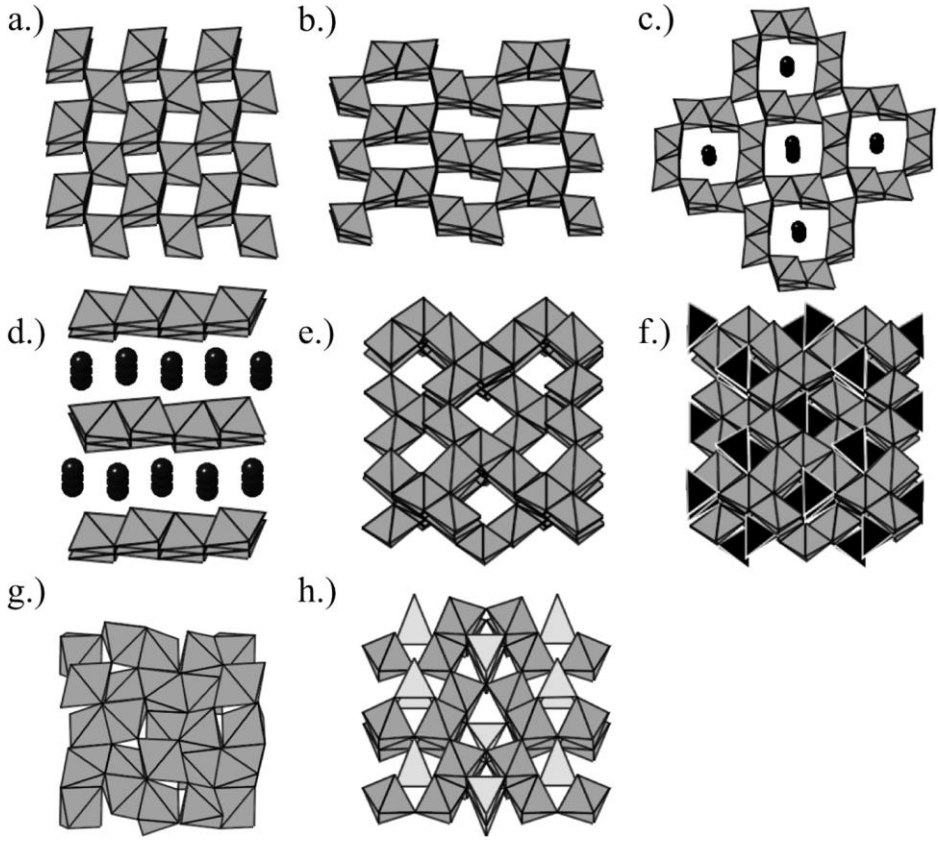

Figure I.8: Structure of manganese oxides: (a) β-MnO_2 (pyrolusite), (b) γ-MnO_2 (ramsdellite), (c) α-MnO_2 (hollandite), (d) δ-MnO_2 (birnessite), (e) λ-MnO_2 (spinel), (f) $LiMn_2O_4$, (g) Mn_2O_3 (bixbyite), and (h) Mn_3O_4 (hausmannite). Mn^{2+} tetrahedra, Mn^{3+} and Mn^{4+} octahedra, and Li^+ tetrahedra are represented by light, dark, and black polyhedra, respectively. Black spheres represent alkaline ions. Taken from ref 47[47].

The OER performances of manganese dioxides as a function of their different structural varieties are also important subjects for application of Mn-based catalysts, which has been carried out by different research groups. Robinson *et al.* studied 8 different polymorph manganese oxide structures containing Mn^{III} and Mn^{IV} for oxygen generation, and they found that five crystalline structures including β-MnO_2, γ-MnO_2, α-MnO_2, δ-MnO_2 and $LiMn_2O_4$ showed no OER activity in the experimental conditions, and the best catalyst was Mn_2O_3, followed by Mn_3O_4 and λ-MnO_2[47]. Frey *et al.* also tested 13 different manganese oxides as OER catalysts with a conclusion that, in terms of catalytic activity, Ca-birnessite > Mn_2O_3 > MnO_2[48]. Ramírez *et al.* compared the OER activity of amorphous MnO_x, Mn_2O_3 and Mn_3O_4, found that Mn_2O_3 acted as the best catalyst whereas Mn_3O_4 was the worst[49]. Pokhrel *et al.* studied 9 different manganese oxide crystalline structures using four commonly used OER evaluation methods and revealed that their OER performances depended on the test electrolyte with the evidence that the best catalyst was Mn_2O_3 for

$[Ru(bpy)_3]^{2+}/S_2O_8^{2-}$/light system and acidic electrolyte, γ-MnO_2 for ceric ammonium nitrate (CAN) electrolyte, and α-MnO_2 for alkaline electrolyte[50]. At the same time, many other reports focus on individual structures to elucidate the OER activity of manganese oxides such as MnO_2 nanorod arrays (NRAs)[51], β-MnO_2[52], mixed-valent MnO_x[53], marokite $CaMn_2O_4 \cdot xH_2O$[54], birnessite-type MnO_2 (δ-MnO_2)[55-57], or amorphous manganese oxides[58]. Meanwhile, the combination of manganese with other active materials has also been reported such as $Mn_3O_4/CoSe_2$[59], Mn and Cr mixed oxide ($Mn_xCr_{1-x}O_{1.5}$)[44], Pt/MnO_x[60], MnO_2/phosphorus[61], $MnCo_2O_4$/polypyrrole[62], or MnO_x/Au[63].

The biomimetic approach of OER catalyst to the natural Mn_4Ca cluster never stops. In recent years, birnessite-type layered structure manganese dioxide (δ-MnO_2) draws more attention than the other crystalline varieties of MnO_2[56,64]. Its basic structural unit is MnO_6 octahedral sheets in which cations (such as H^+, Li^+, Na^+ or Mg^{2+} depending on the preparation conditions) and water molecules occupy different positions in the space between those sheets. Figure I.9 shows the detailed structure of birnessite and the possible site for cation occupation. Comparing with Mn_4CaO_5 clusters in natural OEC, birnessite MnO_2 bares many similarities such as the cubane-like structure, element composition, Mn-Mn distance and Mn oxidation states[55,65]. Theoretical investigations have established optimistic perspectives for birnessite as OER catalyst. Yang *et al.* studied the OER mechanism of birnessite-type MnO_2 using density functional theory (DFT), and found that the intercalation cation has an influence on the energy barrier structure, thus leading to a change in the demand of overpotential for OER, and they claimed the application of Ca-birnessite should be promising[64]. Lucht *et al.* calculated the effect of 13 different intercalated cations and confirmed the great significance of cation insertion on the band gap structure. According to their conclusions, the intercalation of Sr, Ca, B or Al cations would enhance the catalytic activity of birnessite-type MnO_2 for water splitting[65]. Furthermore, these promising perspectives also get support from some experimental results. Pinaud *et al.* prepared a Na-birnessite-type MnO_2 catalyst using electrodeposition, and observed that its band gap structure is the main obstacle to perform photochemical water splitting while the optical, chemical as well as electrical properties appear to be rather satisfying[56]. Wiechen *et al.* investigated birnessite-type MnO_2 with K, Ca, Sr and Mg as intercalated cations, the Ca-birnessite showed the best activity, followed by Sr, and they also confirmed the catalytic role of Ca^{2+} in water splitting[55]. A Cu-birnessite

MnO_x was studied by Thenuwara *et al.* and their conclusion is that the intercalation of Cu cations greatly enhanced the OER activity of MnO_x catalyst [66].

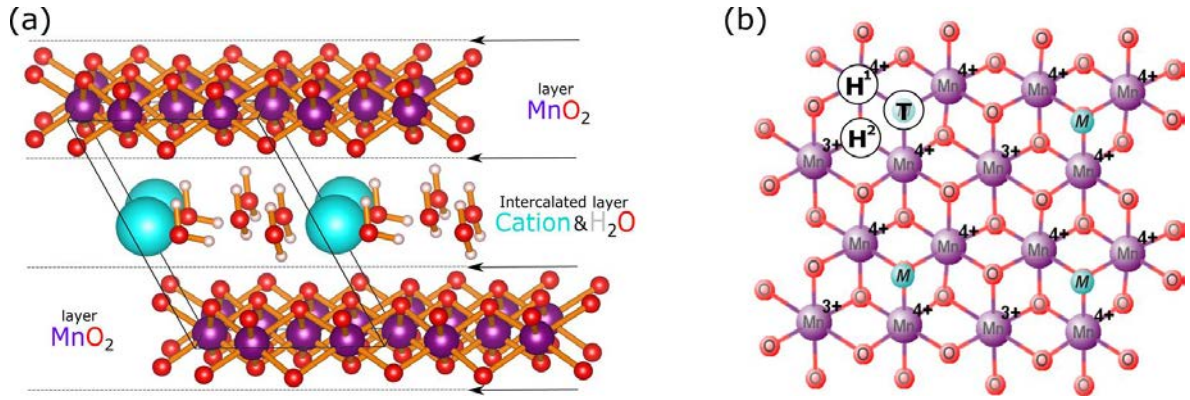

Figure I.9: (a) General structure of birnessite. (b) MnO_2 Birnessite layer with metal cation (water molecules are removed for clarity), the three potential sites for a cation to occupy: H^1, over a Mn cation hollow site; H^2, over an oxygen hollow site, T, over an oxygen top site. Taken from ref 65[65].

Though a great quantity of work has been carried out to investigate the properties of manganese dioxides, the "best" manganese oxide catalyst for OER remains a puzzle and the industrial application is still far from reality.

I.7 Material preparation methods

There is no doubt that the preparation method plays an important role on the surface morphology, crystalline structure as well as the catalytic activity performances of materials. Up to now, a lot of strategies have been exploited successfully for the elaboration of manganese dioxide based catalytic materials. Chemical synthesis methods such as comproportionation using Mn^{2+} and MnO_4^-[55], chemical reduction of $KMnO_4$ with oxalic acid[58], hydrothermal decomposition of $KMnO_4$[60], and precipitation of $Mn(Ac)_2$ and $KMnO_4$[67] are common methods to synthesize manganese oxide catalysts. However, their disadvantage lies mainly on the conditioning of these powders in view of the fabrication of anodic electrode materials. Most materials prepared by chemical synthesis are indeed in the form of powders, while this is not a proper form for electrochemical characterization purposes. A subsequent extra step is necessary in which for example a Nafion paste containing targeted powders is usually used to produce a thin layer catalyst on a substrate like glassy carbon or FTO. On the contrary, electrochemical deposition (electrodeposition in short) is another common strategy to produce thin layer materials. Electrochemical methods such as

cyclic voltammetry (CV)[68], galvanostatic[69,70], and potentiostatic (also called chronoamperometry)[24,56] methods have been widely employed for manganese oxide thin film preparation. Compared with chemical synthesis, the electrodeposited materials could be used immediately in the electrochemical tests without additional treatment. Moreover, the morphology of the generated materials could be easily controlled by adjusting deposition parameters such as electrolyte composition and pH value, operating temperature, current density or potential, and the duration, as these parameters are all known to have a great influence on the nucleation mechanism taking place at the very start of the electrodeposition process[71].

Usually, a three-electrode cell is employed for electrodeposition of thin film catalyst. It includes a working electrode (WE), a counter electrode (CE, also called auxiliary electrode) and a reference electrode (RE). The working electrode is always a well conductive substrate either possess OER activity or just inert support. For example, FTO and ITO are transparent substrate commonly used in photoelectrochemical experiments[72,73], glassy carbon is a typical inert electrode with perfect electric conductivity and chemical stability[74], and precious metals such as Pt and Au are always used as rotating disc or ring electrode[23]. Among them, ITO and FTO are the mostly employed electrode materials because their transparent property allows direct photoelectrochemical water oxidation tests. Template materials are also interesting substrates so as to get specific structures. Saturated calomel electrode (Hg_2Cl_2/Hg, SCE), mercury/mercury oxide electrode (Hg/HgO, MOE), mercury/mercurous sulfate electrode (Hg_2SO_4/Hg, MSE), and silver/silver chloride electrode (AgCl/Ag) are common reference electrodes. The counter electrode is made of a chemically inert metal, for example platinum, with a surface area larger than that of the working electrode in order to eliminate the effect of the counter electrode current density on the working electrode reactions.

Reaction (I.5) shows the redox reaction leading to MnO_2 electrodeposition.

$$Mn^{2+} + 2H_2O \rightarrow MnO_2 + 4H^+ + 2e^- \qquad E°\ (MnO_2/Mn^{2+}) = 1.224\ \text{V vs. NHE} \qquad \text{(I.5)}$$

A Mn^{2+} salt, like $MnSO_4$ and $Mn(Ac)_2$ is always used as the manganese precursor. Abundant background salts (nitrates, sulfates, phosphates) are usually added as additive in order to increase the electrolyte conductivity. The cations in those background salts also play

as intercalated ions in the structure of the generated materials, thus modifying their physical and chemical properties. Most research works use an aqueous solution for electrodeposition. Recently, some researchers reported the use of ionic liquid for MnO_2 electrodeposition at high temperature, which could enhance the deposition rate and lead to a more continuous and fibrous morphology, and the OER activity of the resulted film catalysts was greatly promoted[61,75]. Surfactants such as sodium dodecyl sulfate (SDS) were also found useful to improve the catalytic performance and the stability of electrodeposited manganese oxide, though no effect on the structure and composition was found[76].

I.8 Methods for OER evaluation

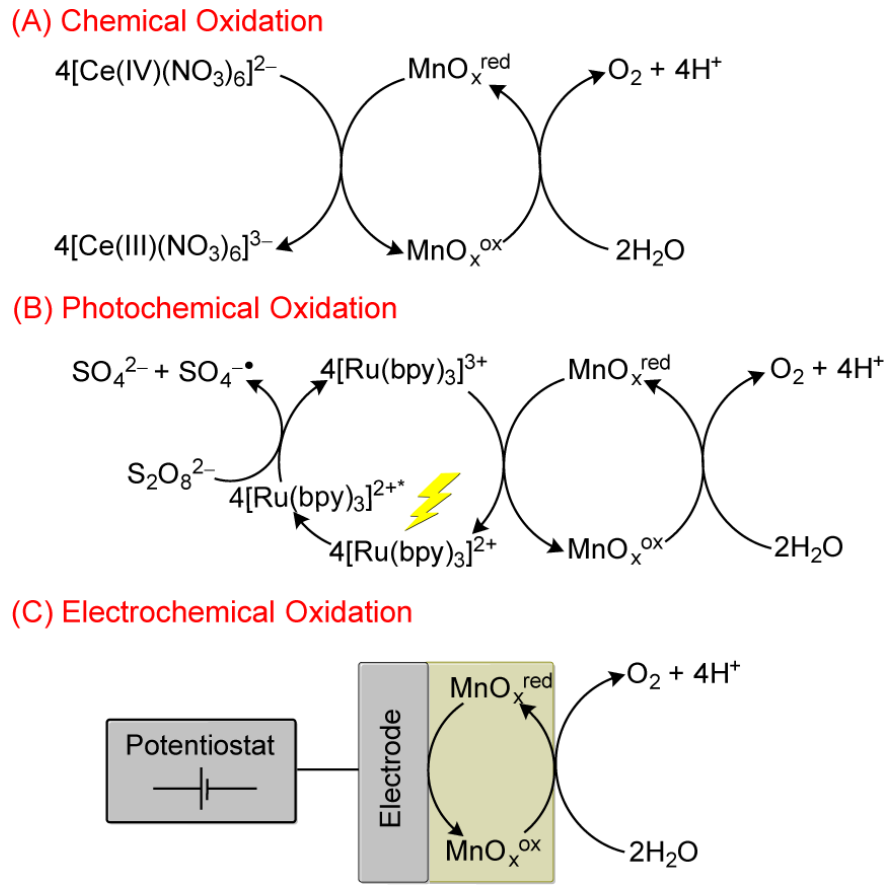

Figure I.10: Three commonly used methods in the evaluation of water-oxidation activities: (A) chemical oxidation using CAN; (B) photochemical oxidation using $[Ru(bpy)_3]^{2+}$, $S_2O_8^{2-}$, and light; and (C) electrochemical oxidation. Taken from ref 50[50].

As discussed by Pokhrel *et al.*, the characterization methods for OER activity evaluation is also a key factor affecting the catalytic performance of catalysts: the employed

chemicals, driven by outer potential bias or react spontaneously under light shining, pH of the electrolyte[50]. Various experimental techniques are particularly relevant in view of the evaluation of the water splitting activities. Among those, three strategies are the most commonly used, and the general reactions are shown in Figure I.10.

The first one is a chemical oxidation method using a chemical oxidant such as ceric ammonium nitrate ($(NH_4)_2Ce(NO_3)_6$, CAN). The oxidants act as the sacrificial species with sufficient oxidizing power to oxidize targeting catalyst, so as to drive the OER. For example, Ce^{4+} in CAN is a one-electron oxidant with a standard potential of about 1.7 V vs. NHE, which could be used to promote water oxidation[77]. During the experiment, the increase of the oxygen concentration can be monitored with the help of an oxygen sensor. The advantage of this method is that it allows studies in bulk solution with large amount of oxygen production, and this largely facilitates the measurement of turnover frequency (TOF) and turnover number (TON)[78]. However, most oxidants have strict use conditions, e.g., CAN is only stable in acidic media with low pH, as it will produce some insoluble compounds otherwise. On the other hand, in acidic conditions, the resistance to acidic corrosion becomes a problem for lots of catalytic materials. Thus, the application of this method is limited.

The second method is the photochemical oxidation, usually using Ruthenium(III) tris(bipyridine) cation ($[Ru^{III}(bpy)_3]^{3+}$). In this system, $[Ru^{III}(bpy)_3]^{3+}$ acts as a one-electron oxidant with a driving standard potential 1.21 V vs. NHE. However, $[Ru^{III}(bpy)_3]^{3+}$ degrades very quickly to $[Ru^{II}(bpy)_3]^{2+}$ in solution, thus the operation duration is largely restricted, as a consequence, $S_2O_8^{2-}$ is usually added to continually generate $[Ru^{III}(bpy)_3]^{3+}$ with the help of light illumination. On the other hand, Ru^{III} and Ru^{II} have unique and different light absorption spectra, making them quite practical media to detect the real-time water oxidation process with the help of UV-visible technique (for Ru complex detection) in order to reveal the process of oxidation equivalents[78]. The disadvantages lie mainly in the high expense and poor stability of the used Ru chemical. This method is, therefore, quite expensive and not suitable for regular tests.

The last one is the electrochemical water splitting, which is the most widely used method for characterizing transition metal oxide catalysts. Usually, a thermodynamic potential of 1.23 V vs. RHE plus extra overpotential is needed to perform oxygen generation. For this overpotential, the smaller, the better. In the electrochemical evaluation method, the

activity of the catalyst can be reflected directly by the overpotential value of a given current density extracted from the cyclic voltammetry or linear voltammetry curve. Compared to the two previous methods, this one is much easier in both construction and operation. The three-electrode cell connected with a potentiostat is enough for this method. During the test, the WE is constituted by the targeted materials, and the electrolyte is always an aqueous solution containing some background salts. Besides, an external light source is also necessary to carry out photoelectrochemical water splitting with nearly no modification on the setup. Except for the activity tests, other experiments can also be performed using the same setup, for instance, chronoamperometry tests to detect the stability, electrochemical impedance spectra to reveal the electric properties of the catalyst, or Mott-Schottky plots to extract the band gap structure[79]. All of these experimental techniques make electrochemical OER test a simple but powerful method to evaluate the performances of catalysts.

I.9 Motivation of this thesis

Hydrogen and oxygen generation from solar water splitting allows the development and extensive use of solar fuel cells. As such, it is a promising method to meet the increasing energy demand of human society and solve the coming energy crisis. Present knowledge indicates that further efforts are necessary to develop a simultaneously cheap and efficient photoelectrocatalyst to carry out the overall water splitting with a low energetic cost. Manganese oxides are promising candidates as water oxidation catalysts, but their efficiency and stability are still not satisfying enough for large-scale industrial applications. In this thesis, we studied electrodeposited MnO_2 thin films by employing various structural and (photo-) electrochemical characterization methods in order to understand the relationships between preparation parameters of these films and their photoelectrocatalytic performances, thus providing and/or confirming basic strategies for preparing efficient and stable manganese oxide based photoelectrocatalysts for water oxidation.

In the first part, the deposition mechanism was investigated using a bulk Pt electrode, and then, different parameters and strategies for electrodeposition was studied in order to find a best way to obtain stable MnO_2 films. After that, electrodeposition of MnO_2 films on ITO and FTO were performed, and the obtained films were characterized to investigate their catalytic activity as OER catalysts. In the meantime, homemade a-CNx electrodes were

introduced as cheap and practical substrates; their capability for electrodeposition was discussed.

In the second part, the influence of heat post treatment was studied on electrodeposited MnO_2 films. Different temperatures were employed for sample calcination. The resulted samples were studied by structural and morphological characterization techniques in order to reveal the heating effect on MnO_2 films. Then the catalytic OER activity was carried out, and a best calcination temperature was proposed. Moreover, photoelectrochemical water oxidation test was carried out on selected samples, promising photocurrents were observed.

In the last part, Na^+, K^+, Ca^{2+} and Mg^{2+} were introduced into the electrodeposition electrolyte in order to study the influence of inserted cations on MnO_2 film structure as well as the OER catalytic performance. EDS spectra were used to confirm the existence of cation elements in the film structure, and homemade Pt electrodes supported on pure silicon were used as substrates so as to eliminate the of impurity signals from ITO and FTO substrates. The crystallinity, morphology and the OER activity were studied as well. Finally, the effect of electrolyte cations was discussed for electrodeposition.

In the next chapter, experimental methods used in the thesis will be described, including the sample preparation, morphological and structural characterization, activity evaluation and the corresponding fundamental knowledge.

Chapter II: Experimental Methods

II.1 Introduction

In this chapter, the experimental setups and methods used in this thesis are introduced, including the adopted chemicals and sample preparation methods. Moreover, morphological, structural, electrochemical and optical characterization methods are presented, as well the photoelectrochemical water oxidation setup.

II.2 Adopted chemicals

All of the chemicals used in this thesis are listed in the following table. All of them are used directly without any purification treatment.

Table II.1: Chemicals used in this thesis

Name	Purity	Company
$MnSO_4 \cdot H_2O$	> 99%	SIGMA
$NaClO_4 \cdot H_2O$	> 99%, for analysis	MERCK
H_2SO_4	95%	VWR PROLABO
$LiClO_4$	> 95%, ACS reagent	SIGMA-ALDRICH
$KClO_4$	> 99%, ACS reagent	SIGMA-ALDRICH
$Mg(ClO_4)_2$	<8 % H_2O, ACS reagent	SIGMA-ALDRICH
$Ca(ClO_4)_2 \cdot xH_2O$	Reagent	Alfa Aesar
NaOH	> 98%, for analysis	PROLABO
KOH	> 86%, for analysis	PROLABO
$K_3Fe(CN)_6$	> 99%, ACS reagent	SIGMA-ALDRICH
$K_4Fe(CN)_6$	> 99%, ACS reagent	SIGMA-ALDRICH
KNO_3	> 99%, for analysis	CARLO ERBA

II.3 Preparation of MnO_2 thin films

For the preparation of MnO_2 thin films, a traditional three-electrode electrochemical cell connected with a bi-potentiostat (VSP, BioLogic) was used, as shown in Figure II.1. The EC-lab software (version 10.37) provided by the same company was adopted to control the electrodeposition procedure and to collect the experimental data. The container was a glass beaker with suitable size. A commercial mercury/mercurous sulfate electrode (K_2SO_4

saturated Hg/Hg_2SO_4, MSE, Radiometer Analytical, 0.248 V vs. NHE at 20 °C) was used as the reference electrode, and the counter electrode was a home-made Pt grid with a large surface area in order to eliminate the influence of anodic reaction on the working electrode.

The reference electrode stability was regularly checked with the help of a commercial calomel electrode (KCl saturated Hg/Hg_2Cl_2, SCE, Radiometer Analytical, 0.244 V vs. NHE at 20 °C). For this purpose, a bulk Pt working electrode was used to get cyclic voltammogram curves in an aqueous electrolytic solution containing potassium ferricyanide/potassium ferrocyanide (2 mM each) and potassium nitrate (0.1 M) using different reference electrodes. The potential difference between two reference electrodes was then calculated from the average values of the anodic and cathodic peak potentials, and compared to the expected value. For the detail of reference electrode calibration, see appendix A.1: Calibration of reference electrode.

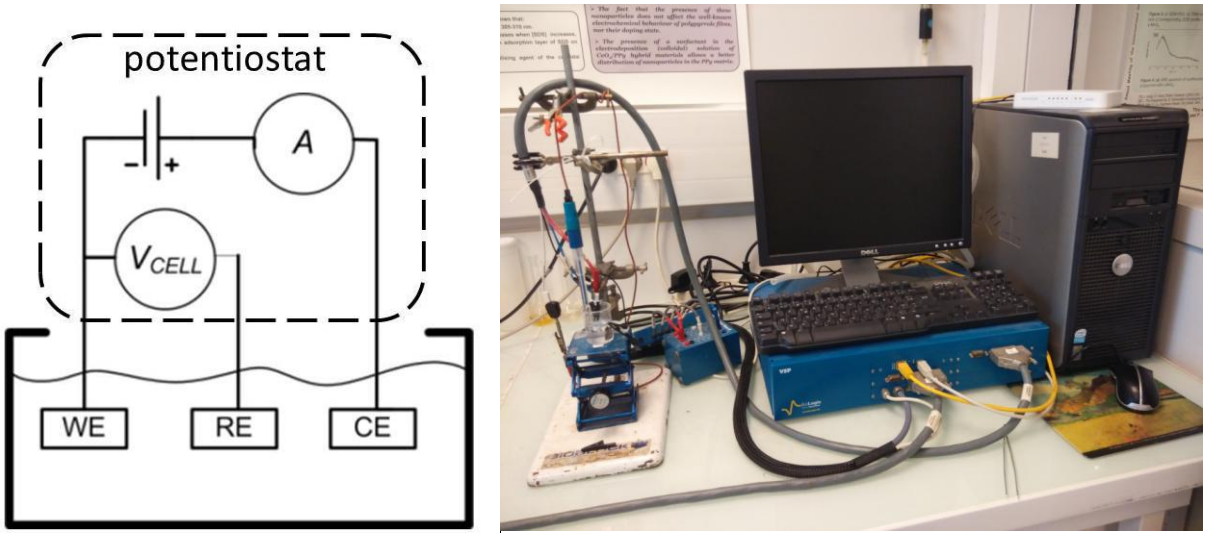

Figure II.1: Configuration and image of three-electrode electrochemical cell used for electrodeposition.

II.3.1 Substrates

In this thesis, different materials were used as working electrode materials depending on the purpose of the experiments:

(1) Two types of Pt electrodes were used for preliminary electrodeposition tests. One is a homemade bulk Pt electrode (diameter 5 mm) with very high mechanical and chemical stability, which allows repeated experiments for the investigation of the influence of different

parameters. The other type is homemade supported Pt film electrodes. The support was either a mica sheet (diameter 50 mm, ruby muscovite, METAFIX) or a pure silicon wafer (Prime FZ, orientation (100), 525 µm thick, resistivity > 20000 Ω.cm). The former electrodes allow numerous topography analysis due to the low cost of fabrication, and the latter ones were used for XRD and EDS analysis due to their pure composition. Prior to the deposition, the supports were cleaned by a chemical process in an ultrasonic bath: 10 min in pure acetone, 10 min in pure ethanol and 5 min in bidistilled water, then dried with argon gas. Depositions of platinum thin films were carried out by RF magnetron sputtering in a commercial reactor (Pfeiffer PLS500). The target was a platinum disk (50 mm diameter×6 mm thick) and the supports were placed at 6 cm from the target. The deposition temperature was 450 °C for mica sheet (kept for one hour before deposition) and ambient temperature for pure silicon; the total pressure in the vacuum chamber for deposition was 2 Pa using argon gas, the target power was kept constant at 50 W and the deposition time was 4 min for mica sheet and 5 min for pure silicon. The estimated thickness for mica/Pt was 80 nm and for Si/Pt was 100 nm.

(2) Indium tin oxide (ITO, thickness: 80 nm, resistance: 30 Ohms) and Fluorine-doped Tin Oxide (FTO or SnO_2:F, thickness: 80 nm, resistance: 80 Ohms) thin films supported on 1 mm thick glass substrates were purchased from SOLEMS. The substrates were cut with the help of a diamond pen into 16 mm × 7 mm pieces from their original size of 50 mm × 7 mm in order to provide adequate surface areas for the targeted electrodes. The cleaning procedure before using was described in Chapter III.

(3) At last, homemade amorphous carbon nitride thin films deposited on boron doped silicon (orientation (100), 380 µm thick, resistivity 0.001-0.005 Ω.cm) electrodes (a-CNx) were prepared using DC magnetron sputtering in a commercial reactor (Plassys MP300S) and used as electrode materials. Before deposition, the silicon substrates were cleaned by a chemical process in an ultrasonic bath (10 min in pure acetone, 10 min in pure ethanol and 5 min in bidistilled water) and then submitted to an RF ionic etching (total argon pressure: 2 Pa, RF power: 160 W, 10 min). The base pressure in the vacuum chamber was kept below 2.5×10^{-7} Torr (about 2.7×10^{-5} Pa) using a turbomolecular pump combined with a rotary pump. The target was a graphite disk (75 mm diameter×5 mm thick, 99.999% pure, NEYCO) and the substrates were placed 7 cm from the target. The total pressure for deposition in the vacuum chamber was 1 Pa using a mixture of pure argon and nitrogen gases with 3 % of N_2

partial pressure, the target power was kept constant at 250 W and the deposition time was 10 min. The as-prepared a-CNx electrodes have a size of 10 mm × 10 mm. They were mounted on a copper tape covered glass support using quick set epoxy adhesive (RS Components Ltd) in order to seal the surrounding conducting part except for the expected a-CNx surface. Silver conductive adhesive was added between a-CNx electrode and the support in order to enhance the conductivity. The surface area of elaborated a-CNx was estimated by their geometric surface area. This carbon-based material was shown to be a very mechanically and chemically stable and cheap electrode material that can be deposited on large surfaces, and different substrates, using the abovementioned deposition technique, which makes it a very interesting and promising electrode material for industrial applications. Moreover, its surface properties, such as electronic conductivity, electrochemical activity and surface functional groups can all be easily tuned by mastering the atomic nitrogen content in these a-CNx thin films according to the well-established relationship existing between the atomic nitrogen content in a-CNx and the partial pressure of nitrogen gas in the deposition chamber.

II.3.2 Deposition electrolytes

Usually, the electrolyte used for electrodeposition contained $MnSO_4$ as a manganese precursor and a neutral salt as a background salt. The concentrations of $MnSO_4$ and alkaline salt were almost systematically 2 mM and 50 mM, respectively. However, a part of the results was carried out in electrolytic solutions with a 0.3 M or 0.1 M concentration for $MnSO_4$ and a 0.3 M or 0.1 M concentration for the neutral salt. Unless specially mentioned, all the electrolytes were used directly without any pretreatment; otherwise, they were saturated by either N_2 (deaeration) or O_2. The deposition conditions will be described in details when necessary.

II.3.3 Electrodeposition techniques

Three electrochemical techniques were exploited for the electrodeposition of MnO_2 thin films: cyclic voltammetry (CV) and chronoamperometry (CA), as shown in Figure II.2. Briefly, during a CV scan, the potential of the working electrode is scanned linearly using a triangular potential waveform, and the resulting current is measured by the potentiostat during the potential sweep. As a consequence, CV is a current response as a function of the applied potential. During a CA experiment, a potentiostat measures the current passing

through the circuit in a period during which a fixed potential bias is applied on the working electrode. Finally a current-time response is recorded and the charge passed through the electrode can be obtained by the integration of current, which shows the quantity of electrochemically treated reactants.

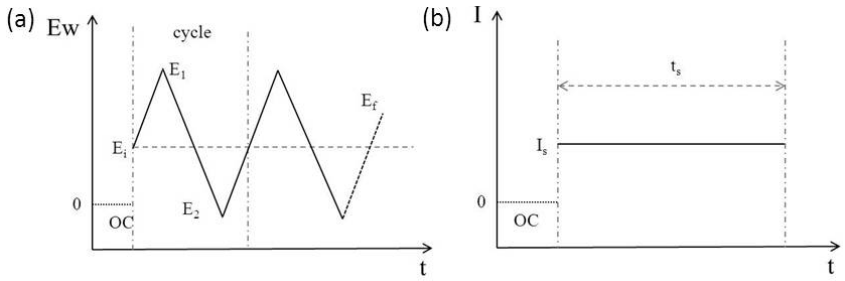

Figure II.2: Schematic diagram of techniques used for deposition: (a) cyclic voltammetry, (b) chronoamperometry.

II.3.4 Post heat treatment

The post heat treatment was performed using a universal tube furnace model CTF 12 (Carbolite Gero) in ambient condition. The diameter of the corundum tube is 75 mm. The temperature is measured by a thermocouple and controlled by a temperature module 301. A glass beaker was used as a container to hold the samples. The samples were heated from room temperature to the setting temperature with a heating rate 10 °C/min, then maintained for 30 min followed by natural air cooling.

II.4 Characterization of structural, morphological and optical properties.

II.4.1 X-ray diffraction spectroscopy

X-ray diffraction spectroscopy (XRD) is a commonly used technique to reveal the crystallinity and structural properties of materials[80,81]. This method is based on the constructive interference of the diffracted X-rays on different crystal planes. Generally, a crystal consists of regular atom arrays, and those atoms play as the scatterers when a beam strikes on them. The incident beam striking on each scatterer causes radiation of a small portion of its intensity as a spherical wave.

According to the Bragg's law:

$$2d_{hkl}sin\theta = n\lambda \quad \text{(II.1)}$$

where n is an integer, λ is the wavelength of X-ray source in nm, d_{hkl} is the inner spacing distance of crystal planes, hkl are the Miller indices of the plane, and θ is the angle of the X-ray diffraction.

Figure II.3 shows the schematic diagram of the XRD diffraction. When scatterers have symmetric arrangement with a spacing separation d, these spherical waves will add constructively in directions where the path-length difference (2dsinθ) equals to an integral multiple of the incident wavelength λ, leading to highly intense reflection. In those cases, part of the incident beam is reflected by an angle 2θ and spots are produced in the diffraction pattern.

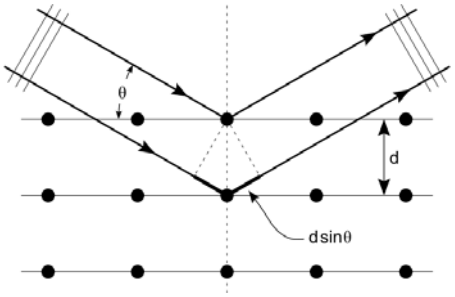

Figure II.3: Schematic diagram of X-ray diffraction.

With the incident beam angle and diffraction intensity of the target material, a XRD spectrum could be created. By comparison with the index of wavelength and the scattering angle 2θ of Miller indices of known materials, the element composition, unit-cell parameters as well as its space group could be defined.

In this thesis, the XRD spectroscopy was acquired using a diffractometer X'Pert Pro (PANanalytical) with Cu-Kα radiation at a wavelength λ = 1.54184 Å as the X-ray source. The scan speed was set to be 4 °/min and the scan range was 8 - 90°. In some cases, a slower scan speed (2 °/min) was used for samples with thin thickness to obtain a better diffraction signal. All samples were characterized directly without any pretreatment.

II.4.2 Field emission gun scanning electron microscopy

The scanning electron microscopy (SEM) technique is a powerful method to study the surface morphology of materials with a nanometric resolution[82]. Generally, a narrow beam

of electrons is focused on the sample surface, scanned over a rectangular area along parallel lines in a fixed direction. The energy of the electrons could reach 30 kV with high speed accelerated by a series of magnetic lenses. Under the interaction between the incident electrons and surface atoms in the sample, various signals such as secondary electrons (SE), back-scattered electrons (BSE) and photons of characteristic X-rays are generated, taking along with the information about the surface topography and composition of the sample. Each of the signals contains different information. A Tungsten filament, LaB_6, Schottky emitter and field-emission tip are commonly used electron sources. To make the best resolution, incident electron beam passes through sets of lenses before reaching the sample surface to narrow its diameter. The usual resolution for a SEM with field-emission tip is typically 1 nm.

Secondary electrons provide the most commonly used signal to obtain the surface topography of the sample. They are generated due to the emission of loosely bonded electrons excited by the incident electron beam. The energy of secondary electrons is about 3-5 eV, thus they can only escape from the near surface area (several nm), thus they can provide the surface information with high resolution, which is commonly used to form the topography image.

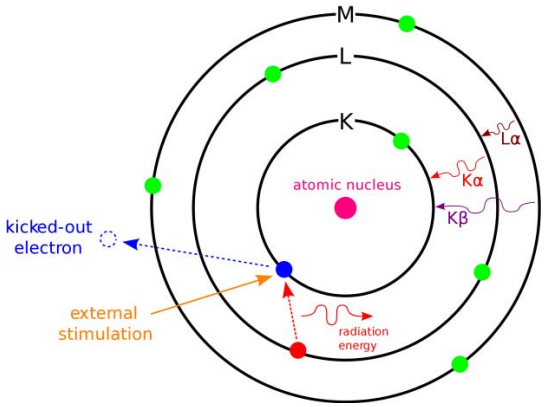

Figure II.4: Schematic diagram of the generation of characteristic X-ray.

As characteristic X-rays contain the chemical information of the sample, thus they are usually used to carry out the composition analysis. The mechanism of the generation of characteristic X-rays is shown in shown in Figure II.4. When the incident electron beam strikes the sample surface, the electron in the inner shell will be exited and escape from the original orbit, which causes a hole in the inner shell. Then the electron in outside shells will jump into inner shell to fill the hole with the emission of X-ray photon. The energy of this

photon differs from an atom to another. Thus by analyzing the X-ray photon energy and quantity, the elemental composition of the sample and proportion of each type of atom could be obtained. This technique is called energy-dispersive X-ray spectroscopy (EDS), which is always associated with SEM as an accessory.

The surface morphology was characterized using a microscopic Supra 55 (Zeiss) equipped with an EDS detector (Bruker) in ultra-high vacuum. The incident electron energy was 5 kV for imaging and 15 kV for EDS, the magnification of the image was set to be 50 X, 100 X and 200 X according to the sample topography. The samples were fixed on the sample holder using conducting adhesive tape and characterized without any pretreatment. Cross-section images were also performed to measure the thickness of the films. To perform such measurements, the sample was cut with a diamond pen to show the cross-section area and the sample holder was tilted by 60 ° or to vertical.

II.4.3 Atomic force microscopy

Atomic force microscopy (AFM) is another commonly used technique to evaluate the topography of materials with a nanometric resolution. According to the operating mode (contact mode or tapping mode), topography of the sample could be acquired. It uses a cantilever, which bears a very sharp and pyramidal tip, to scan over a sample surface line by line, thus forming an image of the topography[83]. Figure II.5 shows the working principle of AFM[84,85]. In the contact mode, as the cantilever goes close to the sample surface, it deflects towards the surface due to the close-range attractive forces between the surface and the cantilever. However, as the tip goes yet closer, until it makes contact with the surface, the repulsive force will increase and cause the cantilever deflect away from the surface. A laser beam is shined on the backside of the cantilever, and any tiny movement of the cantilever could lead to the change of the reflected laser beam direction and therefore to a shift of the laser impact on the photodiode. Then, this change is tracked by a position-sensitive photo diode (PSPD) and transferred to the control software. As the cantilever scans across an interest area on sample surface, the up and down features will be recorded continuously. Meanwhile, a feedback loop controls the height of the tip above the surface in order to maintain constant laser position. In this way, an accurate topography image at high resolution is generated.

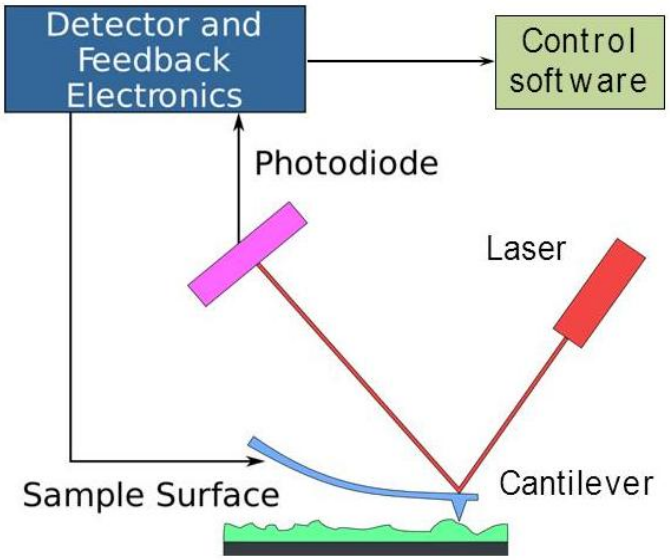

Figure II.5: Working principle of AFM

In addition, AFM also offers the possibility to measure the current crossing the contact area between the AFM tip and the sample surface as a function of a bias applied between the sample and the AFM tip. In this case, a conductive cantilever made either from a conductive material or from an insulating tip coated with a thin conductive layer is necessary. The working mode of AFM allowing the surface conductivity measurement is called the current sensing mode of AFM (CS-AFM). More precisely, this latter allows either the surface conductivity mapping at a constant bias with a nanometric resolution, or the measurement of current-voltage (I-V) characteristics obtained at randomly selected contact areas of the AFM tip with the sample.

AFM experiments reported in this thesis were carried out by using a Picoscan 2100 AFM equipment (Molecular imaging) with a bare silicon AFM probe for tapping mode topography imaging and Pt-Cr covered AFM probe for current-sensing AFM experiments. In CS-AFM tests, an environmental chamber was used to control the humidity in the sample environment by purging pure Ar gas until the humidity rate fell down to 2-3 %, as evidenced with a humidity sensor.

II.4.4 Ultra-violet visible spectroscopy

In the ultra-violet visible spectroscopy (UV-vis), the absorbance, or the reflectance, of targeted materials is measured in the ultraviolet and visible wavelength range. When empty anti-bonding orbital positions exist in materials, electrons could absorb extra energy and

become exited, jump into a higher energy orbital, as shown in Figure II.6. UV-vis spectra uses monochromatic laser as the incident energy source to shine the sample, and the transmission or reflected light is collected. The more easily excited the electrons, the lower the needed photon energy, thus the longer the absorbed light wavelength. In this way, the light absorbance efficiency at each wavelength could be obtained.

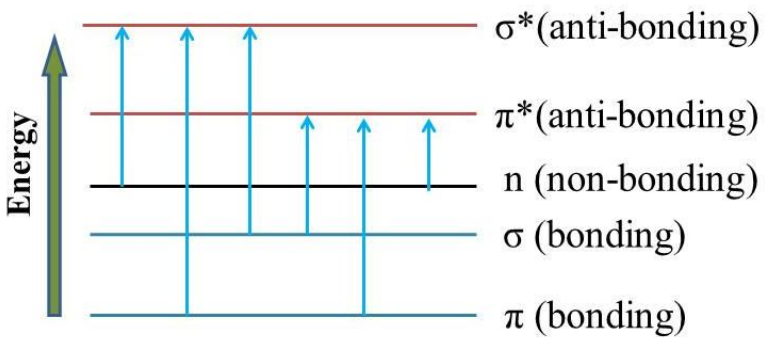

Figure II.6: Electron transition in different orbitals

In addition, Tauc, Davis and Mott proposed a relationship[86]:

$$(h\nu\alpha)^{1/n} = B(h\nu - Eg) \qquad \text{(II.2)}$$

in which h is the Planck's constant, ν is the vibration frequency of incident light, α is the absorption coefficient, Eg is the band gap, B is the proportional constant. In the exponent 1/n, n denotes the transition property of the sample, and its value is ½ for direct allowed transition and 2 for indirect allowed transition. From the plot using $(h\nu\alpha)^{1/n}$ as the vertical axis and hν as the horizontal axis, a curve could be drawn tangent to the linear part and the hν value of the intersection to the horizontal axis is the band gap value. The unit of hν is eV and its value can be calculated by the equation $h\nu = hc/\lambda = 1239.7/\lambda$ eV.

For thin film samples, the value α could be estimated by the equations (II.3) and (II.4):

$$\alpha d = \ln((1 - R^2)/T) \qquad \text{(II.3)}$$

$$\alpha = \ln[(1 - R^2)/T)]\,/d \qquad \text{(II.4)}$$

In which d is the thickness of the thin film sample, R is the reflectance of the sample, T is the transmittance of the sample. Neglect the reflectance, then we could get equation (II.5) from equation II.3:

$$\alpha = \ln(1/T)\ /d \tag{II.5}$$

Considering that:

$$A = \ln(1/T) \tag{II.6}$$

Where A is the absorbance of the sample, (II.5) could be written as:

$$\alpha = \mathrm{A/d} \tag{II.7}$$

Thus, equation (II.2) could be transformed into equation (II.8)

$$(h\nu\frac{A}{d})^{1/n} = B(h\nu - Eg) \tag{II.8}$$

With the result of absorbance at each wavelength and the thickness of the film, the band gap could be derived.

UV-vis spectra were recorded using a UV-vis spectrophotometer U-4001 (HITACHI) equipped with a built-in 60mm Integrating Sphere. A deuterium (D2) lamp is used to generate the excitation light. The UV-vis spectra were recorded in wavelength range 900 – 220 nm in a step of 0.5 nm.

II.4.5 X-ray photoelectron spectroscopy

X-ray photoelectron spectroscopy (XPS) is a surface-sensitive spectroscopic technique that is commonly used to determine the elemental composition and chemical state (oxidation state and surrounding chemical bonds) of atoms of solid samples[87]. It uses an X-ray beam irradiating the sample surface and characteristic photoelectrons escaped from sample surface are detected within a depth of 10 nm in high vacuum. Usually, an XPS spectrum is a plot of the number of excited characteristic photoelectrons against the binding energy. The binding energy is determined by:

$$E_{binding} = E_{photon} - (E_{kinetic} + \psi) \tag{II.9}$$

where $E_{binding}$ is the binding energy of the electron, E_{photon} is the energy of used X-ray photons, $E_{kinetic}$ is the kinetic energy of the electron and ψ is the work function relying on both the

spectrometer and the material. Usually, the binding energy could be given directly by the instrument after calibration. Each element produces characteristic photoelectrons corresponding to the electronic configuration of the electrons within atoms at specific binding energy values, which could be used to determine the existence and quantity of elements on the sample surface.

The chemical state of a species refers to its local bonding environment, which is influenced by its intrinsic oxidation state, the identity of its nearest coordination atom, the bonding type between the species with the nearest coordination atoms, and even the bond with the second nearest coordination atom[88]. This influence causes the binding energy of the questioned species to shift to a higher or lower energy region, which is called chemical shift. The existence of chemical shift makes the binding energy peak of each species in an XPS spectrum a combination of several peaks other than just one peak. By comparison with the standard binding energy of possible coordinate bonding relationship, the XPS peak could be split into several species corresponding to different chemical states, such as the oxidation state.

In this thesis, XPS spectra were collected using an Omicron (ESCA+) X-ray photoelectron spectrometer in ultra-high vacuum (1.10^{-10} mbar), and the X-ray source was an Al Kα (hν = 1486.6 eV, Power: 280 W). All of the samples were characterized as prepared without any other pre-treatments. After the data collection, the calibration of the binding energies was performed with respect to C 1s peak (binding energy = 284.7 eV). The Casa XPS software package was used for all the data analysis.

II.5 Characterization of electrochemical properties

Electrochemical characterization techniques such as cyclic voltammetry (CV), chronoamperometry (CA), and electrochemical impedance spectroscopy (EIS) were performed using the same setup as the one used during the electrodeposition procedure, i.e. a three-electrode electrochemical cell controlled by a potentiostat (VSP, BioLogic). However, the reference electrode was replaced by a commercial mercury/mercuric oxide electrode (0.1 M KOH aqueous solution filled Hg/HgO, MOE, Radiometer Analytical, 0.171V vs. NHE) in order to fit the high alkaline electrolyte solution. Usually, the aqueous electrolytic solution contained 0.1 M NaOH. In some occasions, 1 M NaOH and 1 M KOH solutions were

adopted instead. The MOE was also calibrated as described in chapter II.3, see appendix for details.

II.5.1 Cyclic and linear sweep voltammetry

Cyclic voltammetry (CV) is the most important characterization technique for OER catalysts. It provides the basic parameters for the evaluation of the catalytic performances, such as the onset potential of OER, the faradaic current exclusively related to OER at a given potential and the kinetic performances of the catalytic sample towards OER. In addition, a Tafel plot, which is the most useful graph for the evaluation of catalytic properties of investigated solid catalysts towards OER, could be derived from the linear sweep voltammetry (LSV) curves. According to Butler-Volmer equation for a monoelectronic redox reaction[89]:

$$i = i_0\left[e^{-\alpha f} - e^{(1-\alpha)f}\right] \quad \text{(II.10)}$$

where i_0 is the exchange current in equilibrium potential, α is the charge transfer coefficient, f =F/RT, with F, the Faraday constant (96485 C.mol^{-1}), R, the ideal gas constant (8.31 J.K^{-1}.mol^{-1}) and T, the temperature (in K). is the overpotential, i.e. the difference of the applied potential to the equilibrium potential. When the value is large enough, $e^{-\alpha f} \gg e^{(1-\alpha)f}$, equation (II.10) could be turned to the following simplified form:

$$i = i_0 e^{-\alpha f} \quad \text{(II.11)}$$

$$= \frac{RT}{\alpha F}\ln i_0 - \frac{RT}{\alpha F}\ln i \quad \text{(II.12)}$$

Also, for any number n, there is following relation:

$$\ln n = 2.3\log n \quad \text{(II.13)}$$

Thus formula (II.12) turns to:

$$= 2.3\frac{RT}{\alpha F}\log i_0 - 2.3\frac{RT}{\alpha F}\log i \quad \text{(II.14)}$$

The value $-2.3\ RT/\alpha F$ is called Tafel slope, the smaller this value is, the bigger the value of α, the faster the corresponding half redox reaction. Usually, the current i is replaced

by the current density j in order to make the comparison between different electrodes more reasonable. A Tafel slope extracted from a figure showing the linear variation of the overpotential versus log i, established itself from a LSV curve, provides the ability to estimate the catalytic effect of an electrode material towards OER.

In this thesis, CV curves were acquired in a given potential range verses to the MOE electrode, the scan rate was set to be 10 mV/s. Either single scan or multiple scans was performed depends on the sample. As a comparison, bare substrates were characterized along with MnO_2 samples. Before each CV test, the system was kept at 0 V vs. MOE for 10 s in order to stable the collected data. Most of the cyclic voltammetry curves were iR corrected based on the series resistance measured by EIS at 100 KHz (the title of the potential axis in the cyclic or linear voltammogram figure is "E – iR" instead of "E"). The calculation was based on equation II.15.

$$E = E_{measure} - i_{measure} \times R_{\Omega} \qquad \text{(II.15)}$$

where $E_{measure}$ and $i_{measure}$ are the measured potential and current, R_{Ω} is the measured series resistance.

II.5.2 Chronoamperometry

Chronoamperometry is a simple method to study the stability of electrocatalysts. It consists in fixing the potential bias of the working electrode in a potential region where the sample is known to be active to electrocatalyze water oxidation into oxygen. The current is recorded as a function of time. As for a catalyst with good stability, the faradaic current beyond the current transient in chronoamperometry test should keep the same value over the whole test period. By drawing a i-t curve, i.e. a chronoamperogram, the stability could then be seen clearly. In this thesis, most of the chronoamperometry experiments were performed at 0.9 V vs. MOE with a duration varying from 10 min to 12 hours in order to evaluate the long-time stability of our MnO_2 samples.

II.5.3 Electrochemical impedance spectroscopy

Electrochemical impedance spectroscopy (EIS) is a commonly used electrochemical technique for studying the dynamics of an electrochemical process occurring at the interface

between the electrode surface and the electrolyte. It shows the impedance response of the system on a wide frequency range, providing information about the rate limiting reaction steps and the dominate reaction steps at certain frequencies[89].

In the potential electrochemical impedance spectroscopy (PEIS), which is used in this thesis, the current response is recorded as a function of a small sinusoidal potential perturbation operated for different frequency values, as shown in Figure II.7.

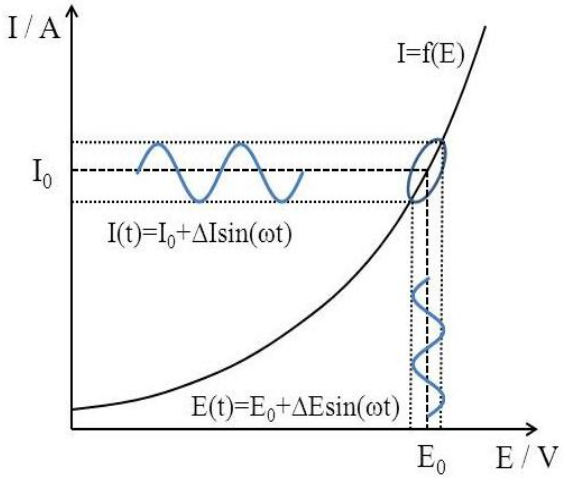

Figure II.7: Schematic diagram of potential electrochemical impedance spectroscopy.

The real time potential E(t) could be expressed by:

$$\mathrm{E(t)} = E_0 + \Delta E \sin(\omega t) \tag{II.16}$$

where E_0 is the set potential which is fixed at the beginning of the test, ΔE is the amplitude of the potential perturbation, ω is the angular frequency calculated from the real time frequency f by $\omega = 2\pi f$. Then we have the expression of the current response I(t):

$$\mathrm{I(t)} = I_0 + \Delta I \sin(\omega t + \varphi) \tag{II.17}$$

where I_0 is the current response to E_0, ΔI is the current response to perturb potential ΔE, and φ is the phase shift between E(t) and I(t). In this case, the impedance corresponding to a given frequency could be calculated by the following relation:

$$\mathrm{Z(\omega)} = \frac{\Delta E(\omega)}{\Delta I(\omega)} = \frac{\Delta E \sin(\omega t)}{\Delta I \sin(\omega t + \varphi)} = Z_0 \frac{\sin(\omega t)}{\sin(\omega t + \varphi)} \tag{II.18}$$

where Z_0 is the original impedance of the system.

In addition, according to Euler's relationship,

$$e^{j\varphi} = \cos\varphi + j\sin\varphi \tag{II.19}$$

The potential could also be written by:

$$E(t) = E_0 + \Delta E e^{j\omega t} \tag{II.20}$$

And the current response is:

$$I(t) = I_0 + \Delta I e^{j(\omega t - \varphi)} \tag{II.21}$$

Thus the impedance has the following form:

$$Z(\omega) = \frac{\Delta E e^{j\omega t}}{\Delta I e^{j(\omega t - \varphi)}} = Z_0 e^{j\varphi} = Z_0 (\cos\varphi + j\sin\varphi) = Z'(\omega) + jZ''(\omega) \tag{II.22}$$

with $Z'(\omega) = Z_0 \cos\varphi$, $Z''(\omega) = Z_0 \sin\varphi$. $Z'(\omega)$ and $Z''(\omega)$ are the real part and imaginary part of the transfer function, respectively. Usually, $Z'$and $Z''$are denoted by Re(Z) and Im(Z).

There are two commonly used graphical representations of the electrochemical impedance:

1) The bode plot. It usually contains a Bode magnitude plot, which expresses the module of the impedance response against the frequency, and a Bode phase plot, which expresses the phase shift against the frequency.

2) The Nyquist plot. It uses the values of –Im(Z) and Re(Z) as the Y axis and X axis, respectively, as shown in Figure II.7. In a Nyquist plot, each data point represents the impedance response to a given frequency.

The Nyquist plot is usually analyzed by fitting to an equivalent circuit model (EC)[90]. An EC model always contains different elements, among which usual electrical components such as resistor (R), capacitor (C) and inductor (L) are the most commonly used elements. However, a Nyquist plot could often be fitted with the help of different equivalent circuits. It

is therefore important to keep in mind that each elementary component in an equivalent circuit should have a reasonable electrical or electrochemical meaning in the evaluated electrochemical system. Generally, an electrochemical system should consider the following elements:

1. Electrolyte resistance. The electrolyte resistance between the working electrode and the counter-electrode should be considered when constructing an equivalent circuit for fitting the impedance spectrum. It depends on the physical properties and chemical composition of the electrolyte solution such as the ionic concentration, identity of ionic species, surface area of the electrodes and also the test temperature.
2. Double layer capacitance. When a potential bias is added to a conductive electrode, electrolyte ions will be absorbed, then the charged electrode and the ions are separated by an single layer of insulating solvent molecules. The separated two layers have opposite polarity, thus behaving like a capacitor. The double layer is located very close to the electrode surface within a distance of the angstrom order, and it is influenced by the applied potential, ionic concentration, electrode material, and surface roughness.
3. Polarization resistance or charge transfer resistance. An electrode becomes polarized when its potential is forced away from the open circuit. The current flow is hindered by electrochemical reactions occurring on the electrode surface, or in other words, a resistance exists between the electrode and the electrolyte. Its value is influenced by the reaction kinetics and reactant diffusion.
4. Diffusion. The impedance caused by diffusion is also called Warburg impedance. It depends on the applied perturbation frequency, knowing that the smaller the frequency, the bigger the Warburg impedance.
5. Constant phase element. Simply using a capacitor is sometimes not enough for fitting impedance spectra, thus a constant phase element is proposed. It has the following form:

$$Z_{CPE} = \frac{1}{Q(j\omega)^{\alpha}} \qquad \text{(II.23)}$$

where Q is the capacitance and α is an exponent lower than 1. For a pure capacitor, the value of α reaches 1, i.e. the maximum.

In Figure II.8, a model of an equivalent circuit corresponding to an impedance spectrum is shown. It has three components, the electrolyte resistance (R_Ω), a charge transfer resistance (R_{ct}) and a double layer capacitance (C_{dl}). The value of each component can be derived by simulation. In this way, the parameters of the electrochemical process become quantitative. Based on the characterization conditions and the mechanism of the reaction, the EC model will contain different components and combinations in order to get the best simulation result and the best representation of the electrochemical phenomena occurring at the working electrode surface.

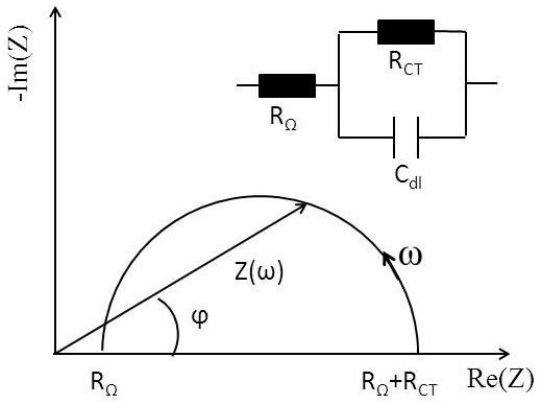

Figure II.8: Nyquist plot and the corresponding equivalent circuit

The fitting of impedance spectra is a most important method to get the information of reaction mechanism, however, the corresponding reaction of the impedance spectra is influence by the catalyst material, reaction potential, electrolyte, pH and so on, thus choosing a fitting equivalent circuit model is the key point to get the most exact and reasonable simulation parameters.

Fitting of spectra has been carried out in numbers of literatures and the equivalent circuit models are different from each other, some of the typical models are listed in the table below, including catalyst material, electrolyte, evaluation potential and the explanation of each element.

Generally, the models are composed of two pairs of R/C combination, like model 10. The other models have some changes in the components:

(1) put one of the R/C pair into series with the resistance in another R/C pair, like model 8;

(2) put a third R/C pair into series with the resistance in one of the R/C pairs, like the model 3;

(3) put a third R/C pair in parallel with those two R/C pairs, like model 7;

(4) remove one of the resistance in one R/C pair, like model 5.

(5) Warburg element is added into series with the resistance in one R/C pair and the capacitor is replaced by a constant phase element if necessary.

Table II.2: Equivalent circuit models reported in literature for impedance spectra fitting

No.	Conditions	model	explanation
1[91]	Electro-deposited MnO_2/Stainless steel; 0.1 M Na_2SO_4	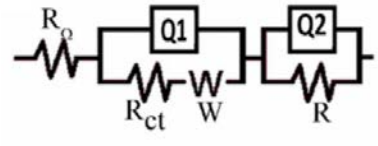	R_Ω: electrolyte resistance, R_{ct}: charge-transfer resistance, Q_1: constant phase element (CPE) used in place of double-layer capacitance (C_{dl}), W: Warburg arising from a diffusion controlled process at low-frequency Q_2: CPE used in place of pseudo-capacitance of the material.
2[92]	0.1 M KOH 0.65 V (1.66 V vs. RHE)	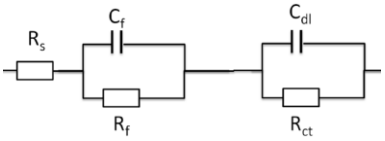	R_s: the resistance of the electrolyte R_f: the resistance of the catalysts layer C_f: the capacitance. C_{dl}: the double layer capacitance R_{ct}: the charge transfer resistance.
3[93]	Ni, Co, Fe, foil or wire; 0.6-0.78 V in NaOH 1 M (Hg/HgO 0.1 M NaOH)	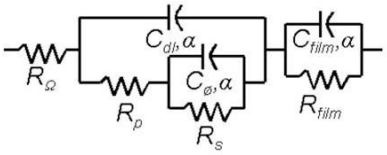	R_Ω: uncompensated solution resistance, C_{film} and R_{film}: related to the dielectric properties and the resistivity of the oxide film C_{dl}: the double layer capacitance. R_p and R_s: connected to the kinetics of the interfacial charge transfer reaction.
4[94,95]	multi-cycled iron oxy-hydroxide films	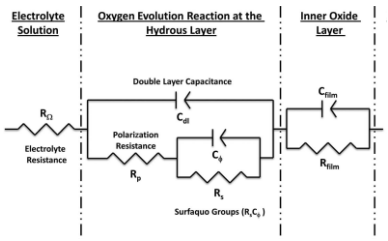	$C_{film}R_{film}$: the dielectric properties and the resistivity of the underlying compact oxide film, respectively. C_{dl}: the double-layer capacitance, R_Ω: the uncompensated electrolyte resistance. Rs and Rp: related to the kinetics of the interfacial charge transfer reaction. C_φ and Rs: the relaxation of the charge associated with a surface intermediate.
5[96]	α-Mn covered Ni foil; 0.3 V vs. SCE 0.1 M Na_2SO_4	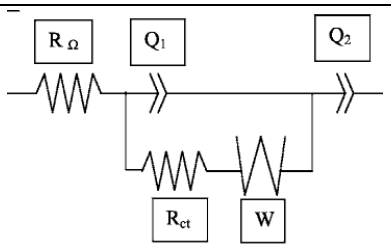	R_Ω: the electrolyte resistance Rct: charge-transfer resistance (equal to diameter of the semicircle), Q_1: constant phase element (CPE) used in place of double-layer capacitance(C_{dl}), W: Warburg arising from a diffusion-controlled process at low frequency Q_2: CPE used in place of the pseudocapacitance of the material.

6[97]	δ-MnO_2 on FTO open circuit potential; open circuit potential1 mol.L^{-1} Na_2SO_4	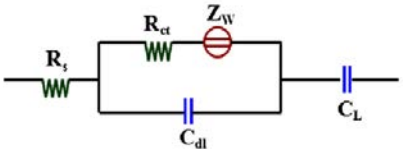	R_s:the electrolyte resistance R_{ct}: the charge transfer resistance, Z_w: the resistance related to the ion diffusion, C_{dl}: the double-layer capacitance C_L:the limit capacitance
7[98]	r-MnO_2 on nickel sheet	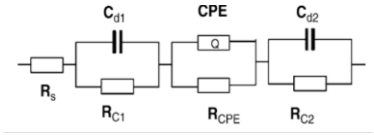	
8[99]	FTO/NiO; 0.40 and 1.50V in a 0.60m borate buffer vs. Ag/AgCl	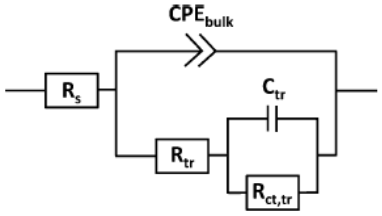	C_{bulk}: the space charge and Helmholtz double-layer capacitances together replaced by a constant phase element, CPE_{bulk} C_{tr}: surface state (trap state) capacitance R_s: the series resistance R_{tr}: trap state resistance, representing resistance caused by the recombination of charge carriers at the surface traps; $R_{ct,tr}$: charge-transfer resistance from the surface states to the electrolyte
9[100]	FTO/IIa-BaSrCoFe; 1.408-1.588 V vs. RHE In 0.1 M KOH	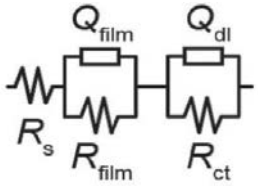	Rs: the solution resistance Q_{film} and R_{film}: the dielectric properties and resistivity of the film; Q_{dl} and R_{ct}: the double-layer capacitance and the interfacial charge-transfer resistance
10[101]	$NiCo_2O_4$; 0.75-0.79 V in O_2 saturated 0.1 M KOH Ag/AgCl (1 M Cl^-, 0.20 V vs. NHE)	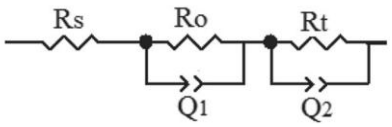	Rs: solution resistance Ro: oxide film resistance, Rt: charge transfer resistance of OER Q: constant phase element (CPE) corresponding to the oxide mass represent (Q1) and the interface between oxide film and electrolyte (Q2)

In this thesis, the EIS spectra were recorded using the electrochemical setup mentioned above. The potential was set to be at 0 V vs. MOE or in OER onset region. Before each test, the electrochemical cell was maintained at test potential for 30 s. The frequency range was from 100 kHz to 100 mHz with a perturbation amplitude of 10 mV. The simulation of the EIS spectra was performed using a Simad software (developed by LISE). The equivalent circuit model extracted from ref [93] was used for simulation. The double layer capacitance (C_{dl}) and film capacitance (C_{film}) were replaced by constant phase element (CPE) in order to make the simulation more accurate, as shown in Figure II.9. The meaning of each component is the same as listed in Table II.2: CPE_{film} and R_{film} represent the dielectric properties and the resistivity of the underlying compact oxide film; CPE_{dl} represents the double-layer capacitance; R_Ω represents the uncompensated electrolyte resistance; Rp is related to the kinetics of the interfacial charge transfer reaction; C_s and R_s represent the relaxation of the charge associated with a surface intermediate.

The value of each component was adjusted until the difference between experimental result and simulation result reached the smallest values in the whole spectrum.

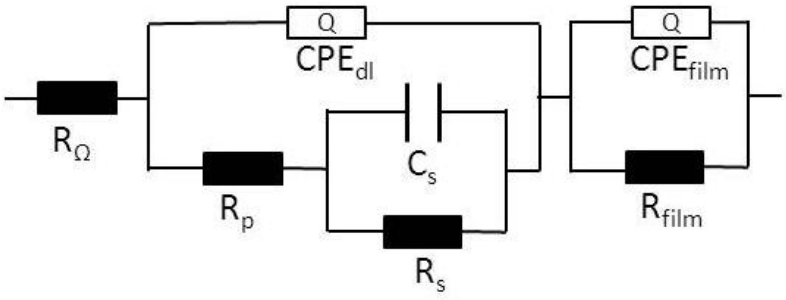

Figure II.9: Equivalent circuit model for EIS simulation

II.6 Photoelectrochemical water splitting

Photoelectrochemical water splitting (PECWS) employing solar light is the final target of this work aimed at investigating photoelectrocatalysts for water oxidation. Solar light is absorbed by water oxidation photoelectrocatalysts to lower the potential demand that is required to allow water oxidation. Also, material properties may change due to the solar energy absorption. For example, their electronic conductivity may become higher under light (photoconductivity) thus facilitating the charge transfer and electron transport efficiencies. In addition, the power and optical spectrum of the absorbed light may have a great influence on the PECWS activity, as higher efficiency provides more photon energy that could be used for water splitting.

In order to carry out PECWS experiments, a special electrochemical reactor was designed and fabricated in LISE (see Figure II.10). According to literature, the absorbance of the MnO_2 is expected to occur within the 300 - 600 nm wavelength range[102,103]. Thus, the reactor contains a quartz crystal window allowing the light to enter the reactor and shine the sample without energy loss in the desired wavelength range. As far as the electrodeposition procedure is concerned, the other parameters kept the same values.

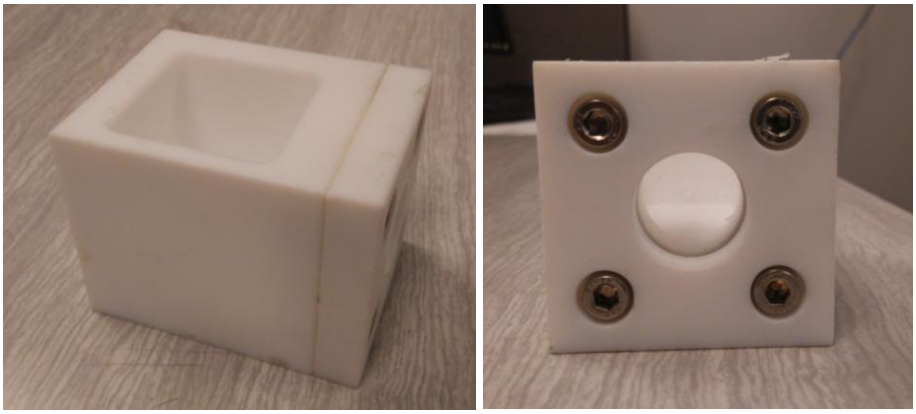

Figure II.10: Reactor used for photoelectrochemical water splitting experiment.

The simulated solar light was provided by a solar simulator (AM 1.5) equipped with a short arc 300 W Xenon lamp as light source (LOT Quantumdesign). An optical fiber linked to the light house was applied to conduct the light in order to ease the setup. The intensity was measured and calibrated by using a radiometer provided by LOT Quantumdesign. For the details of the calibration, see appendix A.2 Calibration of solar simulator. The light power density was set to be 100 mW/cm^2, corresponding to the light power intensity of natural sunlight.

Chapter III: Basic mechanism of electrodeposition of stable MnO_2 thin films on different substrates

III.1 Introduction

Electrodeposition is a technique commonly used for the preparation of thin film materials. However, in the frame of this work, the challenge with this technique is to reach simultaneously a mechanical and chemical stability as well as a (photo-)electrocatalytic activity that will be both promising for the obtained electrodeposited films. In this chapter, electrodeposition procedures were thus confirmed or developed on Pt, Indium Tin Oxide (ITO), Fluorine doped Tin Oxide (FTO) and homemade amorphous carbon nitride (a-CNx) working electrodes so as to study the influence of the electrode material on the mechanical stability and/or (photo-) electrocatalytic activity of resulting MnO_2 thin films.

III.2 Basic mechanism of water oxidation on a clean Pt electrode: preliminary checking experiments.

MnO_2 electrodeposition occurs on many different types of substrates through a 2-electron oxidation reaction from Mn^{2+} cations used as precursors. The mechanism of the formation of MnO_2 thin films on a working electrode has been widely discussed, several mechanisms have been proposed, but it is difficult to define one single route because it is influenced by a large variety of factors such as the ion concentration, pH and deposition techniques[104-107]. As a consequence, a deep understanding of the electrodeposition mechanism is important to obtain a highly active and stable MnO_2 thin film possessing a very good photoelectrocatalytic activity. For this purpose, a bulk Pt electrode was employed as a model electrode material in the first part of our investigations. It offers a smooth surface, a simple chemical composition, and an excellent electronic conductivity, and more importantly, it can be reused easily after polishing, careful cleaning and rinsing.

III.2.1 Electrochemical cleaning of bare platinum electrodes

The surface conditioning of the substrate has a great influence on the properties of the electrodeposited films, as it involves the mastering (selection or suppression) of adsorbed chemicals, oxidized superficial layer and roughness. Thus, it is necessary to treat and clean

the working electrode surface before applying the electrodeposition procedure in order to produce homogeneous films and make sure the obtained results are reproducible.

For an ideally cleaned Pt electrode, the observation of the electroactivity of hydrogen in the negative potential range of a cyclic voltammogram (CV) obtained in a sulfuric acid aqueous solution provides a very convincing test, as shown in Figure III.1. For potential values lower than 0.5 V vs. Ag/Ag_2SO_4, the cathodic peaks reveal the reduction of adsorbed protons whereas the anodic peaks correspond to the oxidation of adsorbed H_2 molecules and the subsequent production of freely diffusing protons. These adsorption phenomena are known to occur only on perfectly clean platinum substrates. The anodic wave appearing in the positive potential region is related to the oxidation of Pt into platinum oxy-hydroxide(s) ($Pt(O)_x(OH)_y$) whereas the cathodic peak situated at 0 V vs. Ag/Ag_2SO_4 reveals the reduction of the abovementioned oxidation product(s) [108]. Moreover, for a perfectly clean platinum electrode, this cyclic voltammogram remains unchanged during consecutive potential cycles. On the other hand, corresponding peak and wave currents may increase in the case of an ongoing electrochemical cleaning.

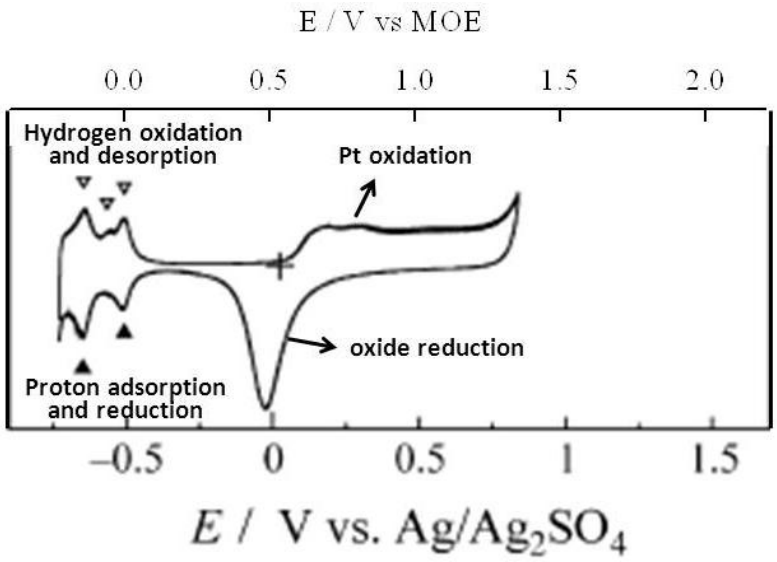

Figure III.1: Cyclic voltammetry curve obtained on a clean Pt working electrode in a H_2SO_4 (0.5 M) aqueous electrolytic solution. Taken from ref [108].

Actually, the global cleaning procedure of a Pt electrode commonly includes first a physical cleaning followed in a second step by an electrochemical cleaning.

The first step is a physical cleaning aimed at removing solid phase materials or adsorbed chemicals by mechanical polishing. Here, in our experiments, Pt electrodes were manually polished using a commercial polishing clothe stuck on a polishing disk, as well as a fine alumina suspension (average grain size 0.3 μm) with ~ 50 8-shape cycles. After polishing, the electrodes were rinsed thoroughly with distilled water.

The second step is an electrochemical cleaning. It is a very important step for Pt electrode cleaning. The most commonly used method is to carry out several CV scans in a wide potential range in a concentrated H_2SO_4 aqueous solution (see Figure III.2). This potential range should be wide enough to make sure the electroactivities of platinum and protons can be exploited in order to get rid efficiently of the contaminants on the platinum surface.

Figure III.2.b (right) corresponds to this situation as it shows the CV scans obtained during the electrochemical cleaning of a Pt working electrode in our experimental conditions. The potential range was set to be -0.2 V – 1.4 V vs. MSE. A 0.5 M H_2SO_4 aqueous solution (pH=0) was employed for this electrochemical cleaning procedure. In this figure, the electroactivities of hydrogen and platinum are in good agreement with the expectations formulated from Figure III.1, indicating that the platinum electrode surface is well cleaned.

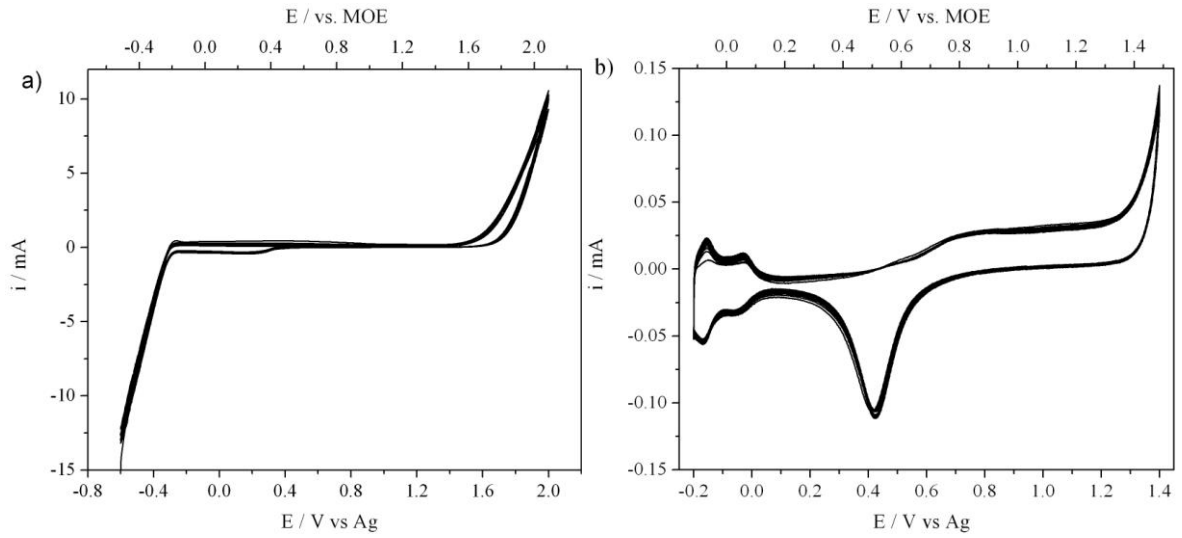

Figure III.2: Consecutive cyclic voltammetry curves obtained during the electrochemical cleaning of a Pt working electrode using a) a large (10 scans) and b) a narrower (20 scans, deaerated) potential range. Aqueous electrolytic solution: H_2SO_4 (0.5 M). Scan rate: 50 mV/s. WE: bulk Pt (diameter 5 mm).

Figure III.2a (left) corresponds to a situation where the potential range is much larger. In this case, oxygen evolution reaction (OER) and hydrogen evolution reaction (HER) occurring respectively in the anodic and cathodic potential ranges of this CV both lead to an intense bubbling on the working electrode surface. This latter is sometimes used to help the removal of undesired adsorbed chemicals or solid film residues at the WE surface.

The influence of the electrochemical cleaning procedure on the cleaning state of a Pt WE is shown in Figure III.3. The black curve shows the original CV of the Pt electrode immediately after physical polishing. The anodic and cathodic peaks intensities related to hydrogen electroactivity are quite weak at the beginning of the test, but they increase slowly during the consecutive CV scans, indicating that the working electrode surface is getting cleaner. Nevertheless, even after one hundred scans, the peaks related to proton reduction are still poorly intense.

The red curve, for which the same Pt electrode was previously cleaned using the large range potential cycling (see Figure III.2a), shows quite intense peaks for hydrogen electroactivity, meaning that the surface is now in a good condition. Also, it should be noticed that during the whole test, the red CV curve shows a good consistency, indicating a good stability of the surface condition.

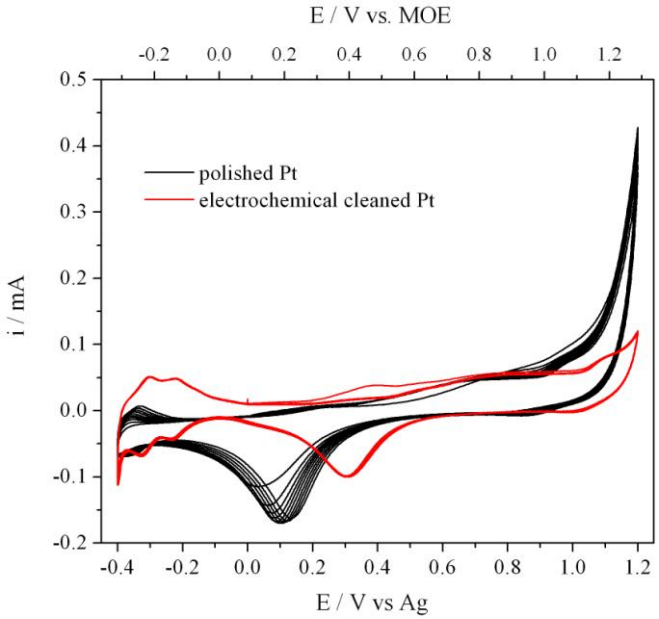

Figure III.3: Consecutive cyclic voltammograms obtained on a Pt working electrode in a H_2SO_4 (0.5 M) aqueous electrolytic solution. Scan rate: 50 mV/s. WE: bulk Pt (diameter 5 mm).

In addition, the positive current appearing on the black curve at potentials higher than 1.0 V, which results from the oxidation of water, has a much higher intensity than the one observed on the red curve, indicating that the surface bears possibly some highly catalytically active species other than pure Pt. However, the cathodic peak observed at 0 – 0.4 V vs. Ag on the black curve, which belongs to the reduction of platinum oxy-hydroxides generated during the oxidation reaction of platinum in the positive potential range, shows different peak intensities from one CV to another. Moreover, this peak moves towards more positive potentials after electrode cleaning, meaning that the electrogenerated platinum based species are more active and more easily reduced.

Based on the results described above, the physical polishing procedure is not sufficient for reaching a satisfying cleaning state on a platinum electrode, which implies that an electrochemical cleaning step is necessary. An electrochemical cycling (consecutive cyclic voltammetry scans over a relevant potential range) is proved to be a useful method to produce and test a clean and stable Pt electrode.

III.2.2 Water oxidation on bare and clean platinum electrodes : influencing parameters

Water oxidation is a complicate multi-step electrochemical reaction; it is sensitive to many experimental parameters. In particular, those defining the composition of the aqueous electrolytic solution, including pH, identity and concentration of ionic species, are always important factors that affect the performance of the electrode material, as shown with the following experiments.

a. Influence of the ionic concentration of the aqueous electrolyte.

Figure III.4 shows the linear sweep voltammetry curves of water oxidation on a Pt electrode in an acidic electrolytic solution for different ion concentrations. These experiments were carried out in a home-made electrochemical cell allowing the relative positioning of the three electrodes to be easily reproduced (see section II.7). In these conditions, one can expect ohmic drop effects that do not depend on the electrode positioning. For $NaNO_3/HNO_3$ solutions (see Figure III-4a), as the salt concentration increases , the anodic current related to water oxidation and measured at a given potential (1.5 V vs. Ag for example) increases too, but when the salt concentration is high enough, for example when $[NaNO_3]/[HNO_3]$ ratios

achieve 7 and 15, this anodic current is lower. However, for the Na_2SO_4/H_2SO_4 solution, this activity increases continuously with the concentration.

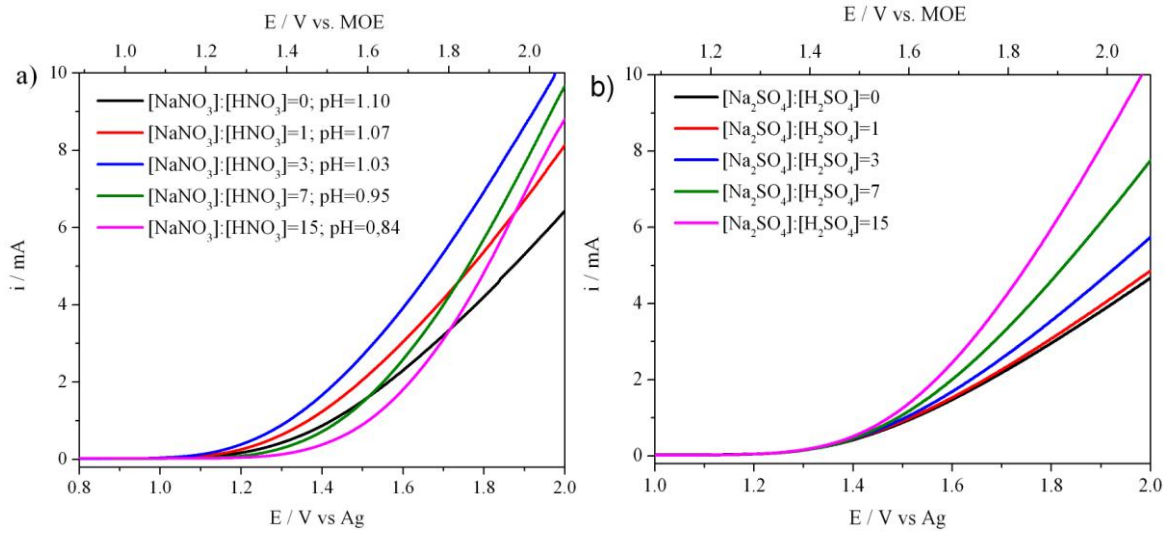

Figure III.4: Linear sweep voltammograms showing water anodic oxidation on a Pt WE in an acidic aqueous medium for different a) $[NaNO_3]/[HNO_3]$ or b) $[Na_2SO_4]/[H_2SO_4]$ ratios. Scan rate: 50 mV/s. WE: bulk Pt (diameter 5 mm).

On the other hand, from the electrolyte resistance values measured by EIS in these electrolytic solutions, and listed in Table III.1, it appears as expected that the electrolyte becomes more ionically conductive as the ionic concentration increases, and the HNO_3 solution has a smaller electrolyte resistance value than the H_2SO_4 solution at the same pH value. This trend does not seem to result from an influence of the limit ionic molar conductivity values for nitrate (71.4 $S.cm^2.mol^{-1}$) and sulfate anions (160 $S.cm^2.mol^{-1}$), respectively. These observations are sufficient to show that anions provided by the electrolyte have a substantial influence on water oxidation, possibly via either a chemisorption or an electrosorption phenomenon, depending on their identity.

Table III.1: Electrolyte resistance of the different test aqueous electrolytes used in this study*.

Salt/acid concentration ratio	0	1	3	7	15
$R_{elec.}(Na_2SO_4/H_2SO_4)$ / Ω	97.4	90.7	69.6	44.1	27.2
$R_{elec.}(NaNO_3/HNO_3)$ / Ω	61.5	51.5	39.8	27.3	19.2

* Resistance values are measured by using the high frequency limit of the EIS spectra recorded in these electrolytes.

Figure III.5 shows the linear sweep voltammograms in alkaline (NaOH) electrolytes in the presence of various concentrations of either sodium nitrate or sodium sulfate. Clearly, as the ion concentration increases, the anodic current related to water oxidation increases markedly. Simultaneously, the pH values of both solutions only slightly decrease, indicating that the high ionic concentrations inhibit the electrochemical reactivity of OH^- in the electrolyte. However, unlike the $NaNO_3/HNO_3$ and Na_2SO_4/H_2SO_4 acidic electrolytic solutions, when the concentration is high enough, the promotion effect becomes more limited, as shown by concentration ratios reaching 7 and 15. Moreover, the activity of the Pt electrode in the high potential region has an inflection, indicating possibly some mechanism changes.

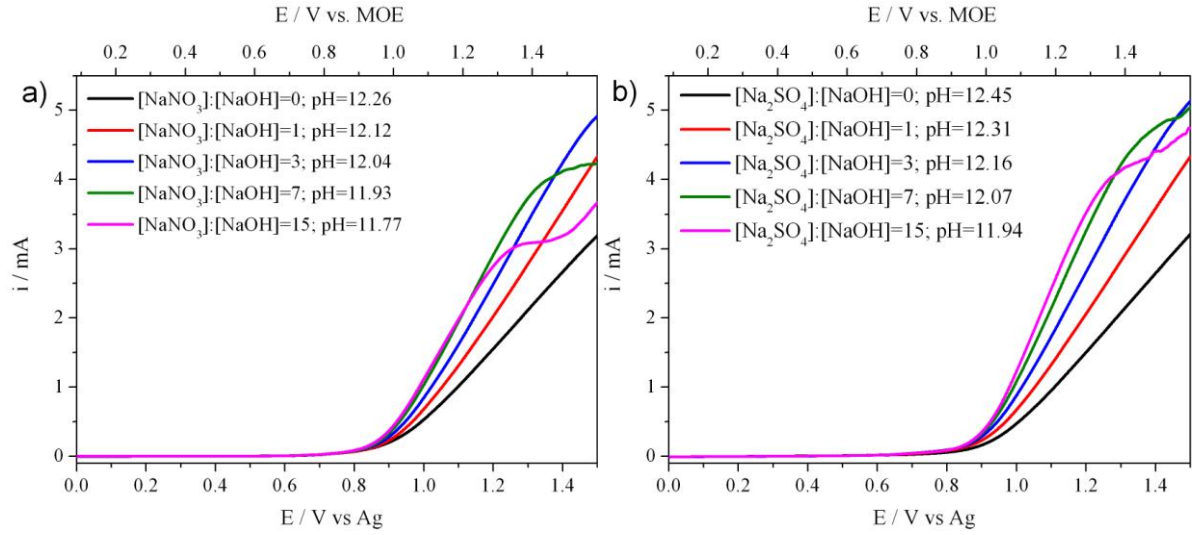

Figure III.5: Linear sweep voltammograms showing water anodic oxidation on a Pt WE in an alkaline aqueous medium for different a) $[NaNO_3]/[NaOH]$ or b) $[Na_2SO_4]/[NaOH]$ ratios. Scan rate: 50 mV/s. WE: bulk Pt (diameter 5 mm).

From the above results, it appears that both the ion concentration and identity of the electrolyte have a great influence on the electrochemical activity of platinum towards water oxidation. Moderately concentrated aqueous electrolytic solutions will promote the water anodic oxidation reaction, which could be ascribed to the increase of the solution conductivity caused by the high ionic concentration. Highly concentrated solutions will make the reaction possibly more complicated (appearance of a shoulder on the anodic wall) or hinder the activity of electrode material, possibly as a consequence of anion adsorption phenomena. One can also observe by comparison between figures III.4 and III.5 that water oxidation appears at much lower anodic potentials when the pH is more alkaline. This is not surprising, knowing that water oxidation is a pH-dependent redox reaction whose Nernst

potential is expected to shift by 60 mV per pH unit towards more cathodic potentials, according to Nernst equation related to the O_2/H_2O redox couple.

b. Influence of pH

The linear sweep voltammograms shown on Figure III.6 were obtained in various electrolytic solutions possessing different pH values. Both series of experiments show that only very alkaline pH values (pH 13) lead to a substantial shift of the water oxidation wave towards cathodic potentials, whereas lower pH values do not produce significantly different LSV curves.

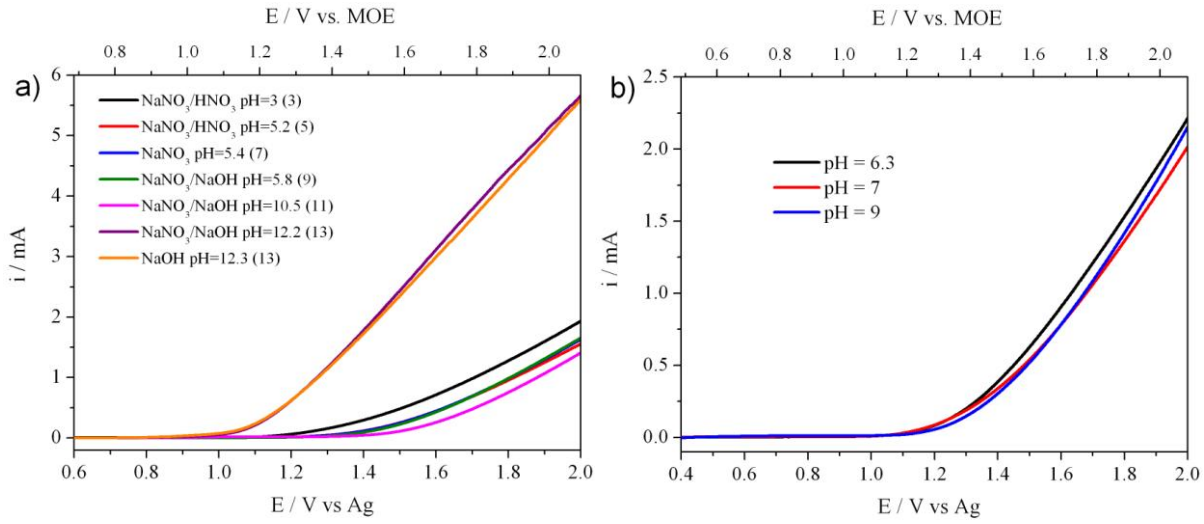

Figure III.6: Linear sweep voltammograms showing water anodic oxidation on a Pt WE in an alkaline aqueous medium for a) different or b) $NaNO_3/HNO_3$ aqueous electrolytic solutions, at different pH values (inside the brackets are the theoretical pH value). Scan rate: 10 mV/s. WE: bulk Pt (diameter: 5 mm).

c. Influence of start potential and scan rate on water oxidation

In addition, it was found that the electrochemical activity of Pt is also related to the starting potential and scan speed of the test, as shown in Figure III.7. As the starting potential increases, the onset potential (or wave foot potential) of water oxidation increases too, which means that the electrochemical activity of Pt is partially inhibited. As the test starts at a higher potential, the Faradaic charge time decreases, which might lower the ion concentration very close to the electrode surface, and make it in a non-equilibrium state, thus hindering the water oxidation reaction. Moreover, a slightly better activity was found when the scan rate increases. This is commonly known and resembles the behavior described by Randles-Sevcik

equation, in which the peak current is proportional to the square root of scan rate ($i_p \propto v^{1/2}$) for a freely diffusing redox species and to the scan rate ($i_p \propto v$) for a redox species grafted on the working electrode surface[109].

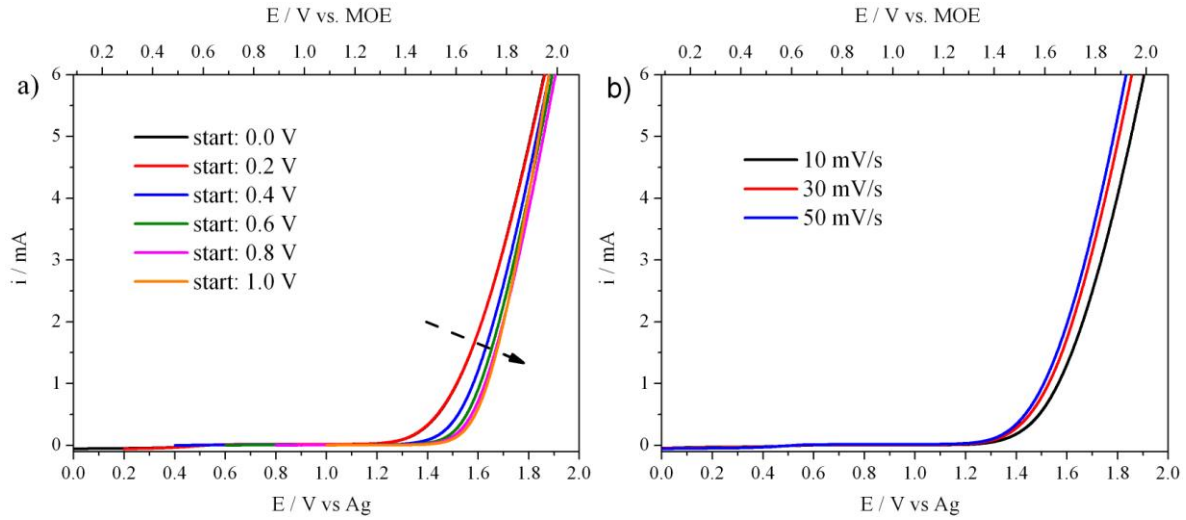

Figure III.7: Linear sweep voltammograms of water oxidation on a bulk Pt electrode with different a) starting potentials and b) scan rates. Aqueous electrolytic solution: H_2SO_4 (pH=1) with Na_2SO_4, $[Na_2SO_4]/[H_2SO_4]=15$.

As discussed above, the electrochemical activity of the working electrode material towards water oxidation is very sensitive to the experimental parameters, whether they are electrochemical or related to the chemical composition of the solution, which makes the comparison of the experimental results very difficult when they come from different research groups. Thus, a unified electrochemical procedure aimed at the evaluation of (photo)-electrocatalysts is necessary to make the obtained results comparable.

III.3 Electrodeposition of MnO_2 films on Pt electrode

III.3.1 Electrodeposition and electrochemical reduction of MnO_2 films

In order to get more familiar with the electrodeposition and electrochemical reduction mechanisms of manganese dioxide in our experimental conditions, a Pt electrode was used as a substrate for MnO_2 electrodeposition. Figure III.8 is the CV curve of Pt electrode in a $MnSO_4/H_2SO_4$ aqueous electrolytic solution (pH 2), which has been employed previously in our group[110]. The anodic peak located in the positive potential range located between 0.5 V

— 1.0 V vs. MSE is ascribed to the oxidation of Mn^{2+} into Mn^{4+}, according to the following redox reaction:

$$Mn^{2+} + 2H_2O \rightarrow MnO_2 + 4H^+ + 2e^- \quad \text{(III.1)}$$

The following anodic wave appearing after this peak at potentials higher than 1.0 V is the start of the water anodic oxidation wave. In the backward scan, a large cathodic wave extending from about 0.6 V vs. MSE to about -0.7 V vs. MSE reveals the complex reduction mechanism of the electrodeposited MnO_2 film. This wave is followed by the electrochemical reduction of protons.

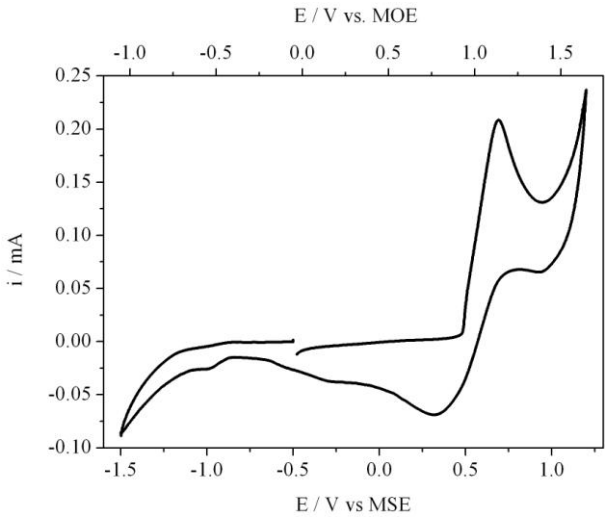

Figure III.8: Cyclic voltammetry curve of MnO_2 electrodeposition and reduction on a bulk Pt working electrode. Electrolyte: $MnSO_4$ (0.3 M), H_2SO_4 (pH 2.0). Scan rate : 10 mV/s.

According to literature, the oxidation of Mn^{2+} to Mn^{4+} is not simply a one-step reaction, but rather a multi-step anodic oxidation mechanism which is also called a ECE mechanism [111-113]. In this model, the first step of MnO_2 electrodeposition is the formation of Mn^{3+}, as given by reaction III.2:

$$Mn^{2+} \rightarrow Mn^{3+} + e^- \quad \text{(III.2)}$$

Then it goes through a hydrolysis reaction, as given by reaction III.3 and III.4:

$$Mn^{3+} + 2H_2O \rightarrow MnOOH + 3H^+ \quad \text{(III.3)}$$

$$MnOOH \rightarrow MnO_2 + H^+ + e^- \quad \text{(III.4)}$$

In this way, MnO_2 is generated on the electrode. At the same time, Mn^{3+} may go through a disproportionation reaction to form Mn^{4+} in concentrated acid aqueous solutions and then form MnO_2, as given by reaction III.5 and III.6:

$$2Mn^{3+} \rightarrow Mn^{2+} + Mn^{4+} \quad \text{(III.5)}$$

$$Mn^{4+} + 2H_2O \rightarrow MnO_2 + 4H^+ \quad \text{(III.6)}$$

In this ECE model, an intermediate MnOOH compound, which is insoluble, forms an insulating film as an intermediate during the formation of MnO_2, and it may remain in the structure of the final electrodeposited film, leading to an inhomogeneous chemical composition. In Figure III.8, the oxidation peak seems to be a single peak with a very brutal increase of the current, and it is thus difficult to separate the different steps of the abovementioned global electrodeposition mechanism.

During the electrochemical reduction of MnO_2, a reverse two-step reduction process is believed to happen, as given by reaction III.7 and III.8:

$$MnO_2 + H^+ + e^- \rightarrow MnOOH \quad \text{(III.7)}$$

$$MnOOH + 3H^+ + e^- \rightarrow Mn^{2+} + 2H_2O \quad \text{(III.8)}$$

Viewing from Figure III.8, the backward scan of the CV clearly shows a multi-step mechanism, with a first step located at 0 - 0.7 V vs. MSE corresponding to reaction III.7 and a second one located at -0.7 - 0 V vs. MSE attributed to reaction III.8. In this sense, MnOOH also plays a significant role in the electrochemical reduction mechanism.

To further investigate the electrodeposition and electrochemical reduction of thick MnO_2 films, a separated two-step electrochemical procedure was performed. MnO_2 films were electrodeposited by 20 CV scans using the potential range situated between 0.45 and -1.2 V vs. MSE, as shown in Figure III.9a and c. The electrochemical reduction was performed in a H_2SO_4 aqueous electrolytic solution with and without the presence of $MnSO_4$, as shown in Figure III.9b and d respectively. During the electrodeposition procedure (curves a and c), it is clear that the first scan shows the highest anodic peak current, and it decreases continuously as the electrodeposition process goes on, without reaching 0, which indicates that the MnO_2 film electrodeposited on the working electrode surface is either not insulating, or insulating but not homogeneous. According to the ECE mechanism described above,

MnOOH forms as an intermediate film only and MnO_2 is expected to be either a poor conductor or a semi-conductor. During the first cycle, MnO_2 is formed on bare and highly electronically conducting Pt surface, thus the faradaic current is high. However, during the subsequent CV scans, further MnO_2 layers are electrodeposited on top of a potentially porous MnOOH/MnO_2-layer, expected to possess a lower conductivity, thus the current is limited. As the electrodeposited MnO_2 film becomes thicker, the current decreases continuously.

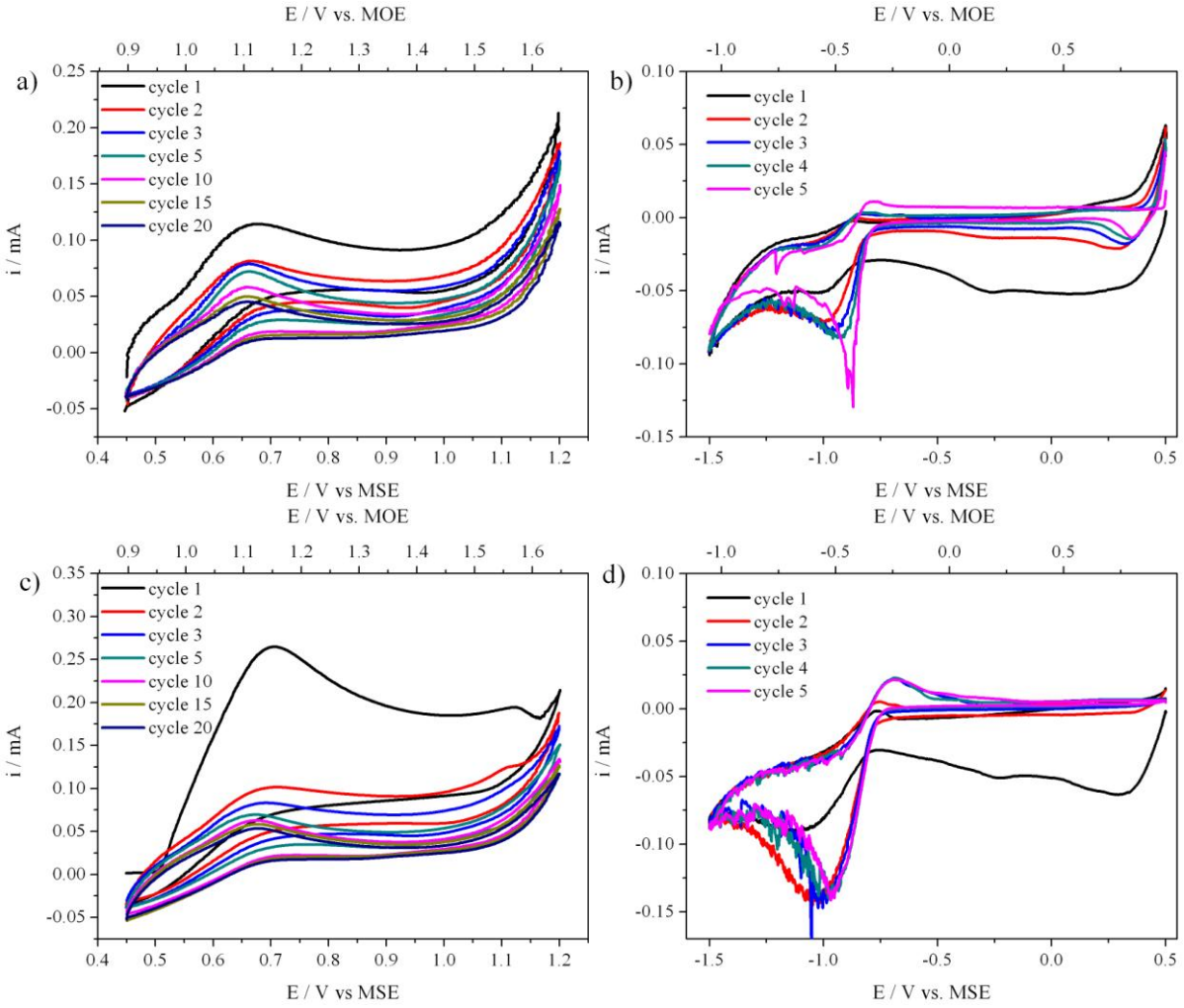

Figure III.9: Cyclic voltammetry curves showing MnO_2 electrodeposition (a and c, 20 consecutive scans) and electrochemical reduction (b and d, 5 consecutive scans) in an aqueous electrolytic solution containing H_2SO_4 (pH=1.8) with (a, b, c) or without (d) $MnSO_4$ (0.3 M). Scan rate: 10 mV/s. WE: bulk Pt (diameter 5 mm).

During the electrochemical reduction procedure in the $MnSO_4$ containing electrolyte (Figure III.9b and d), two cathodic waves can be observed. The one appearing between 0.5 and -0.75 V vs. MSE (wave N° 1) is attributed to the complex multistep electrochemical reduction of MnO_2 into Mn^{2+}; whereas the second one possessing a peak potential close to

-0.95 V vs. MSE (wave N° 2) is attributed to proton reduction and therefore to the production of hydrogen bubbles, which may explain the noisy aspect of this second cathodic peak. In the potential range corresponding to wave N° 2, the curve of the 5th cycle is noisier than the curve of the previous cycles, as a consequence of the likely explosion of electrogenerated H_2 bubbles on the electrode surface.

On Figure III.9b obtained in the presence of $MnSO_4$, the current measured for wave N° 1 in the first cycle is intense but it undergoes a dramatic decrease on the second one whereas the following cycles show a decrease much lower than the one observed between the first and the second scan. This reduction phenomenon indicates that most of the MnO_2 film is electrochemically reduced during the first cycle, and only a small part is reduced during the following cycles. This trend is even more pronounced during the electrochemical reduction test carried out in a H_2SO_4 solution in the absence of $MnSO_4$ (Figure III.9d) as the electrochemical reduction of MnO_2 seems to occur almost exclusively during the first scan. Indeed, it is noteworthy that in Figure III.9d, all of the CV curves are quite flat with little cathodic current in the potential region situated between -0.7 and 0.5 V vs. MSE except for the first cycle. However, when the electrolyte contains $MnSO_4$, as shown in Figure III.9b, a much more intense cathodic current is observed in this potential range. Besides, the presence of $MnSO_4$ allows a small amount of MnO_2 to be electrodeposited during the forward scan, as shown by the presence of a small anodic peak between 0.25 and 0.5 V vs. MSE and a following cathodic peak on Figure III.9b. One can also notice that the ratio of the peak currents of waves N° 1 and 2 appear to be more important on the first cycle of Figure III.9d obtained in the absence of $MnSO_4$ than on the first one of Figure III.9b obtained in the presence of $MnSO_4$. Moreover, wave N° 1 has a different shape on those two figures. Those numerous observations confirm that Mn^{2+} cations initially present in the electrolytic solution do have a real influence on the electrochemical reduction mechanism of MnO_2.

Importantly, although nearly no obvious electrochemical reduction of MnO_2 is observed after 5 reduction cycles on Figures III.9b and d, one can still observe some black material left on the platinum electrode surface, which means that a part of the MnO_2 film could not be reduced. S. Nijjer *et al.* studied the electrochemical oxidation and reduction of MnO_2 in a H_2SO_4 aqueous solution and found that the electrochemical reduction of MnO_2 films firstly takes place at the substrate surface / MnO_2 layer interface and turns MnO_2 to MnOOH through reaction III.7[113]. Therefore, the adhesion of the film to the substrate is

damaged during the first reduction cycle, making the following reduction more difficult, which is consistent with the observation here. This theory is also supported by the fact that the remaining film after reduction can be easily peeled off from the substrate.

Another electrochemical study aimed at better understanding the reduction mechanism of MnO_2 thin films was carried out on a bare platinum electrode in a Na_2SO_4 aqueous electrolytic solution, in the presence (see Figure III-10a) or in the absence (see Figure III-10b) of manganese sulfate. An electrolyte with neutral pH was employed instead of an acidic one so as to preserve from corrosion the Mn metal possibly electrogenerated in the case of the electrochemical reduction of Mn^{2+} cations. In the absence of manganese sulfate (see Figure III.10b, the cyclic voltammogram is almost completely flat and shows therefore mainly a capacitive current, except at potentials lower than -1.1 V vs. MSE where a faradaic current attributed to water (proton) reduction can be observed. In the presence of manganese sulfate in the electrolytic aqueous solution, a cathodic current still appears at potentials lower than -1.1 V vs. MSE although its variation as a function of the potential on a given scan and during ten consecutive scans appears to be substantially different from that observed on the neighboring figure. Such differences are likely to result from the reduction of Mn^{2+} cations into Mn Metal.

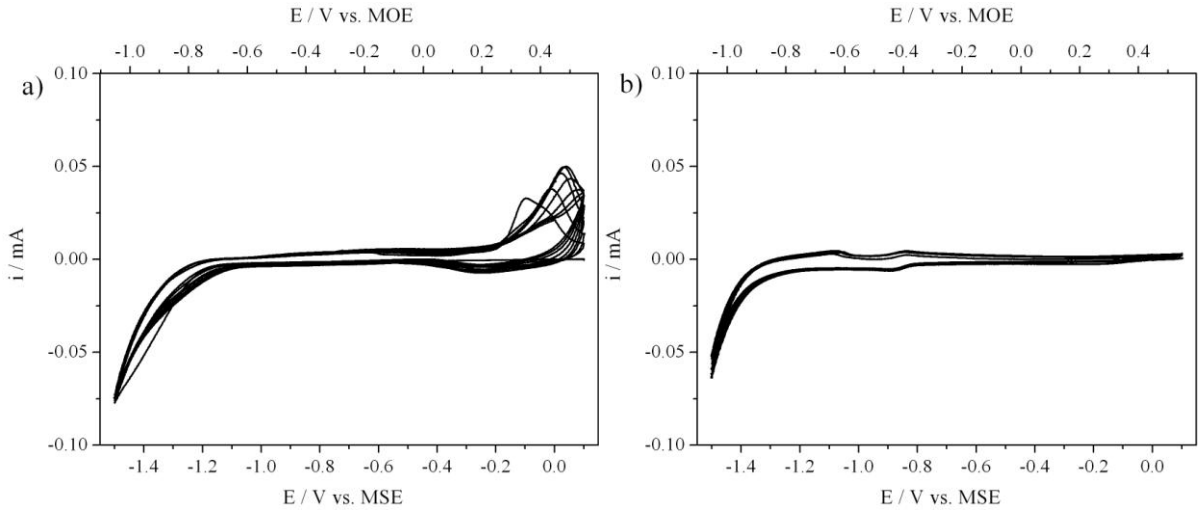

Figure III.10: Cyclic voltammetry curves of Pt electrode in a electrolyte with (left) and without (right) $MnSO_4$. Electrolyte: $MnSO_4$ 0.1 M; Na_2SO_4 0.1 M. Scan rate: 10 mV/s.

Moreover, one can observe anodic peaks on Figure III.10a that do not appear on the neighboring figure obtained in the aqueous electrolyte without $MnSO_4$. Although it appears in a potential range more cathodic than the one corresponding to Mn^{2+} oxidation on Figure

III.9a,c, one can attribute this oxidation potential to MnO_2 electrodeposition possibly shifted as a consequence of a pH effect (see equation III.1), as this is confirmed by a poorly intense cathodic peak between 0 and -0.4 V vs. MSE corresponding to the electrochemical reduction of electrodeposited MnO_2 thin films.

Besides, a small reduction wave shows up in Figure III.10 (right) starting from -0.8 V, this might be caused by the electrochemical reduction of dissolved oxygen traces.

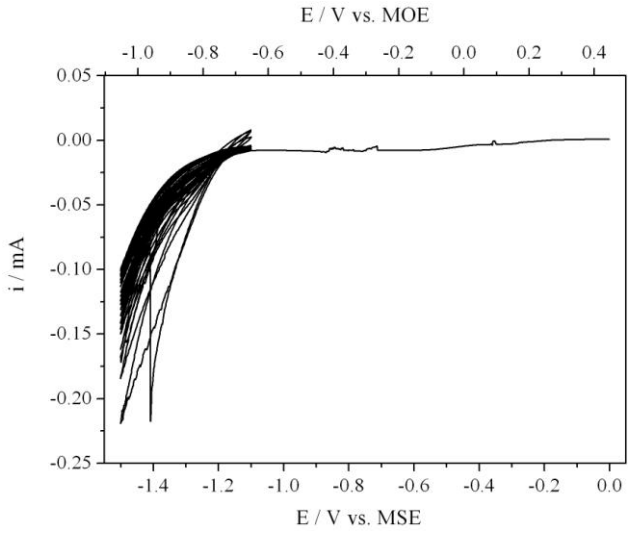

Figure III.11: Cyclic voltammograms (20 consecutive scans) of Mn^{2+} reduction. Aqueous electrolytic solution: $MnSO_4$ (0.1 M), Na_2SO_4 (0.1 M). Scan rate: 10 mV/s. WE: mica/Pt.

In order to verify the hypothesis of the electrogeneration of Mn metal, a further reduction test was carried out, as shown in Figure III.11. A bare Pt electrode was cycled for 20 times in a potential range situated between -1.5 V and -1.1 V vs. MSE, starting from 0.1 V vs. MSE. As a result of this test, a shiny layer of metal was clearly electrogenerated at the surface of the electrode. This shiny layer was characterized by EDS analysis and the existence of a Mn metallic film was confirmed. Thus in the low potential region below -1.1 V vs. MSE, Mn^{2+} is reduced to Mn, as given by reaction III.9, and the anodic peak appearing at around -0.2 V vs. MSE on Figure III.9 possibly contains a contribution of the oxidation of Mn metal into Mn^{2+}.

$$Mn^{2+} + 2e^- \rightarrow Mn \qquad \text{(III.9)}$$

In order to accurately position the oxygen reduction wave, the experiments reported on Figures III.9b and d were repeated by saturating the electrolytic solution with either pure

oxygen gas or pure nitrogen gas. The results are shown in Figure III.12. For a new solution without any gas bubbling, a small cathodic wave starts appearing at -0.1 V vs. MSE (see black curve on Figure III.12). When the solution is saturated using an oxygen bubbling, this cathodic wave becomes much more intense (see red curve on Figure III.12). On the contrary, it disappears when the solution is saturated using nitrogen bubbling (see blue curve on Figure III.12). Thus, this small reduction wave means the solution contains some dissolved oxygen:

$$2H_2O + O_2 + 4e^- \rightarrow 4OH^- \qquad \text{(III.10)}$$

However, the intensity of this wave is always very low and very well differentiated by comparison with the other reduction peak growing from -0.8 V vs. MSE attributed previously to proton reduction in a sulfate-rich electrolytic solution. Generally speaking, the presence of dissolved oxygen does not interfere in most of the water oxidation tests carried out in this thesis.

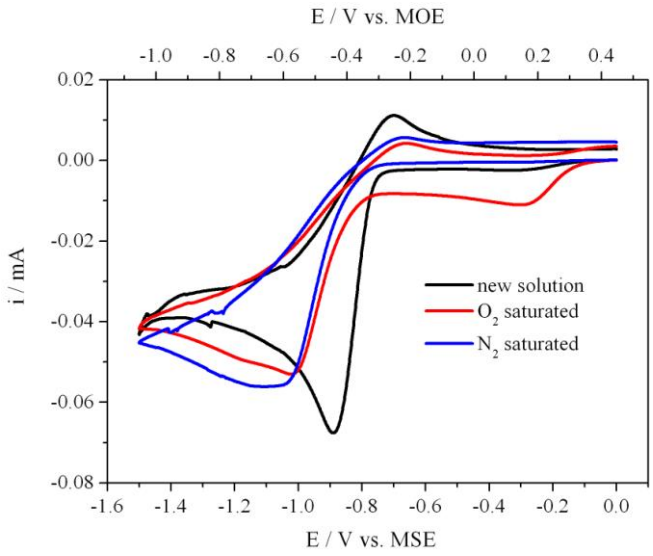

Figure III.12: Cyclic voltammetry curves of a bare bulk Pt electrode in an acidic aqueous solution in the presence of different amounts of dissolved oxygen gas. Electrolyte: $MnSO_4$ (0.1 M), H_2SO_4 (pH 1.8). Scan rate: 10 mV/s.

III.3.2 Influence of electrolyte pH on MnO_2 electrodeposition

The pH value of the electrolytic is always an important factor in electrochemistry. According to the reaction formula III.1, MnO_2 electrodeposition is also sensitive to the pH of the electrolytic solution. Nernst equation provides a method to calculate the relation linking the electrolyte pH with the redox potential:

$$E_{(MnO_2/Mn^{2+})} = E^o{}_{(MnO_2/Mn^{2+})} + \frac{2.3RT}{zF}\log\frac{(a_{H^+})^4}{a_{Mn^{2+}}} \quad \text{(III.11)}$$

where $E_{(MnO_2/Mn^{2+})}$ and $E^o{}_{(MnO_2/Mn^{2+})}$ are respectively the redox potential and the standard potential for MnO_2/Mn^{2+} redox couple, a_{H^+} and $a_{Mn^{2+}}$ are the chemical activities of the H^+ and Mn^{2+} ions respectively, F is the Faraday constant, z is the number of transferred electrons in the redox half-reaction. As $Mn^{2+} \rightarrow MnO_2$ is a two-electron reaction, thus the value of z is 2; 2.3RT/F = 0.059, then equation III.11 has the following form:

$$\begin{aligned} E_{(MnO_2/Mn^{2+})} &= E^o{}_{(MnO_2/Mn^{2+})} + \frac{0.059}{2}\log\frac{(a_{H^+})^4}{a_{Mn^{2+}}} \\ &= E^o{}_{(MnO_2/Mn^{2+})} + \frac{0.059}{2}(\log(a_{H^+})^4 - \log a_{Mn^{2+}}) \end{aligned} \quad \text{(III.12)}$$

Considering that:

$$\mathrm{pH} = -\log a_{H^+} \quad \text{(III.13)}$$

Thus, equation III.12 could be written by:

$$E_{(MnO_2/Mn^{2+})} = E^o{}_{(MnO_2/Mn^{2+})} - \frac{0.059}{2}\log a_{Mn^{2+}} - 0.118\mathrm{pH} \quad \text{(III.14)}$$

This means that in an electrolyte containing a given Mn^{2+} concentration, the higher the pH, the lower the potential needed for the reaction to proceed.

Furthermore, MnO_2, as a metal oxide, is not stable in acidic medium, and it may dissolve progressively in a highly acidic solution. Accordingly, the pH of the electrodeposition electrolytic solution should have a great influence on the properties of electrogenerated films. To evaluate the influence of the pH of the electrolytic solution, MnO_2 electrodeposition was carried out in neutral and acidic electrolytes respectively, using the cyclic voltammetry technique (see Figure III.13a,c). The charges of the anodic peak related to MnO_2 electrodeposition, and of the cathodic peaks related to MnO_2 reduction and dissolution, were calculated for each cycle, and plotted as a function of the cycle number, as shown in Figure III.13b,d. The shape of the consecutive CV curves is similar for both electrolytes (see Figure III.13a,c), except that an anodic wave corresponding possibly to the first one-electron

oxidation step of Mn^{2+} shows up at around 0.4 V vs. MSE on the forward scan in neutral medium (see Figure III.13a). For the current values, it is obvious that the electrodeposition in an electrolyte with neutral pH produces much higher peak current values (1.1 mA for the oxidation peak and - 0.7 mA for the reduction peak on Figure III.13a) by comparison with those in acidic electrolyte (0.75 mA and -0.4 mA respectively on Figure III.13c)). This means that the electrodeposition in an electrolyte with neutral pH is much easier and faster.

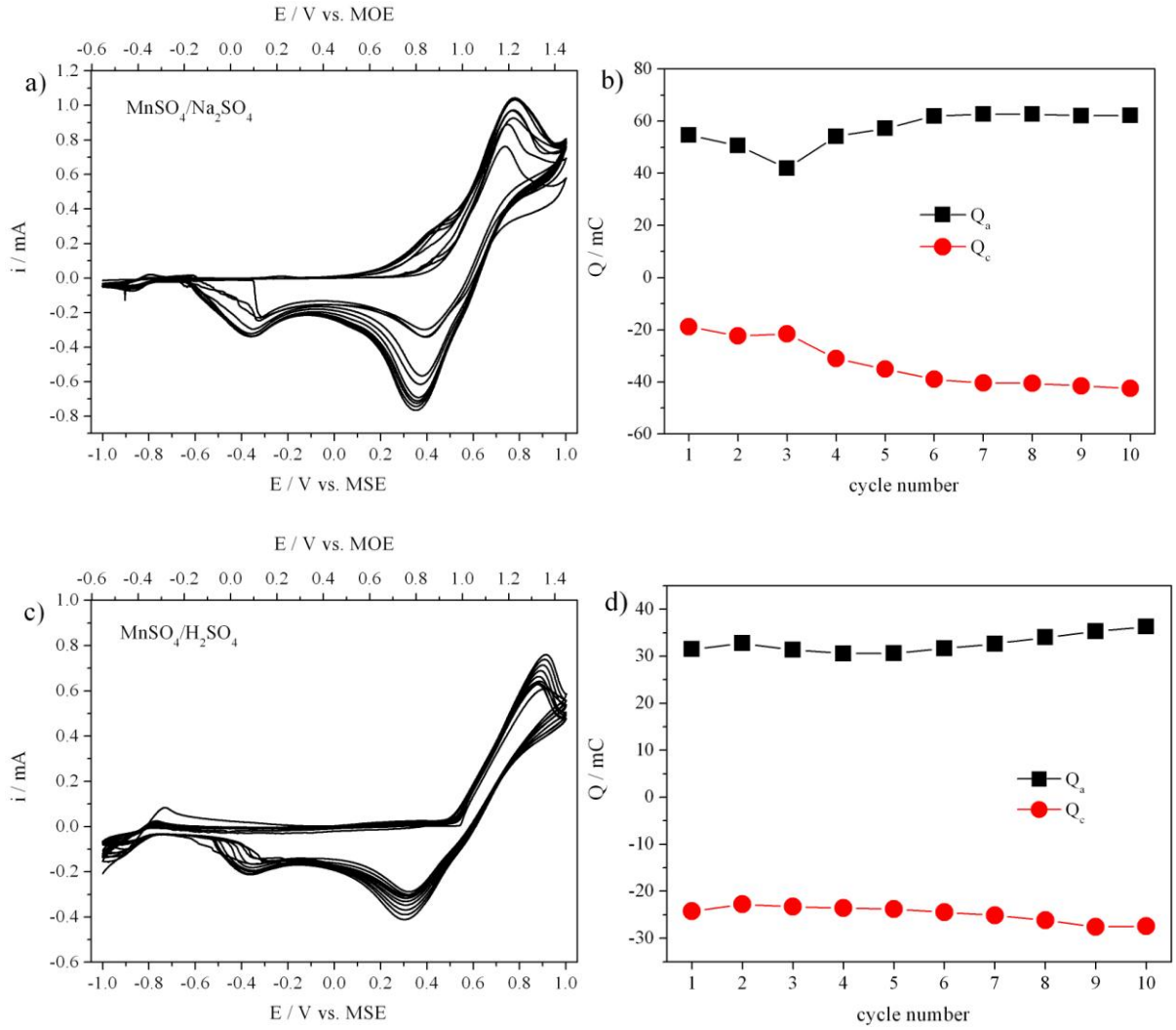

Figure III.13: Cyclic voltammetry curves of MnO_2 electrodeposition on Pt electrode in neutral (a) and acidic (c) electrolytic solutions, and plots of the anodic (Q_a) and cathodic (Q_c) coulombic charges corresponding to the neutral (b) and acidic (d) electrolytic solutions respectively. Electrolytic solution: $MnSO_4$ (0.1 M) and a,b) Na_2SO_4 (0.1 M), c,d) H_2SO_4 (pH 1.8). Scan rate: 10 mV/s. WE: bulk Pt (diameter 5 mm).

In the potential range used for these experiments, we can consider that neither water oxidation nor proton reduction happen. Thus all coulombic charges consumed during these consecutive CV scans are either related to electrochemical oxidation of Mn^{2+} cations into

MnO_2 or to MnO_2 reduction and dissolution into Mn^{2+} cations. In this case, through the difference observed between the anodic and cathodic charges on each scan in both electrolytic solutions, we can determine the amount of moles of electrodeposited MnO_2 as well as the dissolution rate of MnO_2. Figure III.13b and d show the evolution of anodic and cathodic charges as a function of cycle number in the neutral and acidic electrolytic solutions respectively. These charges were determined by calculating the integral below the current-time curve deduced from the CV curves shown on Figures III.13a,c. As the cycle number increases, both oxidation and reduction charges slowly increase beyond the third scan in the two tested electrolytic solutions and the charge values in the neutral electrolytic solution are much greater than those in the acidic electrolyte.

Such observation may not only reflect a faster electrodeposition rate in the neutral medium as this latter appears to be more conducting than the acidic one as a consequence of its higher background salt concentration.

The film thickness (t) could be calculated by following formula:

$$t = \frac{\Gamma \cdot M}{\rho} = \frac{Q}{nFA} \cdot \frac{M}{\rho} \qquad \text{(III.15)}$$

where Γ is the superficial concentration (in $mole.cm^{-2}$), M and ρ are respectively the molar mass (in $g.mol^{-1}$) and bulk density (in $g.cm^{-3}$) of MnO_2. n is the transferred electron number which is 2 for $Mn^{2+} \rightarrow Mn^{4+}$, A is the geometrical area of the working electrode and Q is the total coulombic charge used during the anodic electrodeposition of MnO_2 (see anodic peaks on Figures III-13a,c. The value of bulk density ρ was based on an empirical value 5.026 g/cm^3[110] and other parameters were obtained experimentally. The estimated thickness values are listed in Table III.2.

Table III.2: Estimate thickness of electrodeposited MnO_2 in different electrolyte.

electrolyte	Charge / mC	Thickness / μm
Neutral Elec. ($MnSO_4$+Na_2SO_4)	237.4	1.70
Acidic Elec. ($MnSO_4$+H_2SO_4)	78.3	0.56

Based on the calculated results, it is clear that the film electrodeposited from an acidic electrolyte is much thinner than the one obtained in an electrolyte with neutral pH. According to the ECE mechanism mentioned previously, the first step of the anodic oxidation mechanism of Mn^{2+} into MnO_2 is the formation of Mn^{3+} cations, but these latter are not stable in acidic medium, and they may go through the disproportionation reaction quickly and form Mn^{2+} and Mn^{4+}, as given by reaction III.5, which would thus decrease the electrodeposition rate[112]. In acidic electrolyte, it has been reported that the formation of MnO_2 is inhibited by a high acidic strength [113]. This may therefore also explain the fact that the maximum current intensity in the acidic electrolytic solution is lower than that in the neutral one.

III.3.3 AFM images of MnO_2 films electrodeposited on Pt electrode.

The topography of MnO_2 electrodeposited films was studied by tapping mode AFM in air, which could provide information on their surface morphology as well as on their roughness. Figure III.16 shows three voltammograms allowing the electrodeposition of three different MnO_2 thin films (see Figure III.16a) from a neutral aqueous electrolytic solution as well as an AFM image for each of them. The surface roughness values extracted from these latter are listed in Table III.3. Carrying out similar investigations using the FEG-SEM technique appeared to be difficult because of the bad adhesion of our MnO_2 films on the platinum substrates. As shown in Figure III.16, sample (1), which has been electrodeposited using only one linear voltammogram, has the biggest particle size and the highest roughness value. There are some little bright spots dispersed on the surface that disappeared after thorough rinsing by distilled water. They are thus supposed to be the result of the aggregation of remaining salt species coming from the electrolytic solution in spite of the rinsing and drying steps. For sample (2) obtained after partial electrochemical reduction of the electrodeposited MnO_2 film, the surface becomes less rough and the particle size is also smaller due probably to the reduction step, indicating the surface was partially reduced and then dissolved. For sample (3) obtained after an electrochemical reduction step supposedly exhaustive as deduced from the absence of significant faradaic current at the end of the backward scan, the surface underwent little changes comparing with sample (2) as given by the roughness value (even if the image was taken in a smaller area). From this result, it appears that the first reduction step leading to the formation of MnOOH from MnO_2 dominates the change of morphology, while the following step, i.e. the reduction of solid MnOOH thin film into soluble Mn^{2+} cations has little influence.

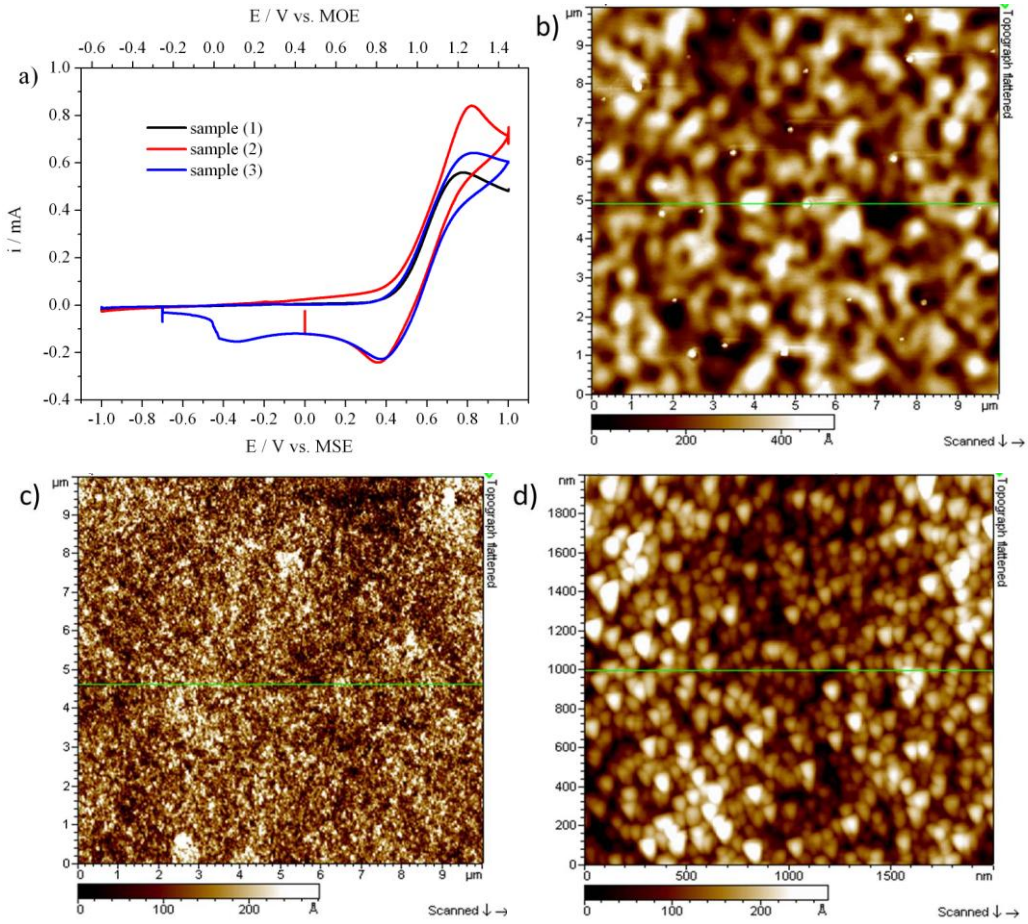

Figure III.14: a) linear or cyclic voltammetry curves allowing MnO_2 electrodeposition on a Pt electrode and b, c, d) the AFM images corresponding to the resulting electrodeposited films. Aqueous Electrolytic solution: $MnSO_4$ (0.1 M), Na_2SO_4 (0.1 M). Scan rate: 10 mV/s. WE: mica/Pt.

Table III.3: Surface roughness of MnO_2 films by different electrodeposition procedures*.

Sample number	(1)	(2)	(3)
RMS / nm	28	15	14

*Values measured on tapping mode AFM images using the AFM software

III.3.4 Optimization of the electrodeposition conditions of MnO_2 films on a Pt electrode

The mechanical stability is a crucial property for a solid catalyst. However, in our experimental conditions, it was very difficult to obtain mechanically stable MnO_2 films on platinum working electrodes using the electrodeposition method. Although the cyclic voltammograms obtained during the electrodeposition step were satisfying, the resulting films were found to crack and explode into flat flakes after drying up, especially in the thick films. This made our investigations and exploitation of this kind of MnO_2 materials quite

difficult on platinum electrodes. In the course of our investigations, a significant number of electrodeposition tests have been carried out using cyclic voltammetry so as to obtain stable MnO_2 films, but nearly all of them failed, whatever the acidic or neutral electrolytic solution was. Figure III.14 shows the SEM image (see Figure III.14b) of a MnO_2 film electrodeposited with the help of the cyclic voltammogram shown on Figure III.14a. We can see that the surface is quite rough and not homogeneous. After drying up, the film is quite fragile and cracks appear all over the film.

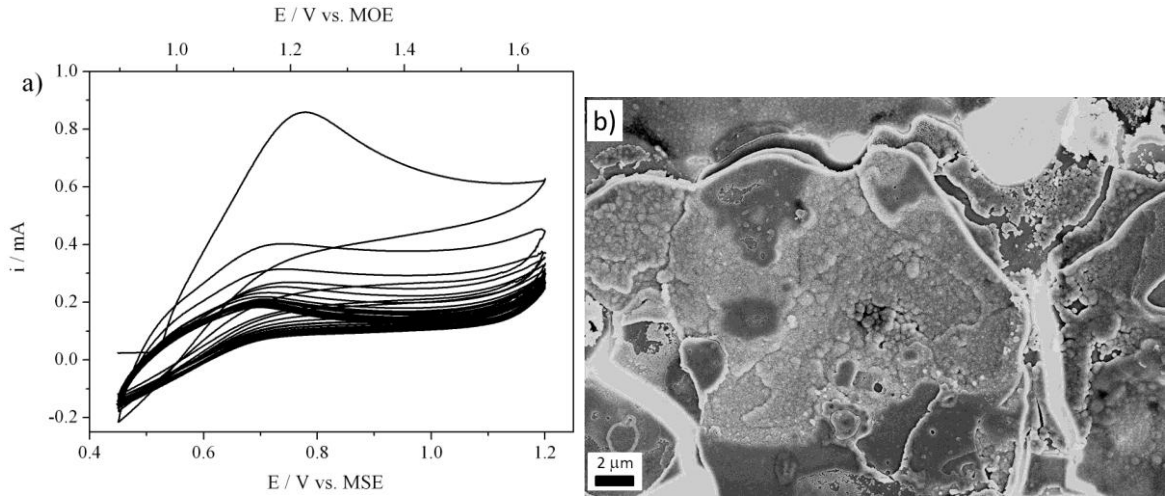

Figure III.15: a) Cyclic voltammogram (20 consecutive scans) allowing MnO_2 electrodeposition from an acidic medium and b) SEM image of the resulting MnO_2 film. Electrolyte: $MnSO_4$ (0.3 M), H_2SO_4 (pH=1.8). WE: mica/Pt.

Another test implying the electrodeposition in a first step (see Figure III.15a) and electrochemical reduction in a second step of a MnO_2 film (see Figure III.15b) was carried out. One can easily observe that the reduction current was much smaller than expected in the given potential range (see Figure III.15b). This observation may indicate that the film had already lost the contact with the substrate, which was caused by the film's mechanical instability. In the FEG-SEM image shown on Figures III-15c, cracks dispersed on the whole surface of the film can be observed, and the film "explosion" is even worse upon drying-up. One can also see some holes on the film, which may be due to the corrosion of MnO_2 film by the acidic electrolyte rather than by electrochemical reduction. It is noteworthy that these films looked flat and stable just after they were taken out of the electrolyte, but they started degrading during the drying-up procedure. Nevertheless, the FEG-SEM image shown on Figures III-15d and obtained with an important magnification shows a very interesting

nanostructuration of the film which offers an important specific area, as usually expected for solid catalysts.

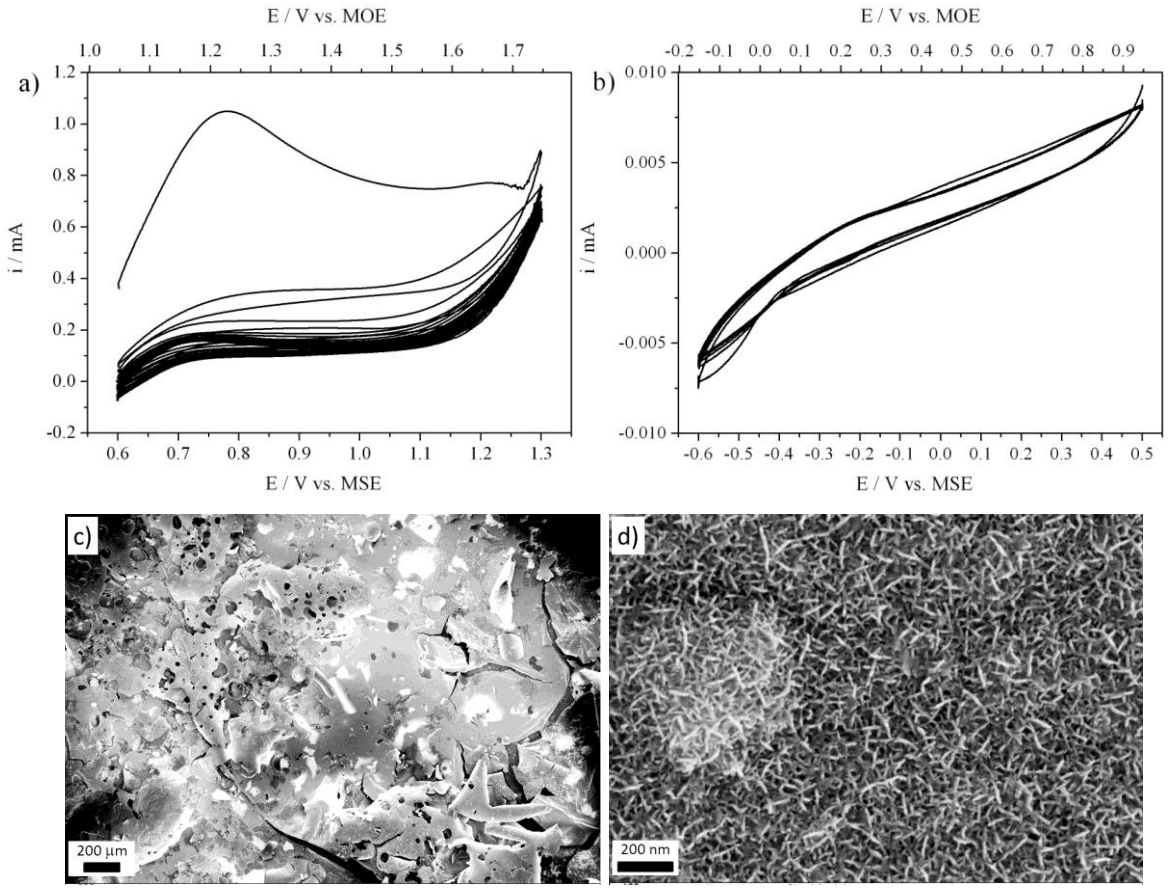

Figure III.16: Cyclic voltammetry curve of MnO_2 electrodeposition (a) and electrochemical reduction (b) and SEM images (c, d) obtained after the reduction step. Electrolyte: $MnSO_4$ (0.3 M) and H_2SO_4 (pH=1.8) for electrodeposition; H_2SO_4 (pH=1.8) for reduction. Scan rate: 10 mV/s.

The reason for this unstable nature of electrodeposited MnO_2 films could be the internal stress created in the bulk of the films upon drying-up. An important thickness makes the situation even worse. In other words, a 20 cycles number may be too much during the electrodeposition procedure. Also, the high Mn^{2+} concentration in the electrolyte, the large potential range and the acidic nature of the electrolyte may also contribute to this result.

Based on these observations, a series of experiments were carried out to optimize the electrodeposition parameters in order to increase the adhesion of MnO_2 films to the platinum substrate, including a decrease of the cycle number, some changes in the chemical composition of the electrodeposition solution, and also the use of another electrodeposition technique such as chronoamperometry. As a conclusion of these investigations, it was shown

that electrodeposition in a concentrated electrolyte makes the resulting films fragile even using a small cycle number and a short deposition time. Chronoamperometry led to better results than cyclic voltammetry, and an electrolyte with neutral pH seemed to favor the formation of stable films.

Conditions: 1 V vs. MSE, 5 min; electrolyte: $MnSO_4$ (0.1 M), H_2SO_4 (pH 1.8)

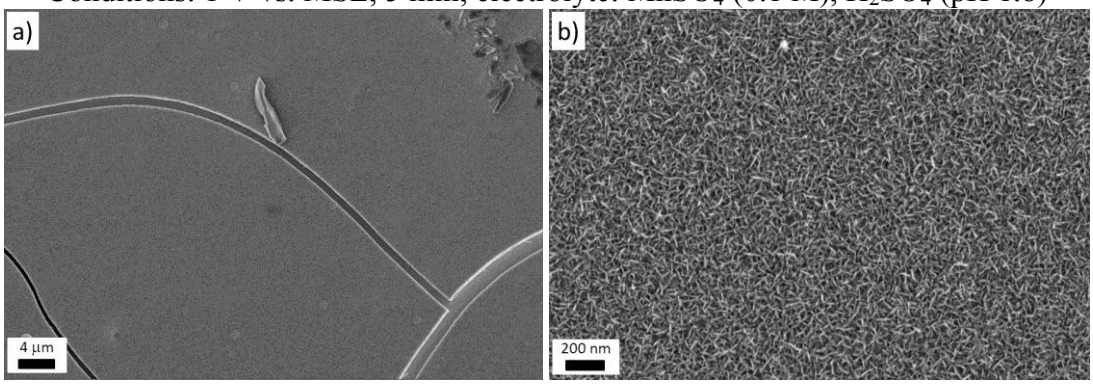

Conditions: 0.75 V vs. MSE, 5 min; electrolyte: $MnSO_4$ (0.1 M), Na_2SO_4 (0.1 M)

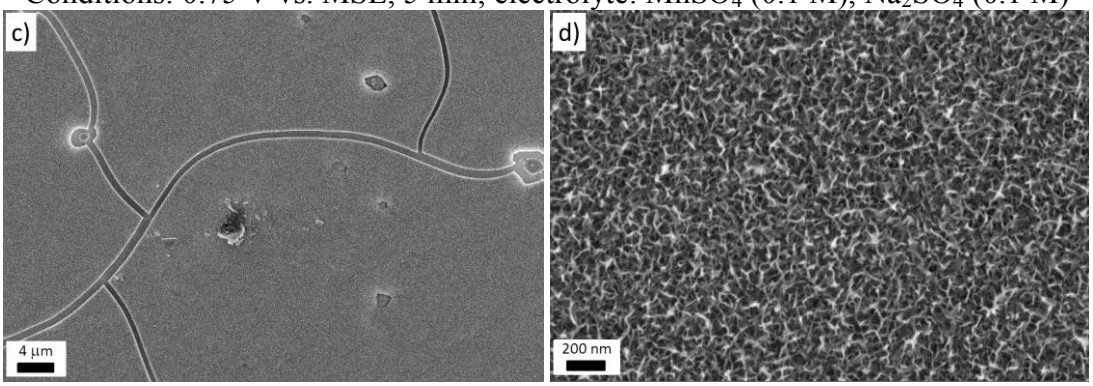

Conditions: 0.6 V vs. MSE, 30 min; electrolyte: $MnSO_4$ (2 mM), $NaClO_4$ (50 mM)

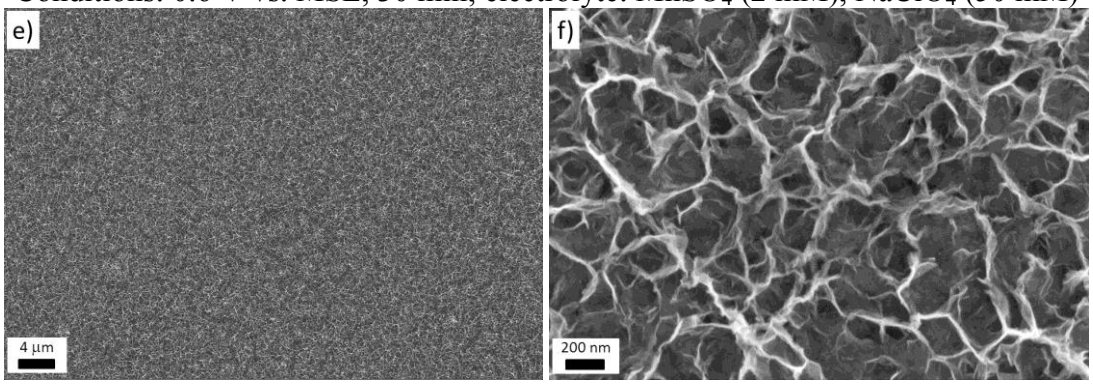

Figure III.17: SEM images of electrodeposited MnO_2 films using chronoamperometry. WE: mica/Pt.

Figure III.17 shows FEG-SEM images of MnO_2 films electrodeposited on platinum by chronoamperometry in different electrolytes. Samples 1 and 2, which were electrodeposited in acidic and neutral solutions highly concentrated in $MnSO_4$, have some

cracks, but the adhesion appeared to be largely promoted. Sample 3, that was electrodeposited in a much less concentrated solution, possessed a much smoother topography and was stable even when they were obtained with a 30 min electrodeposition time. In addition, these films showed different nanostructured morphologies. Sample 1 has the smallest surface structure size, while that for sample 3 is the largest. Samples 1 and 2 show a nanoneedle-like morphology whereas sample 3 rather shows a nanosheet-like morphology. This may be related to the different nucleation mechanisms and growth rates.

Although those films electrodeposited in highly concentrated electrolytic solutions using chronoamperometry were stable after drying up, a part of or the whole film dropped off when they were immersed back in another electrolytic solution, making the evaluation of their electrochemical and electrocatalytic activities very difficult. On the contrary, samples electrodeposited in low concentration electrolytic solutions showed a good stability even after several tests in different solutions.

Based on the results of a variety of experiments, MnO_2 films electrodeposited using chronoamperometry from an aqueous electrolyte containing $MnSO_4$ (2 mM) and $NaClO_4$ (50 mM) showed the best stability and repeatability on Pt electrodes. Thus, this strategy was adopted in the following part of the thesis.

III.4 MnO_2 electrodeposition on ITO

The electrodeposition experiments carried out on Pt electrodes and reported in the previous section revealed the electrodeposition and electrochemical reduction mechanisms of MnO_2, and they allowed an optimized electrodeposition method to be defined in view of getting mechanically and chemically stable MnO_2 thin films. However, Pt is not a suitable material for large-scale applications due to its pronounced scarcity on the earth and to its consequently very high cost. Moreover, transparent electrode materials could be more convenient at least throughout our experiments so as to allow the use of spectroscopic characterization techniques. As a result, an alternative cheap and stable electrode material is strongly required. In this case, a transparent and electronically conducting material such as Indium Tin Oxide (ITO) was employed. It is frequently used in optics experiments and it also allows the use of the light to shine the sample from both front and back sides. Here, a glass

supported ITO electrode was used in order to favor the systematic characterizations and the final target of photoelectrochemical water splitting using the light of a solar simulator.

III.4.1 ITO electrode cleaning

Careful ITO cleaning has been reported in details in several publications. Among them, two methods are commonly used: one is the ultrasonic cleaning and the other is based on acid corrosion [114-116]. According to the first one, glass/ITO electrodes were cleaned in acetone and distilled water for 5 min using an ultrasonic bath, while in the second, which is also called "acid etching", "acid activation" or "acid corrosion" method, glass/ITO electrodes were immersed in a concentrated aqueous HCl solution (37 %) for 40 s, and then rinsed thoroughly with distilled water. Figure III.18 shows the topography of glass/ITO electrodes pretreated by these two methods. As it is shown, the ultrasonic cleaning does not change the surface morphology which is therefore quite smooth, while with the acid corrosion method, a part of the ITO coating is removed and the inner ITO crystals are exposed.

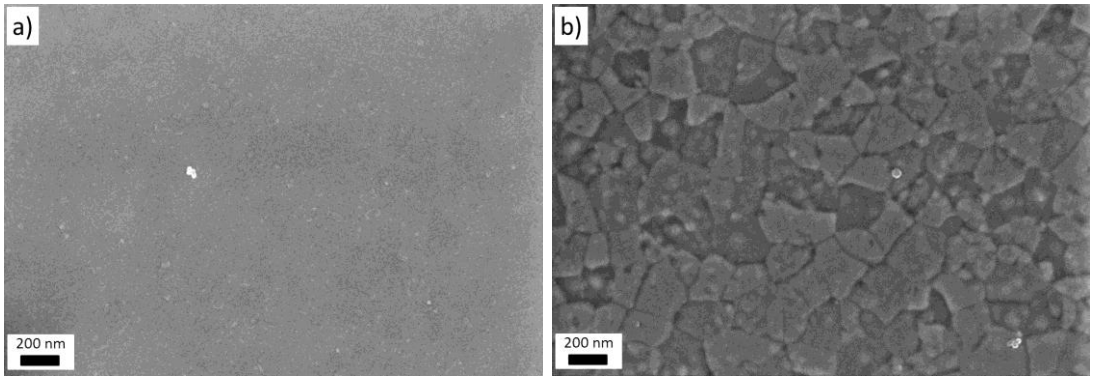

Figure III.18: FEG-SEM images of glass/ITO electrodes cleaned using a) ultrasonic and b) acid corrosion methods.

The crystalline structure of ITO layers before and after acid corrosion cleaning using HCl was characterized by XRD and the spectra are shown in Figure III.19. The diffraction peaks located at 21.4°, 30.5°, 35.4°, 50.9° and 60.7° are all characteristic peaks of In_2O_3. No characteristic signal of crystalline tin oxide is found, meaning that tin oxide is either highly dispersed in the In_2O_3 structure or its amount is too small to be detected. After HCl pretreatment, all peaks related to In_2O_3 disappear, meaning that the In_2O_3 structure is destroyed during acid corrosion.

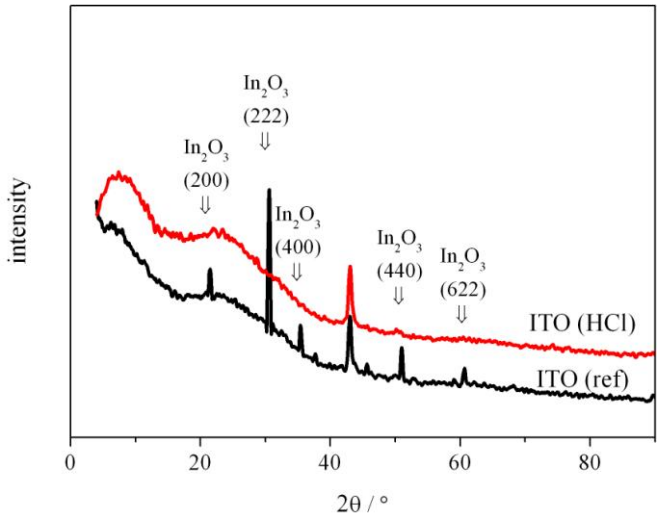

Figure III.19: XRD spectra of bare ITO and HCl pretreated ITO

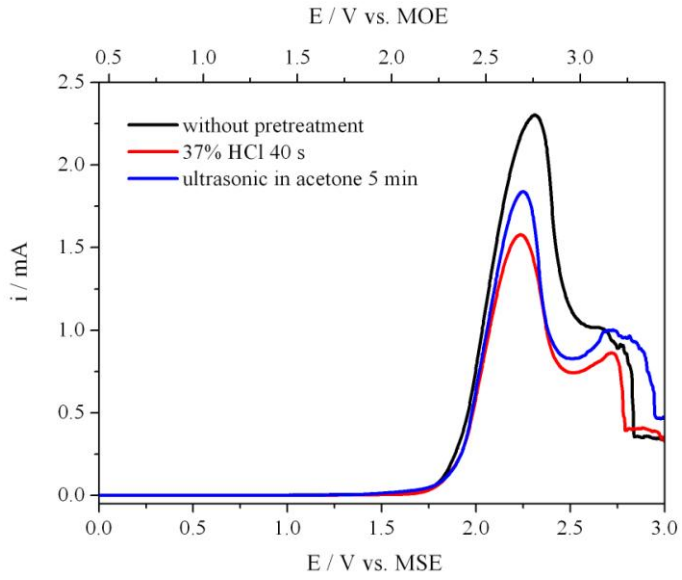

Figure III.20: Linear sweep voltammetry curves obtained on pretreated ITO electrodes in an aqueous acidic electrolytic solution. Electrolytic solution: H_2SO_4 (pH=1.8). Scan rate: 10 mV/s.

In order to evaluate the influence of different cleaning methods on the electrocatalytic activity of glass/ITO electrodes towards OER, linear sweep voltammetry experiments were carried out in an aqueous acidic electrolytic solution, as shown in Figure III.20. Water oxidation starts from ~ 1.5 V vs. MSE, but the oxidation current starts decreasing dramatically at about 2.2 V vs. MSE, to form a plateau followed by another current drop situated at 2.7 or 2.9 V vs. MSE. Moreover, the peak current of water oxidation of the un-cleaned sample is higher than the one observed on clean ITO samples, the one obtained on the ultrasonically cleaned ITO sample being more intense than the one measured on the ITO

sample cleaned in the HCl aqueous solution. Moreover, these ITO electrodes showed little electrocatalytic activity towards water oxidation during the second consecutive LSV test (not shown here), indicating that the ITO layer is severely damaged during the first sweep.

It has been found that ITO reacts quickly with water molecules, carbon oxides or other impurities in atmosphere. Un-cleaned ITO surfaces might bear impurities which can either be oxidized or possess a little electrocatalytic activity, leading thus to an oxidation current that is a little higher than those obtained on the clean ITO substrates [116]. A. Kraft studied the chemical behavior of glass/ITO substrates during strong anodic polarization procedures in neutral aqueous solution and found that Indium was dissolved into the electrolytic solution by loss of the structure oxygen atoms, while tin atoms could stay in the coating by combining with OH^- anions to form tin hydroxide, as given by reaction III.16[117]. M. Senthilkumar *et al.* also studied the performance of glass/ITO substrates in acidic electrolytic solutions during cathodic polarization procedures and found that Sn is more easily dissolved in acidic medium[118]. In our case, the electrolytic solution is acid, thus $Sn(OH)_4$ could not exist as a stable species, which inevitably leads to dissolution of the whole ITO layer, thus making the electrode electrochemically inactive for water oxidation.

$$2In_2O_3 \rightarrow 4In^{3+} + IIIO_2 + 12e^- \quad \text{(III.16)}$$

$$SnO_2 \rightarrow Sn^{4+} + O_2 + 4e^- \quad \text{(III.17)}$$

$$Sn^{4+} + 4OH^- \rightarrow Sn(OH)_4 \quad \text{(III.18)}$$

III.4.2 Electrodeposition of MnO_2 on ITO electrode

A LSV curve was performed in an aqueous and acidic electrolytic solution in the presence of $MnSO_4$ in order to study MnO_2 electrodeposition, as shown in Figure III.21. For pretreated glass/ITO electrodes, the electrodeposition onset potential and peak current were higher than on un-cleaned glass/ITO electrodes, and the acid corrosion pretreatment led to a slightly stronger promotion effect than the ultrasonic cleaning in acetone. This shows the beneficial effect of acid corrosion cleaning on the electrocatalytic activity of glass/ITO electrodes, which is consistent with literature reports indicating that ITO could be more activated by exposition to strong acids [115].

Moreover, water oxidation was observed in a potential range appearing beyond MnO_2 electrodeposition, starting at around 1.9 V vs. MSE for all samples, after a significant current

drop. It therefore appears in a potential range slightly more anodic than on Figure III.20, right before the severe current drop which is ascribed again to the dissolution of the ITO layer. The relatively low current intensity should be ascribed to the coverage of MnO_2 which decreases the contact area between the glass/ITO substrate and the electrolytic solution.

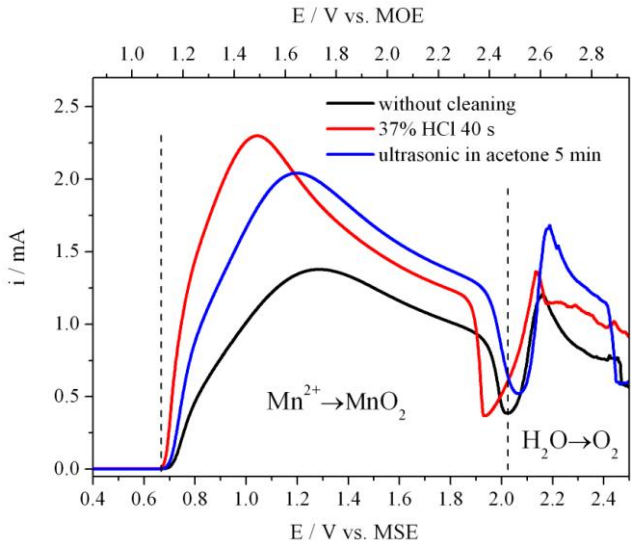

Figure III.21: Linear sweep voltammetry curves obtained on either pristine or pretreated glass/ITO electrodes in an aqueous and acidic electrolytic solution in the presence of $MnSO_4$. Electrolytic solution: H_2SO_4 (pH=1.8), $MnSO_4$ (0.1 M). Scan rate: 10 mV/s.

Based on the electrodeposition tests carried out on Pt substrates, electrolytic solutions containing a low $MnSO_4$ concentration appeared to favor the formation of mechanically and chemically stable MnO_2 films. Thus MnO_2 electrodeposition was performed on glass/ITO substrates in such electrolytic solutions, as shown in Figure III.22. The LSV curves show the same trend as that observed in acidic electrolytic solution, i.e. acid corrosion cleaned ITO substrate has a better electrocatalytic activity than the ultrasonically cleaned and un-cleaned glass/ITO electrodes. Then, the resulting glass/ITO substrates coated with a MnO_2 layer were tested in the alkaline electrolytic solution for the evaluation of their electrocatalytic activity towards OER. As expected, the MnO_2 film electrodeposited on HCl cleaned ITO electrode showed the best electrocatalytic activity towards OER, whereas the ultrasonically cleaned sample has only slightly better activity towards OER than un-cleaned ITO sample, indicating the small promotion effect of this latter cleaning procedure. Comparing with bare ITO electrode, all ITO electrodes covered with a MnO_2 layer show a better activity towards OER, which is ascribed to the electrocatalytic activity of the MnO_2 film, but this improvement is not ideal and the strategy of film preparation needs to be further developed.

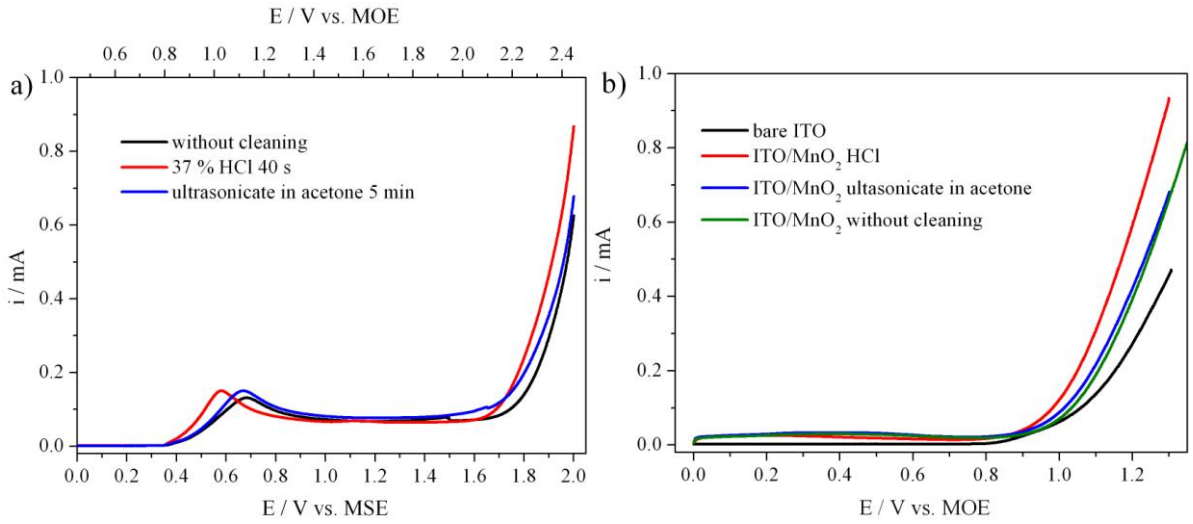

Figure III.22: Linear sweep voltammetry curves of a) MnO_2 films electrodeposition and b) corresponding OER tests in NaOH (0.1 M) on HCl and acetone cleaned ITO substrates. Electrodeposition electrolytic solution: $MnSO_4$ (2 mM) and $NaClO_4$ (50 mM). Electrolytic solution for OER tests : NaOH (0.1 M). Scan rate : 10 mV/s.

It has been reported that exposure of ITO substrates to a concentrated HCl aqueous solution could remove surface absorbates and contaminants, promote the absorption of reactants, and thus promote their electrochemical performances[115]. In our case, the promotion effect is clearly confirmed as HCl cleaning of glass/ITO electrodes favors the MnO_2 electrodeposition and the consequent electrocatalytic activity towards OER comparing with acetone ultrasonic cleaning.

From now on in this work, glass/ITO electrodes were all cleaned by using the acid corrosion method as described in section III.4.1. The MnO_2 films were electrodeposited using chronoamperometry at different potentials and the electrolytic solution contained a low $MnSO_4$ concentration. Figure III.23a shows the linear sweep voltammetry curve obtained in such electrodeposition solution. Oxidation of Mn^{2+} cations starts at 0.40 V vs. MSE and an anodic current peak appears at 0.65 V vs. MSE. The huge current increase appearing from 1.6 V vs. MSE reveals water oxidation. Figure III.23b shows several chronoamperometry curves corresponding to the potentiostatic electrodeposition of MnO_2 using different electrodeposition potential values. Coulombic charge density values were calculated according to integrated coulombic charges and to the geometric surface area of the ITO electrodes. It is obvious that the charge density increases continuously as the deposition potential increases from 0.5 V to 0.7 V vs. MSE, meaning that a higher amount of MnO_2 is electrodeposited per surface unit. Such trend is not observed anymore for higher

electrodeposition potential values. Interestingly, one can also observe on Figure III.23b that the current remains constant during 30 minutes. This indicates that neither the thickening nor the conductivity of the electrodeposited MnO_2 films are able to alter its electrodeposition rate.

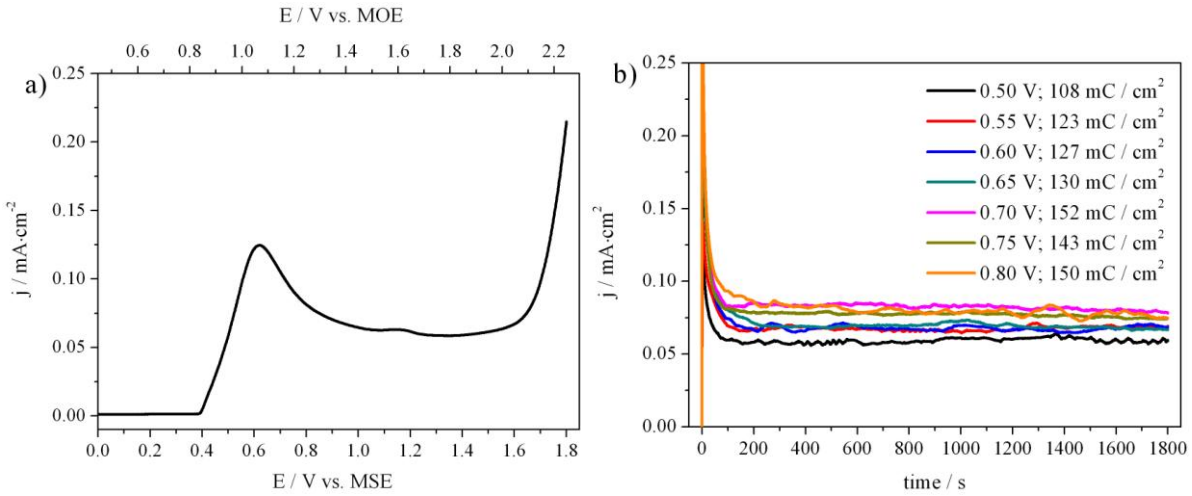

Figure III.23: a) Linear sweep voltammetry curve obtained on an acid corrosion cleaned ITO electrode and b) chronoamperometry curves allowing MnO_2 electrodeposition. Electrolytic solution: $MnSO_4$ (2 mM), $NaClO_4$ (50 mM). Scan rate 10 mV/s.

Figure III.24 shows the XRD spectra of the MnO_2 films that were electrodeposited using the chronoamperometry technique. Apart from In_2O_3 peaks, two other peaks appearing at 12° and 26° are the characteristic peaks of birnessite-type manganese oxide (JCPDS card no. 80-1098)[119]. Only samples electrodeposited at 0.6 and 0.7 V vs. MSE possess the birnessite type crystallinity and the signal intensity of the sample electrodeposited at 0.6 V vs. MSE is much more intense than the one corresponding to the sample electrodeposited at 0.7 V vs. MSE, indicating a better birnessite crystal structure for the first sample. Samples electrodeposited at 0.5 V and 0.8 V vs. MSE show no diffraction peak for Mn species, owing to their likely amorphous structure. This result is consistent with literature reports showing that birnessite crystalline can be obtained only in a narrow potential range.[120].

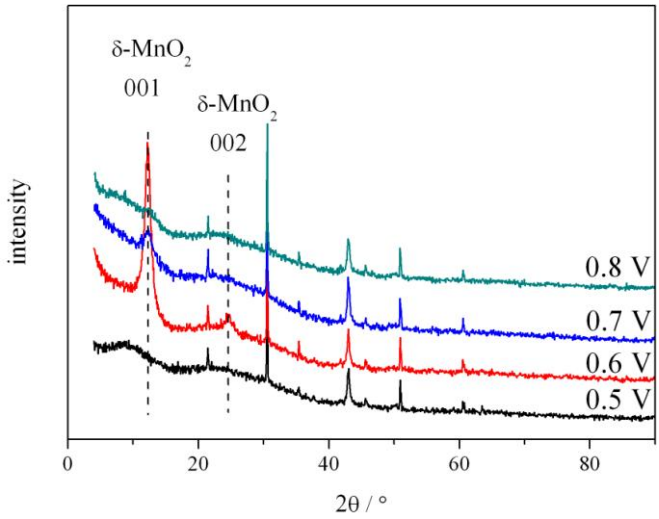

Figure III.24: XRD spectra of MnO_2 films electrodeposited on ITO using the chronoamperometry technique at different potentials for 30 minutes (see Figure III.21).

The morphology of the samples was studied using SEM-FEG and is shown in figure III.25. Obviously, the surface morphology changes dramatically as the electrodeposition potential increases. At 0.5 V vs. MSE, the film is highly porous and it adopts a honeycomb-like morphology. When the potential increases to 0.6 V vs. MSE, the hollow parts in the film are filled and the whole film becomes much denser. The structure of the sample electrodeposited at 0.7 V vs. MSE becomes porous again as a consequence of the aggregation and formation of large particles. In the case of the sample electrodeposited at 0.8 V vs. MSE, the aggregation phenomenon is more obvious and the surface is constructed by little particles resembling sand roses to a certain extent. The MnO_2 sample electrodeposited at 0.6 V vs. MSE is therefore by far the more compact while the others seem to have a lower density and therefore a likely larger specific area. The huge modification of the surface morphology as a function of the electrodeposition potential indicates possibly different nucleation and growth mechanisms. Considering the XRD results, the compact structure favors the formation of birnessite-type crystalline MnO_2 films. The hollow structure of the sample electrodeposited at 0.5 V vs. MSE is not suitable for birnessite formation, while a 0.7 V vs. MSE electrodeposition potential allows the start of a transition towards a particle structure, even though only a 0.6 V vs. MSE value seems to allow the proper nucleation and growth mechanism leading to birnessite formation.

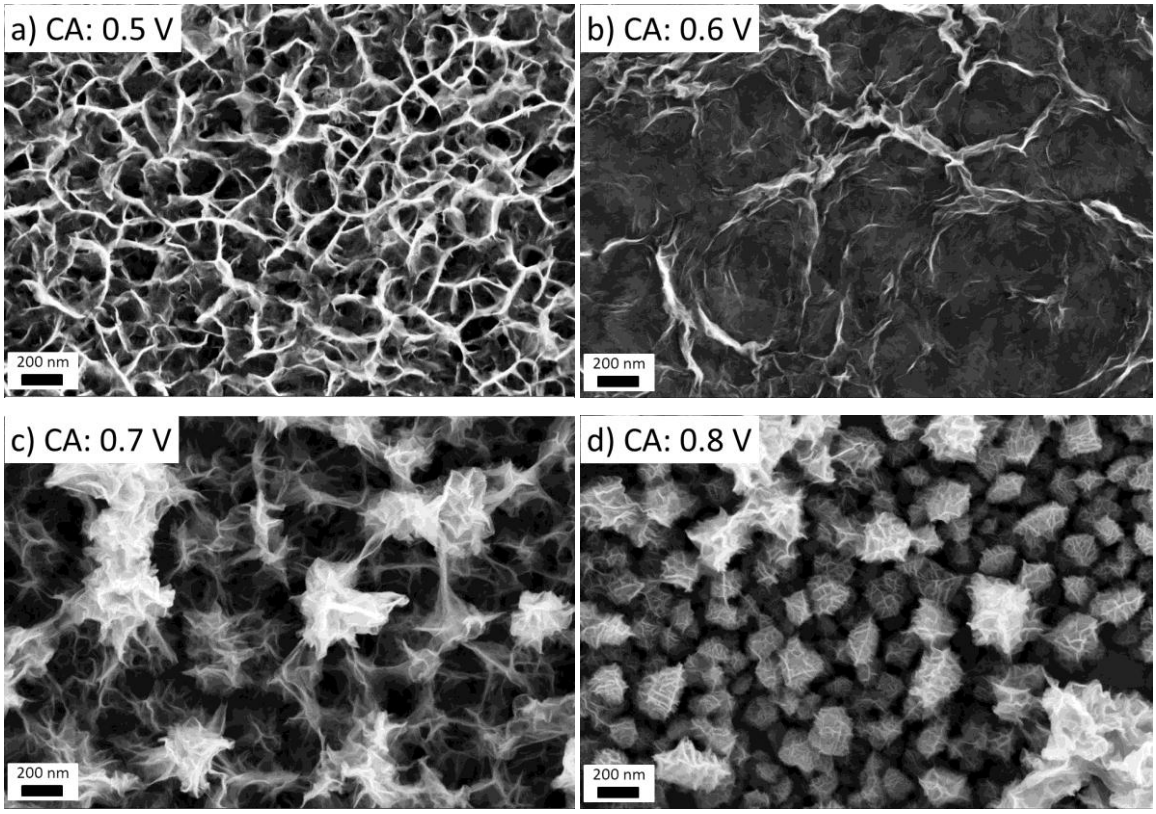

Figure III.25: SEM images of MnO_2 films electrodeposited on ITO using chronoamperometry at different potentials vs. MSE for 30 minutes. Electrolyte: $MnSO_4$ (2 mM); $NaClO_4$ (50 mM).

The optical properties of these MnO_2 films were studied by UV-vis spectrophotometry, as shown in Figure III.26 that contains also the Tauc plots derived from the UV-vis spectra. From the observation of these spectra, bare ITO electrode shows a very small light absorption (see black line in Figure III.26) in the whole tested wavelength range, indicating its good transparency to visible light. For ITO/MnO_2 samples, the light absorbance increases with the electrodeposition potential over the whole wavelength range. This is qualitatively consistent with the evolution of the coulombic charge density values extracted from Figure III.23 as a function of the electrodeposition potential. The absorbance of the MnO_2 sample electrodeposited at 0.6 V vs. MSE is slightly higher than that of the film electrodeposited at 0.5 V vs. MSE, but much lower than that of the film electrogenerated at 0.7 V vs. MSE, indicating possibly an influence of the crystallinity on the optical properties. The optical bandgap values obtained by Tauc plot show a variation with the electrodeposition potential that is the same as that of the absorption: a sample electrodeposited using a higher potential possesses a smaller bandgap value. In this case, such sample should possess a better optical activity expected to be beneficial for the solar water splitting.

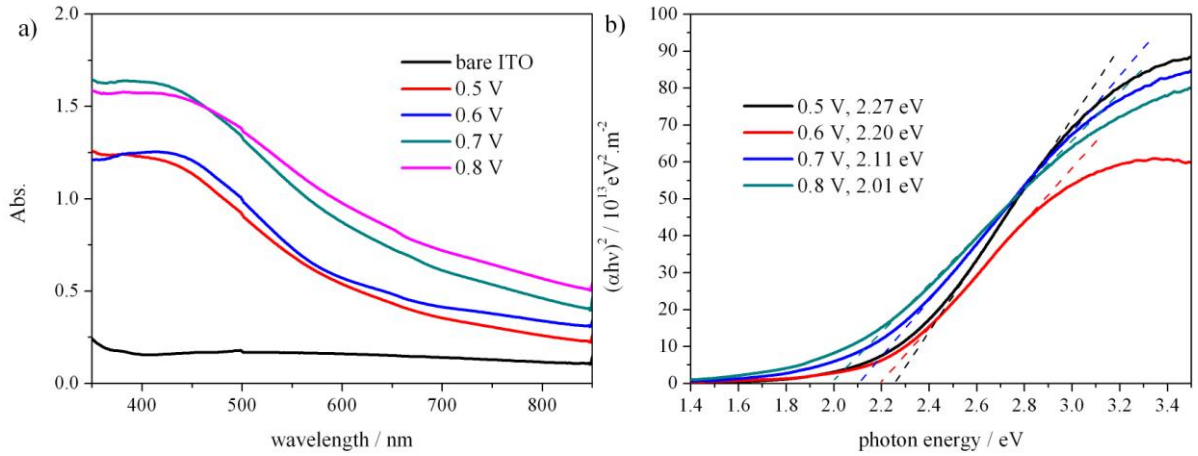

Figure III.26: a) UV-vis spectra and b) Tauc plots of MnO_2 films electrodeposited on ITO using chronoamperometry at different potentials for 30 min.

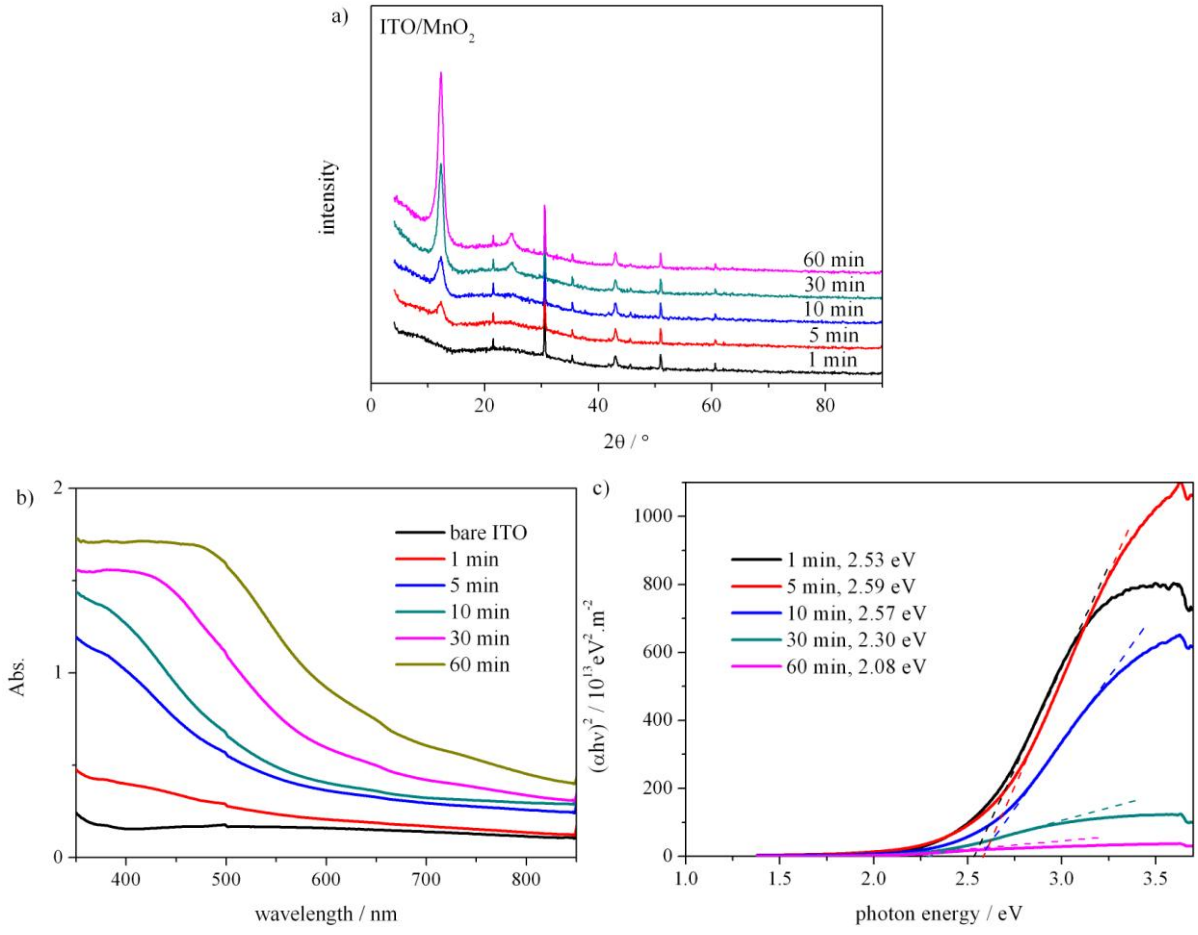

Figure III.27: a) XRD and b) UV-vis spectra and c) Tauc plots of MnO_2 films electrodeposited on ITO using chronoamperometry at 0.6 V vs. MSE with different electrodeposition durations. Electrolyte: $MnSO_4$ (2 mM), $NaClO_4$ (50 mM).

The influence of film thickness on the optical properties was investigated by electrodepositing MnO_2 films using the same potential and different electrodeposition

durations. A 0.6 V vs. MSE value was used for the electrodeposition potential in order to get the birnessite-type crystalline variety. The XRD and UV-vis spectra are shown in Figure III.27. Obviously, with the increase of the electrodeposition duration, the film gets thicker, and the birnessite diffraction peaks become more intense, indicating a better crystallinity. Similarly, the absorbance also increases with the film thickness, whereas the optical bandgap value shows a continuous decrease. Considering that the light absorption of ITO/MnO_2 samples is due to the MnO_2 film only, thus a thicker film leads to a higher absorbance. Moreover, thicker film has a better crystallinity and more pores, thus it may contain more inserted ions and lattice defects, which could modify the electronic structure of the film, thus leading to a smaller bandgap.

III.4.3 I-V curves of electrodeposited ITO/MnO_2 films

The MnO_2 films electrodeposited on ITO were characterized by CS-AFM in order to investigate their surface conductivity. A series of current/bias (I-V) curves were obtained in air for each sample and the location of the contact zone between the AFM tip and the MnO_2 film was chosen randomly for each curve in order to evaluate the homogeneity of the surface conductivity. The scanning direction of the bias range was also chosen randomly although the purpose was to obtain the same number of curves for both scanning directions, i.e. for the upward (from -10 V to +10 V) and downward (from +10 V to -10 V) directions. As shown in Figure III.28b, I/V curves related to the sample electrodeposited at 0.6 V vs. MSE, which belongs to the birnessite-type crystalline variety, and to a less extent those shown on Figure III.28c (0.7 V vs. MSE), are rather noisy and have a lower repeatability than those shown on Figures III.28a and d. Indeed, I-V curves obtained for samples electrodeposited at 0.5 V and 0.8 V vs. MSE (see Figures III.28a and d) are smooth and symmetrical. This observation may indicate some perturbations in the measurement process resulting from parasitic electrochemical phenomena known to occur in the presence of ambient humidity (humidity rate ≈ 50-55 %).

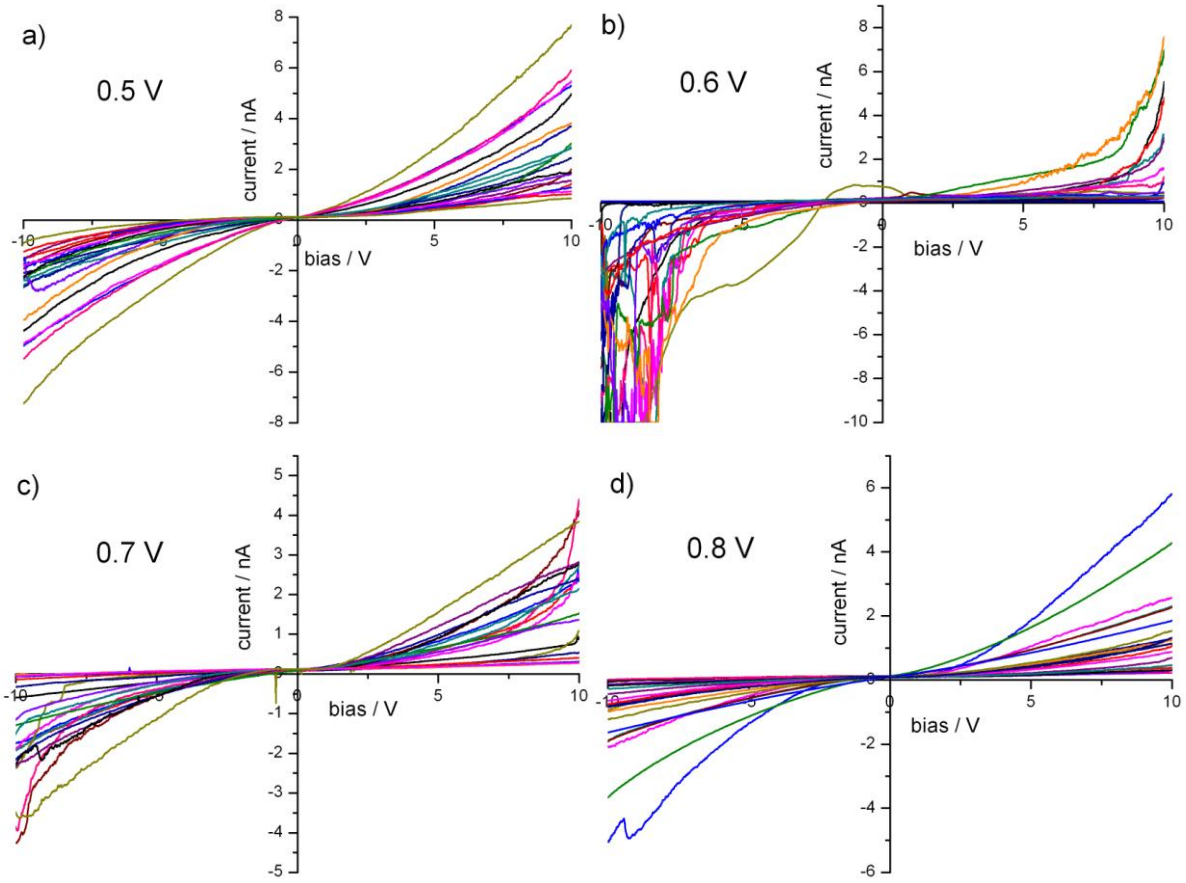

Figure III.28: I-V curves measured using CS-AFM in air of MnO_2 films electrodeposited on ITO using chronoamperometry at different potentials vs. MSE for 30 min. Electrolyte: $MnSO_4$ (2 mM), $NaClO_4$ (50 mM).

In order to confirm the origin of those perturbations observed mainly in Figure III.28b, supplementary I-V curves were performed under an Ar atmosphere, i.e. in the presence of humidity traces (humidity rate ≈ 3-5 %) on the MnO_2 sample electrodeposited at 0.6 V vs. MSE (see Figure III.29). By comparison with Figure III.28b, the I-V curves shown on Figure III.29 do show one of the expected variations of the current as a function of the bias. In general, when such I-V curves reflect only the surface conductivity of the investigated sample, the current obeys a linear, power or exponential law as a function of the bias, according to the theoretical models allowing their fitting. Moreover, the surface conductivity of the nanometric zone tested on the sample can be deduced from the contact resistance. This latter is extracted from the inverse of the slope measured at a 0 V bias on the I-V curve. Unfortunately, the expression of the contact resistance as a function of the resistivity (or conductivity) is still discussed in literature partly as a consequence of the hardly predictable geometry and calculation of the contact area between the conductive AFM tip and the sample. This is especially true in the case of samples possessing a very complex topography.

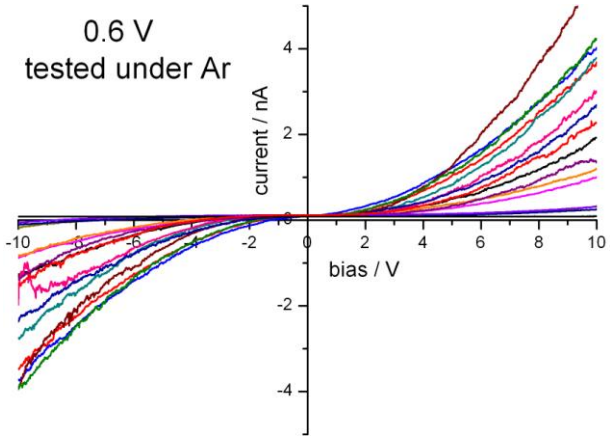

Figure III.29: I-V curves measured using CS-AFM in an Argon atmosphere of a MnO_2 film electrodeposited on ITO using chronoamperometry at 0.6 V vs. MSE for 10 min. Electrolytic solution: $MnSO_4$ (2 mM), $NaClO_4$ (50 mM).

Nevertheless, from a qualitative exploitation of all those I-V curves, it can be seen first that I-V curves shown on Figure III.29 are much less noisy and they cover, over the same bias range, a current range that is approximately the same as those covered on Figures III.28a, c and d. It appears moreover that the sample electrodeposited at 0.7 V vs. MSE has a relatively low conductivity, whereas the one electrodeposited at 0.5 V vs. MSE seems to be the most conducting sample. In the basis of this study and its preliminary interpretation, it seems that the conductivity of the birnessite structure is not as good as the one of the three other samples even though the different MnO_2 films tested in this section possess similar surface conductivities that all appear to be heterogeneous for each sample, as shown by the different contact resistance values observed for each sample.

Neval Yilmaz *et al.* studied the conductivity of a single layer of MnO_2 nanosheet absorbed on a highly oriented pyrolytic graphite (HOPG) electrode by CS-AFM and they obtained a symmetric I-V curve, which is similar to those obtained in our work [121]. They proposed that the conduction mechanism of MnO_2 film is electron hopping rather than tunneling due to the existence of a large number of defects in the structure. The thickness of the MnO_2 film used by Neval Yilmaz *et al.* was only 0.8 nm, while in our case, the film is more than 100 nm thick, but the I-V curves show some similarities, indicating a same conduction mechanism. In the MnO_2 structure, most of the Mn atoms are tetravalent, but there is also a portion of trivalent Mn atoms that justifies the presence of intercalated cations so as to reach electroneutrality in the MnO_2 films. This favors the formation of permitted

states and interface traps between the valence band and the conduction band, thus facilitate the generation of electron–hole pairs, which could increase the conductivity[121].

By far, it is clear from the results exposed in this section that the electrodeposition potential plays an important role in the surface conductivity of MnO_2 films, and the crystallinity and surface morphology are also influenced by the electrodeposition potential. The resulting (photo-) electrocatalytic performances of our MnO_2 films are therefore hardly predictable at this stage and they subsequently need to be investigated in details.

III.4.4 Characterization of electrocatalytic activity of ITO/MnO_2 films towards OER

The electrocatalytic activity of the ITO/MnO_2 films towards OER was investigated in a 0.1 M NaOH aqueous solution, using linear sweep voltammetry, as shown in Figure III.30. MnO_2 samples electrodeposited at 0.5 V and 0.6 V vs. MSE show a better electrocatalytic activity than bare ITO electrode towards OER, and the former is more active than the later one. On the other hand, the electrocatalytic activity of the MnO_2 film electrodeposited at 0.7 V vs. MSE is less active than the bare ITO electrode. It is also noteworthy that all samples experienced a quick degradation during the OER test, i.e. the electrocatalytic activity of all samples towards OER decreased dramatically during the second linear sweep and no advantages were observed anymore comparing with the bare ITO electrode.

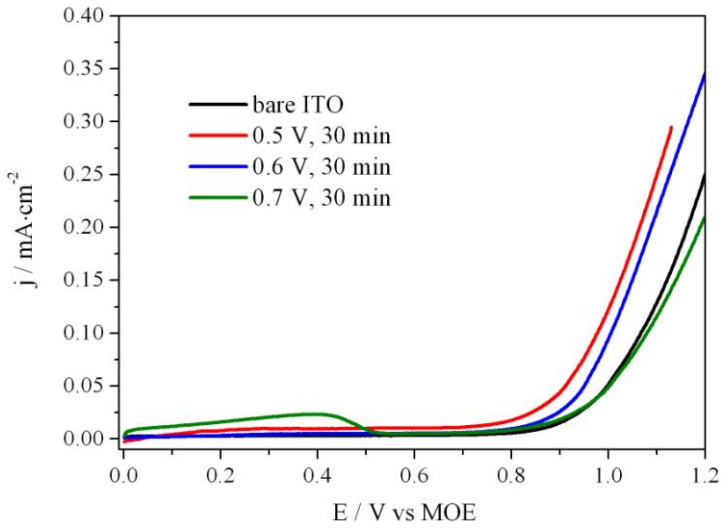

Figure III.30: Linear sweep voltammograms obtained in a 0.1 M NaOH aqueous solution on MnO_2 films electrodeposited on an ITO electrode at different potentials for 30 min. Scan rate 10 mV/s.

Electrochemical Impedance Spectroscopy (EIS) was used to study the kinetics of OER on bare ITO and ITO/MnO_2 samples. Figure III.31 shows the EIS spectra obtained on bare ITO for different potential values that were all situated in the potential range allowing OER. Clearly, all spectra show a semi-loop whose diameter decreases with increasing the test potential. If OER is in the pure kinetic regime all over the potential range used here, the diameter is then the reflection of the charge transfer resistance, thus the value of this resistance is lower at higher potentials, confirming that at higher potentials, charge transfer is easier. Moreover, the difference between 1.05 V and 1.1 V vs. MOE is quite small, which means that at this potential, the charge transfer resistance may reach an extreme value. In this case, choosing the test potential becomes an important factor that will influence the OER performances.

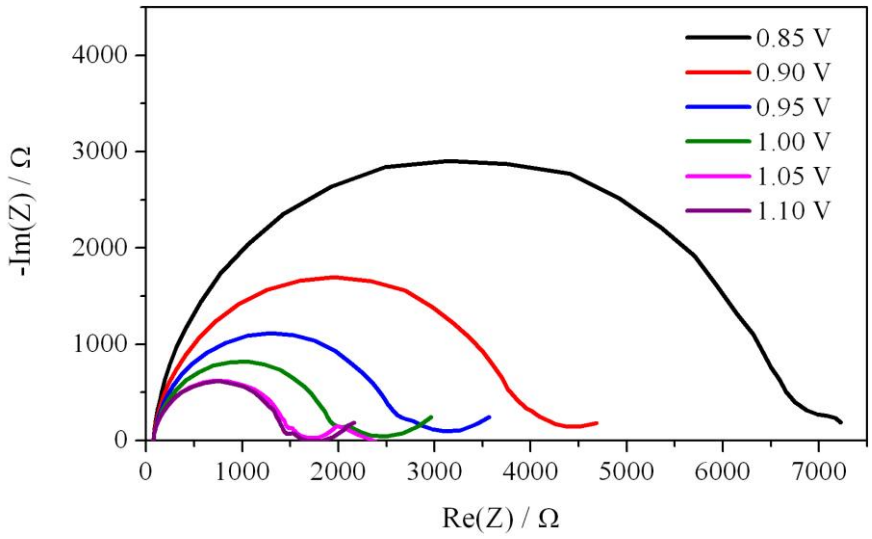

Figure III.31: EIS spectra of bare ITO in a 0.1 NaOH aqueous solution at different potentials. Frequency range: 100 kHz – 100 mHz. Potentials used during EIS tests are vs. MOE and expressed in the figure.

Figure III.32 shows EIS spectra obtained on ITO/MnO_2 films at 1.0 V vs. MOE after a linear sweep voltammetry experiment allowing OER. Clearly, all spectra related to ITO/MnO_2 films have a bigger loop diameter than bare ITO electrode, whatever the electrodeposition potential was for the MnO_2 film. Moreover, the higher this potential was, the larger the loop diameter was, and therefore the higher the charge transfer resistance was. From this result, it is suggested that the presence of a MnO_2 film hinders OER by comparison with a bare ITO electrode. Considering the poor stability of these samples during OER tests, as MnO_2 films nearly lose the mechanical contact with substrate during LSV experiments

allowing OER, the bad adhesion of MnO_2 films on the ITO substrate should be responsible for the high resistance values observed on Figure III.32.

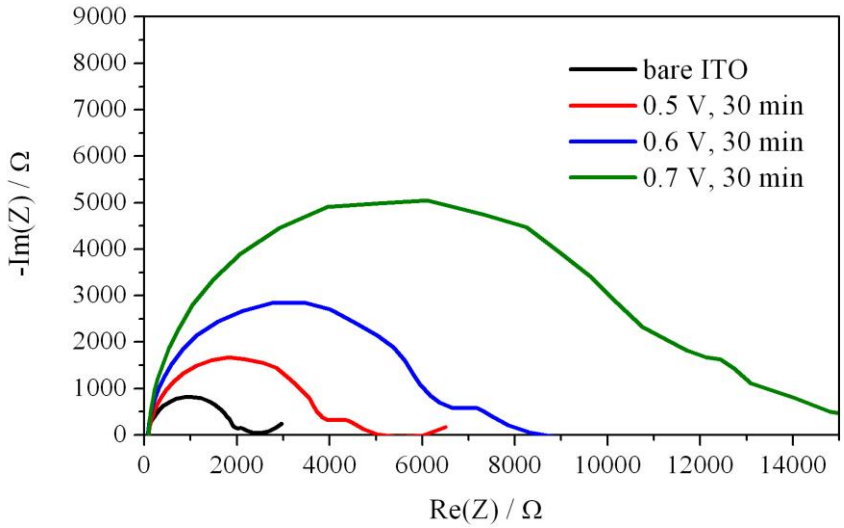

Figure III.32: EIS spectra of ITO/MnO_2 films obtained in a 0.1 NaOH aqueous solution at 1.0 V vs. MOE. Frequency range: 100 kHz – 100 mHz. Potentials used during MnO_2 electrodeposition are vs. MSE and expressed in the figure.

From the results obtained on ITO/MnO2 substrates, it is revealed that the adhesion of the electrodeposited MnO2 films on ITO is a key factor that affects their OER performances. However, it is very difficult to obtain mechanically stable films on ITO substrates even when using the optimized conditions. The continuous dissolution of indium during anodic polarization allowing OER tests might be the reason. As a consequence, ITO electrodes do not seem to be a good substrate for the electrodeposition of MnO2 thin films dedicated to OER (photo-) electrocatalysis.

III.5 MnO_2 electrodeposition on FTO

Fluorine doped Tin Oxide (FTO) is another transparent conducting material commonly used as electrode material for electrodeposition. Comparing with ITO, it has a much better thermal stability, which makes possible a high temperature heat treatment for the sample preparation [122]. Moreover, a FTO electrode is electrochemically more stable than ITO, and it is thus used also as an electrode material in the evaluation of water oxidation catalysts [123].

III.5.1 FTO electrode cleaning

The FTO cleaning procedure was carried out using an ultrasonic bath, as described for ITO cleaning. The acid corrosion is not suitable in the case of FTO electrodes because tin oxide is not stable in acid. Indeed, after 40 seconds of immersion in 37% HCl aqueous solution, FTO electrode loses its conductivity and becomes insulating, indicating that the conducting layer has been totally dissolved. Figure III.33 shows an SEM image as well as XRD spectra of a bare FTO electrode. From the SEM image, we can see clearly that uniformly dispersed FTO grains cover the electrode surface. The average grain size is about 60 nm. In the XRD spectra, peaks appearing at 26.6, 38.9 and 51.8 can be indexed to (110), (111), (211) planes of SnO_2 crystal respectively (JCPDS card No. 41-1445). No fluorine species is detected, indicating the high dispersion state of fluorine atoms, which is expected for FTO [124]. In addition, from the SEM image and XRD results, it appears that ultrasonic cleaning did not change the surface morphology and crystallinity of FTO layer, which is consistent with the results obtained on ITO.

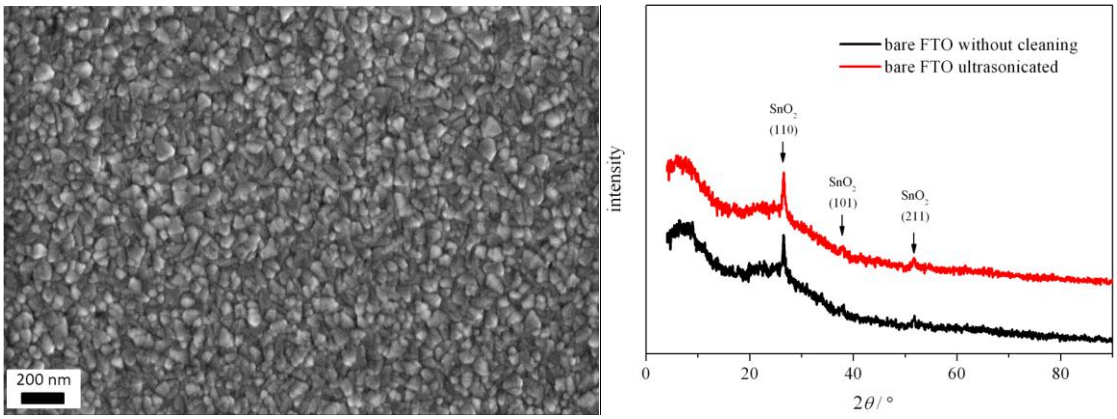

Figure III.33: a) SEM image and b) XRD spectra of a bare FTO electrode

III.5.2 Electrodeposition of MnO_2 films on FTO electrode

MnO_2 films were electrodeposited on ultrasonically cleaned glass/FTO electrodes using the same conditions as those described in the ITO part (see Figure III.22). Figure III.34 shows the linear sweep voltammogram of bare FTO in the electrodeposition solution. It has a similar shape to that obtained on ITO (see Figure III.22). An oxidation peak appears at 0.35 V vs. MSE (peak potential = 0.56 V vs. MSE), which is ascribed to the oxidation of Mn^{2+} to Mn^{4+}, and water oxidation starts at about 1.0 V vs. MSE.

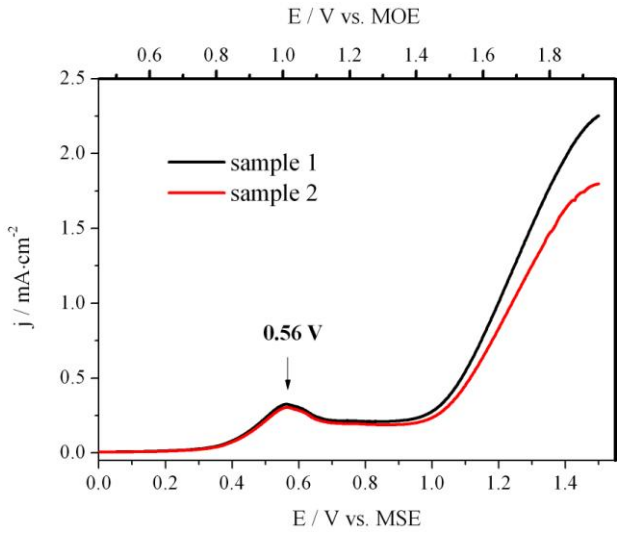

Figure III.34: Linear sweep voltammogram allowing the electrodeposition of a MnO_2 film on 2 different FTO electrodes ultrasonically cleaned in acetone. Electrodeposition electrolytic solution: $MnSO_4$ (2 mM) and $NaClO_4$ (50 mM). Scan rate: 10 mV/s.

A series of MnO_2 films were electrodeposited on glass/FTO electrodes using chronoamperometry and different electrodeposition potentials for 10 min. The electrodeposition curves are shown in Figure III.35. After a current transient corresponding to double-layer charging and nucleation process, they all show a constant current indicating the absence of any degradation or passivation phenomenon. From those curves, the current density and therefore the electrodeposition rate remain nearly unchanged for electrodeposition potentials varying between 0.5 V to 1.2 V vs. MSE (and producing samples S05 to S12). Electrodeposition carried out at 0.5 V vs. MSE and leading to sample S05 produced the lowest current density value, according to the LSV shown on Figure III.34. On the contrary, S14 and S16, electrodeposited at 1.4 V and 1.6 V vs. MSE respectively, produced a large increase of the current density, by comparison with those observed for lower electrodeposition potentials, which can be explained by the fact that at this potential, water oxidation has already started (see Figure III-34). Thus, the increase of the current density should be ascribed not only to the oxidation of Mn^{2+} cations, but also to the electrochemical oxidation of water. Although the current density is high, the amount of deposited MnO_2 is therefore not as high as that calculated from the coulombic charge. This phenomenon is more pronounced for 1.6 V vs. MSE, which led to the biggest current density. From the corresponding XRD spectra, only S6 has the characteristic diffraction peak of birnessite, the other samples have no peak related to Mn species but only those belonging to SnO_2. This trend is consistent with the previous results obtained on ITO (see Figure III.24).

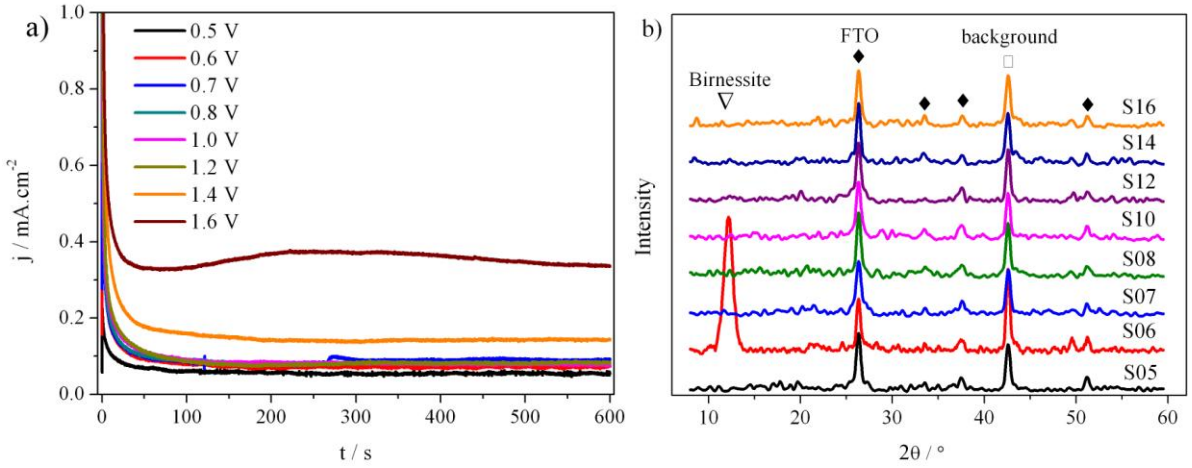

Figure III.35: a) Chronoamperometry curves for MnO_2 electrodeposition for 10 minutes on FTO electrode and b) corresponding XRD spectra. Electrolyte: $MnSO_4$ (2 mM); $NaClO_4$ (50 mM). Scan rate: 10 mV/s. Potentials used during MnO_2 electrodeposition are vs. MSE and expressed in Figure a).

From the topography shown in the SEM images in Figure III.36, it is clear that the morphology changes as the electrodeposition potential increases. This trend is similar to the one extracted from results obtained on ITO (see Figure III.25). S05 has a hollow net structure, whereas that for S06 is much denser. Throughout the electrodeposition process, MnO_2 tends to form particles from an electrodeposition potential close to 0.7 V vs. MSE, and for higher potential values, those particles grow bigger and their boundaries become unclear. In addition, the surfaces become inhomogeneous and rough for films electrodeposited at high potentials, as shown in Figure III.25g,h. In the case of S14, huge particles form on the sample surface and they are more numerous and bigger on S16. This trend is more obvious with the MnO_2 samples electrogenerated during longer electrodeposition times (30 min on Figure III.37b,d instead of 10 min on Figure III.37a,c). The huge electrogenerated particles were characterized by EDS analysis and they were found to have the same chemical composition than those bottom films, suggesting that those particles result only from the abnormal growth of similar MnO_2 grains.

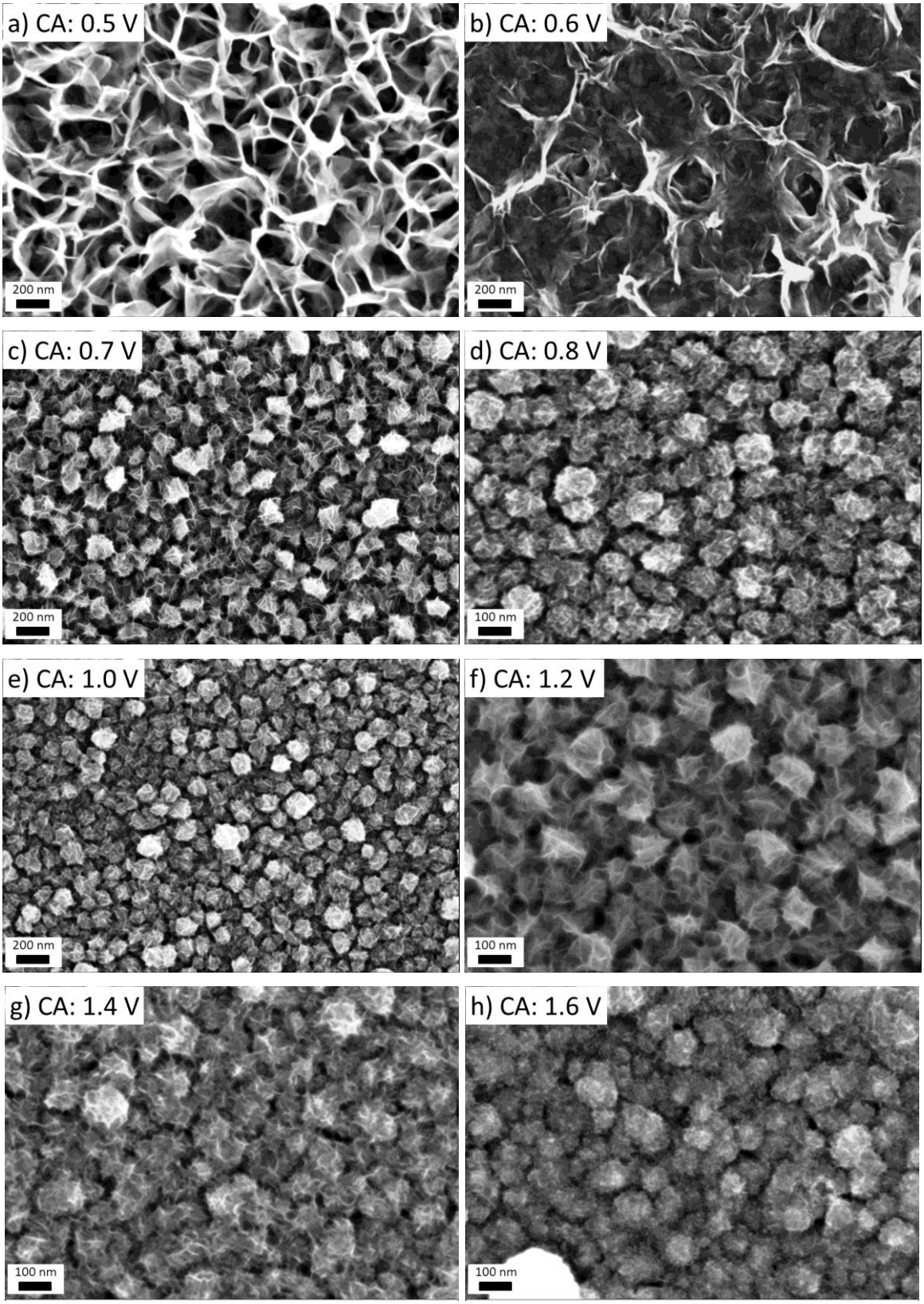

Figure III.36: SEM images of MnO_2 films electrodeposited on FTO using chronoamperometry and different potentials vs. MSE for 10 min. Electrolyte: $MnSO_4$ (2 mM); $NaClO_4$ (50 mM).

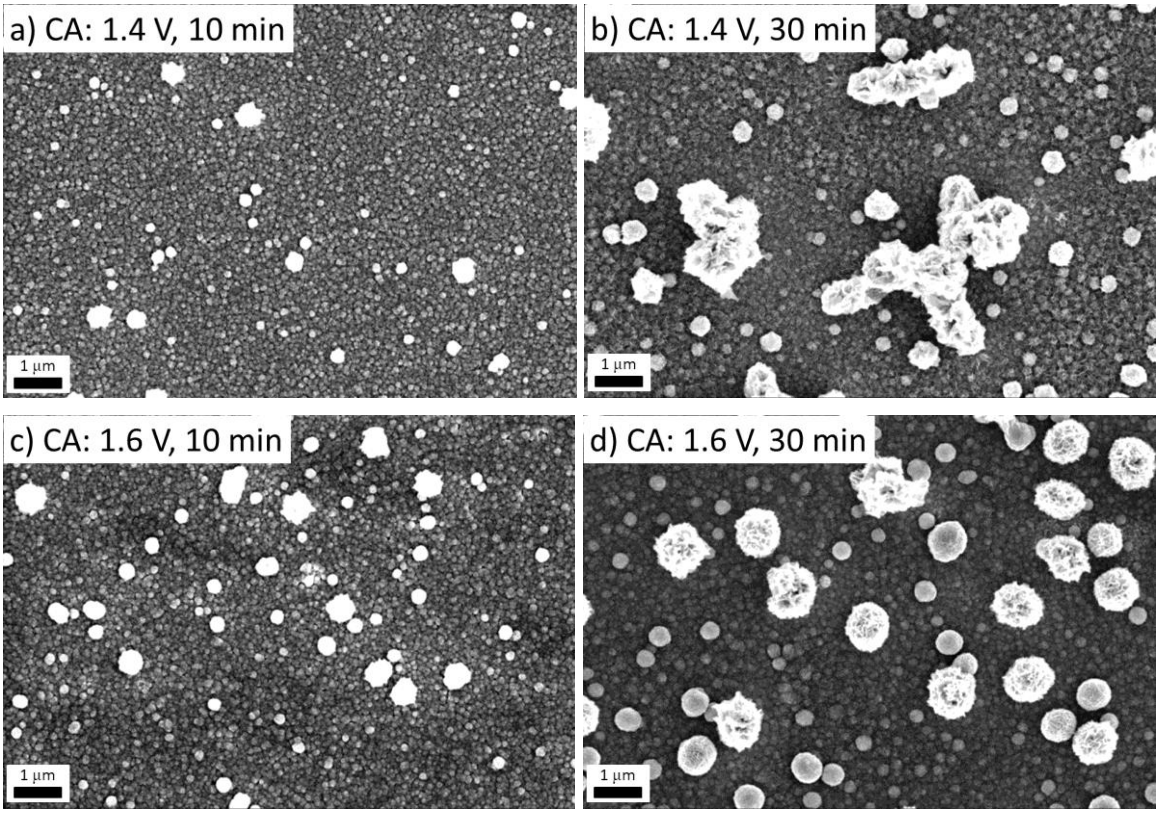

Figure III.37: SEM images of MnO_2 films electrodeposited on FTO using chronoamperometry at 1.4 V and 1.6 V vs. MSE for 10 min and 30 min. Electrolyte: $MnSO_4$ (2 mM); $NaClO_4$ (50 mM).

The electrocatalytic activity of the FTO/MnO_2 films towards OER was investigated in a 0.1 M NaOH aqueous solution using linear sweep voltammetry experiments, and chronoamperometry (CA) tests were performed to evaluate their stability. The results shown in Figure III.38 indicate that the lowest activity was obtained with S07. After one LSV experiment, this sample showed no activity in the following chronoamperometry test, meaning that it was damaged during the former step. In this case, the poor adhesion of the film to the electrode surface could be responsible for its unstable activity. Except this one, the other samples showed a significant electrocatalytic activity towards OER (see Figure III.38a) as well as a good stability, which is revealed by the fact that nearly no current density decrease was observed during the 10 min chronoamperometry tests (see Figure III.38b). However, S06, which belongs to the birnessite-type crystalline variety also showed a poor activity, as it showed a higher onset potential and a lower current density by comparison with the other samples (see Figure III.38a) and its current density value in the CA test is also lower than that of the other samples, which confirms the former result. The best activity was obtained with S08, S10 and S12 samples electrodeposited respectively at 0.8 V, 1.0 V and 1.2

V vs. MSE. They have a similar electrocatalytic activity towards OER in the LSV test and S10 has a slightly higher current density than the other two samples in CA test (see Figure III.38b). S05, whose electrodeposition charge density was lower than the other samples (see Figure III.35a), shows moderate performances. On the contrary, samples electrodeposited at high potentials, like those produced at 1.4 V and 1.6 V vs. MSE, show a degradation of their electrocatalytic activity towards OER on the CA test (see Figure III.38b).

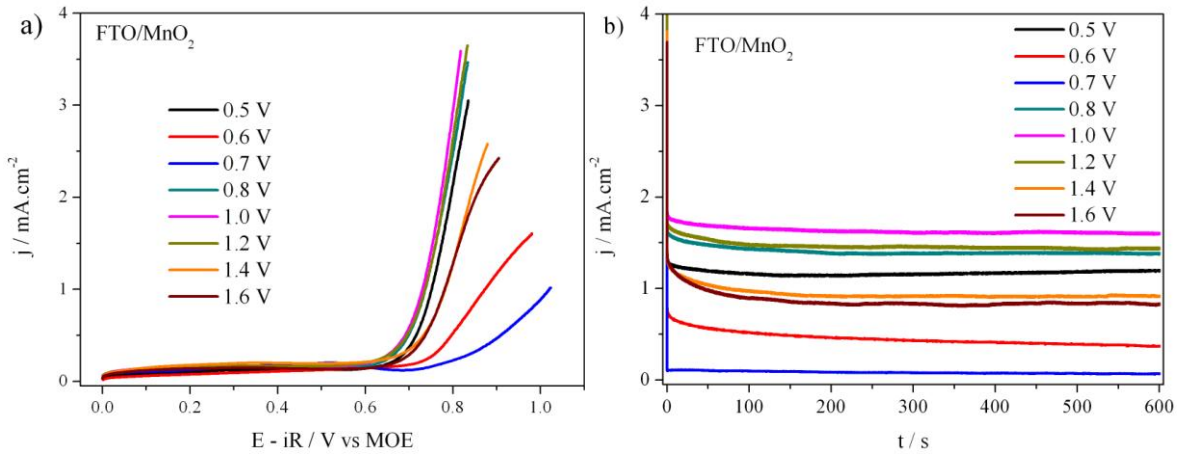

Figure III.38: a) linear sweep voltammetry and b) chronoamperometry curves of OER electrocatalytic activity tests on FTO/MnO_2 films. Electrolyte: NaOH (0.1 M). Scan rate for linear sweep: 10 mV/s. Potential used for chronoamperometry: 0.9 V vs. MOE. Potentials used during MnO_2 electrodeposition are vs. MSE and expressed in this figure.

Tafel plots derived from the linear sweep voltammetry curves presented on Figure III.38a are shown in Figure III.39. Generally, the smaller the slope of the Tafel plot is, the better the electrocatalytic activity is towards OER. In other words, the value of Tafel slope is regarded as a key parameter to evaluate the kinetic parameters of OER and therefore the activity of an OER catalyst. However, this habit is not self-sufficient here, as shown hereafter. The lowest slope value was obtained for S05, while the slope values of S08, S10 and S12, that show the best activity in LSV and CA tests, were also small than those for S06, S14 and S16. This unexpected observation on S05 is not clear, but it is true that the use of the Tafel slope is never sufficient for the evaluation of an OER catalyst.

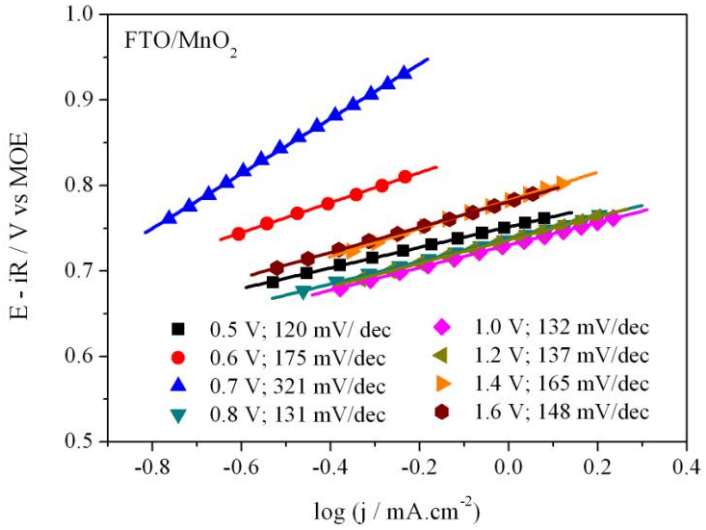

Figure III.39: Tafel plots derived from LSV curves shown on Figure III.38a. Potentials used during MnO_2 electrodeposition are expressed in V vs. MSE in this figure.

EIS spectra obtained at 1.0 V vs. MOE in a NaOH aqueous solution (0.1 M) for each of the investigated samples are shown in Figure III.40. Theoretically, the big semi-loop is partly due to the charge transfer resistance related to OER. Predictably, the larger the diameter of this semi-loop is, the bigger the value of the charge transfer resistance is. In order to check this hypothesis and to further understand the EIS spectra, a fitting procedure was performed using those equivalent circuits proposed in chapter II (see section II.5.3).

According to impedance spectra obtained on our samples, no Warburg diffusion characteristic is observed, and all of the spectra contain a small loop at the beginning of the curve in high frequency region followed by a big loop. In addition, both the small loop and the big loop are flattened other than a regular semicircle, thus the CPE should be used instead of pure capacitor element. After exhaustive trying of the fitting models in literature, model 3 was revealed to possess the best agreement with our spectra with the lowest error signals. Therefore, this model is applied with the impedance spectra fitting, as shown by Figure II.9.

The parameters used for fitting are listed in Table III.4. R_Ω, the electrolyte was found to vary within a narrow range of values, as expected knowing that all EIS experiments were performed in similar electrolytic solutions. R_{film} also varies in a narrow potential range, showing that all the tested MnO_2 films, except S06 (and probably S07 as a consequence of the huge diameter of the main semi-loop of its EIS spectrum), possess similar conductivities. S06 sample have a relatively high film resistance (R_{film}). This result agrees well with the

conductivity studies obtained on ITO/MnO_2 samples and carried out by I-V curves using CS-AFM, i.e. birnessite type MnO_2 films electrodeposited at 0.6 V/SSE was found to have a lower conductivity. R_p values, that are related to the kinetics of the interfacial charge transfer reaction, were found to vary within a narrow value range centered on 92 Ω, except for S06 (and probably S07) whose R_p value is about 7.5 times higher. This seems to indicate that the kinetics of the interfacial charge transfer reaction is much slower on S06 (and S07) than on any other MnO_2 sample tested in this series of samples electrodeposited on FTO using different electrodeposition potential. As far as R_s is concerned, two sets of values were observed. MnO_2 films electrodeposited at low or high potentials, i.e. S05, S06, S14 and S16, all possess R_p values close to 700-800 Ω whereas those electrodeposited at intermediate potentials, i.e. S08, S10 and S12 are much lower and inside the 250-340 Ω range. On the other hand, the three capacitances were found to vary only a little and randomly as a function of the evolution of the electrodeposition potential. They can therefore hardly be used to draw conclusions.

It appears from those observations that there is a very good correlation between the electrocatalytic activity of the tested MnO_2 films towards OER and the R_s value extracted from the corresponding EIS spectra. Indeed, samples that have good OER performances (S08, S10 and S12), i.e. high current density values in LSV and CA tests (see Figures III.38a and c respectively) as well as low Tafel slopes (see Figure III.39) and low R_p values (see Table III.4), also have quite small R_s values. Let us remind that R_s represents the charge relaxation associated with surface intermediate(s) and is related to the charge transfer mechanism, although it is not the charge transfer resistance, according to the complex nature of the water oxidation mechanism. Among those three samples, S10 has the smallest R_s value, which is consistent with the fact that it shows the best electrocatalytic activity towards OER (see Figures III.38a and c respectively).

The EIS spectra are in very good agreement with electrocatalytic activity test towards OER, although they provide much more information on the electrical and electrochemical properties of the electrocatalytic films.

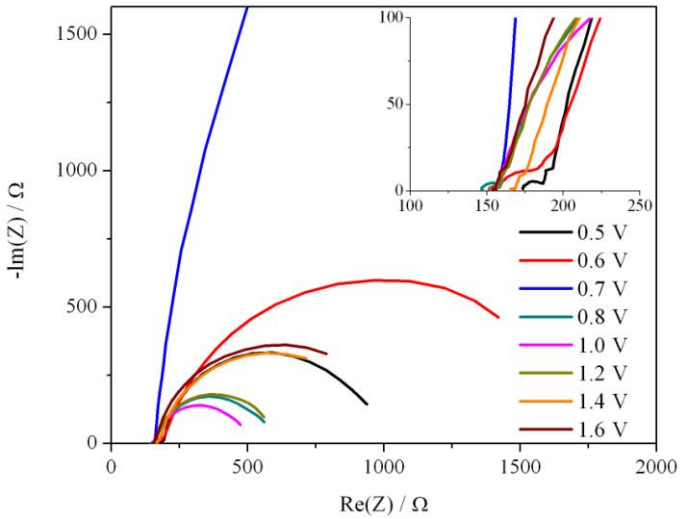

Figure III.40: EIS spectra of FTO/MnO_2 films in a 0.1 M NaOH aqueous solution. Test potential: 1.0 V vs. MOE. Frequency range: 100 kHz – 100 mHz. Potentials used during MnO_2 electrodeposition are vs. MSE and expressed in this figure.

Table III.4: Fitting parameters for FTO/MnO_2 EIS spectra

element	FTO/MnO_2 samples							
	0.5 V	0.6 V	0.7 V*	0.8 V	1.0 V	1.2 V	1.4 V	1.6 V
R_Ω / Ω	153	156.1	-	146.2	150.5	151.5	165	153
R_p / Ω	96.7	679.52	-	83.49	82.95	102	93.3	91.23
R_s / Ω	764.3	813	-	333.26	252.98	331.9	702.8	771
CPE_{dl}	8.11E-04	4.05E-04	-	6.2E-04	8.47E-04	7.43E-04	9.93E-04	8.04E-04
CPE_{film}	7.77E-05	1.17E-04	-	6.39E-05	1.03E-04	4.37E-05	4.89E-04	1.48E-05
Cs / F	2.67E-04	1.10E-04	-	1.64E-04	2.63E-04	2.26E-04	3.57E-04	2.74E-04
R_{film} / Ω	2.8	34	-	12.63	6	7.4	4.5	2.5

* fitting failed on this EIS spectrum

From the electroactivity tests towards OER reported above, MnO_2 films electrodeposited at a moderate potential, i.e. between 0.8 to 1.2 V vs. MSE, seem to possess a better electrocatalytic activity towards OER. Simultaneously, that of the birnessite structure is not confirmed here in our experimental conditions.

III.5.3 Nucleation and growth mechanism of MnO_2 at different potentials

From the former results, it has been demonstrated that the electrodeposition potential has a great influence on the morphology and crystallinity of MnO_2 films. However, the detailed nucleation and growth mechanism of MnO_2 films is rarely reported in literature. Therefore, we performed electrodeposition of MnO_2 films on FTO at 0.6 V and 1.2 V vs.

MSE for different electrodeposition times, and the obtained MnO_2 samples were studied by SEM in order to develop a better understanding of the nucleation and growth mechanism.

Figure III.41 shows the cross-section image of MnO_2 films electrodeposited on FTO for 10 min and 30 min respectively. Clearly, samples electrodeposited at 0.6 V vs. MSE have a layered structure and their thickness increases with time. On the other hand, samples electrodeposited at 1.2 V vs. MSE show a different morphology: the FTO surface is covered by MnO_2 particles and some of them grow very big with increasing time, as already shown in Figure III.41d. These huge particles appearing on the topography image are actually MnO_2 columns as revealed by EDS analysis. The differences pointed out here mean that the electrodeposition mechanisms of these samples must be different.

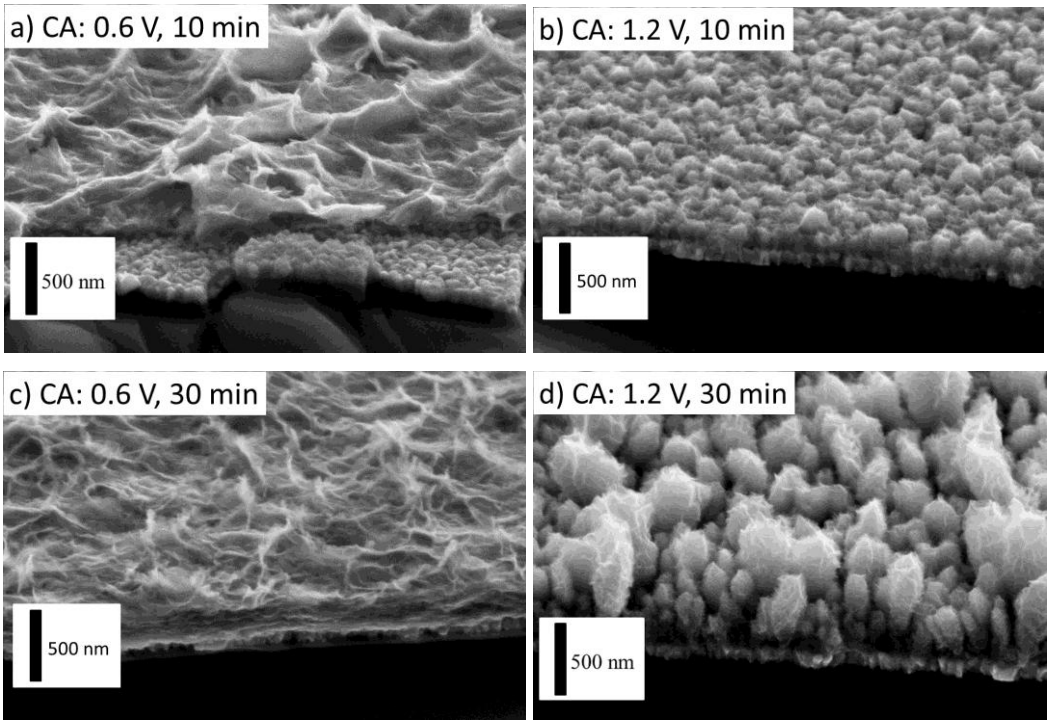

Figure III.41: Cross-section images of MnO_2 films electrodeposited using chronoamperometry at 0.6 V and 1.2 V vs. MSE for 10 min and 30 min. Electrolyte: $MnSO_4$ (2 mM); $NaClO_4$ (50 mM).

In a second step, samples electrodeposited using shorter times were prepared and studied by SEM to elucidate the nucleation and growth differences, the morphology images are shown in Figure III.42. When the electrodeposition at 0.6 V vs. MSE lasted for 30 s, the bottom FTO substrate can still be seen clearly, even though very thin layers of MnO_2 is also visible (see Figure III.42a). When the electrodeposition time extends to 2 min, the

electrodeposited film becomes thicker and the expected morphology of the birnessite type MnO_2 film starts appearing clearly on the FTO substrate (see Figure III.42c). However, when a 1.2 V vs. MSE potential was used for electrodeposition, a granular shaped MnO_2 film is electrogenerated, as shown in Figure III.42b and d, and these particles grow bigger with increasing time. Considering the FTO grain size shown in Figure III.33a, the electrodeposited MnO_2 particles reach quickly a similar size scale, suggesting that the FTO substrate acts as a template and the electrodeposited MnO_2 particles cover FTO grains at the beginning of electrodeposition process.

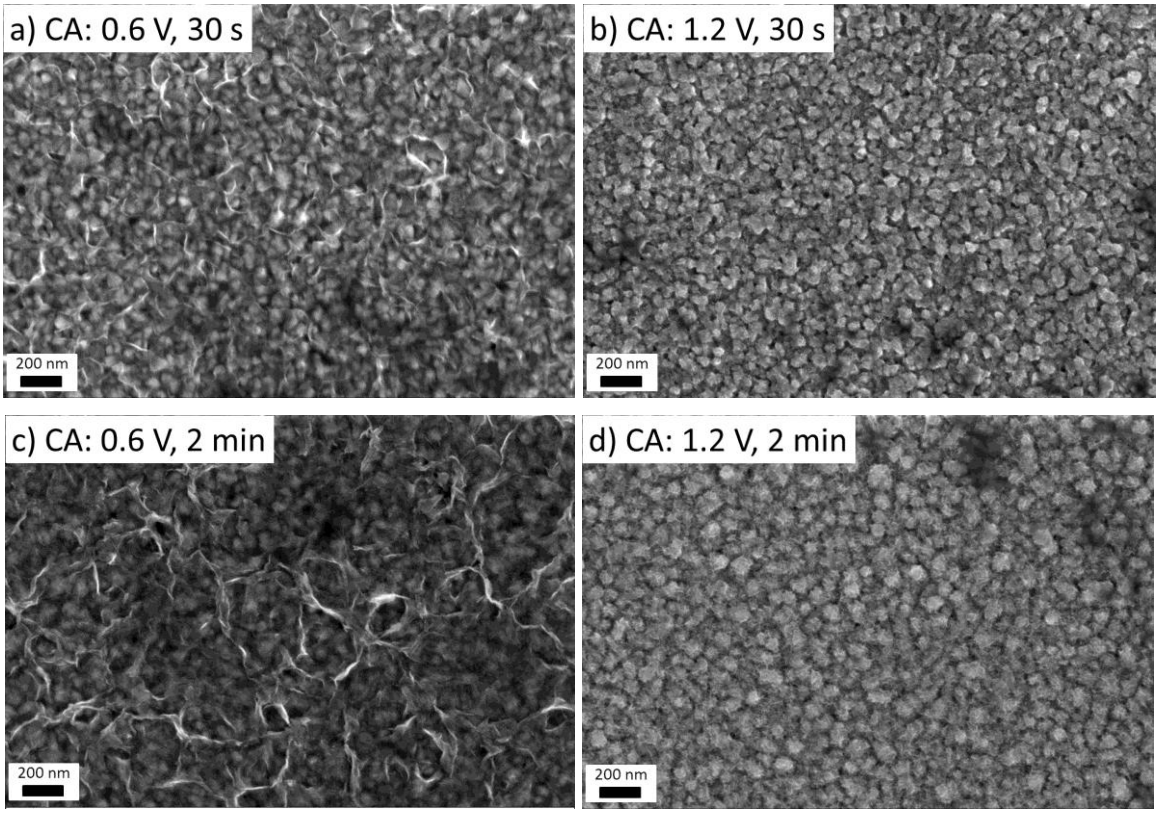

Figure III.42: SEM images of MnO_2 electrodeposited using chronoamperometry at 0.6 V and 1.2 V vs. MSE for 30 s and 2 min. Electrolyte: $MnSO_4$ (2 mM); $NaClO_4$ (50 mM).

Based on the observations described above, two different electrodeposition mechanisms occurring respectively at low and high potentials values are proposed as shown below. When electrodeposition is carried out at 0.6 V vs. MSE, a thin layer of MnO_2 forms on the surface of the substrate, and this layer grows thicker with time, and then replicates itself, one layer at the top of the previous one, leading then to a multilayer structure; while at 1.2 V vs. MSE, electrodeposited MnO_2 tends to cover the surface of FTO grains by forming core-shell structures in the initial step, then these particles grow individually and form MnO_2

columns. The huge columnar structure observed on the high potential electrodeposited sample, as shown in Figure III.41d, is supposed to form from the abnormal growth of some of the little MnO_2 particles.

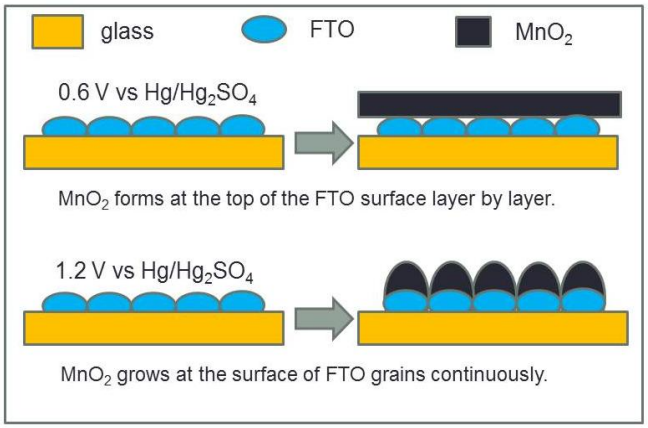

Figure III.43: Scheme showing SEM images of MnO_2 electrodeposited at 0.6 V and 1.2V.

Moreover, from this theory, films electrodeposited at high potential are in closer contact with the FTO grains of the substrate. This could enhance their mechanical stability and their electrical communication with the underlying substrate. As a consequence, the MnO_2 samples electrodeposited using a high potential value may possess in appearance a low charge transfer resistance and a better electrocatalytic activity towards OER.

III.6 Comparison of glass/ITO and glass/FTO electrodes

Although both ITO and FTO are two commonly used transparent substrates for optical analysis, the comparison of their electrocatalytic activity towards OER is scarcely reported in literature. Here we compared the electrocatalytic activity of bare electrodes and MnO_2 film covered electrodes towards OER with the purpose of revealing the influence of the substrate on the catalyst electrocatalytic activity.

The water oxidation tests at bare electrodes are shown in Figure III.44 (see LSV curves on Figure III.44a and Tafel plots on Figure III.44b). From this figure, it appears that FTO electrode shows a much higher electrocatalytic activity towards OER than ITO, the oxidation current density 0.9 V vs. MOE is only 0.011 mA on ITO in the first scan, while that on FTO reaches 0.226 mA, and is therefore more than 20 times higher. In addition, the

derived Tafel slope of ITO is 269 mV/dec, while that of FTO is only 138 mV/dec for the first scan, indicating a much better electrocatalytic activity on FTO than on ITO.

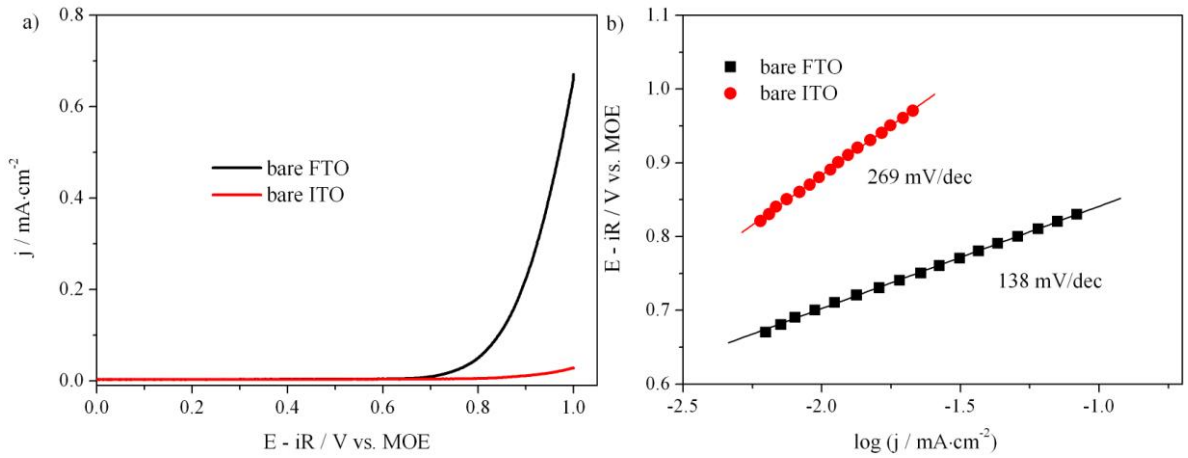

Figure III.44: a) LSV curves and b) Tafel plots related to OER test on bare FTO and ITO electrodes. Aqueous electrolytic solution: NaOH (0.1 M). Scan rate: 10 mV/s.

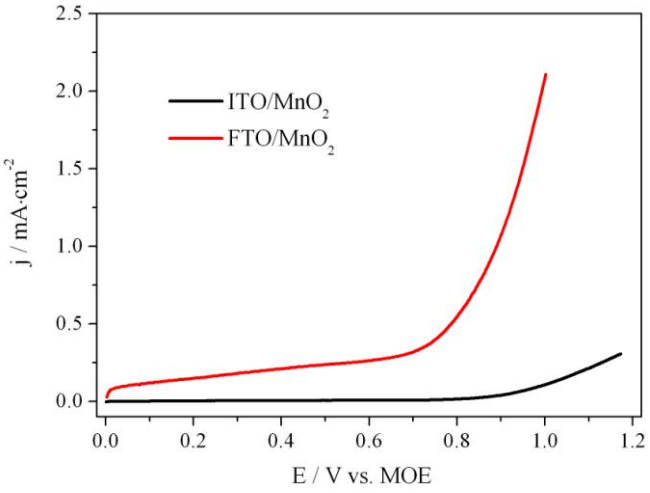

Figure III.45: LSV curves related to OER tests on ITO/MnO_2 and FTO/MnO_2 samples in a 0.1 M NaOH aqueous electrolytic solution. Scan rate: 10 mV/s. MnO_2 films were electrodeposited on ITO or FTO using the chronoamperometry technique at 0.6 V vs. MSE for 30 min in an aqueous electrolytic solution containing $MnSO_4$ (2 mM) and $NaClO_4$ (50 mM).

The electrocatalytic activity of electrodeposited MnO_2 films supported on ITO and FTO towards OER was also tested. Samples were electrodeposited using chronoamperometry at 0.6 V vs. MSE for 30 min. As already shown previously, the expected morphology of these samples is similar, as both of them were shown to adopt the birnessite type structure. Clearly, the FTO/MnO_2 sample shows a much higher activity than the ITO/MnO_2 sample. Indeed, the current density at 1.0 V vs. MOE is 2.091 mA/cm^2 for the FTO/MnO_2 sample instead of

0.108 mA/cm^2 for the ITO/MnO_2 sample, which is about 20 times higher. Moreover, before the start of water oxidation, the FTO/MnO_2 sample also has a higher capacitive current, indicating possibly its better charge capacitance. Considering the similar morphologies and crystalline varieties for both MnO_2 films, the huge difference observed between electrocatalytic activities towards OER should be ascribed to the poor electrochemical activity of the ITO substrate and to the bad adhesion of MnO_2 films on ITO.

Through these preliminary tests, it is confirmed that FTO is a much better electrode material than ITO for MnO_2 electrodeposition, as it favors the formation of highly stable MnO_2 films that are moreover substantially more electrocatalytically active towards OER.

III.7 MnO_2 electrodeposition on a-CNx electrodes

Amorphous carbon nitride (a-CNx) materials constitute a family of cheap electrode materials whose main surface properties, such as surface electronic conductivity, electrochemical activity and population of surface functional groups, depend on their atomic nitrogen content. This latter can take different values and result from the nitrogen gas content in the plasma used for their elaboration. In our laboratory, a-CNx thin films are deposited on various conducting or insulating substrates using the reactive cathodic magnetron sputtering technique. This deposition technique makes those materials even more interesting as it allows their deposition on large substrates, which favors their use for large scale and industrial applications in electrochemistry, unlike other carbon materials. Here, homemade a-CNx electrodes were tested for the first time as electrode materials for MnO_2 electrodeposition. Figure III.46 shows a linear sweep voltammetry curve obtained on a-CNx electrode in the usual electrodeposition electrolyte used in this work for MnO_2 electrodeposition. This LSV curve shows the same shape as those obtained on glass/ITO (see Figures III.22a and III.23a) and glass/FTO electrodes (see Figures III.43). An oxidation peak attributed to Mn^{2+} oxidation appears at 0.64 V vs. MSE. The onset potential of water oxidation wave is difficult to identify, but it is higher than on FTO and lower than on ITO based on the potential region, indicating its good applicability as an electrode material substrate.

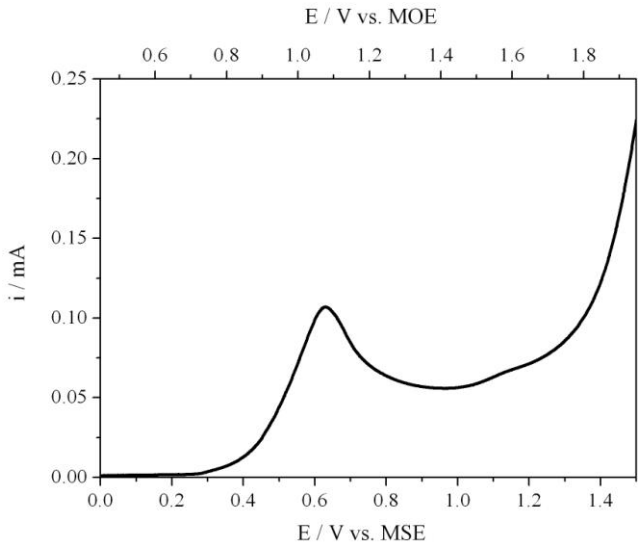

Figure III.46: Linear sweep voltammogram allowing the electrodeposition of a MnO_2 film on a-CNx electrode in MnO_2 electrodeposition electrolyte. Electrolytic solution: $MnSO_4$ (2 mM); $NaClO_4$ (50 mM). Scan rate: 10 mV/s.

A MnO_2 film was then electrodeposited on a a-CNx electrode using chronoamperometry at 0.7 V vs. MSE for 30 min. The obtained MnO_2 film clearly belongs to the birnessite type crystalline variety, as revealed by XRD (see Figure III.47). Its surface morphology is also the same as that of birnessite type MnO_2 films obtained on ITO, FTO or Pt (Figure not shown).

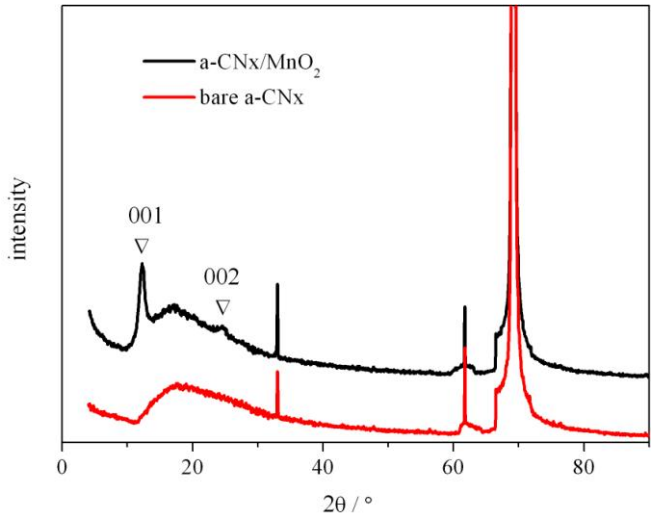

Figure III.47: XRD spectra of bare a-CNx and a-CNx/MnO_2 electrodes. MnO_2 film electrodeposited using chronoamperometry technique at 0.7 V vs. MSE for 30 min. in an electrolyte containing $MnSO_4$ (2 mM) and $NaClO_4$ (50 mM).

OER tests were also carried out in 0.1 M NaOH aqueous solutions with these a-CNx electrodes, as shown in Figure III.48. The onset potential of water oxidation on bare a-CNx electrode is about 1.2 V vs. MOE, which is higher than that on bare ITO and FTO electrodes, meaning that the electrocatalytic activity of bare a-CNx towards OER is not good. After MnO_2 electrodeposition, this electrocatalytic activity becomes even worse: the oxidation current is lower than that on bare a-CNx, suggesting that the electrodeposited MnO_2 has no electrocatalytic activity and hinders the original activity of the substrate. This unexpected result should be ascribed to the electrochemical property of the bottom substrate surface and the insufficient adhesion of the electrodeposited film.

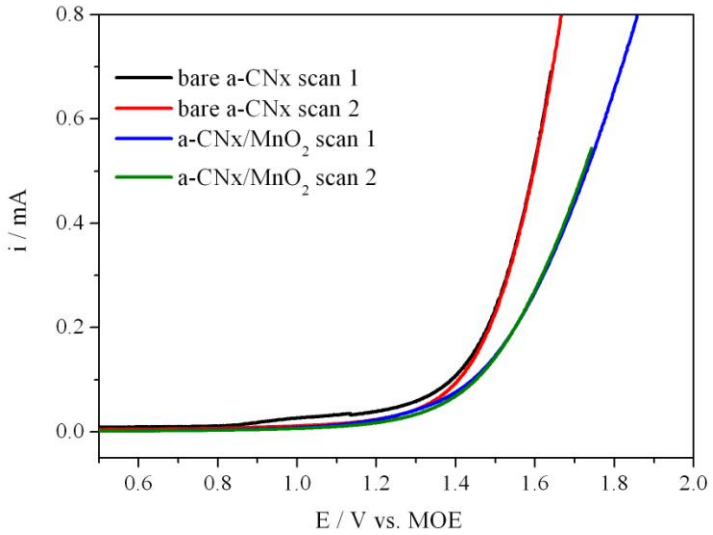

Figure III.48: OER test on ITO/MnO_2 and FTO/MnO_2 samples. Film deposition: $MnSO_4$ (2 mM) and $NaClO_4$ (50 mM); CA 0.7 V 30 min. OER test electrolyte: NaOH 0.1 M. Scan rate: 10 mV/s.

In addition, it was found that the elaboration of the electrode (immobilization of the Si/a-CNx disc on a copper tape covered glass support) is very important for the electronic conductivity pathway and therefore for the electrocatalytic activity of the resulting electrode, whether this latter is covered or not with a MnO_2 film. Indeed, it was observed throughout these studies involving a-CNx electrodes that several electrodes elaborated by using the same conditions actually showed different electrocatalytic activities towards OER. Thus it is necessary to develop a better reproducibility for the elaboration of these a-CNx electrodes in order to allow further investigations in the continuity of those reported above.

III.8 Conclusion

In this chapter, the electrodeposition mechanism of MnO_2 was briefly re-explored and exploited first on Pt working electrodes. In particular, different electrodeposition parameters were evaluated in order to obtain mechanically stable MnO_2 films. As a result, chronoamperometry in an aqueous electrolytic solution containing low concentrations of $MnSO_4$ and $NaClO_4$ provided the best results. Thus this experimental procedure was adopted throughout this chapter and extended to glass/ITO, glass/FTO and Si/a-CNx electrodes.

It was revealed that the adhesion of the MnO_2 film on the initial electrode material influences significantly its electrocatalytic activity towards OER. Moreover, the electrodeposition potential is a very important factor for the electrocatalytic activity of MnO_2 films. In our experimental conditions, an accurate selection of the electrodeposition potential value allows the electrodeposition of either amorphous or birnessite type MnO_2 films possessing respectively granular or layered morphologies. By comparison with ITO, FTO appears to be a much better electrode material due in particular to its high intrinsic electrocatalytic activity towards OER and to the fact that it allows a better adhesion for electrodeposited MnO_2 films. Moreover, the electrocatalytic activities towards OER of MnO_2 films electrodeposited on FTO at different potentials were tested using LSV, chronoamperometry, Tafel plots and EIS. Interestingly, those different electrochemical techniques all led to the same conclusion. Amorphous MnO_2 films electrodeposited at potentials situated between 0.8 and 1.2 V vs. MSE possess a better electrocatalytic activity towards OER than those electrodeposited at lower or higher potentials, whether these latter are amorphous or of the birnessite type variety. On the other hand, UV-visible spectrophotometry technique revealed that MnO_2 films possess low optical bandgap values varying between 2 and 2.6 eV, depending on the electrodeposition conditions. Importantly, on the basis of EIS results, a strong correlation was established between Rs, measuring charge relaxation of surface intermediate(s) and this electrocatalytic activity.

At last, Si/a-CNx electrodes were shown to allow the electrodeposition of MnO_2 films showing a morphology and a crystallinity that were similar to those of MnO_2 films electrodeposited in identical experimental conditions on the other electrode materials, but the electrocatalytic activity of the resulting MnO_2 films towards OER was not good enough, which will justify further investigations in the future to better understand and possibly solve this counter-intuitive conclusion.

Chapter IV: Heat treatment effect on the OER electrocatalysis of FTO/MnO_2 electrodes

IV.1 Introduction

Post heat treatment is an important step for the preparation of solid catalysts, as the dehydration occurring during the heating step will change the structure and the chemical state of the solid catalyst, leading to the formation of more active species and subsequently to better electrocatalytic performances. Fengling Zhou *et al.* reported the post heat treatment effect on MnO_2 catalysts and found great promotion effect on the OER activity [70]. In their work, the catalysts were heated at 50 °C, 70 °C, 90 °C and 120°C for 30 min respectively, and 90 °C was revealed to be the best temperature for heat treatment. A lower temperature was not efficient enough for the heat treatment and a higher temperature led to a degradation effect. The explanation for this phenomenon was ascribed to a dehydration process, which causes a surface phase change as well as an electronic structure change and favors therefore a better electrocatalytic activity. On the contrary, Zaki N. Zahran *et al*. used a much larger temperature range from 150 °C to 750 °C for the heat treatment test. The result showed that the sample heated at 550 °C had the best electrocatalytic activity towards OER and the sample heated at high temperature showed a very good stability [125]. The promotion effect was caused by a phase transition and the formation of α-Mn_2O_3 type crystalline variety during the high temperature heating. Yichuan Ling *et al.* studied hematite films heated at high temperature and found that Sn could diffuse from the FTO substrate into the film structure under high temperature sintering. Sn acts as electron donor and increases the carrier density, and thus increases the OER performances of the hematite based solid catalyst [126]. However, research works related to heat treatment are rarely reported on electrodeposited thin films of solid catalysts, for which the effect and mechanism of heating are therefore still unclear. Based on these observations, investigations related to the heat treatment were carried out on our electrodeposited MnO_2 films in order to evaluate its effect on their electrocatalytic activity towards OER and its stability.

IV.2 Effect of heating at low temperature

To understand the effect of heat treatment on the electrocatalytic activity of MnO_2 films towards OER, several series of samples were prepared and characterized. Based on the

results reported in chapter III, the electrodeposition potential has a great influence on the activity performances, thus several series of samples prepared using the same conditions were used in order to get the same original OER activity.

IV.2.1 On MnO_2 films electrodeposited on FTO at 1.0 V vs. MSE

Figure IV.1 shows the effect of heat treatment at low temperature on the OER activity of MnO_2 films electrodeposited on FTO using chronoamperometry at 1.0 V vs. MSE for 10 min. MnO_2 films electrogenerated in such conditions were shown to be amorphous (see Figure III.35b). From the LSV curves, the electrocatalytic activity of heated samples towards OER is clearly enhanced. The performance of the as-prepared sample was the worst and after the LSV test, MnO_2 film could peel off easily from the FTO substrate, meaning the mechanical stability was poor. This is also confirmed by the fact that in the following CA test, the as-prepared sample had nearly no activity. Heating at 70 °C has a moderate promotion effect, although the current density is higher than that for the as-prepared sample. For samples heated at higher temperatures, the promotion effect becomes much stronger. Sample heated at 110 °C has a slightly higher current density than those heated at 90 °C and 130 °C, while these three samples have identical current densities on the CA curves. Moreover, those heated samples show a constant current density during the CA test duration without any obvious degradation, indicating a good stability. In this case, heat treatment indeed has a positive effect on the catalytic performances and the stability of MnO_2 films.

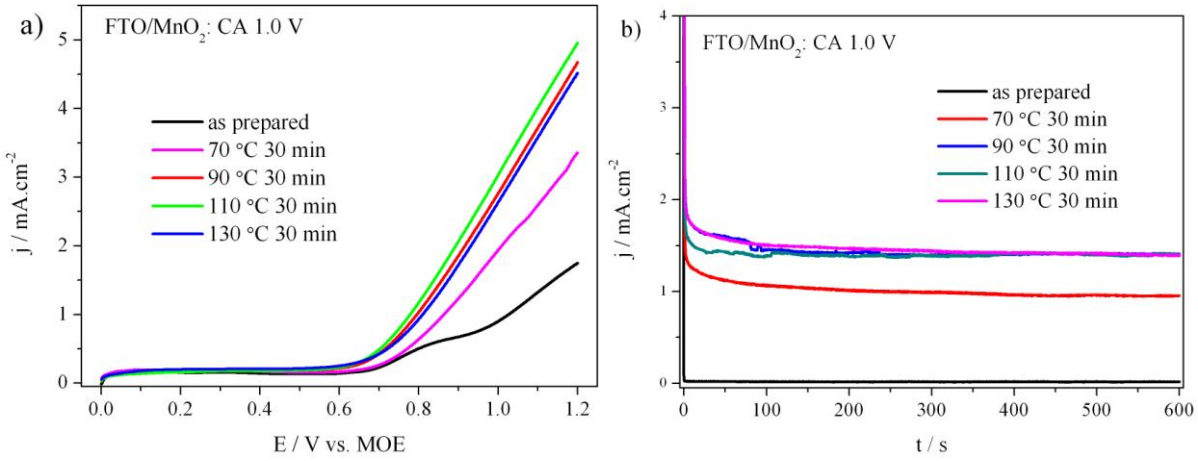

Figure IV.1: a) LSV and b) chronoamperometry curves of FTO/MnO_2 electrodes heated at different temperatures for 30 min. Samples prepared using chronoamperometry at 1.0 V vs. MSE for 10 min. OER tests were carried out in NaOH (0.1 M) electrolyte. Scan rate: 10 mV/s.

In the purpose of confirming the heating effect, another series of samples were prepared and heated using the same conditions. The LSV curves and the corresponding Tafel plots are shown in Figure IV.2a,b. All LSV curves shown in this Figure or hereafter in this manuscript were plotted after an ohmic drop correction applied on the LSV curves obtained experimentally (this was already the case for Figures III.38b and III.44b). From these LSV curves, the as-prepared sample shows the worst activity as in the former series of results. From 70 to 130 °C, the promotion effect of heat treatment increases with increasing temperature, and the sample heated at 130 °C has the highest current density. When the temperature is higher than 150 °C, the activity decreases, indicating that the degradation of the MnO_2 film appears. From the Tafel plots, the as-prepared sample has a higher Tafel slope value than heated samples, meaning the OER reaction is slower on this MnO_2 sample. In this sense, the decrease of its current density could be ascribed to adhesion loss resulting from mechanical or electrochemical damages during the test, which makes the film inactive. For heated samples, the sequence of the slope values is similar to that of current density values measured on LSV curves and the slope value for the sample heated at 130 °C is the lowest.

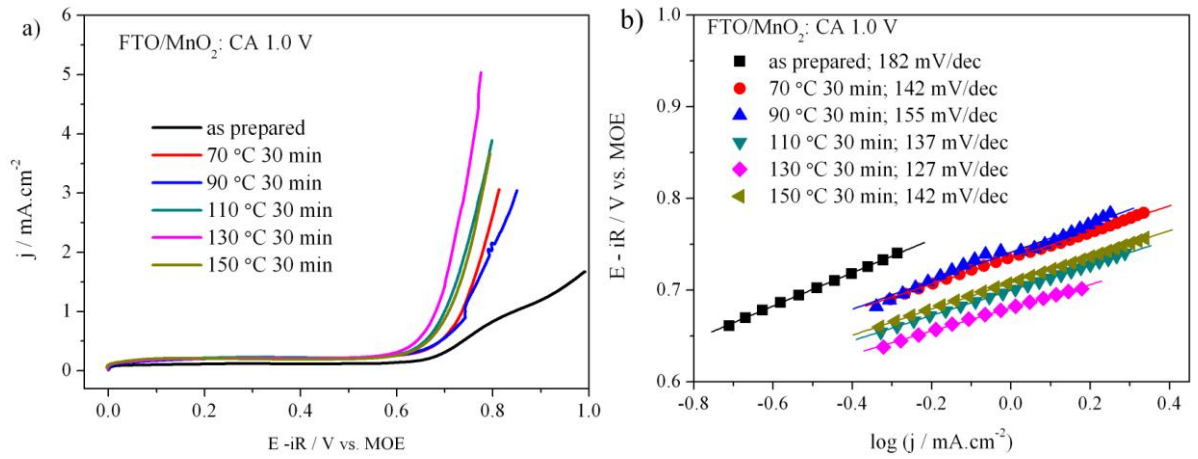

Figure IV.2: a) LSV curves and b) corresponding Tafel plots of FTO/MnO_2 electrodes heated at different temperatures for 30 min. Samples prepared using chronoamperometry at 1.0 V vs. MSE for 10 min. OER tests were carried out in NaOH (0.1 M) electrolytic solution. Scan rate: 10 mV/s.

Through the chronoamperometry test shown in Figure IV.2, sample heated at 130 °C also shows the best performance with the highest current density among those samples, followed by samples heated at 90, 110 and 150 °C. Sample heated at 70 °C has a lower current density, which is consistent with the LSV results. The as-prepared sample also lost its electrocatalytic activity after LSV test, which is ascribed to its poor mechanical stability.

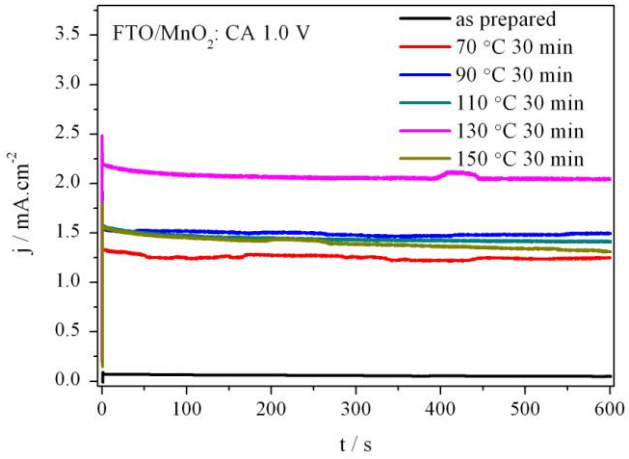

Figure IV.3: Chronoamperometry curves of FTO/MnO_2 electrodes heated at different temperatures for 30 min. Samples prepared using chronoamperometry at 1.0 V vs. MSE for 10 min. Tests were carried out in NaOH (0.1 M) electrolytic solution at 0.9 V vs. MOE.

The XRD spectra and UV-vis spectra shown in Figure IV.4 are aimed at studying the influence of heat treatment on the structural and optical properties of the MnO_2 films. From Figure IV.4a, MnO_2 films electrodeposited at 1.0 V appear to be amorphous, viewing from XRD spectra, no MnO_2 peak could be observed except for those belonging to FTO substrate, indicating that heat treatment did not change the crystallinity of MnO_2 films in this temperature region. Moreover, the existence of a MnO_2 film reduces the diffraction signal of the FTO substrate. Sample heated at 110 °C has some noise signal, and the FTO signal disappears for sample heated at 130 °C, but no obvious changes are related to the MnO_2 films. On the other hand, the UV-vis spectra show that sample heated at 130 °C has the lowest light absorption ability comparing with samples heated at other temperatures, and the as-prepared sample has slightly higher absorbance than heated samples, perhaps caused by the abundant water molecules in its structure. Generally, higher absorbance in high wavenumber region will benefit the solar water splitting reaction. Although the electrocatalytic activity of sample heated at 130 °C is the best, its photoelectrocatalytic performances towards water splitting need to be checked.

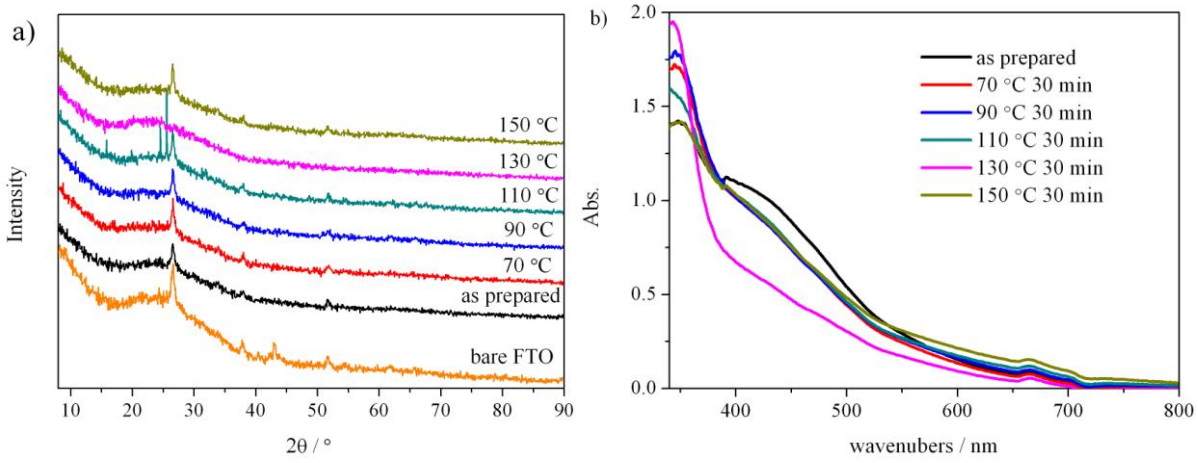

Figure IV.4: a) XRD and b) UV-vis spectra of FTO/MnO_2 electrodes heated at different temperatures for 30 min. Samples prepared using chronoamperometry at 1.0 V vs. MSE for 10 min.

IV.2.2 On MnO_2 films electrodeposited on FTO at 0.6 and 1.2 V vs. MSE

Two more series of samples were prepared using 0.6 and 1.2 V vs. MSE for electrodeposition, and then heated at different temperatures. The CV and CA tests are shown in Figure IV.5. For the MnO_2 films prepared at 1.2 V vs. MSE, sample heated at 110 °C has a little better activity, as observed from the CV curves, followed by samples heated at 90 °C and 130 °C. The sample heated at 150 °C has the lowest current density. This trend is also confirmed by the CA tests. Moreover, all samples show a good stability as revealed by CA tests, in which the current density keeps the same value in the 10 min test duration.

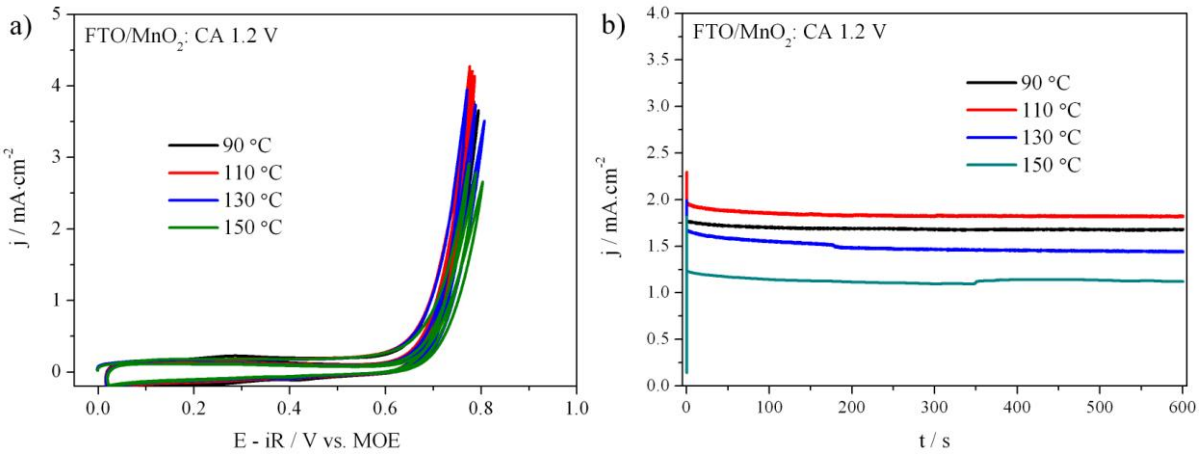

Figure IV.5: a) Cyclic voltammetry and b) chronoamperometry curves of FTO/MnO_2 electrodes heated at different temperatures. Samples prepared using chronoamperometry at 1.2 V vs. MSE for 10 min. OER tests carried out in NaOH (0.1 M) electrolyte. Scan rate: 10 mV/s.

On the contrary, the heating effect is complicated for samples electrodeposited at 0.6 V vs. MSE, as shown in Figure IV.6. From the former results, MnO_2 films electrodeposited at this potential possess the birnessite type crystalline structure (see Figure III.35b) and the OER activity of this type of films was found to be limited. Here, the results are consistent. The as-prepared sample has the lowest activity, which is even lower than the bare FTO electrode. Obviously, heat treatment will increase this activity. As observed with samples heated at 110 °C, 130 °C and 150 °C, the current density increases substantially, while for 90 °C, the promotion effect is limited. Furthermore, it is noteworthy that all samples degrade quickly after each CV scan, especially for those highly active samples. This phenomenon is also observed in the subsequent CA tests obtained after 3 CV scans. The current density values measured during the CA tests increase with the heating temperature, i.e. the higher the heating temperature, the higher the current density. Sample heated at 150 °C has the highest current density, followed by sample heated at 130 °C, while for the other samples heated at lower temperatures, the current density is quite small. Moreover, the current densities measured on the CA curves tend to decrease during the test duration, meaning that the films undergo a continuous degrading.

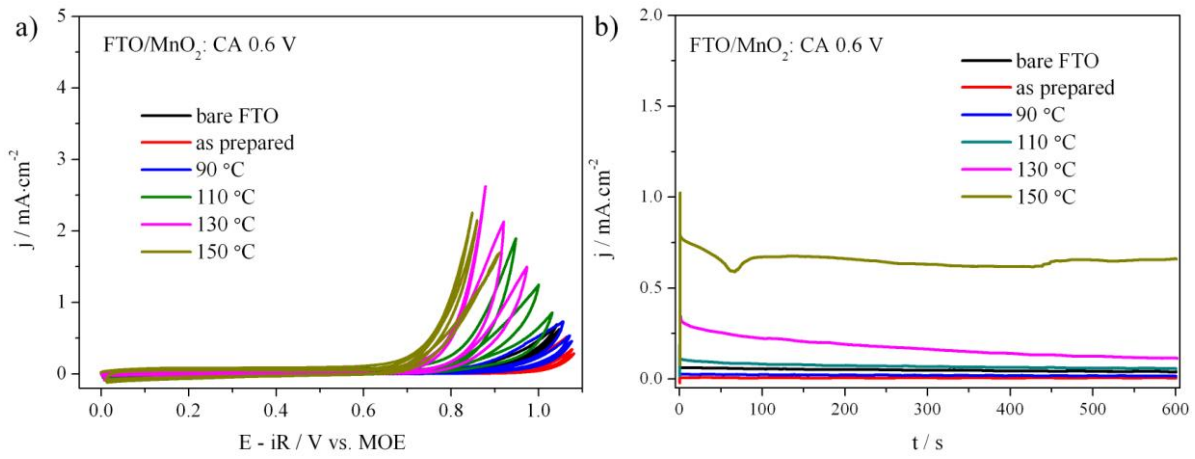

Figure IV.6: a) cyclic voltammetry and b) chronoamperometry curves of FTO/MnO_2 electrodes heated at different temperatures for 30 min. Samples prepared using chronoamperometry at 0.6 V vs. MSE for 10 min. OER tests were carried out in NaOH (0.1 M) electrolyte. Scan rate: 10 mV/s.

Considering those low temperature heated samples investigated above, the highest current density obtained on the series of samples electrodeposited at 0.6 V vs. MSE (~ 2.8 mA/cm^2) is lower than any of those measured on the series of samples electrodeposited at 1.2 V vs. MSE (~ 4.2 mA/cm^2) or 1.0 V (~ 5.0 mA/cm^2), and the stability of those 0.6 V

samples is also worse than that of the other samples after heat treatment. In this sense, the MnO_2 films with birnessite type crystalline structure are not better candidates as OER catalysts than MnO_2 films possessing an amorphous structure.

Meanwhile, an interesting phenomenon was observed during the preparation and evaluation test: when the film was electrodeposited on a recently cleaned and still wet FTO substrate, the activity was good, while when it was electrodeposited on a cleaned and well dried FTO substrate, the electrocatalytic activity was poor even after heat treatment. The OER tests performed on MnO_2 samples electrodeposited at 1.2 V vs. MSE on either wet or dry FTO substrates are shown in Figure IV.7. The main reason of the poor activity of those films electrodeposited on dry substrate is their bad stability: after 3 CV scans, nearly the whole film was peeled off of the substrate, indicating a poor adhesion between the film and FTO substrate surface. After several trials, it is confirmed that the substrate conditioning has a crucial influence on the stability and the subsequent activity of electrodeposited MnO_2 films, i.e. the wet surface of FTO substrate favors the formation of stable, very adherent and highly active MnO_2 films.

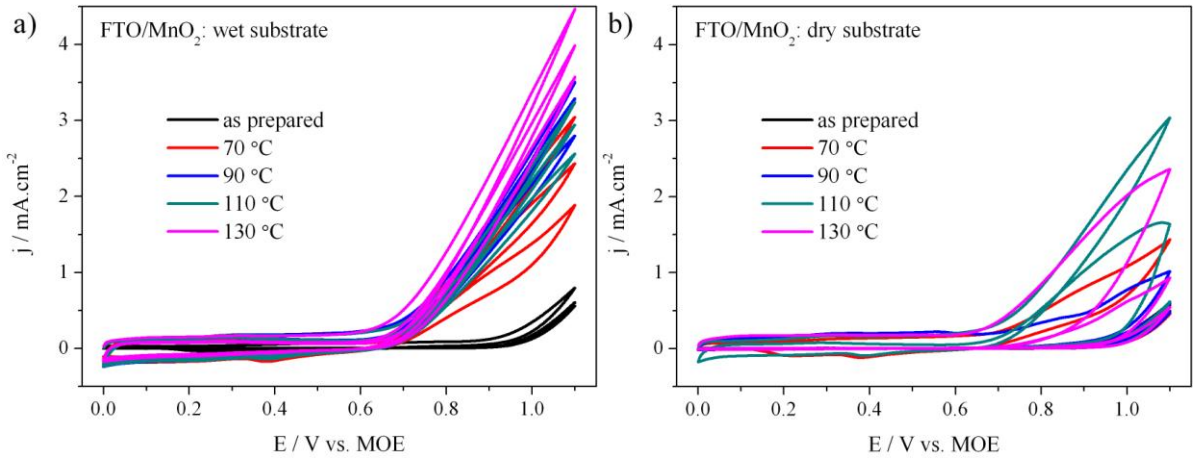

Figure IV.7: Cyclic voltammetry curves of MnO_2 films electrodeposited on a) wet and b) dry FTO substrates and heated at different temperatures for 30 min. MnO_2 samples were prepared using chronoamperometry at 1.2 V vs. MSE for 10 min. OER tests were carried out in NaOH (0.1 M) electrolyte. Scan rate: 10 mV/s.

IV.3 Effect of heating at moderate temperature

In section IV.2, it has been confirmed that the heat treatment has a crucial influence on the electrocatalytic activity of MnO_2 films towards OER. The stability of adhesion

between the MnO_2 film and the substrate is also an important factor affecting the activity of these electrodeposited films. Low temperature heating (70 - 150 °C) investigated in the previous section was expected to cause the dehydration of the MnO_2 films, and thus to slightly change its oxidation state and its crystalline structure. However, these changes are quite limited. Generally, calcination is a key step for the preparation of catalysts. In this step, dehydration and phase transition will lead to huge difference on the crystallinity and the oxidation state of the material, and thus they are expected to cause great change on the electrocatalytic activity of these films. Therefore, choosing a proper temperature for the calcination is one of the most critical aspects to obtain highly active catalysts. In our case, apart from the dehydration and phase transition, the calcination may also increase the adhesion between the film and the substrate, making therefore the MnO_2 films more stable and active.

In order to study the influence of high temperature calcination on the electrocatalytic activity of electrodeposited MnO_2 films towards OER, samples were prepared at 0.6 V and 1.2 V vs. MSE, respectively. The calcination temperature was chose inside a range going from 150 °C up to 600 °C, which is higher than the melting point of MnO_2.

IV.3.1 On MnO_2 films electrodeposited on FTO at 0.6 V vs. MSE

Figure IV.8 shows heating effect on samples electrodeposited at 0.6 V vs. MSE. From the CV curves (see Figure IV.8a), obvious promotion effect is obtained with samples calcinated at high temperatures. By comparison with the samples calcinated at 150 °C, those calcinated at 200 °C and 300 °C show higher current density and the difference between each CV scan is small, indicating a good stability, while for the sample calcinated at 400°C, the activity turns out to be low, meaning that the calcination temperature might be too high. From the Tafel plots (see Figure IV-8b), the low slope values always correspond to highly active samples, but still there are some samples that do not obey this trend.

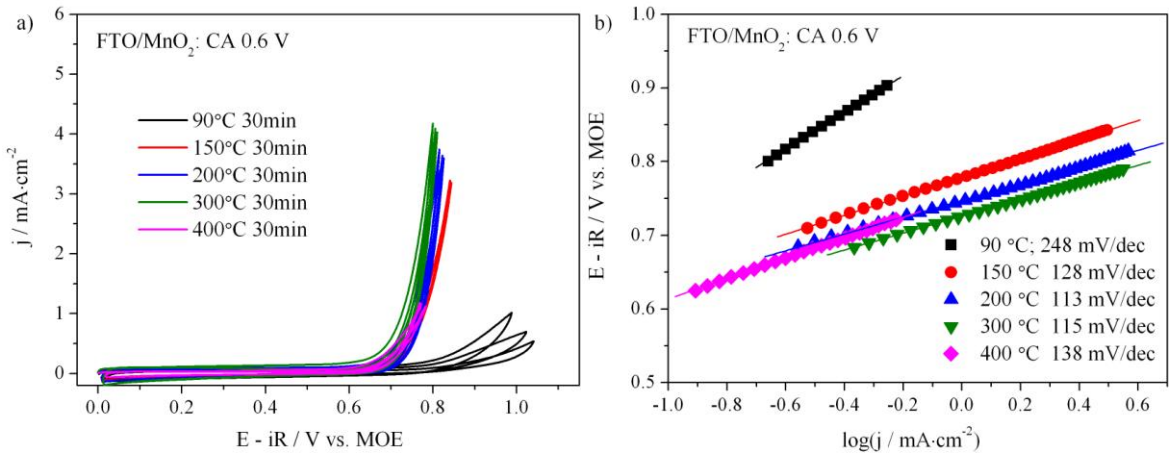

Figure IV.8: a) cyclic voltammetry curves and b) corresponding Tafel plots of FTO/MnO_2 electrodes heated at different temperatures for 30 min. Samples prepared using chronoamperometry at 0.6 V vs. MSE for 10 min. OER tests were carried out in NaOH (0.1 M) electrolyte. Scan rate 10 mV/s.

Birnessite-type crystalline variety is a layered material, and cations and water molecules are inserted into the spaces between those layers. Therefore, dehydration during heat treatment will remove those inserted water molecules and lead to structure deformation, especially for high temperatures. In this case, the XRD technique is well adapted to study this effect. The XRD spectra of heated MnO_2 samples are shown in Figure IV.9. Clearly, with the heating temperature increase, samples lose their birnessite type crystalline structure. The sample heated at 90 °C still has an intense birnessite diffraction peak, while for the sample heated at 150 °C, the intensity of this same diffraction peak becomes quite weak, indicating that the crystalline structure has changed, the peak characteristic of birnessite has almost completely disappeared and the sample turns to amorphous after heating at 250 °C. However, when the temperature reaches 400 °C, the birnessite pattern appears again. That means the crystalline undergoes the birnessite-amorphous-birnessite phase transition. In this case, the disappearance of birnessite structure is due to the dehydration process leading to damages of the layered structure, while the re-appearance could be due to the phase transition of the MnO_2 structure.

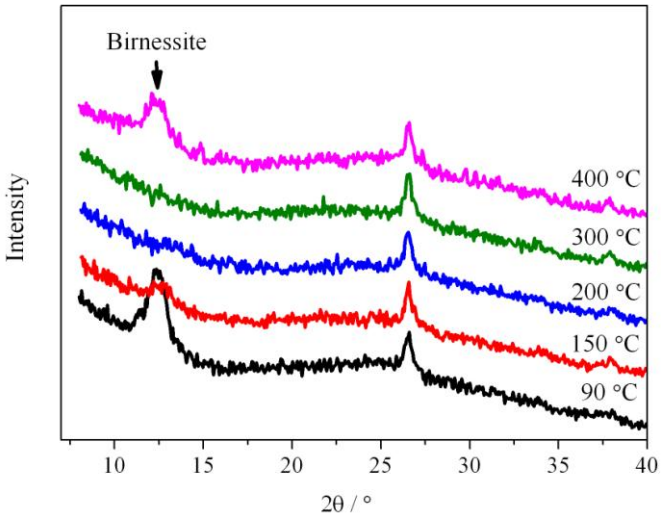

Figure IV.9: XRD spectra of FTO/MnO_2 electrodes calcinated at different temperatures for 30 min. Samples prepared using chronoamperometry at 0.6 V vs. MSE for 10 min.

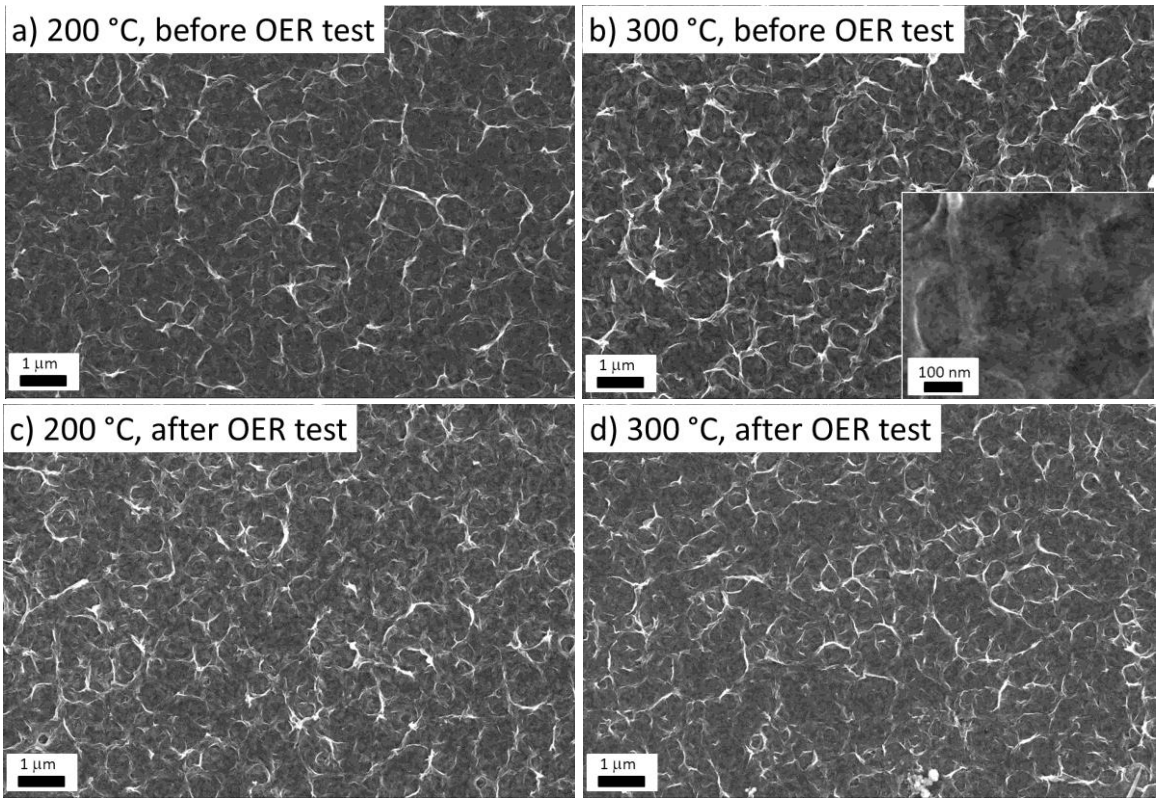

Figure IV.10: SEM images of FTO/MnO_2 films calcinated at 200 °C and 300 °C for 30 min before and after OER tests. Samples prepared using chronoamperometry at 0.6 V vs. MSE for 10 min.

The surface morphology of heated samples shows little difference after comparison with the as-prepared sample, as shown in Figure IV.10. However, small pores appear on the surface of the sample heated at 300°C (see small SEM image included in Figure IV.10a, 3-6

nm diameter), while they are not observed on the one heated at 200 °C (see Figure IV.10a), indicating possibly that the film lost some matter as a consequence of dehydration and calcination at high temperature.

After OER tests, the surface morphology remains unchanged as observed from the SEM images in Figure IV.10c,d. Moreover, most of the pores in the 300 °C heated sample are now closed and become invisible after OER test (see Figure IV.10d), which means the surface of the film rearranges during cyclic voltammetry experiments. The similar morphology of samples before and after OER test also reflects that the films become stable and adherent on the FTO substrate after calcination.

IV.3.2 On MnO_2 films electrodeposited on FTO at 1.2 V vs. MSE

Samples electrodeposited at 1.2 V vs. MSE are initially amorphous after electrodeposition. Their CV curves and the corresponding Tafel plots obtained during OER tests are shown in Figure IV.11. In this series of experiments, samples heated at a moderate temperature show similar electrocatalytic activities that are much higher than that obtained at 150 °C. Heating at 200-250 °C has slightly higher promotion effect as the current density reaches 3.5-4.2 mA/cm^2. Moreover, all samples show good stability during consecutive cyclic voltammetry scans. The Tafel slope values of these samples are close to each other, and lower than that of the sample heated at 150°C, in good agreement with the CV results.

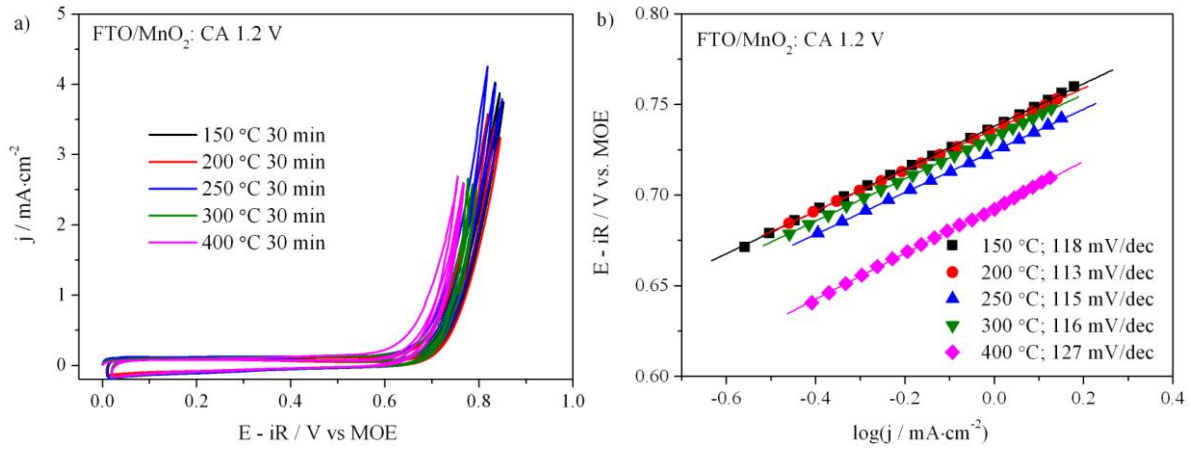

Figure IV.11: a) cyclic voltammetry curves and b) corresponding Tafel plots of FTO/MnO_2 electrodes heated at different temperatures for 30 min. Samples prepared using chronoamperometry at 1.2 V vs. MSE for 10 min. OER tests carried out in NaOH (0.1 M) electrolyte. Scan rate: 10 mV/s.

The XRD spectra of the heated samples (see Figure IV.12) show no difference after comparison with those of the as-prepared sample. Apart from the diffraction peaks of FTO substrate, no other patterns could be observed even for samples heated at 400 °C, suggesting that no phase transition happened at this temperature. The sample heated at 300 °C was characterized again after OER test, and the XRD spectrum remained unchanged, which confirms its high stability.

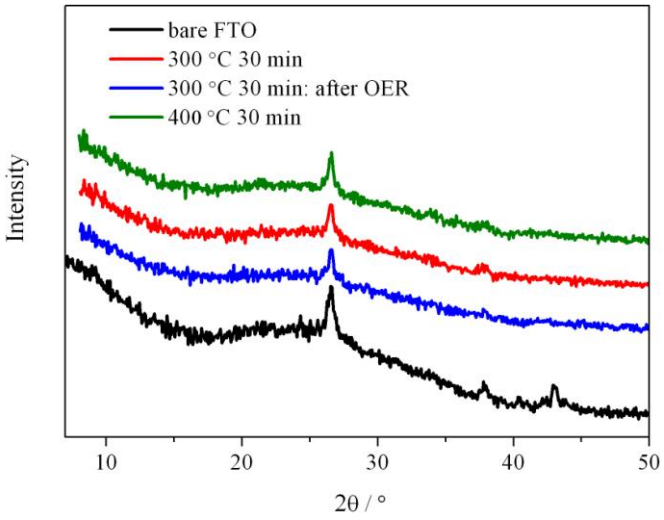

Figure IV.12: XRD spectra of FTO/MnO_2 films calcinated at 300 °C and 400 °C for 30 min. MnO_2 samples prepared using chronoamperometry at 1.2 V vs. MSE for 10 min.

The morphology of these films was studied by SEM (see Figure IV.13). Comparing with the as-prepared sample, the surface morphology of the granular structure does not change a lot after calcination. However, as the calcination temperature increases, the boundaries of each grain become unclear and more difficult to identify, especially for the sample heated at 300 °C. This change could be caused by the fusion and rearrangement of the film under high temperature, indicating probably that the phase transition starts to happen. After OER test, as shown in Figure IV.12, the morphology of those moderate temperature heated samples shows no obvious change as expected, indicating the good stability of the films.

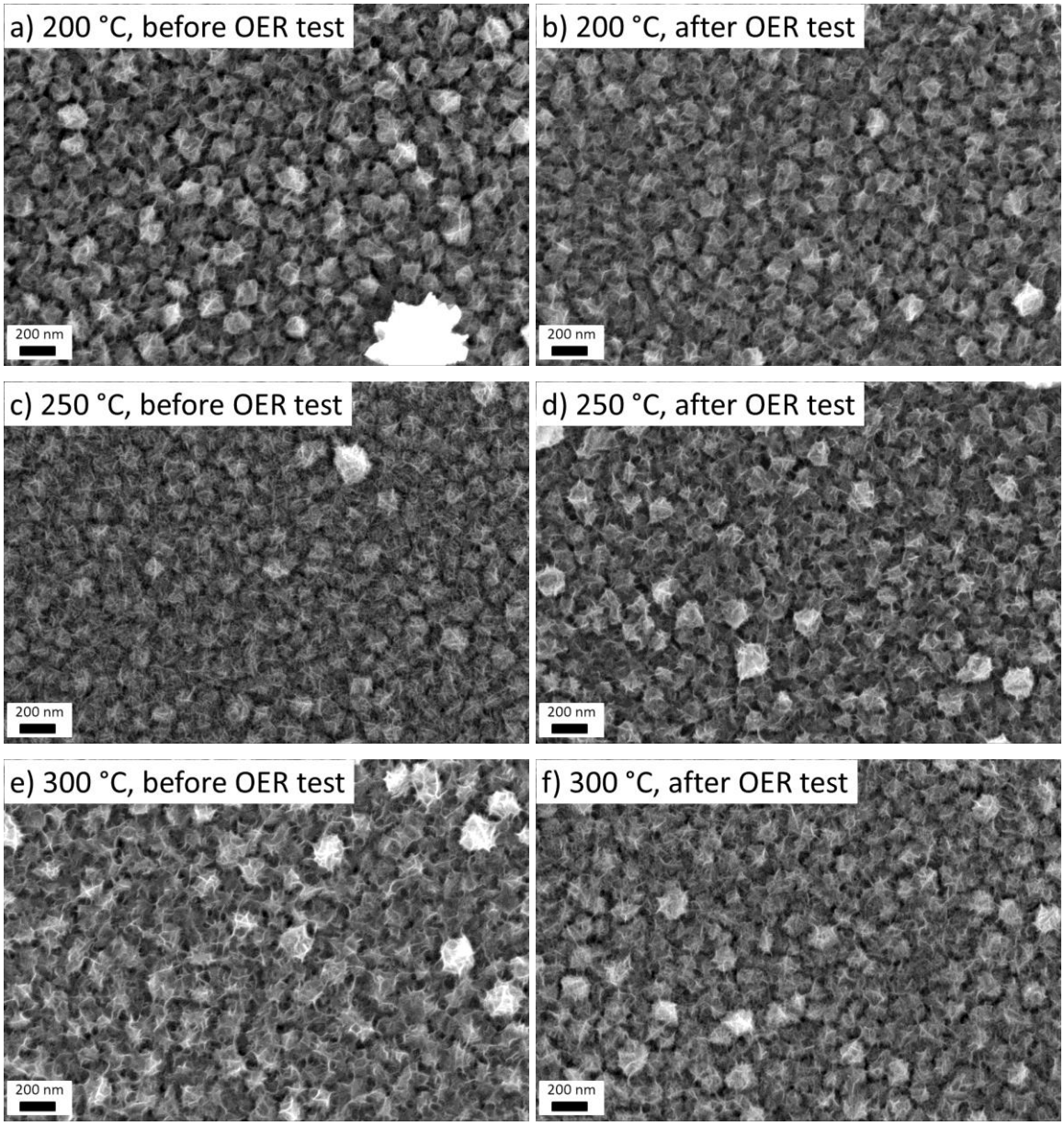

Figure IV.13: SEM images of FTO/MnO_2 films calcinated at 200 °C, 250 °C and 300 °C for 30 min before and after OER tests. Samples prepared using chronoamperometry at 1.2 V vs. MSE for 10 min.

IV.4 Effect of heating high temperature on FTO/MnO_2 films

The heating effect at low temperature (70 – 150 °C) and moderate temperature (150 – 400 °C) has been discussed above. By comparison with the low temperature, moderate temperature led to better promotion effect of the OER performances, especially for birnessite type MnO_2 films electrodeposited at 0.6 V vs. MSE. However, none of these temperatures caused obvious phase transition. The samples heated at 400 °C already showed some signs of melting in the topography, but the phase did not change according to the XRD spectra. The

melting temperature of MnO_2 is about 530 °C. The rearrangement coming after melting could make new crystalline structures with different electrocatalytic performances. Zaki N. Zahran *et al*. observed the formation of α–Mn_2O_3 structure after calcination at 550 °C [125], but the influence of the initial structure caused by the electrodeposition potential has not been studied yet. In order to solve this question, a new series of investigations were carried out after heating at a high temperature.

In this part, two series of samples electrodeposited at 0.6 V and 1.2 V vs. MSE, which possess the birnessite type and amorphous crystalline structure respectively, were employed. The heat treatment temperature ranged from 450 to 600 °C and the duration was 30 min. After heating, samples were evaluated by different characterization methods in order to study the change on the morphology, structure and OER activity of the MnO_2 films.

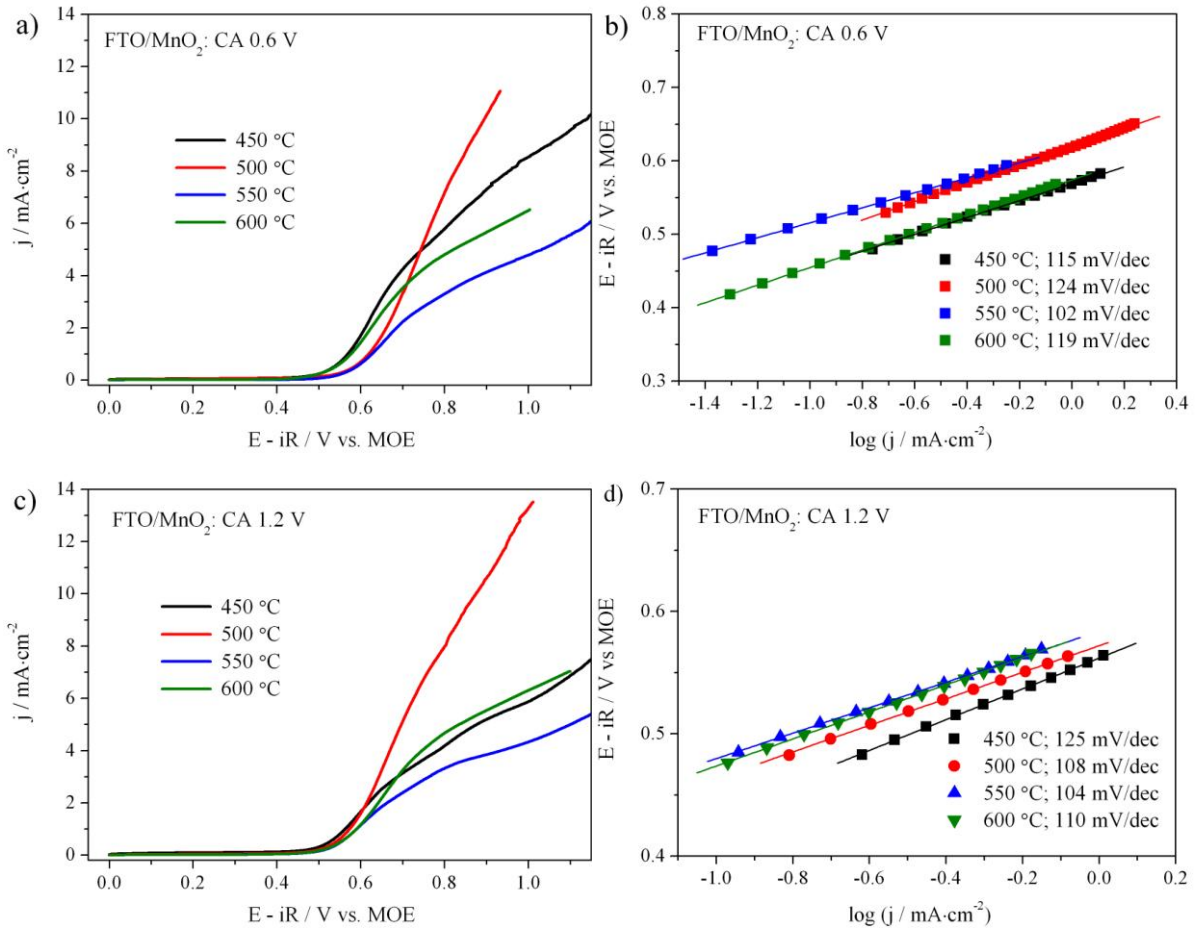

Figure IV.14: a,c) LSV curves and b,d) Tafel plots of FTO/MnO_2 electrodes calcinated at different temperatures for 30 min. Samples prepared using chronoamperometry at 0.6 V and 1.2 V vs. MSE for 10 min. OER tests were carried out in NaOH (0.1 M). Scan rate: 10 mV/s.

The LSV curves related to OER tests are shown in Figure IV.14. For MnO_2 films electrodeposited at 0.6 V vs. MSE (see Figure IV.14a), the MnO_2 sample heated at 450 °C shows slightly better OER activity in low potential region, according to its lower onset potential, while in the high potential region, i.e. above 0.75 V vs. MOE, the MnO_2 sample heated at 500 °C is much better. Heating at a higher temperature such as 550 °C and 600 °C leads to a decrease of the electrocatalytic activity in the high potential region, suggesting that this latter is hindered by high temperature calcination.

For MnO_2 films electrodeposited at 1.2 V vs. MSE (see Figure IV.14c), the MnO_2 sample heated at 500°C has the best OER activity in the whole potential region. The current density values of samples heated at 500 °C are 7.28 and 7.98 mA/cm^2 at 0.8 V vs. MOE for samples electrodeposited at 0.6 and 1.2 V vs. MSE respectively. These latter are the highest current density values obtained on MnO_2 films. Moreover, it is noteworthy that for all samples heated at high temperature, the onset potential of OER is lower (~ 0.5 V vs. MOE) after comparison with the previous results. From the Tafel plots shown on Figure IV.14, although Tafel slope values are lower for these samples heated at 500 °C, they are slightly higher than those of the samples heated at 550°C. In this case, the Tafel slope values do not show the same trend as the current density values measured at 0.8 V vs. MOE, possibly as a consequence of the influence of matter transport existing at this potential. .

More importantly, it is found that the resistance of the FTO substrate increases dramatically when heating is carried out at high temperature, as observed on the EIS spectra shown in Figure IV.15. Usually, the starting point of EIS spectra in high frequency range is ascribed to the uncompensated series resistance, including the electrolyte resistance and the film resistance. Considering the test conditions, all experiments were carried out obviously in the same electrolyte, thus the big difference in the starting point in the EIS spectra should be caused by the change of the FTO film resistance and bottom substrate. In order to elucidate this suggestion, bare FTO substrates were heated using the same conditions and it was found that the resistance increases with heating temperature, and their values were very close to the series resistances measured on MnO_2 samples. Therefore, the high series resistance results come mainly from the conductivity drop of the FTO substrate. When the test potential increases, the current increases, leading to the partial potential shared by the electrolyte and film resistance increases. It could be neglect when the current density is small, but with high

current value, this part of partial potential becomes remarkable, thus at given potential range, samples with high resistance always perform worse OER activity.

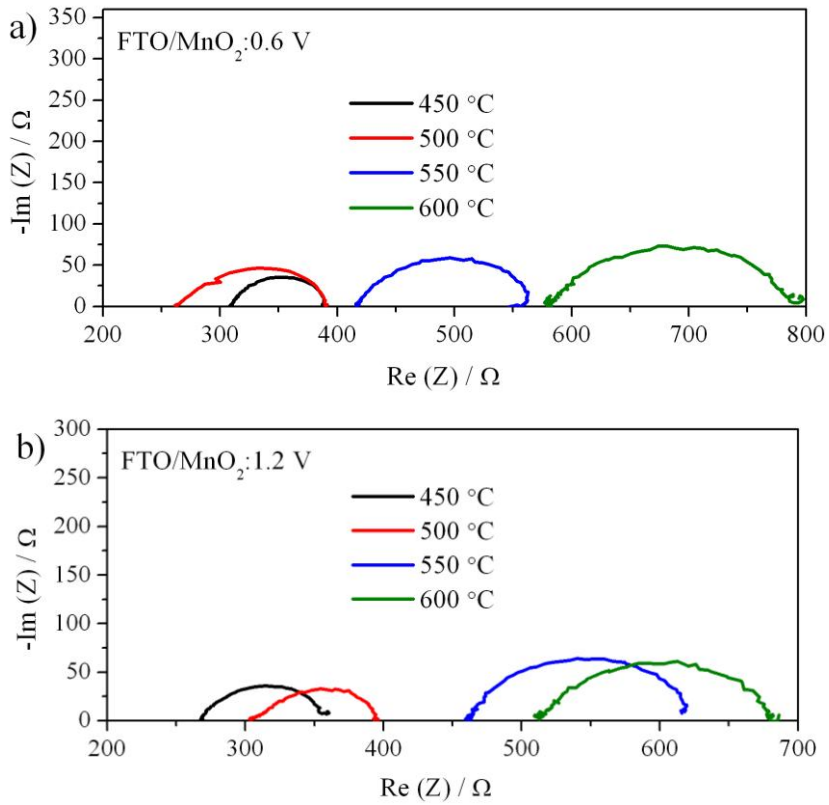

Figure IV.15: EIS spectra of FTO/MnO_2 electrodes calcinated at different temperatures for 30 min. Samples prepared using chronoamperometry at 0.6 V and 1.2 V vs. MSE for 10 min. Test electrolyte: NaOH (0.1 M). Test potential: 0.7 V vs. MOE.

Moreover, along with the increase of the heating temperature, the diameter of the flattened semicircles observed on Figure IV.15 increases too, indicating possibly an increase in the charge transfer resistance. Beyond the effect of the high series resistance values, the new electronic properties of the MnO_2 films after high temperature heating could also contribute to the apparently larger charge transfer resistance.

In this sense, the iR correction involving the series resistance, which is based on the measure of a series resistance including definitely the electrolyte resistance and possibly a series resistance related to the conductivity of the substrate, becomes more significant.

Based on former results, calcination at 400 °C already causes visible changes of the morphology of MnO_2 films. At higher temperatures, a great difference should be observed on the morphology and even on the crystallinity of those films. Thus, the topography of those

samples heated at high temperature was studied by SEM and the images are shown in Figure IV.16 and IV.17.

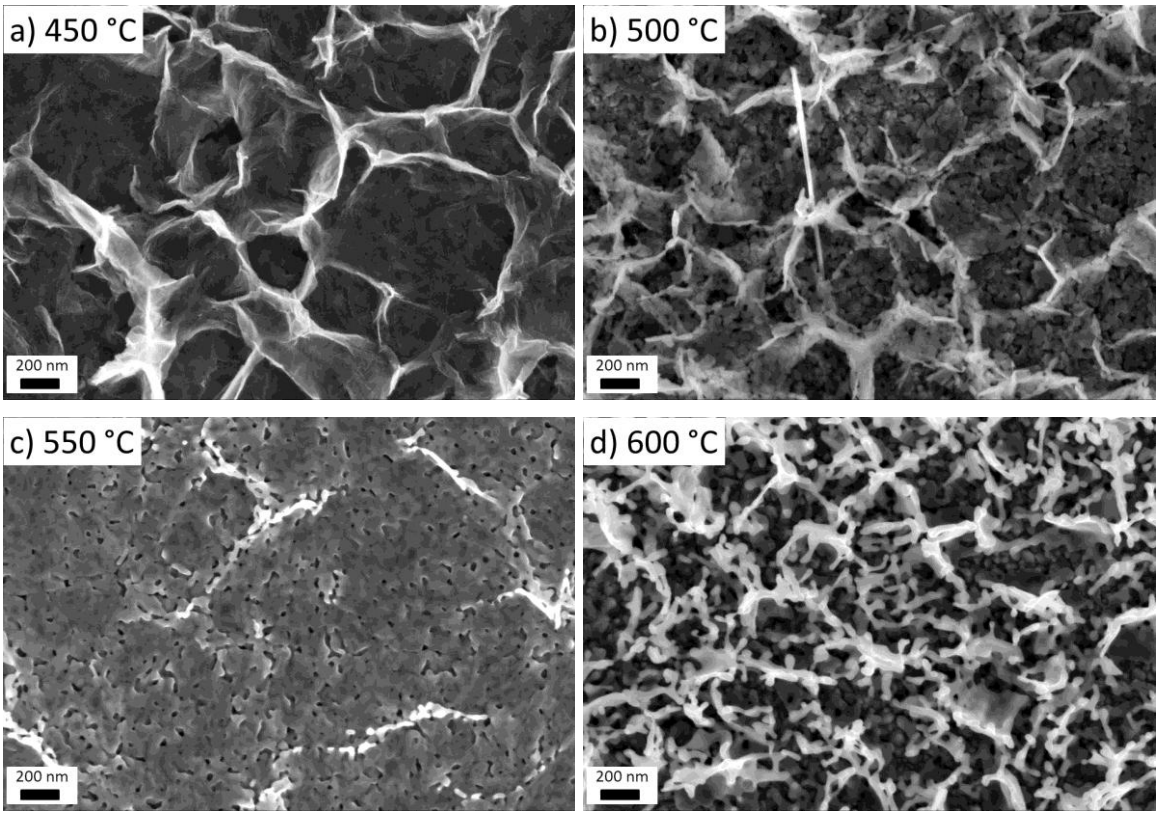

Figure IV.16: SEM images of FTO/MnO_2 electrodes heated at high temperature region for 30 min. Samples prepared using chronoamperometry at 0.6 V vs. MSE for 10 min.

For samples electrodeposited at 0.6 V vs. MSE, calcination at 450 °C did not cause obvious change in the surface morphology (see Figure IV.16a). However, calcination at 500 °C causes obvious decomposition of the film, as the layered structure is smashed and particles start to form (see Figure IV.16b). When the temperature goes up to 550 °C, which is beyond the melting point of MnO_2, the film loses its rough surface and turns to flat laminar structure (see Figure IV.16c). This is a clear evidence of the melting effect: MnO_2 melts and re-disperses during the calcination process at this temperature. After calcination at 600 °C, even the layered structure has disappeared, and it is replaced by a pseudo-dendritic structure.

On the other hand, for the samples electrodeposited at 1.2 V vs. MSE, the morphology appears to adopt another aspect after calcination. The morphology change also begins from 500 °C, as the as-prepared big particles decompose into small rice grain shaped particles (see Figure IV.17b). As the temperature increases to 550 °C, some bigger nanorods start to grow

at the bottom of the surface while the top of the film shows no obvious changes (see Figure IV.17c). When the temperature increases to 600 °C, the surface is totally replaced by big long nanorods, indicating those small rice grain shaped particles combine together during calcination (see Figure IV.17d). The FTO substrate was also calcinated and analyzed by SEM, but no obvious changes happens after calcination at 600 °C, showing its good thermal resistance.

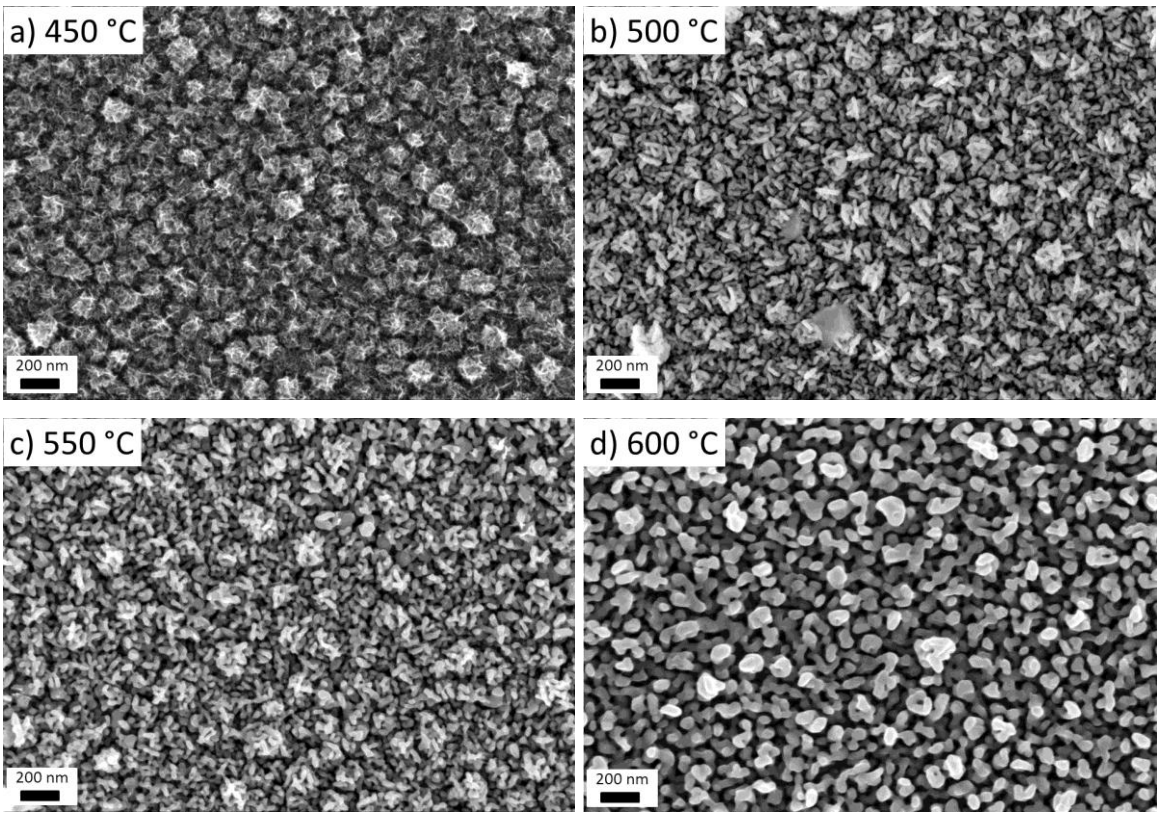

Figure IV.17: SEM images of FTO/MnO_2 films heated at high temperature region for 30 min. Samples prepared using chronoamperometry at 1.2 V vs. MSE for 10 min.

The crystalline structure of those samples were characterized by XRD on new MnO_2 samples prepared using a 30 min electrodeposition duration (instead of 10 min), in order to get clear diffraction patterns for MnO_2 films. From the XRD spectra shown in Figure IV.18, the crystallinity of FTO shows no obvious change after calcination. However, the samples electrodeposited at 0.6 V vs. MSE show the characteristic peaks of birnessite (12.8° and 38.2°), which disappear after heating at low temperature. Those peaks are more clear and intense on the XRD spectra corresponding to samples electrodeposited during 30 min and heated at 550°C for 30 min (see Figure IV.18). A re-formation phenomenon of birnessite was observed on a sample heated at 400 °C (see Figure IV.9), and it is confirmed again here at

550°C. For samples electrodeposited at 1.2 V vs. MSE, no obvious changes on the crystalline structure are observed. Besides, the peaks at 32.9° and 55.2° could be ascribed to the diffraction pattern of α-Mn_2O_3 (JCPDS card No. 89-4836)[127,128], which is consistent with the result of Zaki N. Zahran *et al.* [125]. In this case, the phase transition has begun due to the high temperature calcination, but the crystallinity of α-Mn_2O_3 is not good, perhaps because of the short calcination time or the mixed crystalline structure of the films.

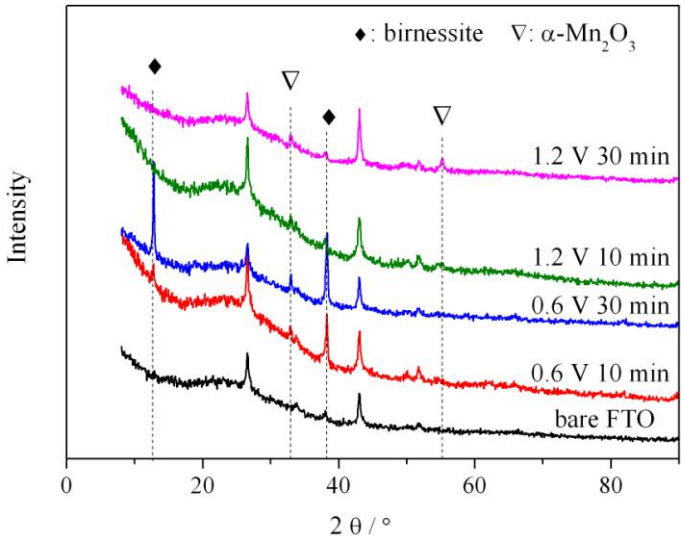

Figure IV.18: XRD spectra of FTO/MnO_2 films calcinated at 550 °C for 30 min. Samples prepared using chronoamperometry for 10 or 30 min at 0.6 V or 1.2 V vs. MSE.

It has been found that the resistance of FTO increases dramatically after calcination at high temperature (see EIS results in Figure IV.15). However, there is no obvious change on the crystallinity and on the surface morphology of bare FTO samples heated at 550°C. Thus the reason for the conductivity change should come from an electronic structure change, either in the bulk of the FTO layer or at the FTO/MnO_2 interface, rather than from the crystallinity or a phase transition.

Based on the results described above, heating treatment at high temperature (500°C) substantially provided the best improvement of the electrocatalytic activity of MnO_2 films towards OER, while a moderate temperature has only a moderate beneficial effect.

IV.5 Solar water splitting on heated FTO/MnO_2 films

The final target of this study is to investigate the performance of electrodeposited MnO_2 films as catalysts for photoelectrochemical water splitting. As a consequence, the test of the photo-electrocatalytic activity of MnO_2 films under solar light is a key step to evaluate their performances, and if necessary, their practical applications. Natural sunlight is not a constant light source because the light intensity changes with time and is influenced by the weather. In this case, an artificial light source with stable and adjustable light intensity is more practical. Here, we used a commercial solar simulator equipped with a xenon lamp to provide the needed solar light (see section II.6 for description and Appendix A.2 for calibration).

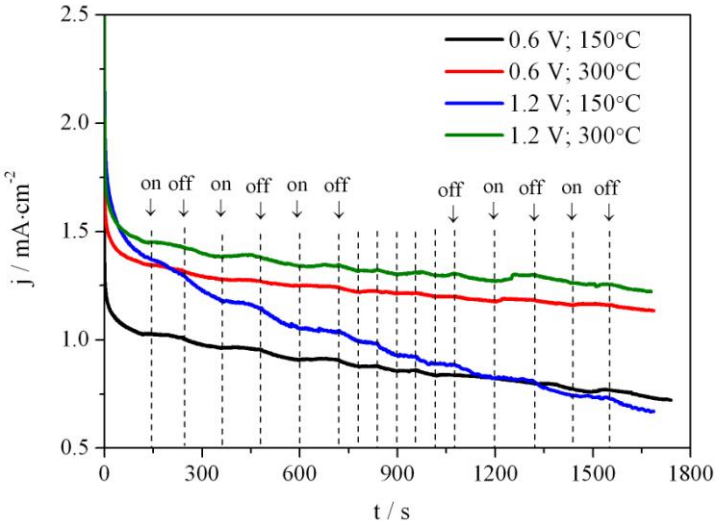

Figure IV.19: Chronoamperometry of photoelectrochemical water splitting tests carried out on FTO/MnO_2 electrodes under the chopped light of a solar simulator. Samples prepared using chronoamperometry at different electrodeposition potentials for 30 min. Electrolyte: NaOH (0.1 M). Test potential: 0.9 V vs. MOE. Light intensity: 100 mW/cm^2.

The photoelectrochemical water splitting tests were carried out under manually chopped lightening on selected samples electrodeposited at 0.6 V and 1.2 V vs. MSE and then heated at different temperatures. The light was set to be on for one or two minutes and the light intensity was set to be 100 mW/cm^2, which is equal to the natural sun light AM 1.5 G. The results are shown in Figure IV.19.

In this test, all samples show a more or less progressive degradation during the test. It is thus difficult to evaluate the photocurrent generated by the solar simulator lightening. However, it is obvious that the decreasing trend of the current is significantly stopped and even a small increase of the current can be observed during the lightening periods. For

samples heated at 150 °C, whether they belong to the amorphous or birnessite crystalline variety, the current density decrease is fast, indicating the poor stability of these films. On the contrary, in the case of samples heated at 300 °C, the current density decrease is much slower, indicating that the stability of the films is enhanced by this heat treatment. The appearance of a photo-electrocatalytic activity is consistent with the predictions. Moreover, the samples electrodeposited at 0.6 V vs. MSE show smaller current density values than those electrodeposited at 1.2 V vs. MSE, whereas the photocurrent values of each MnO_2 variety are difficult to distinguish between them.

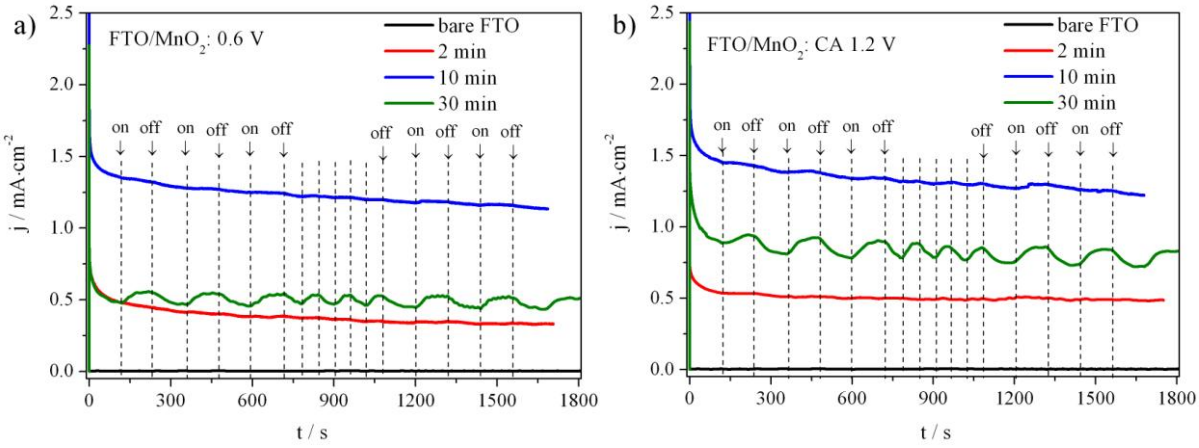

Figure IV.20: Chronoamperometry of photoelectrochemical water splitting test on FTO/MnO_2 electrodes under the chopped light of a solar simulator. Samples prepared using chronoamperometry at a) 0.6 V and b) 1.2 V vs. MSE and heated at 300 °C for 30 min. Electrolyte: NaOH (0.1 M). Test potential: 0.9 V vs. MOE. Light intensity: 100 mW/cm^2.

The absorbance of a MnO_2 film may be influenced by the thickness of the film, as revealed by UV-vis spectra (see Figure III.27c), as the absorbance increases with the electrodeposition time. Thus, the influence of the film thickness on the photoelectrocatalytic activity towards water splitting was studied. The results are shown in Figure IV.20.

The bare FTO sample has no photoelectrocatalytic activity, as evidenced by Figure IV.20, in which no current density enhancement was observed for this sample. For samples electrodeposited at 0.6 V vs. MSE, clearly, a 2 min electrodeposition duration is not enough to observe a photoelectrocatalytic activity, because of the thin thickness of the film. Moreover, the dark electrocatalytic activity of the film is limited as well. On the other hand, for a 10 min electrodeposition time, this latter is multiplied by three, and a small photocurrent can also be observed. When the electrodeposition time is extended to 30 min, the dark

electrocatalytic activity is not much higher than the one observed for a 2 min electrodeposition duration, but an obvious photocurrent is observed. This trend remains the same for samples electrodeposited at 1.2 V vs. MSE. Furthermore, it is noteworthy that all the samples electrodeposited at this potential have a higher current density than those of the MnO_2 films electrodeposited at 0.6 V vs. MSE, indicating a better photoelectrocatalytic activity towards OER.

The current density values measured at the end of each lightening period for samples electrodeposited for 30 min were extracted from the chronoamperometry test shown on Figure IV.20, and plotted as a function of time, as shown in Figure IV.21.

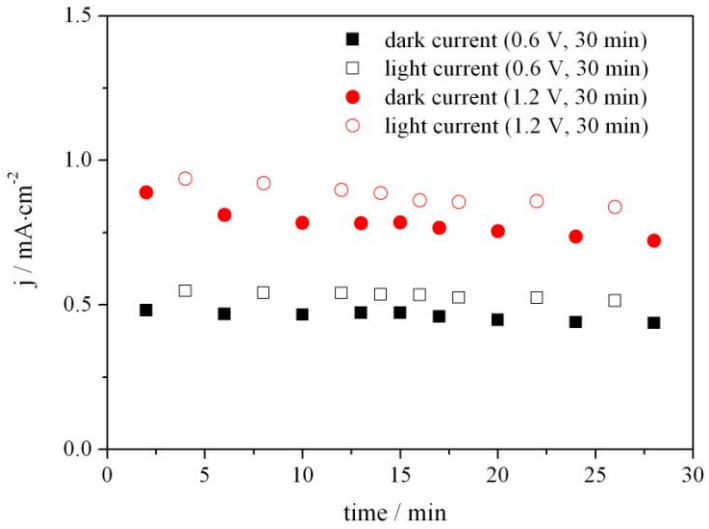

Figure IV.21: Current density values measured at the end of each lightening period. Data extracted from Figure IV.20.

Considering that the current density is continuously decreasing during the test, the photocurrent value is calculated by formula (IV.1).

$$I_{photo\ current} = I_{light\ current} - \frac{(I_{dark\ current\ before} + I_{dark\ current\ after})}{2} \qquad \text{(IV.1)}$$

The calculated photocurrent values are listed in Table IV.1. Clearly, the photocurrent values of sample electrodeposited at 0.6 V vs. MSE is 72.4 µA/cm^2, which is smaller than that of sample electrodeposited at 1.2 V vs. MSE, 104.0 µA/cm^2. However, considering the ratio of photocurrent versus dark current (I_{photo}/I_{dark}), the sample electrodeposited at 0.6 V vs. MSE provides a slightly higher ratio (15.7%) than the sample electrodeposited at 1.2 V vs.

MSE (13.4%), meaning that the first one has a little higher photoelectrocatalytic activity than the second one.

Table IV.1: calculated photo current of FTO/MnO_2 samples

sample		1	2	3*	4	5	6*	7	8	average
0.6 V vs. MSE	Photo current / $\mu A/cm^2$	73.5	75	72	64	68	71	80	75.5	72.4
	I_{photo}/I_{dark} / %	15.49	16.06	15.35	13.56	14.59	15.64	18.02	17.22	15.7
1.2 V vs. MSE	Photo current / $\mu A/cm^2$	87	123.5	114.5	103	86	95	113	109.5	104.0
	I_{photo}/I_{dark} / %	10.24	15.49	14.61	13.14	11.08	12.48	15.15	15.01	13.4

*the value might not be accurate because the chopped durations before and after are different.

These two samples were calcinated at 300 °C, and the phase transition did not happen yet, thus the samples conserved the as-prepared morphologies, in which the sample electrodeposited at 0.6 V vs. MSE has the layered structure while the one electrodeposited at 1.2 V vs. MSE has the columnar structure. Moreover, the later one has a lot of big columns (see Figure III.37), which increases the surface area of the film. Both samples were amorphous without any crystalline diffraction patterns as observed from the XRD results. It appears therefore that the sample electrodeposited at a higher potential seems to be more active towards the photoelectrochemical water splitting.

IV.6 Conclusions

In this chapter, the influence of post heat treatment on the photoelectrocatalytic activity of FTO/MnO_2 electrodes was studied. Three temperature regions were investigated respectively: low temperature region (70 - 150 °C), moderate temperature region (200 – 400 °C) and high temperature region (450 - 600 °C). The MnO_2 samples were prepared using chronoamperometry at different electrodeposition potentials (0.6 V, 1.0 V or 1.2 V vs. MSE) and for different electrodeposition times (10 min or 30 min). Through the structural and morphological analysis, the phase transition of the electrodeposited MnO_2 films starts from 500 °C. Below this temperature, no obvious changes could be observed, while above this temperature, the morphology experiences clearly melting and re-arrangement. The birnessite structure (samples electrodeposited at 0.6 V vs. MSE) could be seen at low and high temperatures whereas it disappears at moderate temperature, while no obvious structure

changes were observed for amorphous MnO_2 samples (samples electrodeposited at 1.2 V vs. MSE). High temperature calcination was shown to increase the electrical resistance of FTO substrate, thus leading to lower performances of FTO/MnO_2 samples as OER electrocatalysts. In this case, the iR correction is necessary to get the real electrocatalytic activity of MnO_2 films. It is found that samples heated at 500 °C have the best OER activity, and samples electrodeposited at 1.2 V vs. MSE are always better than those electrodeposited at 0.6 V vs. MSE. Moreover, the stability of FTO/MnO_2 films could be significantly enhanced by heat treatment, especially for samples electrodeposited at 0.6 V vs. MSE. From the photoelectrochemical water splitting tests, considerable photocurrents were obtained on thick FTO/MnO_2 samples, indicating the great capability of MnO_2 as a powerful photoelectrocatalyst for solar water splitting.

Chapter V: Influence of cations insertion on the electrocatalytic activity of MnO_2 films towards OER

V.1 Introduction

Material structures are hardly homogeneous and usually contain impurities and defects, which are included during the preparation step. Since the natural OEC was found to be a Mn_4CaO_5 cluster, the study of biomimetic fabrication of OER catalysts draws much attention. Among them, the birnessite-type MnO_2 bares high potential to be an efficient catalyst due to its similarity to the Mn_4CaO_5 cluster[129]. It consists of metal oxide layers with cations and water molecules inserted in the space between layers. The presence of cations is the result of the oxidation state of Mn atoms. For instance, the theoretical oxidation state of Mn in MnO_2 is +4, meanwhile +3 and +2 oxidation states also exist due to defects or dislocation during the growth of the structure. Those inserted cations are necessary to balance the negative charge brought by oxygen atoms and to keep the structure stable. A lot of researches focus on the structure of MnO_2 or other Mn-based oxides [49,50]. However, the inserted cation is also an important factor that would affect the electrocatalytic performances of the catalyst. It has been reported that the photosystem II (PSII) would be inactive for oxygen evolution if the Ca atom was removed from the Mn_4CaO_5 cluster [130]. The nature of the cation determines the extent of the insertion, as a consequence of its diameter, valence state, and migration rate. Different cations have been involved in the formation of birnessite type MnO_2 structure. The results show that the cations have a great influence on the electrocatalytic activity of electrogenerated MnO_2 catalysts towards OER. Mathias Wiechen *et al*. prepared birnessite-type MnO_2 powders by comproportionation reactions of Mn^{2+} and MnO_4^- in solutions containing K^+, Ca^{2+}, Sr^{2+} or Mg^{2+} cations. They found that the structure of those samples have similar atomic structure although the inserted cations are different. However, the sample containing Ca^{2+} show the highest OER activity, followed by sample containing Sr^{2+} [55]. Venkata Bharat Ram Boppana *et al*.[131] prepared K^+ and Na^+ inserted δ-MnO_2 and replaced those cations by H^+ through ion exchange. The oxygen evolution activity of K-MnO_2 and Na-MnO_2 was similar while that of H-MnO_2 was one order of magnitude lower than that of the original K-MnO_2 sample although the crystalline structure did not change much. They ascribed this to the stabilization of the layered structure by alkaline cations instead of attributing them a role into the catalytic reaction. The MnO_2 samples in

these reports were prepared using chemical synthesis. On the other hand, the influence cation insertion on the electrocatalytic activity of electrodeposited MnO_2 films towards OER was never reported. J.N. Broughton and M.J. Brett studied the electrochemical capacitance of MnO_2 films electrodeposited from solutions containing NaAc, KAc or NH_4Ac and found that the cations had no significant influence on the electrodeposition behavior and on the capacitance value of MnO_2 films[132]. On the other hand, electrodeposition has been proved viable for preparation of birnessite-type MnO_2 films [56,132] but the influence of inserted cations on the electrodeposition of MnO_2 films and on their properties still remain poorly documented.

In this chapter, we tried to evaluate the influence of different cations on the electrodeposition and the electrocatalytic activity of MnO_2 films. Alkaline metals cations such as Na^+, K^+ (valence state +1) and alkaline earth metal cations such as Ca^{2+} and Mg^{2+} (valence state +2) were studied respectively for this purpose.

V.2 Preparation of FTO/C-MnO_2 films containing different cations (C)

In chapter III, FTO was found to be a better substrate than ITO for OER electrocatalysis using a MnO_2 catalyst, as concluded from the results obtained from a $MnSO_4/NaClO_4$ electrolyte. Therefore, the samples were all electrodeposited on a FTO electrode. The solution for electrodeposition contained $MnSO_4$ (2 mM) and alkaline metal or alkaline earth metal perchlorate salt (50 mM), as those used in previous chapters. LSV curves carried out on bare FTO electrode in the electrodeposition solutions are shown in Figure V.1. For these 4 solutions, the curves are similar with the electrochemical oxidation of Mn^{2+} cations appearing at a potential close to 0.57 V vs. MSE. An additional and irreversible oxidation peak appears at about 1.5 V vs. MSE before the oxidation of water. This peak could also be observed on the bare FTO electrode in the same solution in the absence of $MnSO_4$. Thus, this oxidation peak may reveal the oxidation of FTO possibly favored by the perchlorate salt. In a $MnSO_4$ containing solution, this peak becomes more intense. One can observe that solutions containing Ca^{2+} or Mg^{2+} cations lead to a higher intensity for this peak than those containing Na^+ and K^+ cations, which could be due to their higher ionic strength. Moreover, though the pH value of each solution is different, the peak position is always the same, indicating the weak influence of pH on this oxidation peak. The cathodic peaks

appearing close to 0.4 V and -0.5 vs. MSE are attributed to the partial electrochemical reduction of MnO_2.

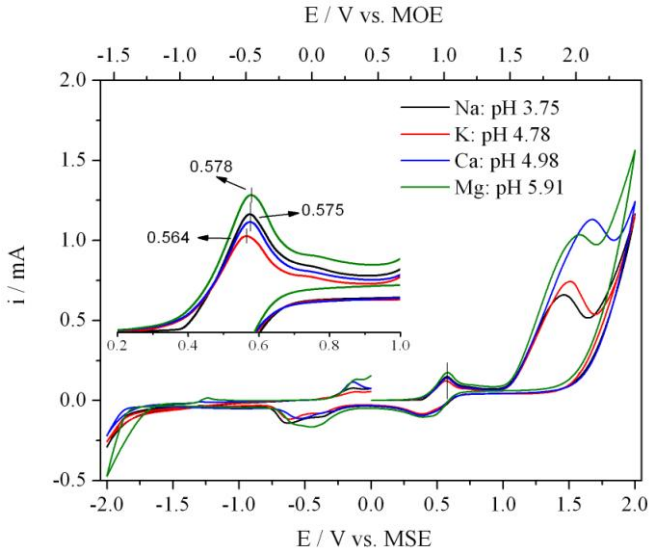

Figure V.1: LSV curves showing MnO_2 electrodeposition and reduction in solutions containing different cations. Electrolyte: $MnSO_4$ (2 mM); (Na, K, Ca, Mg) ClO_4 (50 mM). Scan rate: 10 mV/s.

Chronoamperometry was employed for the preparation of FTO/MnO_2 samples. Electrodeposition potential was set to be 0.6 V and 1.2 V vs. MSE with electrodeposition time of 10 or 30 min in order to obtain the birnessite and amorphous crystalline varieties respectively. Then, the obtained samples were heated at 90 and 300 °C to increase their stability. The samples are denoted by the cations included in the electrodeposition solution, i.e. Na-MnO_2, K-MnO_2, Ca-MnO_2 and Mg-MnO_2.

V.3 OER tests on electrodeposited FTO/C-MnO_2 films

The cyclic voltammetry curves of OER tests on MnO_2 samples introduced above are shown in Figure V.2. From these CV curves, the same trend as that found in chapter IV is observed. It is obvious that samples electrodeposited at 0.6 V vs. MSE and heated at 90 °C have the worst electrocatalytic activity, no matter what the inserted cation is. This is consistent with our previous conclusions and could be ascribed to the poor stability of the MnO_2 films. On the other hand, MnO_2 films electrodeposited at 1.2 V vs. MSE and heated at 90 °C all show a better electrocatalytic activity towards OER, except the K-MnO_2 sample that shows an activity worse than the other samples (Na-MnO_2, Ca-MnO_2 and Mg-MnO_2

electrodeposited at 1.2 V vs. MSE and heated at 90 °C), and the CV curves degrade quickly, which means that the adhesion of this sample is not well established. On the contrary, after heating at 300 °C, great promotion effect appears on samples electrodeposited at 0.6 V vs. MSE and the difference between samples electrodeposited at different potentials becomes very small. In other words, after comparison between them, samples heated at 300°C have similar electrocatalytic activities (red and green curves in Figure V.2). This is ascribed to the heating effect, which increases the adhesion of the samples, especially for the MnO_2 samples electrodeposited at 0.6 V vs. MSE. For samples electrodeposited at 1.2 V vs. MSE, heating at 300 °C also slightly promotes the OER activity comparing with heating at 90 °C (see blue and green curves). From the Tafel plots shown on Figure V.2b,d,f,h, MnO_2 samples heated at 300°C (see red and blue lines) have much lower Tafel slope values than samples heated at 90 °C (see black and green lines) for all series, agreeing with the performances of their electrocatalytic activities. The Tafel slope values of samples heated at 300 °C between 100 and 110 mV/dec (except one : Mg-MnO_2 at 1.2 V vs. MSE, 300°C), while the Tafel slope values for the samples heated at 90°C are dispersed in a larger range of values.

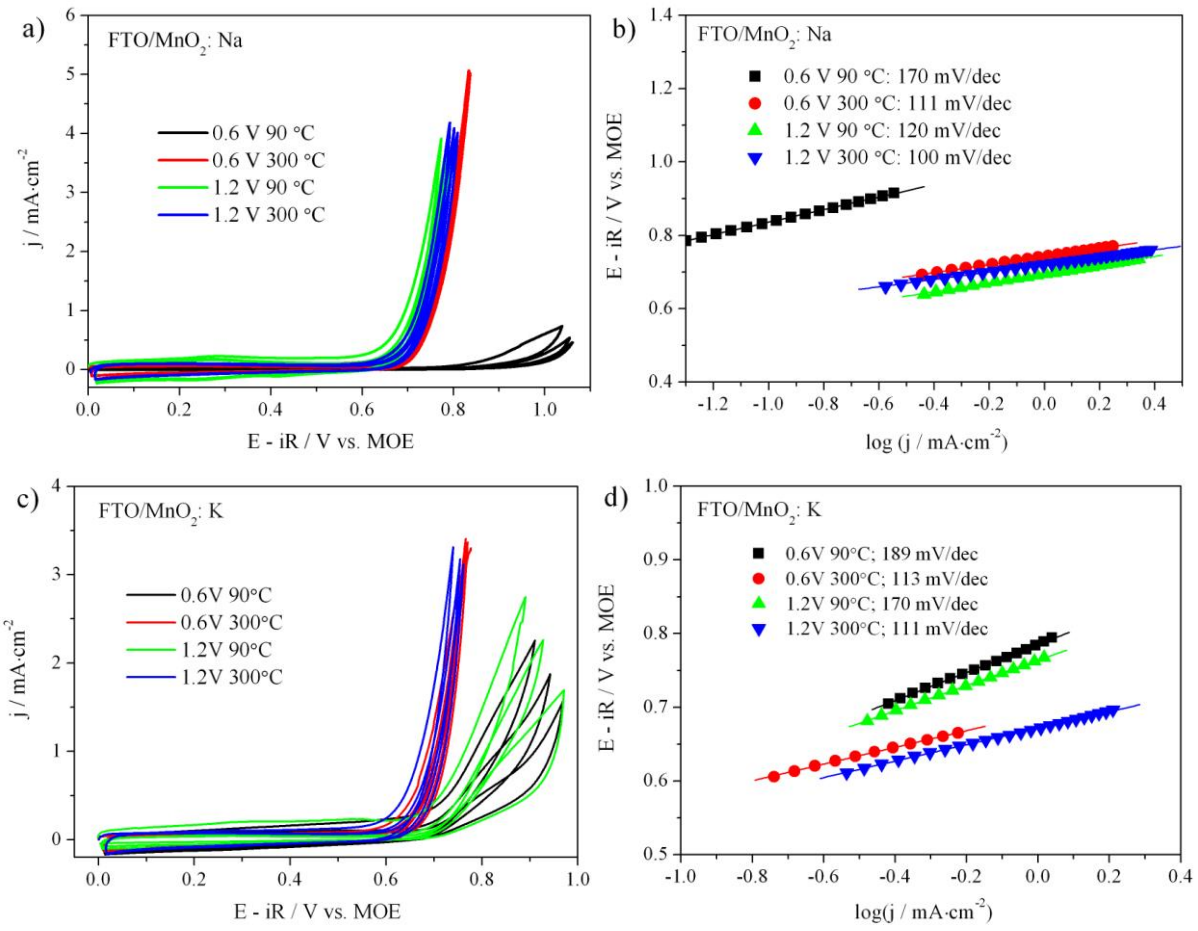

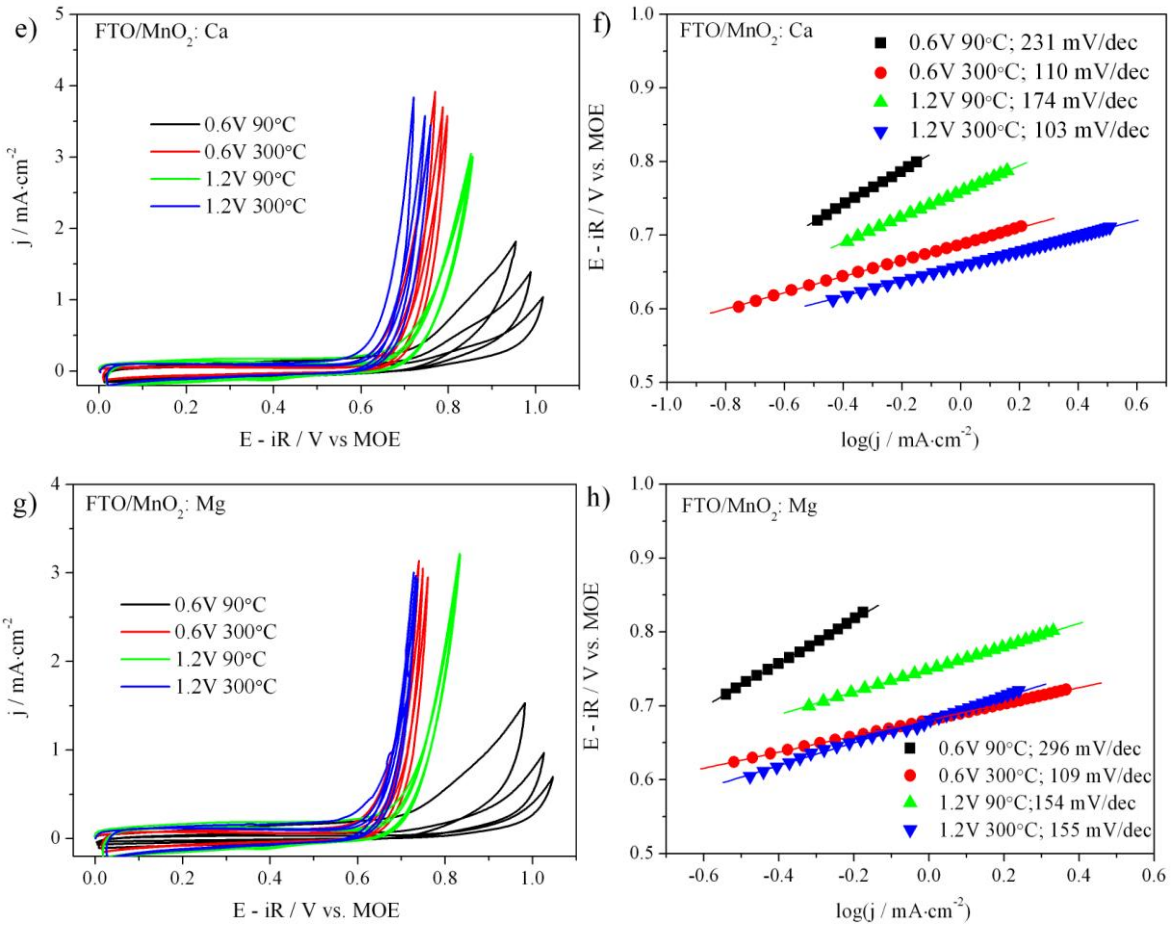

Figure V.2: a, c, e, g) cyclic voltammetry curves and b, d, f, h) Tafel plots of MnO_2 films electrodeposited on FTO in Na^+, K^+, Mg^{2+} and Ca^{2+} containing solutions (iR corrected) . Samples prepared by chronoamperometry for 10 min. Test solution: NaOH (0.1 M). Scan rate: 10 mV/s.

In order to understand the influence of cations and make the comparison more clear, the MnO_2 samples prepared using the same experimental conditions (same electrodeposition potential and same heating temperature) are put together and the results are shown in Figures V.3 (CV curves) and V.4 (Tafel plots). For samples electrodeposited at 0.6 V vs. MSE and heated at 90 °C (see Figures V.3a and V4a) which possess the birnessite structure, K-MnO_2 has the best activity, followed by Ca-MnO_2 and Mg-MnO_2, whereas Na-MnO_2 has the lowest activity. On the other hand, it is noteworthy that all these samples degrade very quickly during the consecutive scans of cyclic voltammetry, suggesting the poor adhesion of these films. On the contrary, after heating at 300 °C, both the activity and stability of all these samples increase significantly. The activity follows the sequence: Mg-MnO_2 > K-MnO_2 ≈ Ca-MnO_2 > Na-MnO_2. For MnO_2 samples electrodeposited at 1.2 V vs. MSE, Na-MnO_2 turns out to be the best catalysts after heating at 90 °C, and followed by Mg-MnO_2 and Ca-MnO_2.

K-MnO_2 is the worst one because of its bad adhesion and its poor stability. After a 300 °C heating, the activities of these samples are similar between them and the differences between their CV curves are quite small.

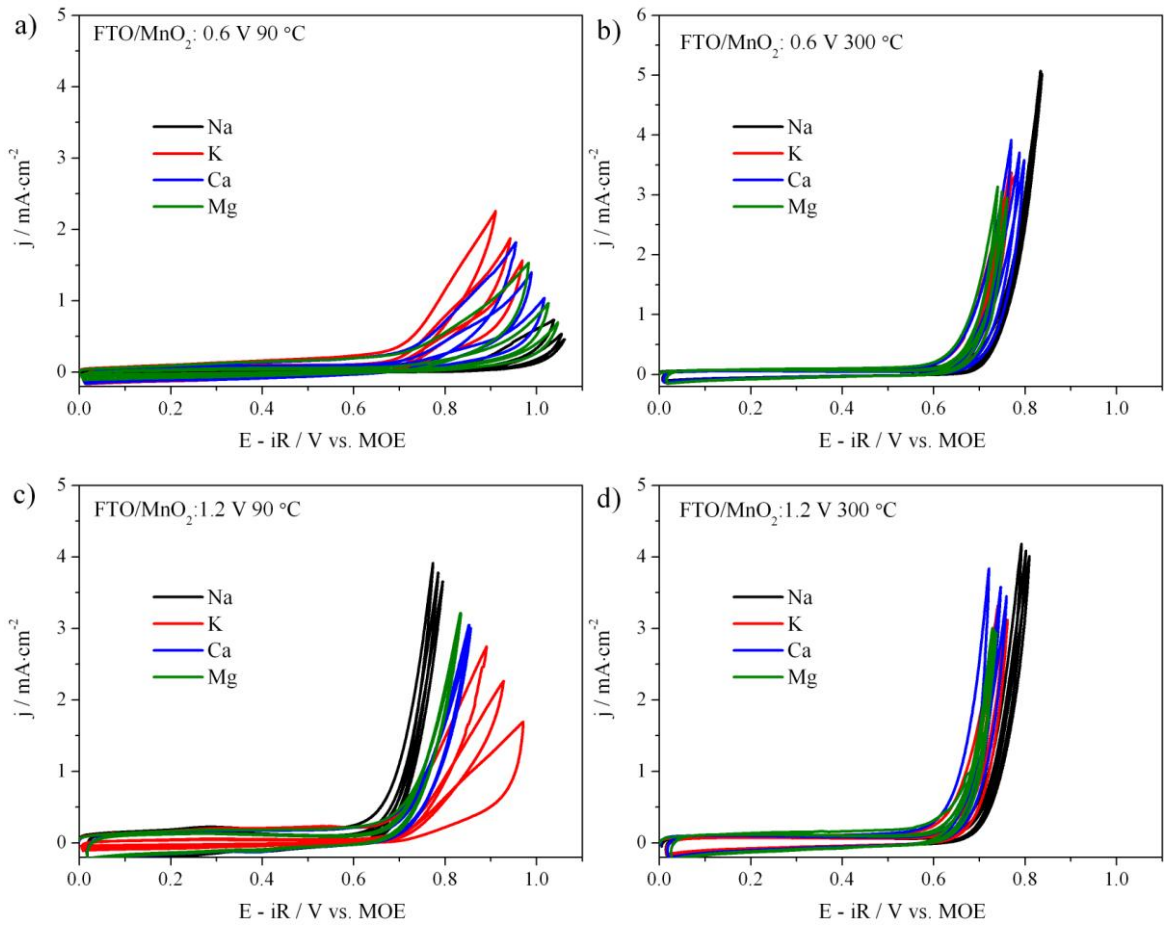

Figure V.3: Cyclic voltammetry curves of MnO_2 films electrodeposited on FTO in Na^+, K^+, Mg^{2+} and Ca^{2+} containing solutions. Samples prepared by chronoamperometry for 10 min. Test solution: NaOH (0.1 M). Scan rate: 10 mV/s.

From the Tafel plots shown on Figure V.4, among the MnO_2 films electrodeposited at 0.6 V vs. MSE (birnessite variety), Na-MnO_2 has the smallest slope value (170 mV/dec) among the samples heated at 90°C, while Mg-MnO_2 has the largest (296 mV/dec), which disagree with the sequence of the corresponding CV curves (see Figure V.3a). This suggests that the kinetics of the OER reaction on these samples may be quite different. This phenomenon is also observed for samples electrodeposited at 1.2 V vs. MSE and heated at 90 °C (see Figure V.4c), where K-MnO_2 has lower activity according to CV curves but its Tafel slope value is slightly smaller than that of the Ca-MnO_2 sample. In this case, the differences between the CV curves could come from the influence of the stability of those

samples. After a 300 °C heating, the Tafel slope values of the birnessite type MnO_2 samples are nearly identical (see Figure V.4b), meaning that the specificities of those films are removed due to the heating effect. This is also suitable for samples electrodeposited at 1.2 V vs. MSE, whose differences observed after heating at 90 °C disappeared after heating at 300 °C. The abnormal value of Mg-MnO_2 sample might be due to the bad linearity of this Tafel plot (possibly as a consequence of O_2 bubble production during the OER test).

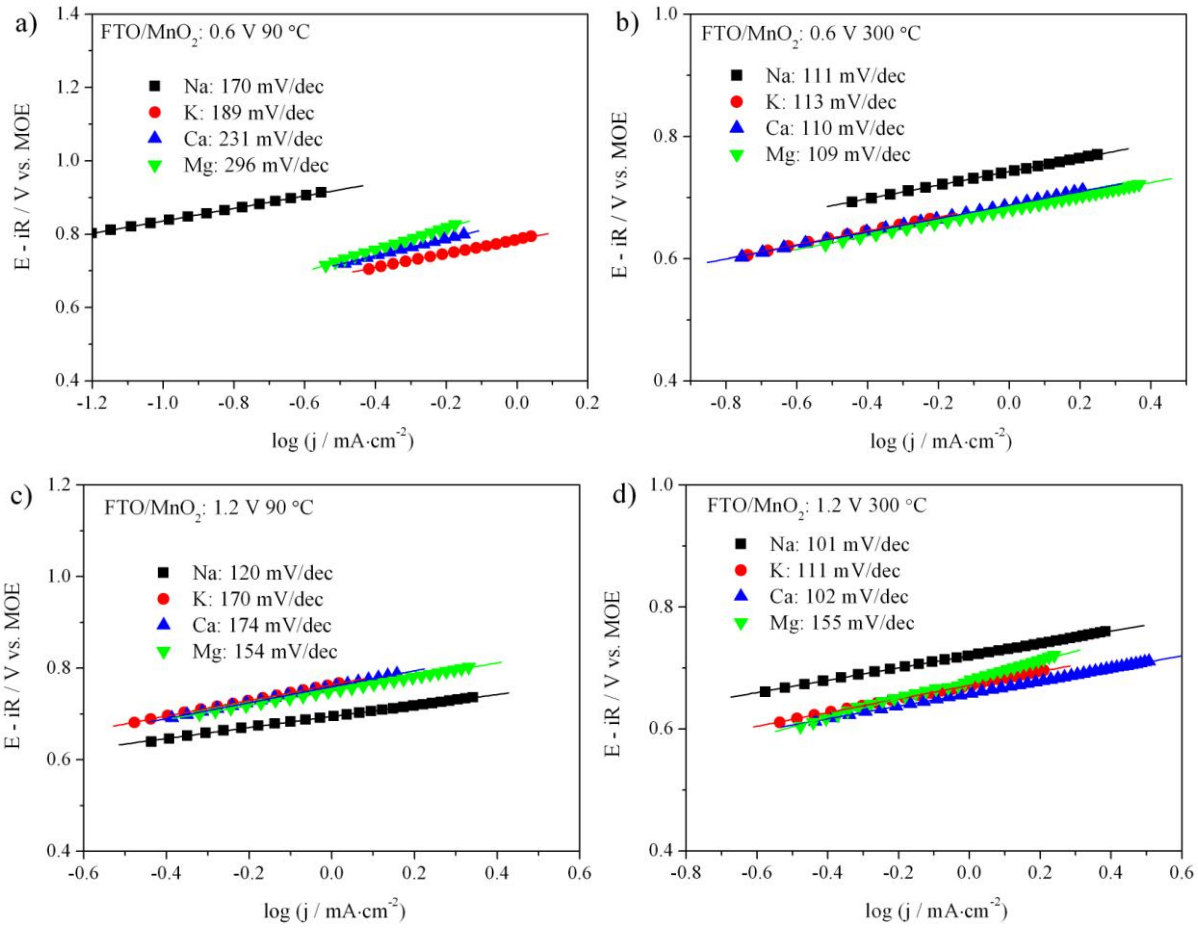

Figure V.4: Tafel plot of MnO_2 films electrodeposited on FTO in Na^+, K^+, Mg^{2+} and Ca^{2+} containing solutions. Samples prepared by chronoamperometry for 10 min. Test solution: NaOH (0.1 M). Scan rate: 10 mV/s.

From these tests, it is supposed that the influence of the cations are more remarkable in the birnessite structure rather than in the amorphous structure. After moderate temperature heating (300°C), this influence becomes almost invisible.

V.4 Structural and morphological analysis of electrodeposited FTO/C-MnO_2 films

To further understand the effect of inserted cations on the electrocatalytic performances of MnO_2 films, the structure and morphology of these samples were characterized. The XRD spectra are shown in Figure V.5. As expected, for all series, only samples electrodeposited at 0.6 V vs. MSE and heated at 90 °C show the characteristic diffraction peaks of birnessite structure. After heating at 300 °C, these peaks disappear, suggesting that the birnessite structure is destroyed. Samples electrodeposited at 1.2 V vs. MSE have no diffraction peak of any MnO_2 species, indicating their amorphous structure. This result is consistent with the observations reported previously. In addition, from the intensity of the birnessite peaks observed on the black curves, the crystallinity of Na-MnO_2 and Ca-MnO_2 are better than that of the other two samples, while Mg-MnO_2 has the lowest birnessite-type crystallinity.

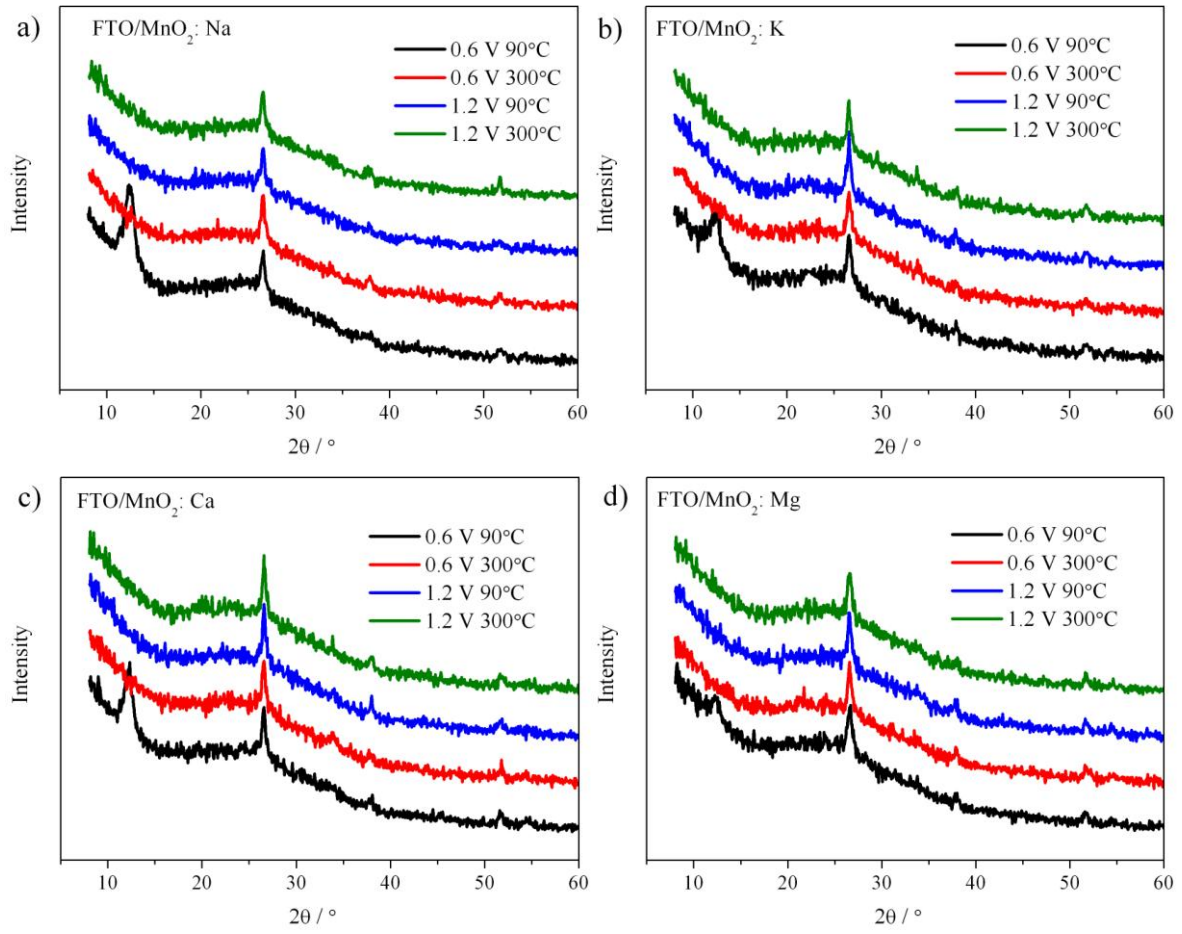

Figure V.5: XRD spectra of MnO_2 films electrodeposited in Na^+, K^+, Mg^{2+} and Ca^{2+} containing solutions. Samples prepared by chronoamperometry for 10 min.

On the other hand, birnessite-type samples are supposed to be unstable as concluded from the results of the OER tests, which is the main reason hindering their catalytic activity.

Apart from the birnessite type MnO_2 samples, the other samples are all amorphous, and their electrocatalytic activities are much higher and close to each other, indicating the great advantage of the amorphous structure.

In addition to the crystallinity, surface morphology is another key factor for the electrocatalytic performances. The SEM topography images are shown in Figures V.6-9, corresponding to Na-MnO_2, K-MnO_2, Ca-MnO_2 and Mg-MnO_2 respectively.

According to the results obtained on Na-MnO_2 films in Chapters III and IV, it has been found that the electrodeposition at 0.6 V vs. MSE will lead to a layered structure whereas the one at 1.2 V vs. MSE will lead to a granular structure, as shown in Figure V.6. This trend is also suitable for K-MnO_2, Ca-MnO_2 and Mg-MnO_2.

For K-MnO_2 samples, electrodeposition at 0.6 V vs. MSE (see Figure V.7a) leads to a typical birnessite morphology that is similar to that obtained in Na^+ containing solution (see Figure V.7a). Heating at 90 or 300 °C does not change much the morphology (see Figure V.7a,b), while for the sample electrodeposited at 1.2 V vs. MSE, the granular structure becomes not as clear after heating at 300 °C, by comparison with that at 90 °C, which should be caused by the melting process (see Figure V.7c,d).

In the case of Ca-MnO_2 series, electrodeposition at 0.6 V vs. MSE (see Figure V.8a) leads to a more porous material than with Na-MnO_2 or K-MnO_2 samples (see Figures V.6a and V.7a). Also, little difference is found after heating at 90 and 300 °C (see Figure V.8a,b). Samples electrodeposited at 1.2 V vs. MSE have the same granular morphology and a little melting is observed for samples heated at 300 °C (see Figure V.8c,d).

When Mg^{2+} is the inserted cation, the bulk of the sample electrodeposited at 0.6 V vs. MSE becomes much more porous (see Figure V.9a), even more than the one shown above for the Ca-MnO_2 sample (see Figure V.8a). The structure resembles more a hollow frame and the bottom FTO grains can be seen on the image (see Figure V.9a). After heating at 300 °C, the hollow structure collapsed and the hollow portions of the initial film are filled and closed (see Figure V.9b). This could be ascribed to the heating effect. For Mg-MnO_2 samples electrodeposited at 1.2 V vs. MSE (see Figure V.9c), the surface morphology is no longer

granular as it is replaced by a small net structure, which is similar to the one of the sample heated at 300 °C (see Figure V.9d).

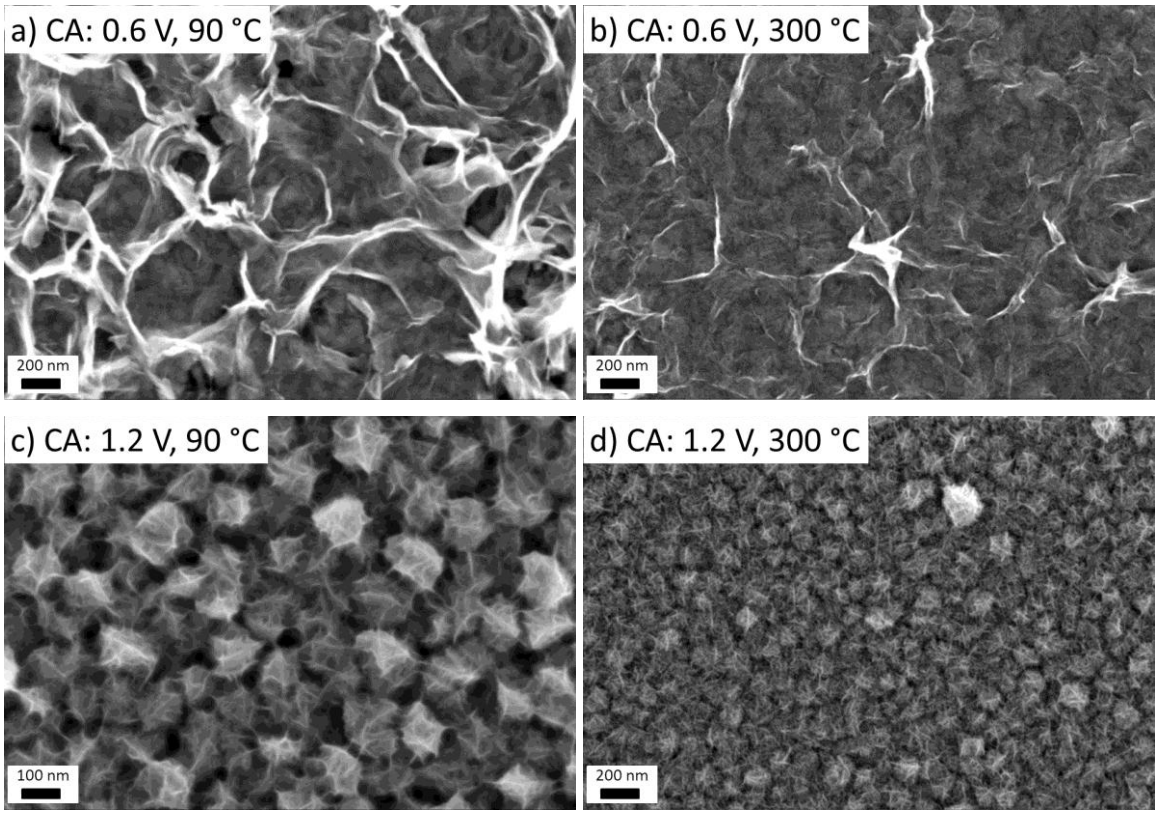

Figure V.6: SEM images of Na-MnO_2 films electrodeposited on FTO at 0.6 and 1.2 V vs. MSE and heated at 90 and 300 °C.

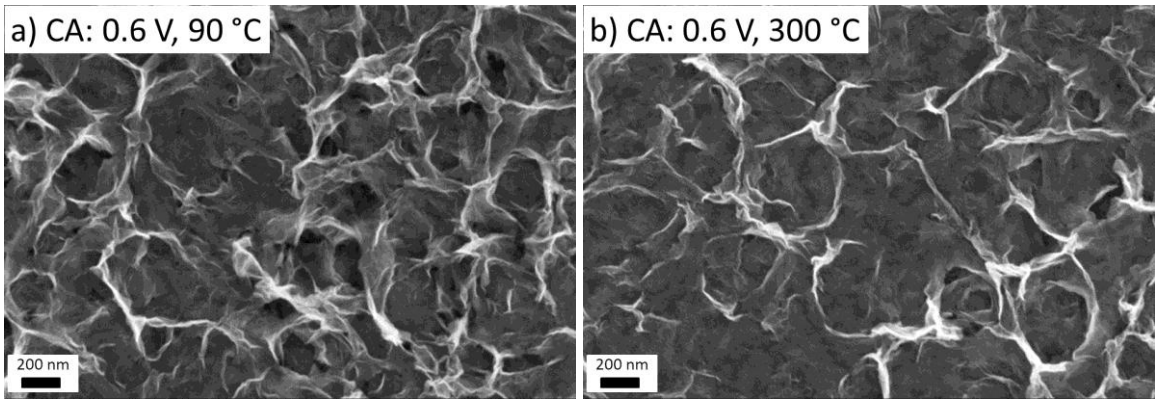

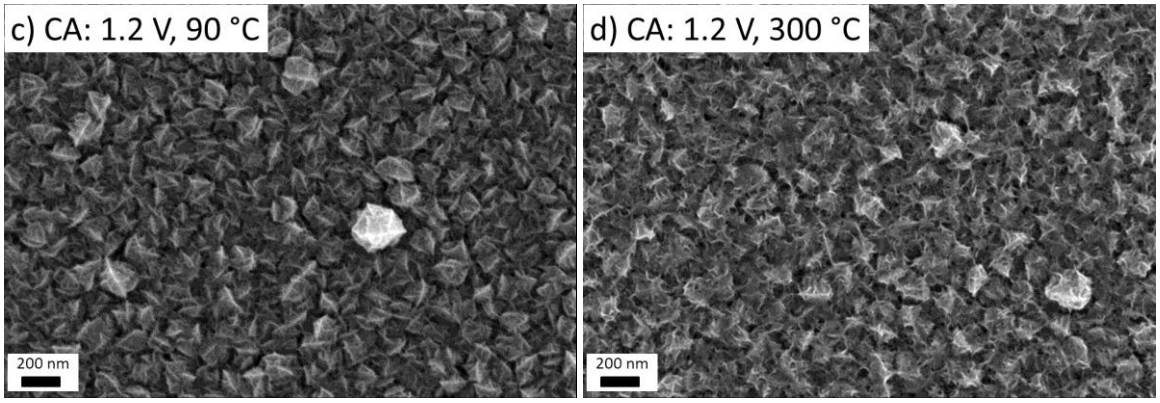

Figure V.7: SEM images of K-MnO_2 films electrodeposited on FTO at 0.6 and 1.2 V vs. MSE and heated at 90 and 300 °C.

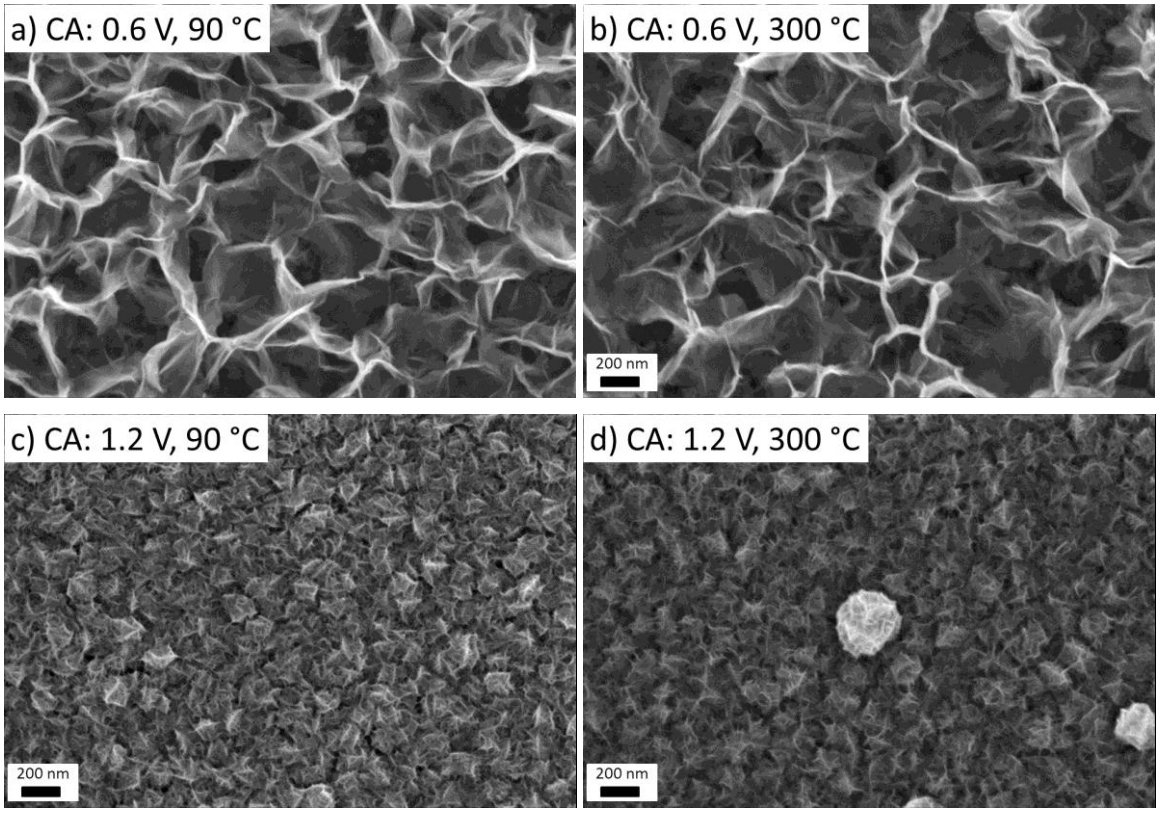

Figure V.8: SEM images of Ca-MnO_2 films electrodeposited on FTO at 0.6 and 1.2 V vs. MSE and heated at 90 and 300 °C.

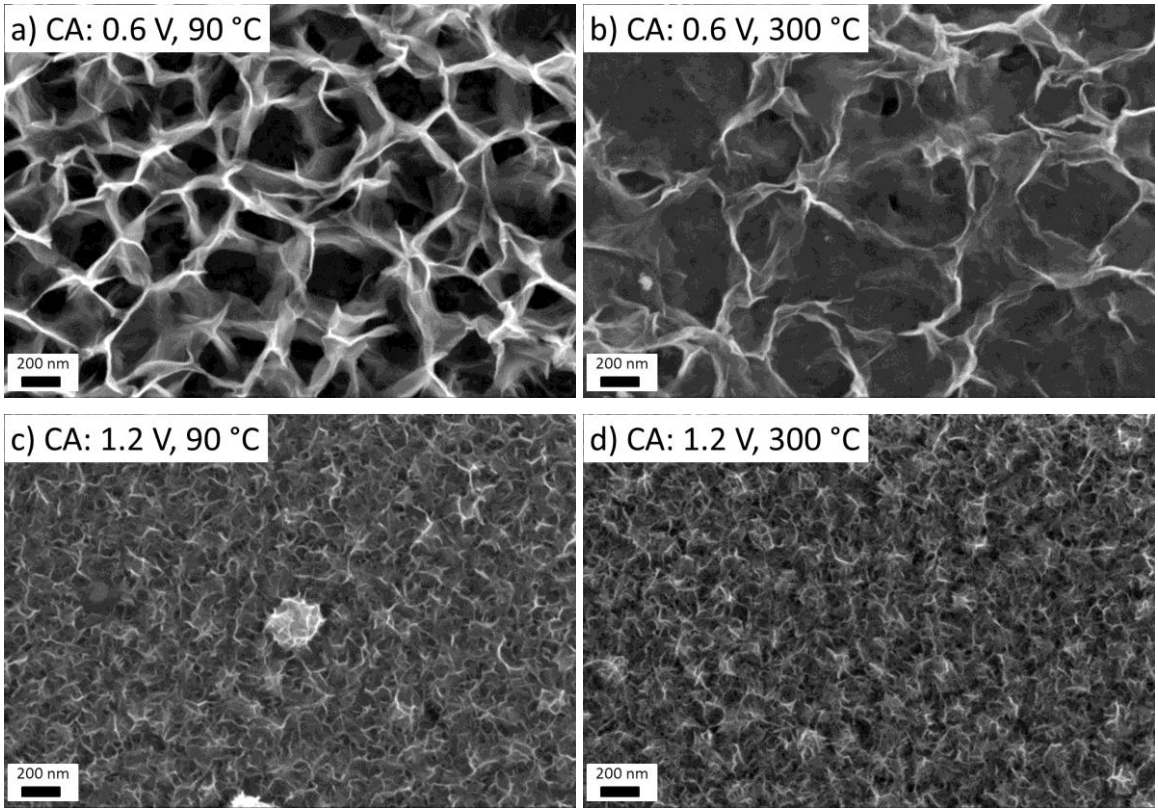

Figure V.9: SEM images of Mg-MnO_2 films electrodeposited on FTO at 0.6 and 1.2 V vs. MSE and heated at 90 and 300 °C.

Considering the birnessite-type samples (electrodeposited at 0.6 V vs. MSE and heated at 90°C), Na-MnO_2 and K-MnO_2 films have tighter and more porous morphologies than Ca-MnO_2 and Mg-MnO_2 films, indicating the influence of cation valence state (+1 or +2) on the morphology of the MnO_2 films. Theoretically, a porous structure has a higher specific area than a tight one, which could provide more active sites and promote the reaction. This could be a reason why Ca-MnO_2 and Mg-MnO_2 films have better electrocatalytic performances towards OER than Na-MnO_2 films. While the high activity of K-MnO_2 films is not clear, it might be related to its electrical properties. On the contrary, after heating at 300 °C, all samples electrodeposited at the same potential have similar morphologies and their electrocatalytic activities are close. For samples electrodeposited at 1.2 V vs. MSE, the morphology of Mg-MnO_2 sample has a little difference with that of the others, but no obvious difference is observed on the OER activity and this difference becomes smaller after heating at 300 °C.

V.5 Element analysis of electrodeposited FTO/C-MnO_2 films

From the topography images obtained by SEM, cations added in the electrodeposition solution have a clear influence on the morphology of electrodeposited birnessite-type MnO_2 films, while their influence on the amorphous structure is not so clear. Then, what is their influence on the chemical composition of the MnO_2 films and, before that, are these cations inserted into the film structure? In order to evaluate the composition of those electrodeposited MnO_2 films, EDS spectra were carried out. The EDS spectra of glass/ITO and glass/FTO substrates are shown in Figure V.10. From these spectra, In and Sn were detected in ITO substrate while only Sn was found in FTO. No signal was detected for the F element. However, both substrates contain some Na, Mg and Ca signals and a quite intense Si signal. These signals should be ascribed to the bottom glass support. Moreover, the signal position of Ca is overlapped with that of Sn. The existence of these signals will hinder the elemental analysis of the inserted cations, thus these two substrates are not adapted for the EDS analysis.

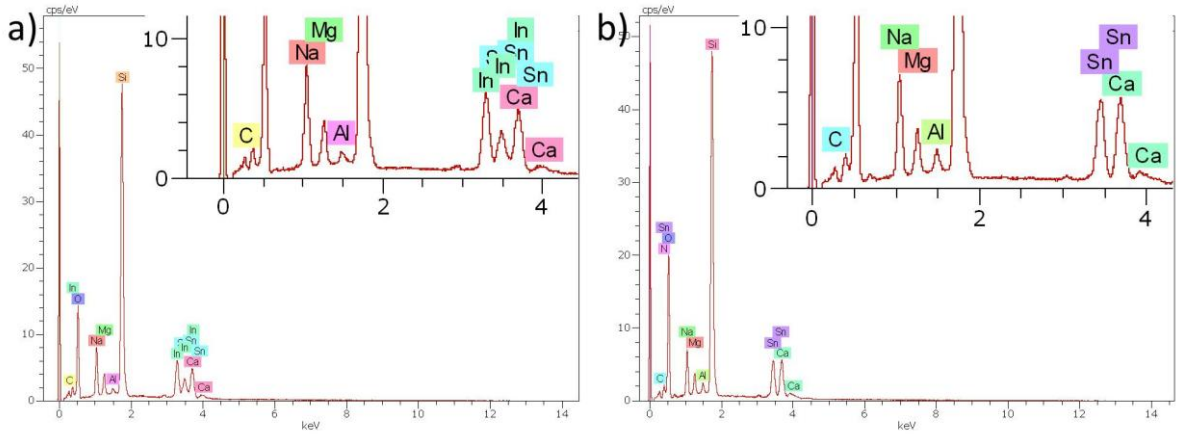

Figure V.10: EDS spectra of a) ITO and b) FTO substrates

In chapter III, MnO_2 films were electrodeposited on Pt, ITO and FTO electrodes and the results show that the morphology and crystalline variety are the same for similar electrodeposition parameters. Thus, a Pt electrode without any other impurities could be a good substrate for EDS analysis. In this sense, electrodes based on pure silicon substrates coated with a thin layer of Pt were fabricated successfully in our lab and used for the electrodeposition of MnO_2 films (for the fabrication method, see section II.3.1). Figure V.11 shows the EDS spectrum of such homemade Si/Pt substrates. On this spectrum, only Si and Pt signals were detected, which makes it an ideal substrate for EDS analysis.

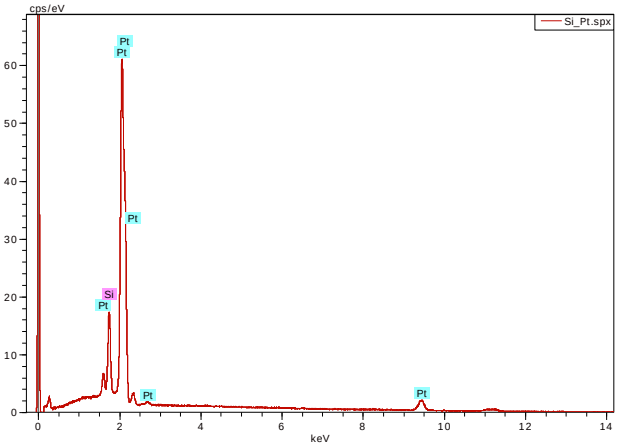

Figure V.11: EDS spectrum of a homemade Si/Pt substrate

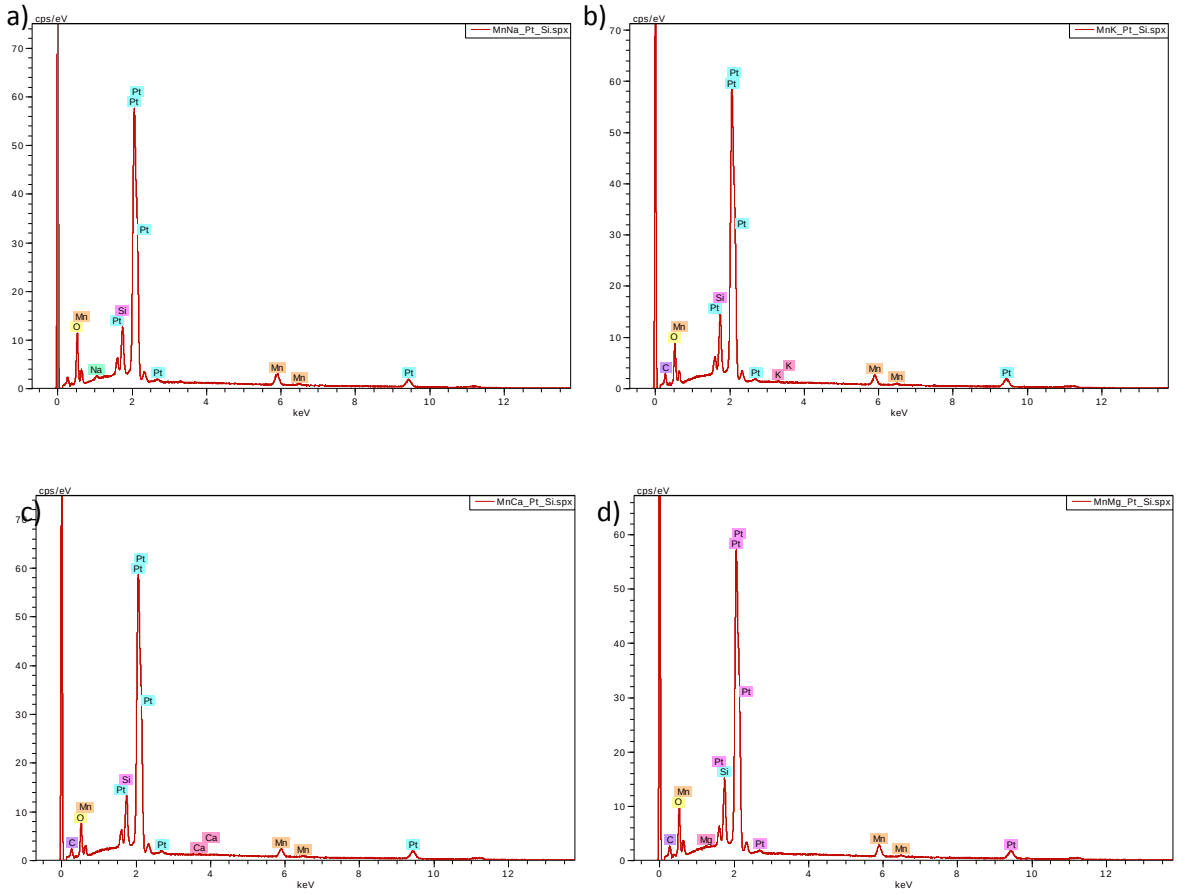

Figure V.12: EDS spectra of MnO_2 films electrodeposited at 0.6 V vs. MSE for 10 min on a Si/Pt substrate in the presence of a) Na^+, b) K^+, c) Ca^{2+} and d) Mg^{2+} cations and heated at 90°C for 30 min.

The MnO_2 films were electrodeposited on Si/Pt substrate using 0.6 V vs. MSE for 10 min in order to obtain the birnessite-type variety. Electrodeposition using 1.2 V vs. MSE failed because of the intense water oxidation reaction on the Pt surface. The obtained films

were heated at 90 °C for 30 min to remove water, and then analyzed by EDS. The resulting EDS spectra are shown in Figure V.12. Apart from the Si and Pt peaks, Mn element was detected in all samples. However, only Na element was clearly detected in the EDS spectra of Na-MnO_2 sample, while the detected amounts of inserted K^+, Ca^{2+} and Mg^{2+} cations were under the limit of detection of the instrument, suggesting that the amounts of inserted cations are very small. In other words, these three cations are hardly included in the structure and the birnessite structure can only contain protons and water molecules.

The results reported above were obtained on samples electrodeposited with a 10 min duration, which suggests that the estimated thickness of these films is about 100-150 nm. As the bottom Pt/Si substrates can still be detected, these films might be too thin. As a consequence, another series of MnO_2 films were prepared by 30 min electrodeposition at 0.6 V vs. MSE and they experienced the same post-treatment procedure. Figure V.13 shows the XRD spectra of these thick films. Clearly, all samples have the birnessite type crystalline variety. However, the Ca-MnO_2 film has the most intense peak, which means that its crystallinity is the best, while that for Mg-MnO_2 film is the weakest. Na-MnO_2 and K-MnO_2 films have similar spectra. This agrees with the results obtained on FTO substrate (see Figure V.5). In this case, all of these films possess the layered birnessite structure and are able to accommodate cations.

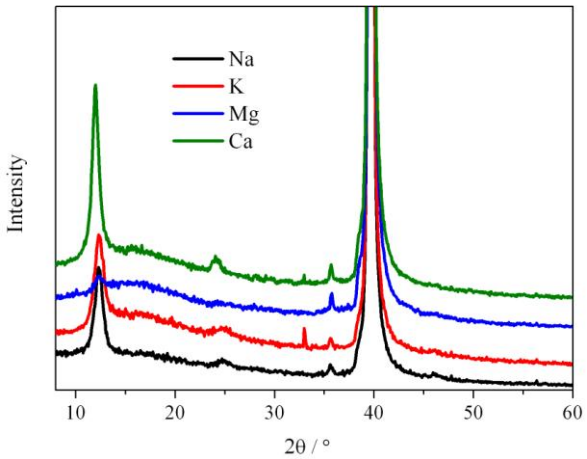

Figure V.13: XRD spectra of MnO_2 films electrodeposited at 0.6 V vs. MSE for 30 min on a Si/Pt substrate in the presence of Na^+, K^+, Ca^{2+} or Mg^{2+} cations, and heated at 90°C for 30 min.

The EDS spectra of these films are shown in Figure V.14. After comparison with the spectra obtained from 10 min electrodeposited samples, the peak intensity of Mn element is

much stronger in contrast with the Pt signal. In addition, all cations were detected in the corresponding samples, indicating that the cations were successfully inserted in the films and could contribute to the formation of birnessite-type crystallinity.

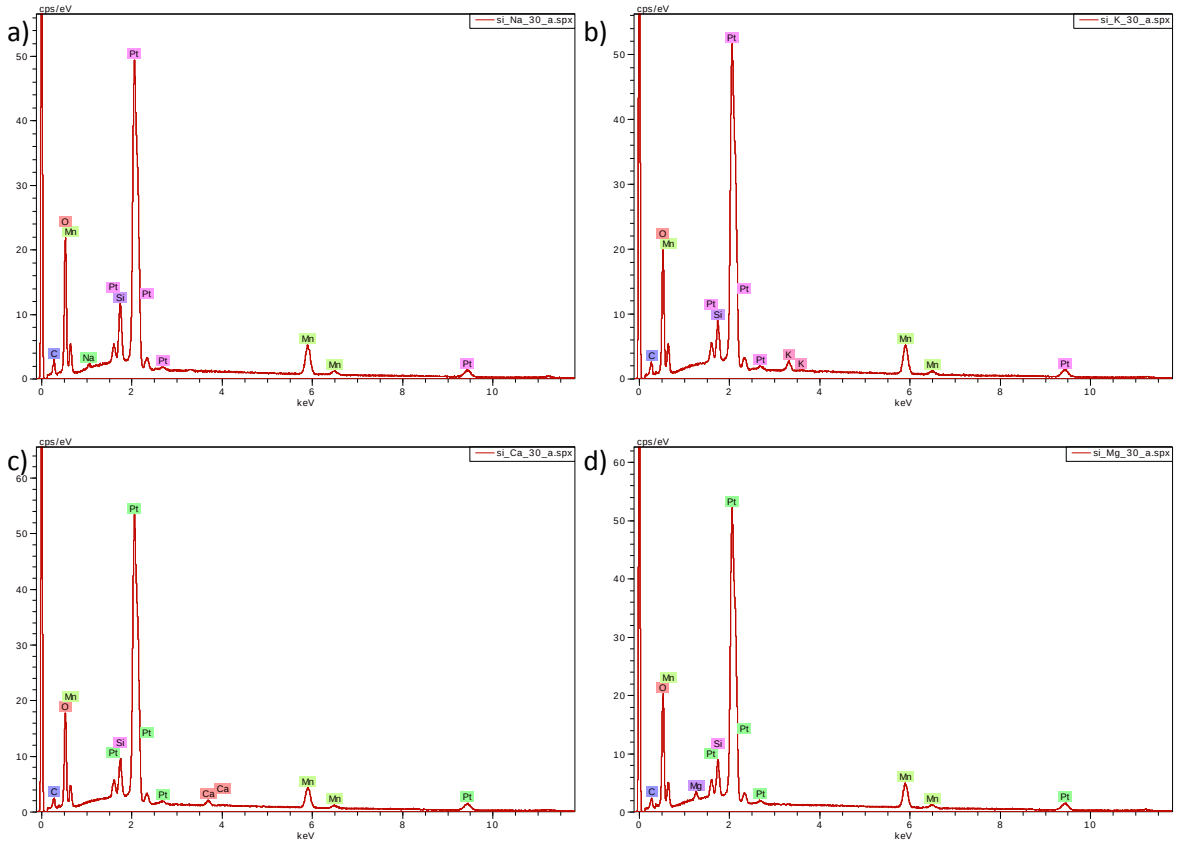

Figure V.14: EDS spectra of MnO_2 films electrodeposited at 0.6 V vs. MSE for 30 min on Si/Pt substrate with the presence a) Na^+, b) K^+, c) Ca^{2+} and d) Mg^{2+} cations, and heated at 90°C for 30 min.

The ratio of each element was calculated by the peak intensity using only the peaks of Mn, O and inserted cation. The results are shown in Table 5.1. From the atomic content of cations, K^+ has the highest percentage, followed by Mg^{2+} and Ca^{2+}, while Na^+ has the lowest content. The ratio of cations and Mn atom was also calculated. The value for all samples ranges from 8.67 % to 12.83 %, which is lower than the expected value for typical birnessite composition. It should be mentioned that for Ca^{2+} and Mg^{2+}, the common valence state is +2, while that for Na^+ and K^+ is +1. As a consequence, the existence of one Ca or Mg cation could provide 2 positive charges while Na or K only provide one but this trend is not observed in the EDS analysis.

Table V.1: Element content of MnO_2 films deposited with different cations

Element	Na-MnO_2		K-MnO_2		Ca-MnO_2		Mg-MnO_2	
	Norm.C [wt.%]	Atom.C [at.%]	Norm.C [wt.%]	Atom.C [at.%]	Norm.C [wt.%]	Atom.C [at.%]	Norm.C [wt.%]	Atom.C [at.%]
Mn	57.79	28.82	54.09	26.81	53.25	25.88	56.60	27.98
O	40.11	68.68	40.97	69.75	42.88	71.55	40.55	68.84
Na	2.10	2.5						
K			4.94	3.44				
Ca					3.86	2.57		
Mg							2.84	3.18
Cat./Mn	3.63	8.67	9.13	12.83	7.25	9.93	5.02	11.36
Ave. Mn state	+4.68		+5.07		+5.33		+4.69	

Generally, the valence state of O atom is -2, thus the average oxidation state of Mn could be calculated by following formula:

$$V(Mn) = \frac{n(O) \times V(O) - n(cation) \times V(cation)}{n(Mn)} \quad \text{(V.1)}$$

where n means the number of atoms, V means the oxidation state. The absolute values are 2 for O, 1 for Na and K, 2 for Ca and Mg. The calculated result is shown in Table V.1. For all samples, the average oxidation state of Mn is higher than the common value +4. Considering that O atoms come not only from MnO_2 but also from water molecules, while H atom cannot be detected by EDS, thus the contribution of water molecules cannot be eliminated.

As mentioned above, except for Na, the other cations cannot be detected in samples electrodeposited by 10 min, but in 30 min electrodeposited ones, all cations are detected. The elemental content of Na-MnO_2 samples electrodeposited for different duration was studied, as shown in Table V.2. The Na to Mn atom ratio of samples electrodeposited for 10 min and 20 min are similar, with values close to 20 %, suggesting large amount of Na ions are inserted into the structure. However, this ratio for 30 min electrodeposited sample decreases to 8.67 %, indicating a low cation concentration in the structure. On the other hand, if we estimate the

average oxidation state of Mn by using formula V.1, the values increase with electrodeposition time. It is clear that this change is mainly caused by the increase of O atom ratio and the corresponding decrease of Mn atom ratio. This is hardly ascribed to the oxidation valence state change of Mn atoms. As mentioned above, the existence of water molecule cannot be detected by EDS, thus abnormal amount of O atom could be caused by the water molecules contained in the structure. As the electrodeposition time increases, films becomes thicker and thicker, thus more interlayer spaces and empty spaces are generated, which could accommodate more water molecules into the structure, leading to the high O atom ratio. On the other hand, thick films may also hinder the removal of water molecules during heat treatment, thus more water molecules will remain in the structure, leading to the high ratio of O atoms.

Table V.2: Element content of MnO_2 films electrodeposited with the presence of Na^+ using different electrodeposition durations

Element	10 min		20 min		30 min	
	Norm.C [wt.%]	Atom.C [at.%]	Norm.C [wt.%]	Atom.C [at.%]	Norm.C [wt.%]	Atom.C [at.%]
Mn	60.81	32.01	57.70	29.21	57.79	28.82
O	33.99	61.45	37.10	64.50	40.11	68.68
Na	5.2	6.54	5.20	6.29	2.10	2.50
Cat./Mn	8.55	20.43	9.01	21.53	3.63	8.67
Ave. Mn state	3.635		4.2		4.68	

V.6 Discussion

Based on the results reported above, an electrodeposition step for 10 min can hardly allow insertion of cations into the film structure except for Na^+. Considering that the OER test in chapter V.2 was carried out on samples electrodeposited for 10 min on FTO substrate, the influence of cation insertion would be limited. On the contrary, although no K, Ca or Mg element signals were detected, the films still possess the birnessite structure. In this case, the inserted cations should be protons rather than the targeted ones. Even in Na^+

containing films, existence of H^+ is very likely, but because of the lack of detection techniques, this hypothesis cannot be confirmed.

On the other hand, all cations were detected on samples electrodeposited for 30 min, which are all very thick films. Again, birnessite structure was confirmed by the XRD spectra. Considering the results obtained from samples electrodeposited for 10 min, it is hard to say what the influence of those cations on the structure is. They may act as inserted cations to balance the total charge of the film and play a role in the structure, or they may just stay in the inter-laminar space independently.

Moreover, these cations indeed have an influence on the birnessite crystallinity of the electrodeposited MnO_2 films, while their influence on the amorphous structure is limited. From the OER tests, the electrocatalytic activities of those birnessite-type MnO_2 films are substantially different. However, after heating at 300 °C, all films show activities identical with those of amorphous structures as well as similar topographies. Based on this, it is highly possible that it is the inserted water molecules rather than cations that contribute mostly to the birnessite structure and the heating procedure removes them thus leading to identical structures and morphologies.

As a conclusion, the presence of cations in the electrodeposition solution will affect the amount of inserted water molecules, and thus change the crystallinity of the electrodeposited MnO_2 films. Heating at 300 °C could remove the water molecules inside the film structure, and thus make the film structures and morphologies identical, which leads to a similar electrocatalytic activity for these MnO_2 films.

Conclusions

From the results reported in this manuscript, the following conclusions can be underlined:

The electrochemical oxidation mechanism of Mn^{2+} cations leading to the electrodeposition of MnO_2 films is a multistep reaction. The chemical composition of the electrodeposition solution greatly affects the electrodeposition process of MnO_2 films. Their growth is faster in a neutral aqueous electrolytic Na_2SO_4 solution than in an acidic H_2SO_4 solution. Using less concentrated $MnSO_4$ aqueous solutions favors the formation of mechanically stable (i.e. strongly adherent) and homogeneous MnO_2 films possessing a birnessite-type crystallinity.

The electrode material also has a great influence on the electrocatalytic activity of the electrodeposited MnO_2 films towards OER, while its influence on the crystallinity and morphology of electrodeposited MnO_2 films is limited. By comparison with an ITO electrode, a FTO electrode is a much better electrode material, which could dramatically promote the electrocatalytic activity of the electrodeposited MnO_2 films for oxygen evolution reaction. This is ascribed partly to the initial higher electrochemical activity of the FTO material itself and to the better adherence of the MnO_2 films. Homemade a-CNx thin layer electrodes were used successfully as substrates for the electrodeposition of MnO_2 films but the electrocatalytic activity of the electrodeposited films towards OER requires further optimization efforts.

The electrodeposition potential used during chronoamperometry experiments is a key parameter for the properties of the electrodeposited MnO_2 films, as a consequence of the different nucleation and growth mechanisms of MnO_2 thin films. For a low electrodeposition potential, layered MnO_2 structure is formed and it finally leads to the birnessite type crystalline variety. At a high electrodeposition potential region, the electrode material acts as a template and the growing MnO_2 structures tend to form a core-shell structure on each substrate grain, which leads to a film made of separated MnO_2 columns. This latter film is expected to be more mechanically stable, which is beneficial for the electrocatalytic activity of the MnO_2 films towards OER.

A heat treatment has a huge promotion effect on the electrocatalytic activity of birnessite-type MnO_2 films, and it is also effective for the amorphous MnO_2 films. A phase transition happens from 500 °C. Below this temperature, no obvious morphology change can be observed while above this temperature, the morphology changes dramatically but still depends on the initial structure. Heating at 500 °C has the best promotion effect on the electrocatalytic activity of MnO_2 films towards OER. Also, it was found that heat treatment can enhance the mechanical and electrochemical stability of MnO_2 films. This promotion effect can be due to a dehydration process occurring during the heat procedure, which removes the water molecules from the structure and modify the oxidation state of Mn atoms in the film, making reactive sites more electrocatalytically active and maybe also more numerous. Further investigations are required to confirm the mechanism of the heating process.

The influence of cation insertion in MnO_2 films during the electrodeposition process is real but limited in our experimental conditions. For birnessite-type MnO_2 films, inserted cations are able to affect the film crystallinity, possibly by changing the dispersion of water molecules in the structure. After heat treatment, the structural differences disappear, and the electrocatalytical activities of the MnO_2 films are similar, whatever the cations inserted during the electrodeposition phase were.

Finally, birnessite type and amorphous MnO_2 films appear to be promising candidates as catalysts for photoelectrochemical water splitting as they are able to generate considerable photocurrents under solar light illumination. In this purpose, thick and amorphous films with proper heat treatment are supposed to produce the best performances.

References

1. Ferreira Kristina N., Iverson Tina M., Maghlaoui Karim, Barber James, and Iwata So, *Architecture of the Photosynthetic Oxygen-Evolving Center.* Science, 2004. 303(5665): p. 1831.
2. Lewis Nathan S. and Nocera Daniel G., *Powering the planet: Chemical challenges in solar energy utilization.* Proceedings of the National Academy of Sciences, 2006. 103(43): p. 15729-15735.
3. Shafiee Shahriar and Topal Erkan, *When will fossil fuel reserves be diminished?* Energy Policy, 2009. 37(1): p. 181-189.
4. Nakicenovic Nebojsa and (Eds) Rob Swart, *Special Report on Emissions Scenarios.* 2000: p. 7.
5. Joskow Paul L. and Parsons John E., *The economic future of nuclear power.* Daedalus, 2009. 138(4): p. 45-59.
6. Ansolabehere S., Deutch J., Driscoll M., Gray P. E., Holdren J. P., Joskow P. L., Lester R. K., Moniz E. J., and Todreas, *The Future of Nuclear Power: An Interdisciplinary MIT Study*.
7. Europe SolarPower, *Global market outlook for solar power 2015–2019.* Euoropean Photovoltaic Industry Association, Bruxelles, Tech. Rep, 2015.
8. Barber James, *Photosynthetic energy conversion: natural and artificial.* Chemical Society Reviews, 2009. 38(1): p. 185-196.
9. Nocera Daniel G., *The Artificial Leaf.* Accounts of Chemical Research, 2012. 45(5): p. 767-776.
10. Umena Y., Kawakami K., Shen J. R., and Kamiya N., *Crystal structure of oxygen-evolving photosystem II at a resolution of 1.9 A.* Nature, 2011. 473(7345): p. 55-60.
11. McEvoy James P. and Brudvig Gary W., *Structure-based mechanism of photosynthetic water oxidation.* Physical Chemistry Chemical Physics, 2004. 6(20): p. 4754.
12. Siegbahn and E.M. Per, *Theoretical studies of O− O bond formation in photosystem II.* Inorganic chemistry, 2008. 47(6): p. 1779-1786.
13. Styring Stenbjörn, *Artificial photosynthesis for solar fuels.* Faraday Discuss., 2012. 155: p. 357-376.
14. Gust Devens, Moore Thomas A., and Moore Ana L., *Realizing artificial photosynthesis.* Faraday Discuss., 2012. 155: p. 9-26.
15. Maeda Kazuhiko and Domen Kazunari, *Photocatalytic Water Splitting: Recent Progress and Future Challenges.* The Journal of Physical Chemistry Letters, 2010. 1(18): p. 2655-2661.
16. Molecular Materials Research Center Backman Institute. *Solar Photoconversion*. Available from: http://mmrc.caltech.edu/BB/photoconversion.html
17. Chen D., Chen C., Baiyee Z. M., Shao Z., and Ciucci F., *Nonstoichiometric Oxides as Low-Cost and Highly-Efficient Oxygen Reduction/Evolution Catalysts for Low-Temperature Electrochemical Devices.* Chem Rev, 2015. 115(18): p. 9869-921.
18. Abbas Muhammad A. and Bang Jin Ho, *Rising Again: Opportunities and Challenges for Platinum-Free Electrocatalysts.* Chemistry of Materials, 2015. 27(21): p. 7218-7235.
19. Andreiadis E. S., Chavarot-Kerlidou M., Fontecave M., and Artero V., *Artificial photosynthesis: from molecular catalysts for light-driven water splitting to photoelectrochemical cells.* Photochem Photobiol, 2011. 87(5): p. 946-64.
20. Blakemore J. D., Crabtree R. H., and Brudvig G. W., *Molecular Catalysts for Water Oxidation.* Chem Rev, 2015. 115(23): p. 12974-3005.
21. Karkas M. D., Verho O., Johnston E. V., and Akermark B., *Artificial photosynthesis: molecular systems for catalytic water oxidation.* Chem Rev, 2014. 114(24): p. 11863-2001.
22. Bofill R., Garcia-Anton J., Escriche L., and Sala X., *Chemical, electrochemical and photochemical molecular water oxidation catalysts.* J Photochem Photobiol B, 2015. 152(Pt A): p. 71-81.

23. McCrory C. C., Jung S., Peters J. C., and Jaramillo T. F., *Benchmarking heterogeneous electrocatalysts for the oxygen evolution reaction.* J Am Chem Soc, 2013. 135(45): p. 16977-87.
24. Gorlin Yelena and Jaramillo Thomas F., *A Bifunctional Nonprecious Metal Catalyst for Oxygen Reduction and Water Oxidation* Journal of the American Chemical Society, 2010. 132: p. 3.
25. Mamaca N., Mayousse E., Arrii-Clacens S., Napporn T. W., Servat K., Guillet N., and Kokoh K. B., *Electrochemical activity of ruthenium and iridium based catalysts for oxygen evolution reaction.* Applied Catalysis B: Environmental, 2012. 111-112: p. 376-380.
26. Reier Tobias, Oezaslan Mehtap, and Strasser Peter, *Electrocatalytic Oxygen Evolution Reaction (OER) on Ru, Ir, and Pt Catalysts: A Comparative Study of Nanoparticles and Bulk Materials.* ACS Catalysis, 2012. 2(8): p. 1765-1772.
27. Osterloh F. E., *Inorganic nanostructures for photoelectrochemical and photocatalytic water splitting.* Chem Soc Rev, 2013. 42(6): p. 2294-320.
28. Wang J., Cui W., Liu Q., Xing Z., Asiri A. M., and Sun X., *Recent Progress in Cobalt-Based Heterogeneous Catalysts for Electrochemical Water Splitting.* Adv Mater, 2016. 28(2): p. 215-30.
29. Doyle R. L., Godwin I. J., Brandon M. P., and Lyons M. E., *Redox and electrochemical water splitting catalytic properties of hydrated metal oxide modified electrodes.* Phys Chem Chem Phys, 2013. 15(33): p. 13737-83.
30. Galán-Mascarós José Ramón, *Water Oxidation at Electrodes Modified with Earth-Abundant Transition-Metal Catalysts.* ChemElectroChem, 2015. 2(1): p. 37-50.
31. Singh Archana and Spiccia Leone, *Water oxidation catalysts based on abundant 1st row transition metals.* Coordination Chemistry Reviews, 2013. 257(17-18): p. 2607-2622.
32. Sartorel Andrea, Carraro Mauro, Toma Francesca Maria, Prato Maurizio, and Bonchio Marcella, *Shaping the beating heart of artificial photosynthesis: oxygenic metal oxide nano-clusters.* Energy & Environmental Science, 2012. 5(2): p. 5592-5603.
33. Burke Michaela S., Enman Lisa J., Batchellor Adam S., Zou Shihui, and Boettcher Shannon W., *Oxygen Evolution Reaction Electrocatalysis on Transition Metal Oxides and (Oxy)hydroxides: Activity Trends and Design Principles.* Chemistry of Materials, 2015. 27(22): p. 7549-7558.
34. Burke M. S., Zou S., Enman L. J., Kellon J. E., Gabor C. A., Pledger E., and Boettcher S. W., *Revised Oxygen Evolution Reaction Activity Trends for First-Row Transition-Metal (Oxy)hydroxides in Alkaline Media.* J Phys Chem Lett, 2015. 6(18): p. 3737-42.
35. Lu Z., Qian L., Tian Y., Li Y., Sun X., and Duan X., *Ternary NiFeMn layered double hydroxides as highly-efficient oxygen evolution catalysts.* Chem Commun (Camb), 2016. 52(5): p. 908-11.
36. Long X., Xiao S., Wang Z., Zheng X., and Yang S., *Co intake mediated formation of ultrathin nanosheets of transition metal LDH-an advanced electrocatalyst for oxygen evolution reaction.* Chem Commun (Camb), 2015. 51(6): p. 1120-3.
37. Gupta S., Kellogg W., Xu H., Liu X., Cho J., and Wu G., *Bifunctional Perovskite Oxide Catalysts for Oxygen Reduction and Evolution in Alkaline Media.* Chem Asian J, 2016. 11(1): p. 10-21.
38. Wang F., Shifa T. A., Zhan X., Huang Y., Liu K., Cheng Z., Jiang C., and He J., *Recent advances in transition-metal dichalcogenide based nanomaterials for water splitting.* Nanoscale, 2015. 7(47): p. 19764-88.
39. Zhan Yi, Lu Meihua, Yang Shiliu, Xu Chaohe, Liu Zhaolin, and Lee Jim Yang, *Activity of Transition-Metal (Manganese, Iron, Cobalt, and Nickel) Phosphates for Oxygen Electrocatalysis in Alkaline Solution.* ChemCatChem, 2016. 8(2): p. 372-379.
40. Lu X., Yim W. L., Suryanto B. H., and Zhao C., *Electrocatalytic oxygen evolution at surface-oxidized multiwall carbon nanotubes.* J Am Chem Soc, 2015. 137(8): p. 2901-7.
41. Cheng Yi, Xu Changwei, Jia Lichao, Gale Julian D., Zhang Lili, Liu Chang, Shen Pei Kang, and Jiang San Ping, *Pristine carbon nanotubes as non-metal electrocatalysts for oxygen*

evolution reaction of water splitting. Applied Catalysis B: Environmental, 2015. 163: p. 96-104.
42. Messaoudi Bouzid, Joiret Suzanne, Keddam Michel, and Takenouti Hisasi, *Anodic behaviour of manganese in alkaline medium* Electrochimica Acta, 2001. 46: p. 12.
43. Post Jeffrey E, *Manganese oxide minerals: Crystal structures and economic and environmental significance.* Proceedings of the National Academy of Sciences, 1999. 96(7): p. 3447-3454.
44. Song Xiuli, Yang Tailai, Du Haiyan, Dong Wenyan, and Liang Zhenhai, *New binary Mn and Cr mixed oxide electrocatalysts for the oxygen evolution reaction.* Journal of Electroanalytical Chemistry, 2016. 760: p. 59-63.
45. Devaraj S and Munichandraiah N, *Effect of crystallographic structure of MnO2 on its electrochemical capacitance properties.* The Journal of Physical Chemistry C, 2008. 112(11): p. 4406-4417.
46. Boppana V. B. and Jiao F., *Nanostructured MnO2: an efficient and robust water oxidation catalyst.* Chem Commun (Camb), 2011. 47(31): p. 8973-5.
47. Robinson D. M., Go Y. B., Mui M., Gardner G., Zhang Z., Mastrogiovanni D., Garfunkel E., Li J., Greenblatt M., and Dismukes G. C., *Photochemical water oxidation by crystalline polymorphs of manganese oxides: structural requirements for catalysis.* J Am Chem Soc, 2013. 135(9): p. 3494-501.
48. Frey Carolin E. and Kurz Philipp, *Water Oxidation Catalysis by Synthetic Manganese Oxides with Different Structural Motifs: A Comparative Study.* Chemistry - A European Journal, 2015. 21(42): p. 14958-14968.
49. Ramírez Alejandra, Hillebrand Philipp, Stellmach Diana, May Matthias M., Bogdanoff Peter, and Fiechter Sebastian, *Evaluation of MnOx, Mn2O3, and Mn3O4Electrodeposited Films for the Oxygen Evolution Reaction of Water.* The Journal of Physical Chemistry C, 2014. 118(26): p. 14073-14081.
50. Pokhrel R., Goetz M. K., Shaner S. E., Wu X., and Stahl S. S., *The "Best Catalyst" for Water Oxidation Depends on the Oxidation Method Employed: A Case Study of Manganese Oxides.* J Am Chem Soc, 2015. 137(26): p. 8384-7.
51. Chen Shuang, Zhai Teng, Lu Xi-Hong, Zhang Man-Zhi, Li Zhuo-Ying, Xu Chang-Wei, and Tong Yexiang, *Large-area manganese oxide nanorod arrays as efficient electrocatalyst for oxygen evolution reaction.* International Journal of Hydrogen Energy, 2012. 37(18): p. 13350-13354.
52. Fekete Monika, Hocking Rosalie K., Chang Shery L. Y., Italiano Cristina, Patti Antonio F., Arena Francesco, and Spiccia Leone, *Highly active screen-printed electrocatalysts for water oxidation based on β-manganese oxide.* Energy & Environmental Science, 2013. 6(7): p. 2222.
53. Indra A., Menezes P. W., Zaharieva I., Baktash E., Pfrommer J., Schwarze M., Dau H., and Driess M., *Active mixed-valent MnO(x) water oxidation catalysts through partial oxidation (corrosion) of nanostructured MnO particles.* Angew Chem Int Ed Engl, 2013. 52(50): p. 13206-10.
54. Najafpour M. M., Ehrenberg T., Wiechen M., and Kurz P., *Calcium manganese(III) oxides (CaMn2O4.xH2O) as biomimetic oxygen-evolving catalysts.* Angew Chem Int Ed Engl, 2010. 49(12): p. 2233-7.
55. Wiechen Mathias, Zaharieva Ivelina, Dau Holger, and Kurz Philipp, *Layered manganese oxides for water-oxidation: alkaline earth cations influence catalytic activity in a photosystem II-like fashion.* Chemical Science, 2012. 3(7): p. 2330.
56. Pinaud Blaise A., Chen Zhebo, Abram David N., and Jaramillo Thomas F., *Thin Films of Sodium Birnessite-Type MnO2: Optical Properties, Electronic Band Structure, and Solar Photoelectrochemistry.* The Journal of Physical Chemistry C, 2011. 115(23): p. 11830-11838.
57. Takashima T., Hashimoto K., and Nakamura R., *Mechanisms of pH-dependent activity for water oxidation to molecular oxygen by MnO2 electrocatalysts.* J Am Chem Soc, 2012. 134(3): p. 1519-27.

58. Iyer Aparna, Del-Pilar Joselyn, King'ondu Cecil K., Kissel Edward, Garces Hector F., Huang Hui, El-Sawy Abdelhamid M., Dutta Prabir K., and Suib Steven L., *Water Oxidation Catalysis using Amorphous Manganese Oxides, Octahedral Molecular Sieves (OMS-2), and Octahedral Layered (OL-1) Manganese Oxide Structures.* The Journal of Physical Chemistry C, 2012. 116(10): p. 6474-6483.
59. Gao M. R., Xu Y. F., Jiang J., Zheng Y. R., and Yu S. H., *Water oxidation electrocatalyzed by an efficient Mn3O4/CoSe2 nanocomposite.* J Am Chem Soc, 2012. 134(6): p. 2930-3.
60. Najafpour Mohammad Mahdi, Hosseini Seyedeh Maedeh, Hołyńska Małgorzata, Tomo Tatsuya, and Allakhverdiev Suleyman I., *Platinum/manganese oxide nanocomposites as water-oxidizing catalysts: New findings and current controversies.* International Journal of Hydrogen Energy, 2015. 40(34): p. 10825-10832.
61. Izgorodin Alex, Hocking Rosalie, Winther-Jensen Orawan, Hilder Matthias, Winther-Jensen Bjorn, and MacFarlane Douglas R., *Phosphorylated manganese oxide electrodeposited from ionic liquid as a stable, high efficiency water oxidation catalyst.* Catalysis Today, 2013. 200: p. 36-40.
62. Cao Xuecheng, Yan Wenning, Jin Chao, Tian Jinghua, Ke Ke, and Yang Ruizhi, *Surface modification of MnCo2O4 with conducting polypyrrole as a highly active bifunctional electrocatalyst for oxygen reduction and oxygen evolution reaction.* Electrochimica Acta, 2015. 180: p. 788-794.
63. Gao Qiang, Ranjan Chinmoy, Pavlovic Zoran, Blume Raoul, and Schlögl Robert, *Enhancement of Stability and Activity of MnOx/Au Electrocatalysts for Oxygen Evolution through Adequate Electrolyte Composition.* ACS Catalysis, 2015. 5(12): p. 7265-7275.
64. Yang Jingxiu, An Hongyu, Zhou Xin, and Li Can, *Water Oxidation Mechanism on Alkaline-Earth-Cation Containing Birnessite-Like Manganese Oxides.* The Journal of Physical Chemistry C, 2015. 119(32): p. 18487-18494.
65. Lucht Kevin P. and Mendoza-Cortes Jose L., *Birnessite: A Layered Manganese Oxide To Capture Sunlight for Water-Splitting Catalysis.* The Journal of Physical Chemistry C, 2015. 119(40): p. 22838-22846.
66. Thenuwara A. C., Shumlas S. L., Attanayake N. H., Cerkez E. B., McKendry I. G., Frazer L., Borguet E., Kang Q., Zdilla M. J., Sun J., and Strongin D. R., *Copper-Intercalated Birnessite as a Water Oxidation Catalyst.* Langmuir, 2015. 31(46): p. 12807-13.
67. Najafpour M. M. and Abbasi Isaloo M., *The mechanism of water oxidation catalyzed by nanolayered manganese oxides: New insights.* J Photochem Photobiol B, 2015. 152(Pt A): p. 133-8.
68. Gorlin Y., Lassalle-Kaiser B., Benck J. D., Gul S., Webb S. M., Yachandra V. K., Yano J., and Jaramillo T. F., *In situ X-ray absorption spectroscopy investigation of a bifunctional manganese oxide catalyst with high activity for electrochemical water oxidation and oxygen reduction.* J Am Chem Soc, 2013. 135(23): p. 8525-34.
69. Babakhani Banafsheh and Ivey Douglas G., *Anodic deposition of manganese oxide electrodes with rod-like structures for application as electrochemical capacitors.* Journal of Power Sources, 2010. 195(7): p. 2110-2117.
70. Zhou F., Izgorodin A., Hocking R. K., Armel V., Spiccia L., and Macfarlane D. R., *Improvement of catalytic water oxidation on MnOx films by heat treatment.* ChemSusChem, 2013. 6(4): p. 643-51.
71. Babakhani Banafsheh and Ivey Douglas G., *Effect of electrodeposition conditions on the electrochemical capacitive behavior of synthesized manganese oxide electrodes.* Journal of Power Sources, 2011. 196(24): p. 10762-10774.
72. Kawashima Takuya, Ezure Tetsuya, Okada Kenichi, Matsui Hiroshi, Goto Kenji, and Tanabe Nobuo, *FTO/ITO double-layered transparent conductive oxide for dye-sensitized solar cells.* Journal of Photochemistry and Photobiology A: Chemistry, 2004. 164(1–3): p. 199-202.
73. Yang Xunyu, Wolcott Abraham, Wang Gongming, Sobo Alissa, Fitzmorris Robert Carl, Qian Fang, Zhang Jin Z, and Li Yat, *Nitrogen-doped ZnO nanowire arrays for photoelectrochemical water splitting.* Nano Letters, 2009. 9(6): p. 2331-2336.

74. Zhang Li, Fang Zhen, Ni Yonghong, and Zhao Guangchao, *Direct electrocatalytic oxidation of hydrogen peroxide based on nafion and microspheres MnO2 modified glass carbon electrode.* Int. J. Electrochem. Soc, 2009. 4: p. 407-413.
75. Zhou Fengling, Izgorodin Alexey, Hocking Rosalie K., Spiccia Leone, and MacFarlane Douglas R., *Electrodeposited MnOx Films from Ionic Liquid for Electrocatalytic Water Oxidation.* Advanced Energy Materials, 2012. 2(8): p. 1013-1021.
76. Osowiecki W. T., Sheehan S. W., Young K. J., Durrell A. C., Mercado B. Q., and Brudvig G. W., *Surfactant-mediated electrodeposition of a water-oxidizing manganese oxide.* Dalton Trans, 2015. 44(38): p. 16873-81.
77. Hayes Scott A., Yu Pu, O'Keefe Thomas J., O'Keefe Matthew J., and Stoffer James O., *The Phase Stability of Cerium Species in Aqueous Systems: I. E-pH Diagram for the Ce - HClO 4 - H 2 O System.* Journal of The Electrochemical Society, 2002. 149(12): p. C623-C630.
78. Parent A. R., Crabtree R. H., and Brudvig G. W., *Comparison of primary oxidants for water-oxidation catalysis.* Chem Soc Rev, 2013. 42(6): p. 2247-52.
79. Shi X., Cai L., Ma M., Zheng X., and Park J. H., *General Characterization Methods for Photoelectrochemical Cells for Solar Water Splitting.* ChemSusChem, 2015. 8(19): p. 3192-203.
80. Clegg William, *Crystal structure determination.* Oxford Chemistry Primers, 1998. 60(1): p. ALL-ALL.
81. Giacovazzo Carmelo, *Fundamentals of crystallography*. Vol. 7. 2002: Oxford University Press, USA.
82. Todokoro H. and Ezumi M., *Scanning electron microscope*. 1999, Google Patents.
83. Eaton Peter and West Paul, *Atomic force microscopy*. 2010: Oxford University Press.
84. Meyer ERNST, *Atomic force microscopy.* Progress in surface science, 1992. 41(1): p. 3-49.
85. Legleiter Justin and Kowalewski Tomasz, *Atomic Force Microscopy.* 2006. 4: p. 315-334.
86. Wooten Frederick, *Optical properties of solids*. 2013: Academic press.
87. Watts John F, *X-ray photoelectron spectroscopy.* Surface science techniques, 1994: p. 5-23.
88. Paterson E and Swaffield R, *X-ray photoelectron spectroscopy*, in *Clay Mineralogy: Spectroscopic and Chemical Determinative Methods*. 1994, Springer. p. 226-259.
89. Bard Allen J, Faulkner Larry R, Leddy Johna, and Zoski Cynthia G, *Electrochemical methods: fundamentals and applications*. Vol. 2. 1980: Wiley New York.
90. Lasia Andrzej, *Electrochemical impedance spectroscopy and its applications*. 2014: Springer.
91. Suhasini, *Effect of deposition method and the surfactant on high capacitance of electrochemically deposited MnO2 on stainless steel substrate.* Journal of Electroanalytical Chemistry, 2013. 690: p. 13-18.
92. Meng Y., Song W., Huang H., Ren Z., Chen S. Y., and Suib S. L., *Structure-property relationship of bifunctional MnO2 nanostructures: highly efficient, ultra-stable electrochemical water oxidation and oxygen reduction reaction catalysts identified in alkaline media.* J Am Chem Soc, 2014. 136(32): p. 11452-64.
93. Lyons Michael E. G. and Brandon Michael P., *The significance of electrochemical impedance spectra recorded during active oxygen evolution for oxide covered Ni, Co and Fe electrodes in alkaline solution.* Journal of Electroanalytical Chemistry, 2009. 631(1-2): p. 62-70.
94. Doyle R. L. and Lyons M. E. G., *Kinetics and Mechanistic Aspects of the Oxygen Evolution Reaction at Hydrous Iron Oxide Films in Base.* Journal of the Electrochemical Society, 2013. 160(2): p. H142-H154.
95. Doyle R. L. and Lyons M. E., *An electrochemical impedance study of the oxygen evolution reaction at hydrous iron oxide in base.* Phys Chem Chem Phys, 2013. 15(14): p. 5224-37.
96. Devaraj S. and Munichandraiah N., *Electrochemical Supercapacitor Studies of Nanostructured α-MnO[sub 2] Synthesized by Microemulsion Method and the Effect of Annealing.* Journal of The Electrochemical Society, 2007. 154(2): p. A80.
97. Wu Yuanzhan, Liu Suqin, Zhao Kuangmin, He Zhen, Lv Kezhou, and Ye Guangying, *Synthesis of δ-MnO2 film on FTO glass with high electrochemical performance.* Ionics, 2015.

98. Chou Shulei, Cheng Fangyi, and Chen Jun, *Electrodeposition synthesis and electrochemical properties of nanostructured γ-MnO2 films.* Journal of Power Sources, 2006. 162(1): p. 727-734.
99. Singh A., Fekete M., Gengenbach T., Simonov A. N., Hocking R. K., Chang S. L., Rothmann M., Powar S., Fu D., Hu Z., Wu Q., Cheng Y. B., Bach U., and Spiccia L., *Catalytic Activity and Impedance Behavior of Screen-Printed Nickel Oxide as Efficient Water Oxidation Catalysts.* ChemSusChem, 2015. 8(24): p. 4266-74.
100. Zhang C., Berlinguette C. P., and Trudel S., *Water oxidation catalysis: an amorphous quaternary Ba-Sr-Co-Fe oxide as a promising electrocatalyst for the oxygen-evolution reaction.* Chem Commun (Camb), 2016. 52(7): p. 1513-6.
101. Jin Chao, Lu Fanliang, Cao Xuecheng, Yang Zhenrong, and Yang Ruizhi, *Facile synthesis and excellent electrochemical properties of NiCo2O4 spinel nanowire arrays as a bifunctional catalyst for the oxygen reduction and evolution reaction.* Journal of Materials Chemistry A, 2013. 1(39): p. 12170.
102. Wang Lianzhou, Omomo Yoshitomo, Sakai Nobuyuki, Fukuda Katsutoshi, Nakai Izumi, Ebina Yasuo, Takada Kazunori, Watanabe Mamoru, and Sasaki Takayoshi, *Fabrication and characterization of multilayer ultrathin films of exfoliated MnO2 nanosheets and polycations.* Chemistry of materials, 2003. 15(15): p. 2873-2878.
103. Omomo Yoshitomo, Sasaki Takayoshi, Wang Lianzhou, and Watanabe Mamoru, *Redoxable nanosheet crystallites of MnO2 derived via delamination of a layered manganese oxide.* Journal of the American Chemical Society, 2003. 125(12): p. 3568-3575.
104. RODRIGUES SHALINI, MUNICHANDRAIAHà N., and SHUKLA A. K., *A cyclic voltammetric study of the kinetics and mechanism of electrodeposition of manganese dioxide.* Journal of Applied Electrochemistry, 1998. 28: p. 7.
105. Clarke Colin J., Browning Gregory J., and Donne Scott W., *An RDE and RRDE study into the electrodeposition of manganese dioxide.* Electrochimica Acta, 2006. 51(26): p. 5773-5784.
106. Huynh Michael, Bediako D. Kwabena, Liu Yi, and Nocera Daniel G., *Nucleation and Growth Mechanisms of an Electrodeposited Manganese Oxide Oxygen Evolution Catalyst.* The Journal of Physical Chemistry C, 2014. 118(30): p. 17142-17152.
107. Broughton J. N. and Brett M. J., *Variations in MnO2 electrodeposition for electrochemical capacitors.* Electrochimica Acta, 2005. 50(24): p. 4814-4819.
108. Kodera Fumihiro, Kuwahara Yu, Nakazawa Akira, and Umeda Minoru, *Electrochemical corrosion of platinum electrode in concentrated sulfuric acid.* Journal of Power Sources, 2007. 172(2): p. 698-703.
109. Aljabali A. A., Barclay J. E., Butt J. N., Lomonossoff G. P., and Evans D. J., *Redox-active ferrocene-modified Cowpea mosaic virus nanoparticles.* Dalton Trans, 2010. 39(32): p. 7569-74.
110. Cherchour N., Deslouis C., Messaoudi B., and Pailleret A., *pH sensing in aqueous solutions using a MnO2 thin film electrodeposited on a glassy carbon electrode.* Electrochimica Acta, 2011. 56(27): p. 9746-9755.
111. Rogulski Z, Chotkowski M, and Czerwinski A, *Electrochemical behavior of MnO2/RVC system.* Journal of New Materials for Electrochemical Systems, 2006. 9(4): p. 401.
112. Dupont Madeleine F. and Donne Scott W., *Nucleation and Growth of Electrodeposited Manganese Dioxide for Electrochemical Capacitors.* Electrochimica Acta, 2014. 120: p. 219-225.
113. Nijjer S, Thonstad J, and Haarberg GM, *Oxidation of manganese (II) and reduction of manganese dioxide in sulphuric acid.* Electrochimica acta, 2000. 46(2): p. 395-399.
114. Ratcliff Erin L., Lee Paul A., and Armstrong Neal R., *Work function control of hole-selective polymer/ITO anode contacts: an electrochemical doping study.* Journal of Materials Chemistry, 2010. 20(13): p. 2672.
115. Marrikar F Saneeha, Brumbach Michael, Evans Dennis H, Lebrón-Paler Ariel, Pemberton Jeanne E, Wysocki Ronald J, and Armstrong Neal R, *Modification of indium-tin oxide electrodes with thiophene copolymer thin films: Optimizing electron transfer to solution probe molecules.* Langmuir, 2007. 23(3): p. 1530-1542.

116. Michael Brumbach, P. Alex Veneman, F. Saneeha Marrikar, Thomas Schulmeyer, Adam Simmonds, Wei Xia, Paul Lee, and Armstrong Neal R., *Surface Composition and Electrical and Electrochemical Properties of Freshly Deposited and Acid-Etched Indium Tin Oxide Electrodes.* Langmuir, 2007. 23: p. 11.
117. Kraft A, Hennig H, Herbst A, and Heckner K-H, *Changes in electrochemical and photoelectrochemical properties of tin-doped indium oxide layers after strong anodic polarization.* Journal of Electroanalytical Chemistry, 1994. 365(1-2): p. 191-196.
118. Senthilkumar M., Mathiyarasu J., Joseph James, Phani K. L. N., and Yegnaraman V., *Electrochemical instability of indium tin oxide (ITO) glass in acidic pH range during cathodic polarization.* Materials Chemistry and Physics, 2008. 108(2-3): p. 403-407.
119. Huang M., Zhang Y., Li F., Zhang L., Ruoff R. S., Wen Z., and Liu Q., *Self-assembly of mesoporous nanotubes assembled from interwoven ultrathin birnessite-type MnO2 nanosheets for asymmetric supercapacitors.* Sci Rep, 2014. 4: p. 3878.
120. Zhou Y. K., Toupin M., Bélanger D., Brousse T., and Favier F., *Electrochemical preparation and characterization of Birnessite-type layered manganese oxide films.* Journal of Physics and Chemistry of Solids, 2006. 67(5-6): p. 1351-1354.
121. Yilmaz Neval, Ida Shintaro, and Matsumoto Yasumichi, *Electrical conductivities of nanosheets studied by conductive atomic force microscopy.* Materials Chemistry and Physics, 2009. 116(1): p. 62-66.
122. Kawashima Takuya, Matsui Hiroshi, and Tanabe Nobuo, *New transparent conductive films: FTO coated ITO.* Thin Solid Films, 2003. 445(2): p. 241-244.
123. Cid C. C. Plá, Spada E. R., and Sartorelli M. L., *Effect of the cathodic polarization on structural and morphological proprieties of FTO and ITO thin films.* Applied Surface Science, 2013. 273: p. 603-606.
124. Han Chi-Hwan, Han Sang-Do, Gwak Jihye, and Khatkar S. P., *Synthesis of indium tin oxide (ITO) and fluorine-doped tin oxide (FTO) nano-powder by sol–gel combustion hybrid method.* Materials Letters, 2007. 61(8-9): p. 1701-1703.
125. Khan M., Xiao J., Zhou F., Yablonskikh M., MacFarlane D. R., Spiccia L., and Aziz E. F., *On the Origin of the Improvement of Electrodeposited MnOx Films in Water Oxidation Catalysis Induced by Heat Treatment.* ChemSusChem, 2015. 8(11): p. 1980-5.
126. Ling Y., Wang G., Wheeler D. A., Zhang J. Z., and Li Y., *Sn-doped hematite nanostructures for photoelectrochemical water splitting.* Nano Lett, 2011. 11(5): p. 2119-25.
127. Lei Shuijin, Tang Kaibin, Fang Zhen, Liu Qiangchun, and Zheng Huagui, *Preparation of α-Mn2O3 and MnO from thermal decomposition of MnCO3 and control of morphology.* Materials Letters, 2006. 60(1): p. 53-56.
128. Wang Hong-En and Qian Dong, *Synthesis and electrochemical properties of α-MnO2 microspheres.* Materials Chemistry and Physics, 2008. 109(2-3): p. 399-403.
129. Wiechen M., Berends H. M., and Kurz P., *Water oxidation catalysed by manganese compounds: from complexes to 'biomimetic rocks'.* Dalton Trans, 2012. 41(1): p. 21-31.
130. Boussac Alain, Zimmermann Jean-Luc, and Rutherford A William, *Factors influencing the formation of modified S2 EPR signal and the S3 EPR signal in Ca2+-depleted photosystem II.* FEBS letters, 1990. 277(1-2): p. 69-74.
131. Boppana Venkata Bharat Ram, Yusuf Seif, Hutchings Gregory S., and Jiao Feng, *Nanostructured Alkaline-Cation-Containing δ-MnO2for Photocatalytic Water Oxidation.* Advanced Functional Materials, 2013. 23(7): p. 878-884.
132. Arias Carlota Ridruejo, Debiemme-Chouvy Catherine, Gabrielli Claude, Laberty-Robert Christel, Pailleret Alain, Perrot Hubert, and Sel Ozlem, *New Insights into Pseudocapacitive Charge-Storage Mechanisms in Li-Birnessite Type MnO2 Monitored by Fast Quartz Crystal Microbalance Methods.* The Journal of Physical Chemistry C, 2014. 118(46): p. 26551-26559.

Appendix

A.1 Calibration of reference electrode

The reference electrode plays an important role in electrochemistry as the applied potential values systematically refer to it in a three-electrode cell. The potential of the reference electrode might vary due to a change of the expected composition of the inside electrolyte solution or to a chemical contamination. Thus, the potential value of a reference electrode needs to be checked regularly after a time of use.

In order to measure the potential value of each reference electrode, cyclic voltammetry experiments were carried out in a three-electrode cell containing an electrolytic aqueous solution in the presence of the well-known $K_4Fe(CN)_6/K_3Fe(CN)_6$ redox couple using different reference electrodes. Typical CV curves are shown below.

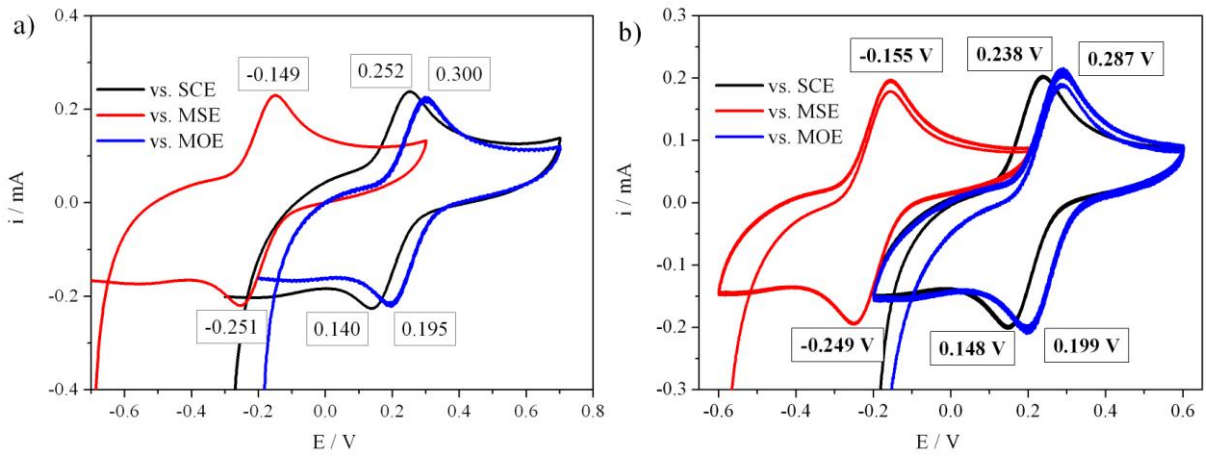

Figure A.1: Cyclic voltammograms dedicated to potential measurement of reference electrodes. Electrolytic solution: $K_4Fe(CN)_6/K_3Fe(CN)_6$ (2 mM), KNO_3 (0.1 M). Scan rate: 100 mV/s. Deaerated by N_2 for 30 min before each test.

From the figure shown above, all of the CV curves have the same shape no matter which reference electrode is used. The peak potential values measured on this Figure are listed in Table A.1. According to this table, the potentials of these two reference electrodes have slightly shifted in those two tests, but the shifts are very small. The average peak potential values were used to calculate the potential difference between two different reference electrodes and the result is shown in Table A.2.

Here, the new purchased commercial SCE electrode was used as a standard. Its theoretical potential value is 0.244 V vs. NHE. The calculated potential difference is -0.396 V for MSE vs. SCE and 0.051 V for MOE vs. SCE. Thus, the potential difference versus NHE is 0.640 V for MSE and 0.193 V for MOE.

Table A.1: Peak potential in CV curves / V

Reference electrode	Peak potential / V vs. MSE		Peak potential / V vs. SCE		Peak potential / V vs. MOE	
	anodic	cathodic	anodic	cathodic	anodic	cathodic
Test 1	-0.251	-0.149	0.140	0.252	0.195	0.300
Test 2	-0.249	-0.155	0.148	0.238	0.199	0.287
difference	0.002	-0.006	0.008	-0.014	0.004	-0.013
Average	-0.250	-0.152	0.144	-0.245	0.197	0.294

Table A.2: Potential difference between reference electrodes / V

Potential difference	Anodic	Cathodic	Average	Potential vs. NHE
SSE vs. SCE	-0.394	-0.397	-0.396	0.640
MOE vs. SCE	0.053	0.049	0.051	0.193

For a given electrolyte, the reaction potential verses NHE can be calculated according to the pH of the electrolyte using the following equation:

$$E_{NHE} = E_{measure} + E_{Ref} + 0.05916\text{pH}$$

For the OER test, the measured pH of 0.1 M NaOH electrolyte is 12.5, thus the potential versus NHE can be calculated by:

$$E_{NHE} = E_{measure} + 0.193 + 0.05916\times 12.5 = E_{measure} + 0.9325$$

A.2 Calibration of solar simulator

The light intensity is a key parameter for solar water splitting. Usually, an artificial light identical to the intensity of natural sunlight (about 100 mW/cm^2) is used for such experiments. The simulated solar light used in this thesis is provided by a xenon lamp, and then conducted through an optical fiber to the surface of MnO_2 samples. Thus, a calibration procedure is needed to make the results convincing and reproducible.

The output of the solar simulator was set to be 15 A with the 300 W xenon lamp in order to get stable and safe solar light. The influence factor includes the distance from the sample surface to the output of the optical fiber and the aperture size. The influence of the distance from the light source to the radiometer on the delivered light intensity is shown below, and clearly, the relation between the light intensity and the distance is linear, and can therefore be modeled using the formula that is shown inside the figure. According to the result, a distance of 26.2 cm will provide the correct position to deliver light intensity of one sun on the sample.

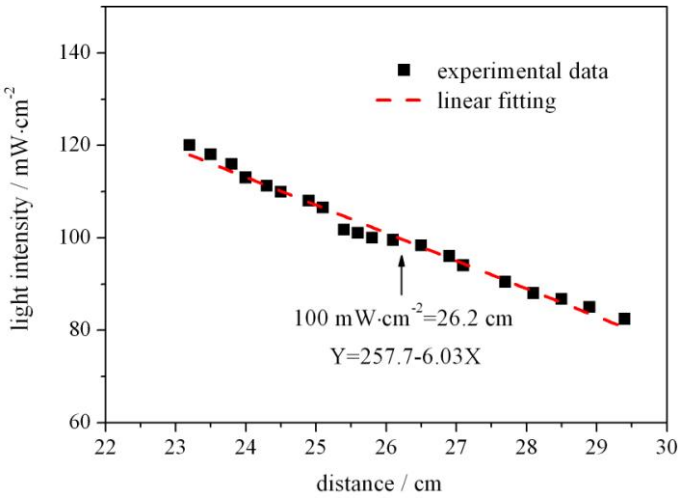

Figure A.2: Test of the distance between the light source and the radiometer.

In order to confirm the optimized distance, the light illuminated the radiometer from vertical and horizontal directions respectively, and the result is shown on Figure A.3. Obviously, no matter which direction was chosen, the optimized distance leading to one sun light intensity is around 26.2 cm, which is consistent with the result given above.

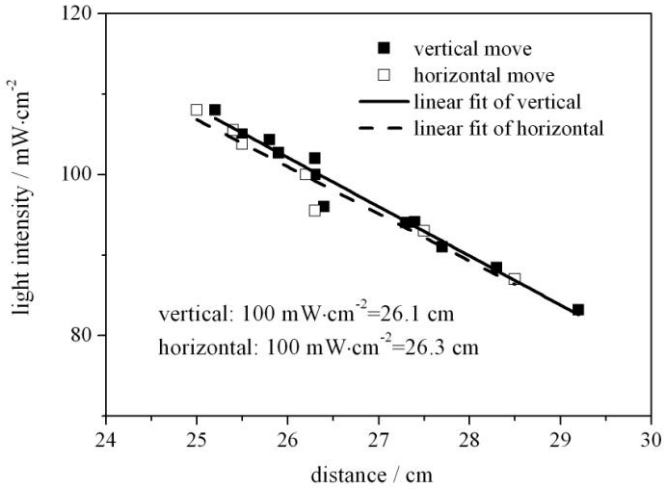

Figure A.3: Light intensity variation as a function of the distance between the light source and the radiometer from two directions.

In addition, changing the aperture size is another way to adjust the intensity of the simulated solar light. The result of the test is shown below. Either the light intensity or the distance was fixed. Clearly, the distance and the aperture size both have a linear correlation when the light intensity is fixed to 1 sun. However, when the distance is fixed, the light intensity is saturated at the aperture position 4.0 cm (here the position means the distance of the knob to the original point where the aperture is totally closed.), thus the full aperture will always provide the most intense light at given output parameters. It is also noteworthy that with 10 cm distance, the full light intensity could reach about 500 mW/cm^2, which is nearly 5 times the power of natural solar light. Thus, shortening the distance between the light source and the sample surface provides a practical method to obtain solar water splitting activity under high-energy light illumination.

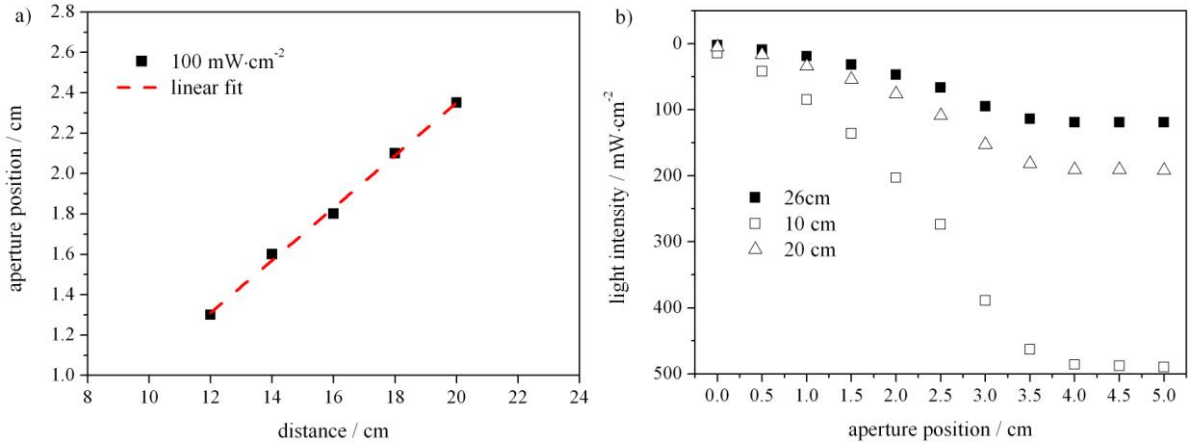

Figure A.4: Intensity test for different aperture positions.

Since the simulated light illuminates through a transparent quartz disc, there might be some attenuation due to the absorbance and reflection of the quartz. To evaluate the influence, the light intensity measurement with and without quartz disc was carried out and the result is listed in Table A.3. In average, about 6 % of attenuation appears after the light crosses the quartz disc, thus the distance in Figure A.3 should be corrected to 25.1 cm in order to get one-sun light intensity.

Table A.3: The influence of quartz window

Light intensity without quartz	Light intensity with quartz	difference	Decrease percentage / %
105.5	99.2	6.3	5.971564
109	102.5	6.5	5.963303
115.3	108.6	6.7	5.810928
108	102	6	5.555556
104	97.8	6.2	5.961538
100	94.4	5.6	5.6

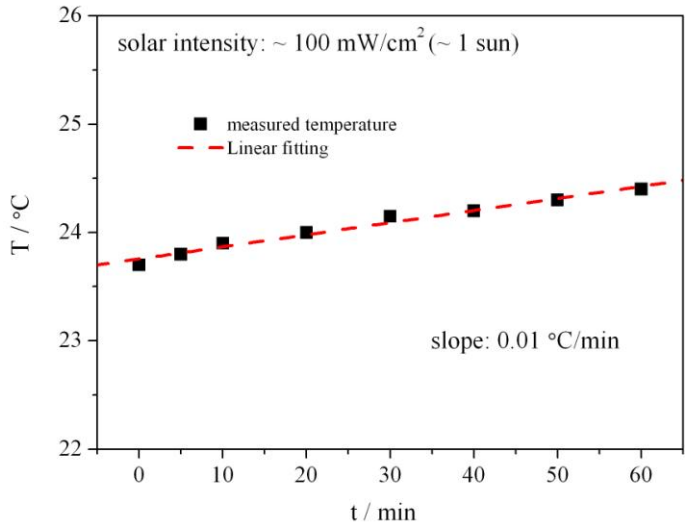

Figure A.5: Heating effect test under light illumination

Moreover, the temperature is also an important factor for the electrocatalytic performances of materials. The heating effect should also be considered when using 1 sun light illumination. In this sense, the temperature change under light illumination was evaluated. As shown in Figure A5, the temperature of the electrolyte increases a bit under lightening, while the change is only 0.01 °C/min, which is a really small value. Considering

that the solar water splitting tests were carried out with a duration shorter than 30 min, the heat effect should not be considered as an explanation for electrocatalytic activity changes observed under light illumination.

Table list

Figure list

ABSTRACT: The basic electrodeposition mechanism of MnO_2 films was studied first on bulk Pt electrodes in various aqueous. It was revealed that MnO_2 electrodeposition is a multi-step reaction that is sensitive to pH and ionic strength. Chronoamperometry coupled to low concentration neutral aqueous solutions favors the electrodeposition of stable MnO_2 films. FTO was found to be a better substrate than ITO, because it has a higher electrochemical activity and could enhance the mechanical stability of electrodeposited MnO_2 films. Moreover, the potential used for electrodeposition has great influence on both the structure and the morphology of MnO_2 films. Amorphous MnO_2 films obtained at high potential possess higher electrocatalytic activity and stability than the birnessite-type MnO_2 variety. The heat treatment can greatly enhance the electrocatalytic activity and mechanical stability. A phase transition of MnO_2 films appears at 500 °C. The morphology changes dramatically after heating above this temperature. Samples heated at 500 °C are found to have the best electrocatalytic activity towards OER. Na^+, K^+, Ca^{2+} and Mg^{2+} cations were found to be inserted in small amounts into the structure of MnO_2 films during the electrodeposition procedure but they influence the structure and morphology of the films. Finally, birnessite type and amorphous MnO_2 films appear to be promising candidates as catalysts for photoelectrochemical water splitting, as they are able to generate considerable photocurrents under solar light illumination. In this purpose, thick and amorphous films with 500 °C heat treatment are supposed to produce the best performances.

Keywords: electrodeposition, MnO_2 thin films, PhotoElectroChemical Water Splitting, Oxygen Evolution Reaction, heat treatment, cation insertion

RESUME: Le mécanisme élémentaire de l'électrodépôt de films de MnO_2 fût étudié sur des électrodes de Pt massif dans des électrolytes aqueux. Il se révèle être une réaction multi-étapes sensible au pH et à la force ionique. La chronoampérométrie couplée à des électrolytes neutres peu concentrés favorise l'électrodépôt de films stables de MnO_2. Le FTO est un meilleur substrat que l'ITO parce qu'il présente une activité électrochimique plus élevée et favorise la stabilité mécanique de films électrodéposés de MnO_2. De plus, le potentiel d'électrodépôt influence à la fois la structure et la morphologie des films de MnO_2. Les films amorphes de MnO_2 obtenus à potentiel élevé possèdent une activité électrocatalytique et une stabilité plus élevées que la birnessite. Un traitement thermique peut améliorer amplement leur activité électrocatalytique et leur stabilité mécanique. Une transition de phase des films de MnO_2 apparaît à 500 °C. Leur morphologie change de façon dramatique après chauffage au-delà de cette température. Les échantillons chauffés à 500 °C ont la meilleure activité électrocatalytique pour l'OER. Les cations Na^+, K^+, Ca^{2+} and Mg^{2+} sont insérés en petites quantités dans la structure des films de MnO_2 au cours de la démarche d'électrodépôt, mais ils influencent néanmoins la structure et la morphologie des films. Finalement, les films de birnessite ou amorphes apparaissent comme des candidats prometteurs en tant que catalyseurs pour la dissociation photoélectrochimique de la dissociation de l'eau, puisqu'ils génèrent des photocourants considérables sous lumière solaire. Pour cela, des films de MnO_2 épais, amorphes et recuits à 500 °C produisent les meilleures performances.

Mots-clés: électrodépôt, couches minces de MnO_2, dissociation photoélectrochimique de l'eau, réaction de production de l'oxygène, traitement thermique, insertion de cations